Technische Universität München

Max-Planck-Institut für Astrophysik

Exploring the Diversity in Hydrogen-Deficient Supernovae

Stefan Taubenberger

Vollständiger Abdruck der von der Fakultät für Physik der Technischen Universität München zur Erlangung des akademischen Grades eines

Doktors der Naturwissenschaften (Dr. rer. nat.)

genehmigten Dissertation.

Vorsitzender:	Univ.-Prof. Dr. L. Oberauer
Prüfer der Dissertation:	
1.	Hon.-Prof. Dr. W. Hillebrandt
2.	Univ.-Prof. Dr. R. Krücken

Die Dissertation wurde am 22. 2. 2008 bei der Technischen Universität München eingereicht und durch die Fakultät für Physik am 11. 4. 2008 angenommen.

Contents

List of Tables

List of Figures

1

Introduction

The interest in supernovae (SNe) nowadays is manifold. They are among the best tools to study the star formation history out to a redshift $z > 1$, give an important contribution to the chemical enrichment of the universe through the release of the progenitor star's and their own nucleosynthesis products into space, and can be used to constrain the late evolutionary phases of stars. Moreover, they may be the key for understanding long-duration γ-ray bursts (GRBs), which some core-collapse SNe are associated with. SN shock waves trigger vigorous bursts of star formation by compressing dense molecular clouds, and accelerate cosmic particles to extraordinarily high energies, far beyond the capabilities of any human-made accelerator, thus potentially opening a window to new physics beyond the standard model of particle physics. The strong neutrino signal of a Galactic SN (core-collapse SNe release 99% of their energy in form of neutrinos) could be used to better study these elementary particles, likewise improving the standard model of particle physics. Last but not least, SNe are the most precise distance indicators in the distant universe to date, and have contributed a lot to our present cosmological understanding, including the establishment of some kind of Dark Energy. Still they are considered the primary tool to further constrain the properties of this Dark Energy.

Most of these 'applications' only need very specific, limited input from SNe. For precision cosmology, a recipe to calibrate the absolute luminosity of Type Ia SNe to a standard value, along with a guarantee that the SN properties do not evolve significantly on cosmic timescales, would be sufficient. Similarly, for star-formation-history studies, only exact, type-dependent SN rates and delay-time distributions are of interest.

To be able to supply these quantities and relations with the required preci-

TABLE 1.1— Historical Galactic supernovae during the past millennium (Fesen, 2005; Stephenson & Green, 2005).

Date	Constell.	α	δ	m_{app}	Type	Remnant
1006 Apr 30	Lup	15h 02.8m	$-41°57'$	-9	Ia	PKS 1459-41
1054 Jul 4	Tau	05h 34.5m	$+22°01'$	-6	II_{pec}	M1 Crab Nebula
1181 Aug 6	Cas	02h 05.6m	$+64°49'$	-1	II_{pec}	3C 58
1572 Nov 6	Cas	00h 25.3m	$+64°09'$	-4	Ia	3C 10 (Tycho)
1604 Oct 9	Oph	17h 30.6m	$-21°29'$	-3	?	3C 358 (Kepler)
1680 ?	Cas	23h 23.4m	$+58°50'$	?	Ib/c or IIb	Cas A

sion, a decent understanding of the underlying SN physics is usually essential. Hence, the advance in a number of fields in astronomy, astrophysics and cosmology sensitively depends on the progress made in SN research, making it not an end in itself, and justifying strong efforts. Of course, being among the most violent and energetic events in the universe, SNe are also worthwhile studying on their own merit.

1.1 Historical overview and SN classification

Over centuries people have been fascinated and threatened at the same time by Galactic supernovae, some of which were bright enough to be visible during daytime with the naked eye (see Table 1.1). For some of these 'guest stars' detailed records of their brightness evolution and remarkably precise astrometry exist. The lack of a parallax found for the SNe in 1572 and 1604 by Tycho Brahe and Johannes Kepler, respectively, contradicted the Aristotelean view of a cosmos organised in spheres, the earth in their centre and with no changes allowed in the most distant sphere. Eventually, these observations and their interpretation by Kepler and Galileo Galilei paved the way for a new, heliocentric view of the world (Gingerich, 2005; Lombardi, 2005; Shea, 2005). For other two SNe in 1054 and 1181 no reports on European observations are known. However, these events were recorded by Chinese and other East-Asian astronomers, like most other Galactic SNe of the past millennium as well (Stephenson & Green, 2005; Wang, 2005). The exception is the Cas A SN which escaped detection except, maybe, for a controversy sighting by Flamsteed in 1680. Nowadays the gaseous and compact remnants of these Galactic SNe are studied at all frequencies from γ-rays and X-rays to the radio regime to infer the explosion kinematics, nucleosynthesis yields and spatial distribution of the various chemical species within the ejecta, providing information complementary to that collected through direct observations of newly discovered SNe.

The onset of modern SN research, however, dates back to 1885, when a 'new star' was discovered in the Andromeda galaxy (see de Vaucouleurs & Corwin, 1985, for a historical review on this event). For the first time, astronomers equipped with telescopes could study the brightness evolution of an extragalactic SN, an object which even at maximum brightness was at best marginally visible to the unaided eye. Ironically, with its very narrow light-curve peak and an extremely fast rise to and decline from maximum brightness (de Vaucouleurs & Corwin, 1985), this first modern-time SN showed highly peculiar photometric properties, and seems to fit into none of the later-defined SN classes (though some authors consider it an underluminous SN Ia, cf. van den Bergh 1994, Fesen et al. 1999 and Fesen et al. 2007). In fact, it has almost no counterpart in the present-day archives containing thousands of SNe except, maybe, for some objects of the newly established class of Ibn SNe (Pastorello et al., 2008).

In the 20^{th} century, pioneering work in SN observations was mainly done by Fritz Zwicky and Walter Baade. After Lundmark (1920) had realised that SNe were distinct from ordinary novae, separated by several orders of magnitude in luminosity, it was them who actually invented the term 'supernova'. Between 1936 and 1941, Baade and Zwicky conducted the first systematic supernova search using the Palomar 18-inch Schmidt telescope, which led to the discovery of 19 SNe. From spectroscopic observations it soon became evident that at least two classes of SNe existed: those which showed broad lines of the hydrogen Balmer series in their spectra, and those which did not. Minkowski (1941) labelled them Type II and Type I, respectively, thus laying the foundation for the SN classification scheme still in use. By the 1960s, thanks to international SN searches coordinated by Zwicky, ~ 100 SNe had been discovered, and three other SN types were added (III, IV and V, Zwicky 1964). All these SNe showed evidence of hydrogen in their spectra, but peculiar light curves compared to the classical Type II SNe. The prototype of the Type V objects was the famous SN 1961V. Nowadays we believe that the Type V objects are likely not genuine SNe, but super-outbursts of luminous blue variable stars resembling η Carinae (Goodrich et al., 1989; Filippenko et al., 1995b). As a step towards modern SN taxonomy, in the 1980s the hydrogen-deficient Type I SNe were further divided into Type Ia (with characteristic, strong Si II features in the maximum-light spectra, and quite homogeneous in their appearance), Type Ib (with strong He I lines) and Type Ic SNe (with neither strong Si II nor He I). While a thermonuclear disruption of a white dwarf was established as the most promising model for SNe Ia, Type Ib and Ic SNe have been interpreted as core-collapse events in massive stars which, in contrast to the progenitors of Type II SNe, had lost their H (Type Ib) or their H and He envelopes (Type Ic) prior to explosion.

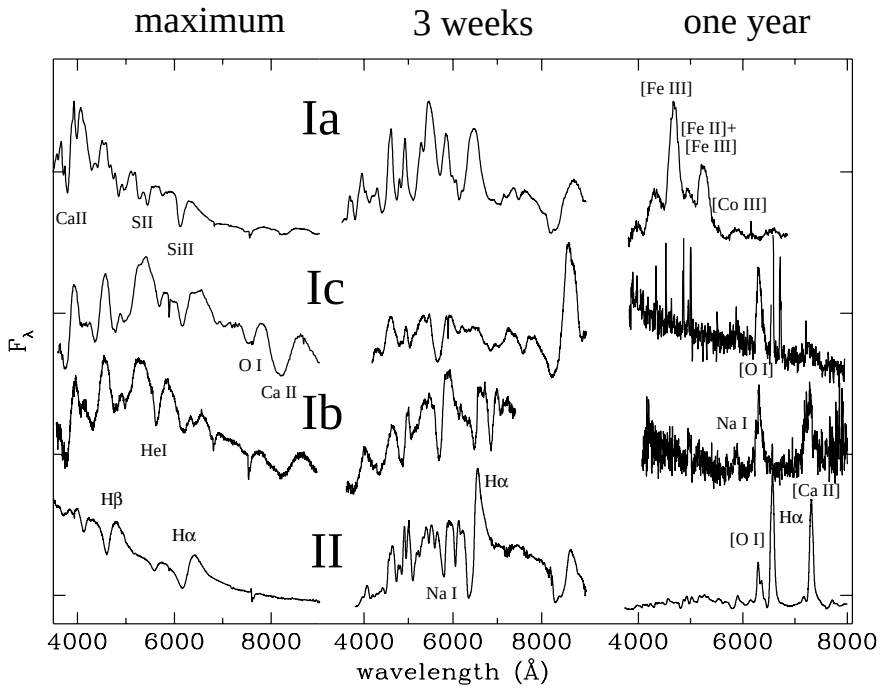

FIGURE 1.1— Classical distinction into Type Ia, Ib, Ic and Type II SNe on the basis of representative spectra (from Turatto 2003).

Accounting for objects with transitional character, for SNe interacting with a dense circumstellar medium (CSM) and for otherwise peculiar objects, by now a large number of further subclasses has been added, and no end in sight whatsoever. The most recent attempt of a classification scheme provided by Turatto, Benetti & Pastorello (2007) is shown in Fig. 1.2.

The complexity of this scheme arises from the diversity in SN appearance which only became evident as the sample of well-observed objects was growing, and from improved instrumental capabilities compared to the old times, most notably the advent of CCD technology in astronomical imaging in the early 1980s. However, in parts it is also motivated by the desire to implement theoretical understanding about SN explosion mechanisms or CSM interaction in the classification scheme, which in its original version was based merely upon spectroscopic characteristics, disregarding the underlying physics (hence the little intuitive and often confusing division into Type Ia SNe as thermonuclear explosions on the one hand and Type Ib/c and Type II SNe as core-collapse explosions on the other hand).

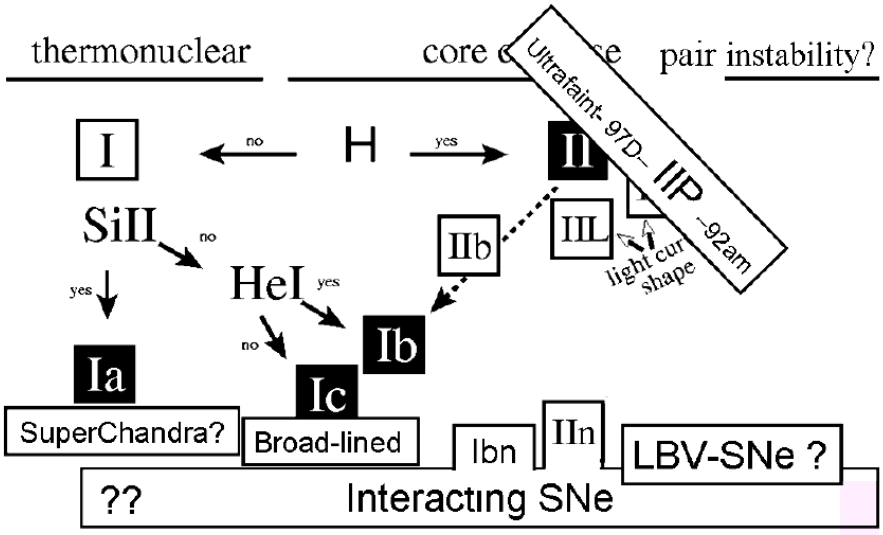

FIGURE 1.2— Up-to-date SN classification scheme, with a number of recently established subclasses added (from Turatto et al. 2007).

A milestone in SN research was the case of the Type II SN 1987A in the Large Magellanic Cloud. Being the closest extragalactic SN ever observed (50 kpc), it was extensively studied not only at optical wavelengths, but throughout the electromagnetic spectrum from X-rays to the radio. For the first time it was possible to identify the SN progenitor in pre-explosion images, and to detect the neutrino signal from the core collapse. Ongoing observations over 20 years have revealed strong asphericity of the SN ejecta, and complex interaction of the SN shock with circumstellar material. In fact, for several years now the emission caused by interaction vastly exceeds that of the actual SN ejecta powered by the decay of the long-lived ^{57}Co and ^{44}Ti isotopes (Leibundgut & Suntzeff, 2003). The still ongoing evolution from a SN to a SN remnant could be observed for the first time in SN 1987A.

The tremendous interest in SNe, but also the technological progress, can be estimated comparing the discoveries of extra-galactic SNe per year in the old days and now. While before 1980 only a handful of SNe were discovered every year, by the early 1990s this number had grown to $\sim$50. Last year about 500 new SNe were discovered, the majority of them in the course of large professional search programmes such as LOSS (Lick Observatory Supernova Search), the SN factory or the SDSS (Sloan Digitized Sky Survey) SN search. However, still a respectable number of SNe is found by amateurs using very similar automated

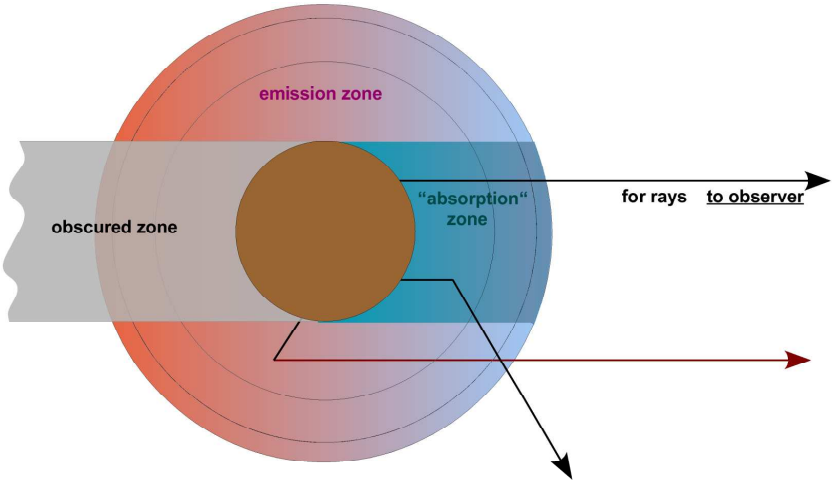

FIGURE 1.3— Formation of P-Cygni line profiles in expanding atmospheres. Absoption and emission regions are indicated in the figure (image courtesy: Stephan Hachinger).

methods of template subtraction and source identification as the professionals.

Many of the discovered SNe are at intermediate or high redshift and hence too faint for a detailed study. To obtain an optimal data set, a SN should be sufficiently nearby ($cz \lesssim 6000$ km s^{-1}), not too strongly extinguished by interstellar dust, and discovered soon after the explosion, as the eariest phases carry important information on the outermost layers of the ejecta. This can be understood by memorising that the ejecta of a SN are expanding homologously ($r = v\,t$), and that the matter density and opacity therefore decrease with time. Hence, during the evolution of a SN, the line-formation region is receding, deeper and deeper layers being exposed. A time series of spectra can thus be considered a scan through the SN ejecta.

As long as the ejecta are not transparent, SN spectra are characterised by P-Cygni line profiles, which are the characteristic signature of an expanding, back-lit atmosphere. P-Cygni profiles consist of a blueshifted absorption component, and an emission component centred approximately at the line's rest wavelength (see Fig. 1.3 for more details on the formation of this kind of profile). Owing to the large ejecta velocities in SNe, the lines are significantly Doppler-broadened; the blueshift of the absorption component gives an estimate of the expansion velocity of the shell in which the line predominantly forms. There is no real continuum in the spectra of Type I SNe (in Type II SNe a thermal continuum is present during the first one or two weeks after explosion). Instead, there is strong overlap and blending of the Doppler-broadened P-Cygni lines,

generating something that is often referred to as pseudo-continuum. Since at all wavelengths line opacity is the dominant form of opacity in SN envelopes, the definition of a photosphere is not straightforward either. Rather, different lines form at different depths depending on their strength, weaker lines forming in deeper layers than stronger ones. Examining weak lines, one can obtain a lower boundary of the line-formation region, and may define this as a pseudo-photosphere (often just referred to as photosphere), which can be useful as inner computational boundary for radiative-transfer calculations (cf. Chapter 4.6.1).

Once the ejecta have sufficiently expanded to be optically thin, the appearance of the spectra changes completely. They are now dominated by forbidden emission lines, which can occur when the material is excited through non-thermal processes (scattering of γ-rays and positrons produced in the β^+-decay of ^{56}Co), but the ambient matter density is too low for collisional de-excitation. This phase is referred to as 'nebular phase', in contrast to the optically thick 'photospheric phase'.

In Type II SNe with their extended hydrogen envelopes, the spectrophotometric behaviour is dominated by recombination of H initially ionised by UV radiation. The recombination causes a plateau phase of almost constant luminosity, with a duration of some 60–100 d from the explosion (Fig. 1.4). The Balmer-series lines of H, mostly in emission, dominate the optical spectra of SNe II from shortly after shock breakout to very late phases. In this way, the prevalence of hydrogen effectively shades deeper layers which are expected to show stronger signatures of the core-collapse itself. Studying explosions from progenitors which have shed their outer layers through stellar winds or binary interaction (i.e., Type Ib and Ic SNe) is therefore particularly rewarding.

In this thesis I exclusively concentrate on hydrogen-deficient SNe, of both thermonuclear (Type Ia) and core-collapse (Type Ib/c) origin. Special attention is paid to objects 'with a difference', i.e., SNe with characteristics that distinguish them from what is thought to be normal,[1] thus exploring the degree of diversity encountered within the respective classes. Because of the significant differences in the progenitor systems and the physics underlying the explosions, the thesis is organised in two major parts, one dealing with thermonuclear SNe, the other investigating the properties of hydrogen-deprived core-collapse events.

[1] However, for Type Ib/c SNe it may be openly questioned whether something like 'normal', 'generic', 'prototypical' objects exist.

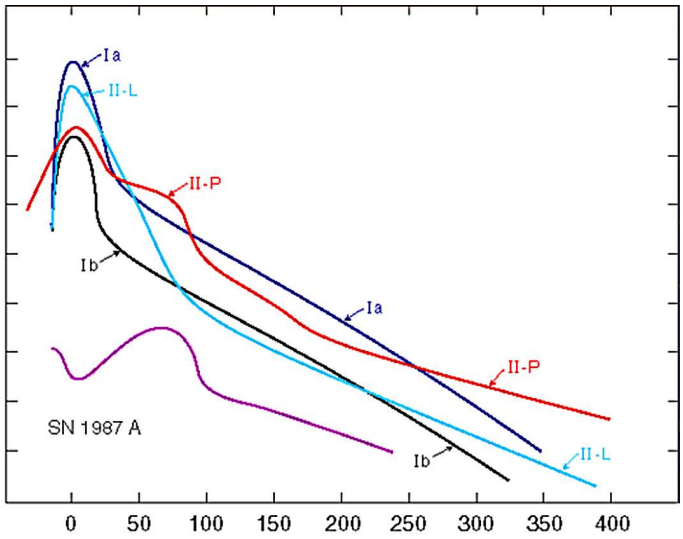

FIGURE 1.4— Schematic light curves of different SN classes (from Wheeler & Harkness 1990).

1.2 Thermonuclear supernovae

1.2.1 Explosion mechanisms

While it is commonly accepted that SNe Ia are thermonuclear explosions of carbon-oxygen white dwarfs (WDs), many details about the progenitor systems and explosion mechanisms of these events are yet unknown. Since a WD is an inert system, some kind of activation is definitely necessary to make it explode. This activation is expected to be provided by a companion star, implying that the WD is part of a binary system. The companion can either be a non-degenerate main-sequence or red-giant star (single-degenerate or SD scenario), or another WD (double-degenerate or DD scenario).

In the DD scenario (Webbink, 1984; Iben & Tutukov, 1984; Paczyński, 1985) the system of two WDs loses angular momentum by gravitational-wave emission, thus slowly decreasing the orbital radius until the WDs eventually merge. What makes this scenario an attractive candidate for SNe Ia is the natural explanation for the lack of hydrogen observed in SN-Ia spectra (Livio 2000; but see Hamuy et al. 2003 for the probable case of a SN Ia interacting with H-rich circumstellar material), as both WDs have previously lost their H layers. Moreover, a number of WD binary systems expected to merge in less than a Hubble time are known (Saffer, Livio & Yungelson, 1998), yielding about the right number for SNe Ia (Livio, 2000). However, so far numerical simulations

are not fully conclusive about the fate of such a merging system. It may well be that the outcome is an explosion similar to what we observe as SN Ia (e.g., Höflich & Khokhlov, 1996), but in most 3D models the formation of an O-Ne-Mg white dwarf and subsequent collapse to a neutron star is favoured (Bravo & García-Senz, 1999, and references therein). Of course, the result may sensitively depend on the absolute masses of the two WDs and their mass ratio, making general predictions even more delicate. The latter is also the reason why the DD scenario is often not regarded a good model at least for the majority of rather homogeneous 'normal' SNe Ia: there seems to be no mechanism to guarantee the observed homogeneity.

This is exactly the strength of the SD scenario, at least in its standard configuration of a carbon-oxygen WD exploding when reaching the Chandrasekhar mass M_{Ch} (Hoyle & Fowler, 1960; Arnett, 1969). In this model, the WD accretes matter from a non-degenerate companion by Roche-lobe overflow. Approching M_{Ch}, the core of the WD compresses and heats up, rendering nuclear reactions more efficient. For a period of another ~ 1000 yr, the energy thus generated is mostly compensated by neutrino losses, so that the temperature growth is attenuated. However, at some point the energy production by nuclear burning exceeds a rate that can be balanced by neutrino losses. As a consequnce the temperature increases significantly. Contrary to a non-degenerate gas, the equation of state of WDs does not support self-regulation in a sense that the WD would react to a higher temperature by expansion and cooling. Instead, owing to the steep temperature dependence of the involved nuclear reactions, a positive-feedback cycle takes over: a higher temperature entails higher reaction rates, stronger heat production, and, consequently, a further temperature increase. A thermonuclear runaway (Arnett, 1969; Woosley & Weaver, 1986) is triggered, resulting in a disintegration of the entire star.

The propagation of the microscopically thin burning front through the WD could in principle be subsonic (deflagration) or supersonic (detonation). Especially for deflagrations (Fig. 1.5), turbulence was shown to be one of the key ingredients, as it wrinkles the flame front and enlarges its surface, thus increasing the burning speed (cf. Hillebrandt & Niemeyer, 2000, and references therein). This is essential as otherwise the star would have too much time to expand, and the density would drop below the critical value needed to sustain the flame. Large parts of the WD would hence remain unprocessed, contrary to what is observed.[2] Moreover, a strongly turbulent flame (Fig. 1.5) causes

[2] A typical SN Ia releases $\sim 0.7 M_{\odot}$ of nuclear-statistical-equilibrium (NSE, i.e., Fe-group) material, $\sim 0.4 M_{\odot}$ of intermediate-mass elements such as Si, S and Mg, and only $\sim 0.3 M_{\odot}$ of unburned fuel.

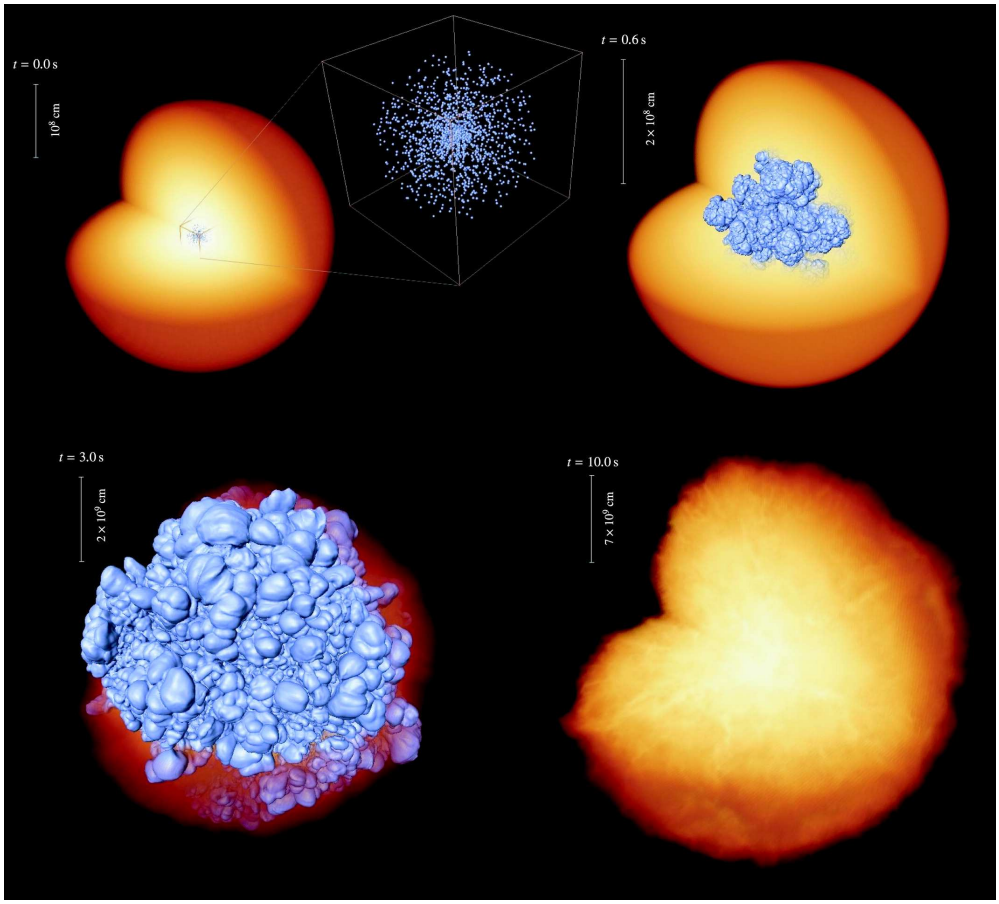

FIGURE 1.5— Snapshots of a full 3D multi-spot-ignited simulation of a SN-Ia deflagration (first three panels). Orange tones mark the WD itself, the blue surface is the flame front. Structures from Rayleigh-Taylor instabilities ('mushrooms') are evident. In the bottom-right panel the density structure of the ejecta is shown (from Röpke et al. 2007).

large-scale mixing in the ejecta, to some degree matching the requirements from observed spectral time series (Stehle et al., 2005). However, the mixing in pure deflagrations tends to be even too strong (Röpke et al., 2007), and it is also challenging to synthesise more than $\sim 0.6 M_\odot$ of radioactive ^{56}Ni, needed to reproduce the bright end of the observed SN Ia distribution.

A prompt detonation, however, is no alternative. The rapidly moving flame front would give the star no time to expand, so that the entire buring would take place at high density, producing too little intermediate-mass material and leaving almost no fuel unburned (Hillebrandt & Niemeyer, 2000). A possible and

widely favoured solution is a combination of the two modes, with the explosion starting out as a deflagration, and after a while when the star is sufficiently pre-expanded, making a transition into a detonation (Khokhlov, 1991a; Woosley & Weaver, 1994). This model could combine the positive aspects of both pure scenarios while not inheriting their flaws. In particular, the detonation in the pre-expanded star would leave sufficient partially burned and unburned material behind, and effectively avoid too strong mixing of the ejecta. Moreover, the radius at which the deflagration-detonation transition (DDT) takes place has been suggested as key parameter responsible for the observed luminosity differences among SNe Ia (Höflich & Khokhlov, 1996), SNe with an earlier DDT producing more ^{56}Ni. However, in present-day models the DDT mostly has to be inserted by hand (Röpke & Niemeyer, 2007), and it is not fully understood what it could be triggered by in reality (Niemeyer 1999; but see Röpke 2007).

A very specific implementation of a DDT is the model of a Gravitationally Confined Detonation (Plewa, Calder & Lamb, 2004; Kasen & Plewa, 2005; Plewa, 2007), which consists of a near-centre ignition of a deflagration that results in the formation of a buoyancy-driven ascending bubble that burns only little of the WD before it reaches the surface at supersonic velocities. The ashes – confined by gravity – then sweep around the WD, converging at the point opposite to the bubble breakout and triggering a detonation there, which runs once more through the star and burns most of the residual material left unburned by the deflagration before. While this model is quite successful in reproducing the observed properties of SNe Ia (Kasen & Plewa, 2007), there are doubts whether the collimation of the surface wave can be sufficiently precise to reach detonation conditions at the opposite pole. So far, numerical models of different groups disagree in this respect (Röpke, Woosley & Hillebrandt, 2007; Plewa, 2007).

Skipping the $M_{\rm Ch}$-constraint, sub-Chandrasekhar-mass models have first been proposed by Weaver & Woosley (1980), Nomoto (1980) and Woosley (1980), and investigated thereafter in a number of studies. The basic idea in these models is that the explosion is externally triggered, by a detonation taking place in the accreted He-layer on the WD surface. This would drive a shock into the the C + O core of the WD, and initiate a second C detonation at the convergence spot. While not favoured for normal SNe Ia, sometimes these sub-$M_{\rm Ch}$ explosions have been proposed to explain underluminous events (Ruiz-Lapuente et al., 1993). The most recent 2D simulations, however, suggest a rather efficient production of ^{56}Ni, making sub-$M_{\rm Ch}$ too bright for underluminous SNe Ia (Fink, Hillebrandt & Röpke, 2007). What is particularly challenging about the sub-$M_{\rm Ch}$ models is the predicted presence of high-velocity He and Ni in the outermost ejecta, not observed in any SN-Ia spectrum to date.

Just opposite to the sub-$M_{\rm Ch}$ models, super-$M_{\rm Ch}$ models have become fashionable recently. They are supposed to provide a possible explanation of a newly-discovered class of SNe Ia which are overluminous by about a factor two with respect to normal events, suggesting a ^{56}Ni-mass of $\sim 1.2 M_\odot$ and requiring a total ejecta mass exceeding $1.4 M_\odot$ to reproduce the observed spectra rich in IMEs (Howell et al., 2006; Branch, 2006; Hicken et al., 2007). The basic idea is that WDs could also be stabilised to significantly super-$M_{\rm Ch}$ masses if strong differential rotation is present (Howell et al., 2006; Branch, 2006). However, Hillebrandt, Sim & Röpke (2007) have demonstrated that about the right luminosity can also be achieved with a strongly off-centre ignition of a $M_{\rm Ch}$-WD if such an event is seen at the proper viewing angle. Moreover, there are indications that too strong a differential rotation suppresses the formation of Rayleigh-Taylor instabilities in the flame, resulting in a rather weak explosion and an underluminous event (Pfannes, 2006). Alternatively, a merger of two WDs with a total mass exceeding $M_{\rm Ch}$ has been proposed for an overluminous SN Ia (Hicken et al., 2007).

1.2.2 Observational facts

At all relevant phases, the luminosity of SNe Ia is powered by the radioactive decay of ^{56}Ni and its daughter nucleus ^{56}Co. γ-rays produced by this decay undergo multiple scattering processes until, eventually, optical photons are released. The exact shape of the bolometric light curve of SNe is a complex interplay of γ-ray production (decreasing roughly exponentially with time) and opacity (following approximately a power-law). After the explosion, the luminosity increases for about 2 to 3 weeks, reaches a maximum and thereafter decreases again. The post-maximum decline is slower in intrinsically more luminous objects and vice versa (Phillips, 1993; Kasen & Woosley, 2007). About 20 to 40 d after the peak, the luminosity decline slows down, henceforth tracing the radioactive decay of ^{56}Co with its decay time of 111 d (Fig. 1.4).

There are significant differences between the SN Ia light curves (LCs) in different broad-band optical and near-IR filters. While the blue (U and B) bands' initial post-maximum decline is more rapid than that of the bolometric LC, the far red and near-IR bands first decline as well, but then rise again to reach a secondary maximum after some 30 d. The occurrence of this secondary peak has been explained as an enhanced release of photons redistributed from bluer wavelengths because of an increased opacity there (Kasen, 2006). The latter is caused by a drop in temperature and the according changes in the ionisation state of the matter, in particular that of Fe. Underluminous SNe Ia

similar to SN 1991bg are an exception in not having double-peaked I-band and near-IR LCs.

Optical spectra of normal SNe Ia before and around maximum light are characterised by P-Cygni features of IMEs, most notably Si II λ6355, S II (a 'W'-shaped feature near 5500 Å), Ca II (H&K and the near-IR triplet) and Mg II λ4481 (Fig. 1.1). Fe II lines are also present, contributing to the absorption troughs around 4300 and 4800 Å. The UV-part of the spectra is even dominated by Fe-group elements, which effectively suppress the UV-flux by blanketting of a multitude of lines, and redistribute it to longer wavelengths. During the weeks after maximum light, when the photosphere recedes into the inner parts of the ejecta dominated by NSE-material, Fe II lines begin to dominate also the optical part of SN-Ia spectra, whereas lines of IMEs fade away with exception of the Ca near-IR triplet. At phases later than ~ 100 d, SNe Ia enter the nebular phase, which is mostly characterised by forbidden [Fe II], [Fe III] and [Co III] emission lines (see Fig. 1.1).

Overluminous SNe Ia such as SN 1991T show hot pre-maximum spectra, with a lack of lines from singly-ionised species. Even Si II λ6355 is absent. Instead, Fe III dominates the spectrum. After maximum, overluminous SNe Ia behave like normal SNe Ia. Underluminous, 1991bg-like SNe, on the contrary, are cool, show comparatively strong O I λ7774 lines and an absorption trough between 4000 and 4400 Å formed mainly by Ti II lines. During the nebular phase they are similar to most other SNe Ia, but with significantly narrower [Fe] lines and an additional strong emission feature identified as [Ca II] $\lambda\lambda$7291, 7323 which is not present in normal-luminosity objects.

1.2.3 SNe Ia as cosmological tools

It has been known for a long time that SNe Ia are rather homogeneous with respect to their spectroscopic appearance. In terms of light-curve morphology and peak absolute luminosity this similarity also holds. This property, together with their high luminosities, has made SNe Ia the longed for tool to expand the cosmic distance ladder to much larger distances, allowing statements about the fundamental structure of the cosmos to be made. However, SNe Ia are *no* standard candles: there is a true variation in peak luminosity, and since the discovery of the peculiar SNe 1991T (Filippenko et al., 1992a; Phillips, Wells, Suntzeff, Hamuy, Leibundgut, Kirshner & Foltz, 1992; Ruiz-Lapuente et al., 1992; Mazzali, Danziger & Turatto, 1995) and 1991bg (Filippenko et al., 1992b; Leibundgut et al., 1993; Ruiz-Lapuente et al., 1993; Turatto et al., 1996; Mazzali et al., 1997) it is known to amount to a factor of about 10 (2.5 mag) between the most and the least luminous objects. However, considering spectro-

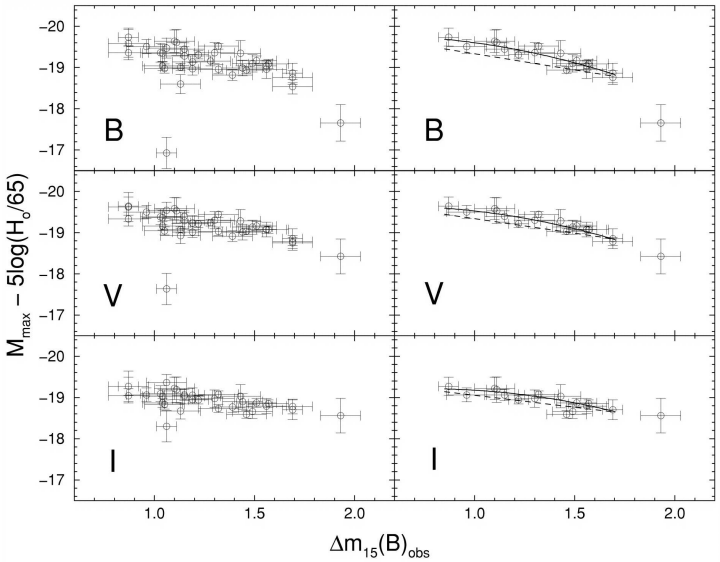

FIGURE 1.6— Peak absolute magnitudes of SNe Ia as a function of their LC decline rate in the B band, $\Delta m_{15}(B)$. The left column includes all SNe discussed by Phillips et al. (1999), the right column a subsample with no significant host-galaxy reddening. The solid lines are the best quadratic fits to the reddening-free data (from Phillips et al. 1999).

scopically normal SNe Ia only (which make up about 70% of the whole sample, Li et al. 2001a), the variation is significantly reduced to less than a factor of 2. In 1993, Phillips (1993) established a relation between the peak absolute magnitude of SNe Ia and their light-curve decline rate, expressed as the dimming in magnitudes from maximum light to 15 d after in the B band, $\Delta m_{15}(B)$. Employing this relation, SNe Ia turned into standardisable candles, in a sense that from the LC-shape alone the true peak luminosity of the SN could be inferred and used for distance measurements. Over the years, the Phillips relation has been refined (Phillips et al. 1999; see Fig. 1.6), and alternative implementations of LC shape – luminosity relationships have been developed (Riess, Press & Kirshner, 1996; Perlmutter et al., 1997), which thereafter were successfully coupled to large high-redshift SN search and monitoring programmes.

The luminosity distance to a SN is given by $d_L = \left(\frac{L_{\rm true}}{4\pi\, F_{\rm obs}}\right)^{1/2}$, where $F_{\rm obs}$ is the observed flux of the SN, and $L_{\rm true}$ the absolute luminosity it is expected to have according to its light curve. Assuming that the Cosmological Principle holds, and adopting the Robertson-Walker metric, the luminosity distance in

an expanding universe can be expressed as (Leibundgut, 2001):

$$d_L = \frac{(1+z)c}{H_0|\Omega_k|^{1/2}}\ \mathcal{S}\left\{|\Omega_k|^{1/2}\int_0^z\left[\Omega_k\,(1+z')^2+\sum_i\Omega_i\,(1+z')^{3(1-w_i)}\right]^{-1/2}dz'\right\} \tag{1.1}$$

where $\Omega_i = \rho_i/\rho_c$, and the curvature term Ω_k is given by $\Omega_k = 1 - \sum\Omega_i$. $w_i \equiv p_i/(\rho_i\,c^2)$ is the equation-of-state parameter, which is $= 0$ for non-relativistic matter, $= 1/3$ for radiation and $= -1$ for a Cosmological Constant Λ. $\mathcal{S}$, finally, is a function of the form

$$\mathcal{S}(x) = \begin{cases} \sin(x) & \Omega_k < 0 \\ x & \Omega_k = 0 \\ \sinh(x) & \Omega_k > 0 \end{cases}$$

Eq. 1.1 links the luminosity distance d_L to the redshift z through the parameters of the cosmological model. The latter can in turn be constrained if d_L and z are measured independently. Doing so, the Supernova Cosmology Project (SCP; Perlmutter et al. 1998, Perlmutter et al. 1999) and the High-z Supernovae Search (Riess et al., 1998) consistently found that SNe Ia at $z \sim 0.5$ appeared ~ 0.3 mag dimmer than expected for an empty, freely coasting universe. This suggests that the expansion of the universe is accelerated, driven by a Cosmological Constant Λ or some time-dependent sort of Dark Energy (Fig. 1.7).

The data base of high-z SNe Ia has been growing ever since, pushed forward by intensive programmes using both ground-based and space-based (HST) facilities. In this way, statistical errors could be reduced significantly, and it could be shown that the equation-of-state parameter w of any kind of Dark Energy in the present universe has to be close to the value obtained for a Cosmological Constant, i.e., -1. Attempts have been made to constrain also the time-evolution of w (Riess et al., 2004; Riess et al., 2007) in order to distinguish between a static Cosmological Constant and time-dependent Dark-Energy models. However, this requires fitting with one more free parameter, and so far the results are not fully conclusive. While a Cosmological Constant does not seem to lie in the very centre of the probability ellipses, it is still in good agreement with the data, no matter which additional priors are assumed (cf. Fig. 1.7 and Riess et al. 2004; Riess et al. 2007).

The main problem in using SNe Ia for this kind of high-precision cosmological measurements are the possible systematic errors. While statistical errors are reduced by increasing the sample of high-z SNe, any systematic error is not. Systematic errors could be introduced if there is a second parameter besides

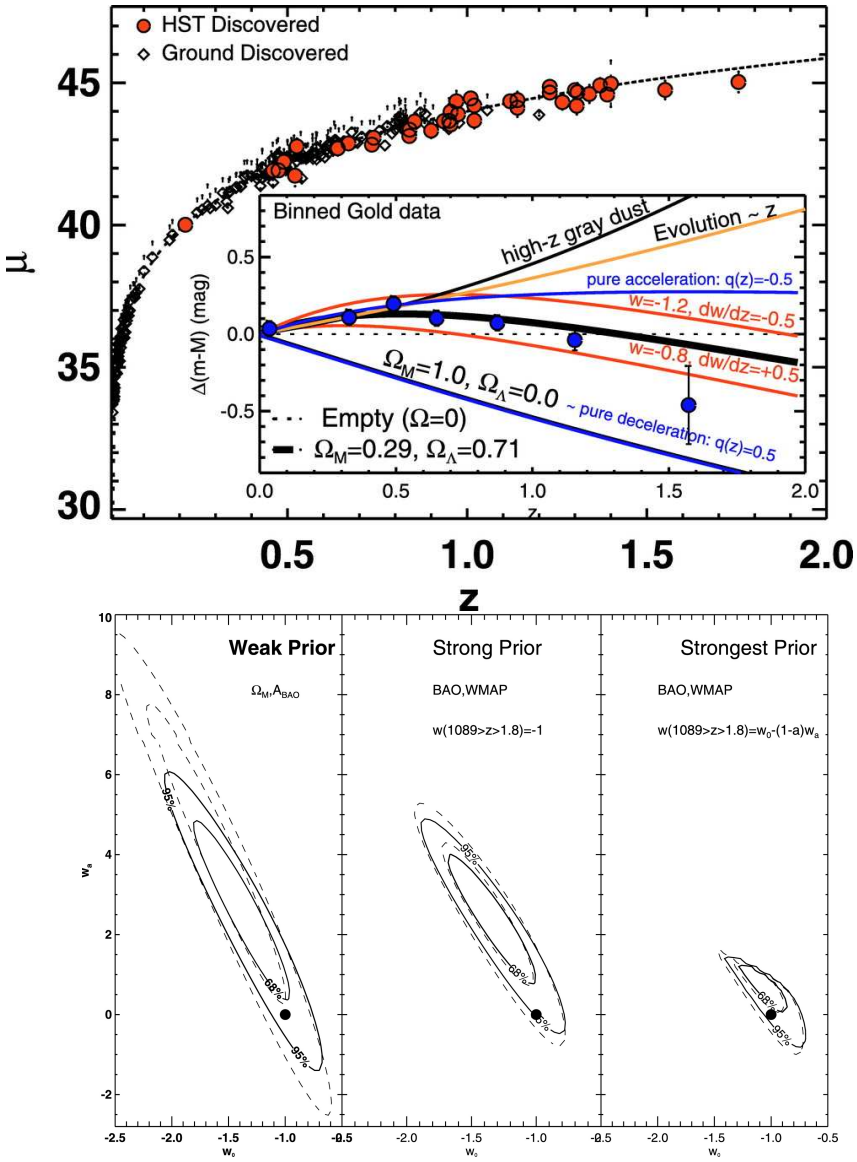

FIGURE 1.7— *Top panel:* SN-Ia Hubble diagram (i.e., distance modulus plotted vs. redshift). The best-fitting flat ΛCDM (Cosmological Constant + Cold Dark Matter) cosmology ($\Omega_{\rm M} = 0.27$, $\Omega_\Lambda = 0.73$) is overplotted on the observed data. The inset compares different cosmological models, normalised to an empty universe, and their ability to explain the observed trend in the SN data.
Bottom panel: Confidence contours for a parametrisation of the equation-of-state parameter as $w = w_0 + w_{\rm a} z/(1+z)$, obtained from high-$z$ SN data using different priors. The position of a Cosmological Constant is marked as filled point (both figures from Riess et al. 2007).

$\Delta m_{15}(B)$ which affects the peak luminosity of SNe Ia. For instance, such a parameter might be the ratio of stable NSE material to ^{56}Ni synthesised in the explosion. While the peak luminosity is solely determined by the amount of ^{56}Ni, the light-curve width is affected by the opacity created by both stable and radioactive Fe-group elements (Mazzali & Podsiadlowski, 2006). As long as such an effect produces a random scatter in the Phillips relation, it acts as another contribution to the statistical error in the cosmological context if uncorrected. However, once such an effect turns out to be metallicity-dependent, it would introduce a systematic trend, since the average metallicity was lower in the early universe. Another critical issue is the correction of foreground dust extinction applied to the high-z data, but also the local calibration sample. Several studies of highly-extinguished SNe Ia unanimously found a smaller total-to-selective-extinction ratio (which is linked to the grain size of the extinguishing material) than for average Milky-Way dust (see Chapter 3.3). Such a deviation can be safely determined only if an excellent spectrophotometric data set, from rest-frame optical to near-IR wavelengths, is available, out of reach for very distant SNe. Hence, at high z an incorrect extinction correction might be applied, and things become even worse if dust parameters such as the grain size change on cosmic timescales (which is not totally unexpected). All these concerns, and also some more like the possibility that distant SNe are on average dimmed by gravitational lensing, are extensively discussed by Leibundgut (2001) in his review on SN cosmology.

As a bottom line, extensive studies of nearby SNe Ia are essential to identify and investigate possible systematic errors in SN cosmology. Even though the effects may be small, in the limit of negligible statistical errors they become important, as they limit the achieveable precision in cosmological measurements. For a reliable determination of $\dot{w}$ a maximum systematic error of ~ 0.02 mag should be the aim.

1.2.4 Delay times

SNe Ia are found in host galaxies of all Hubble types, from early-type ellipticals with their predominantly old stellar population and their lack of interstellar gas and recent star formation, to late-type spirals and irregular galaxies with significant ongoing star formation.

Since stars with an initial mass $\gtrsim 8M_{\odot}$ are supposed to proceed nuclear burning all the way to Fe, develop a central Fe core and undergo core collapse, the progenitors of SNe Ia must be less massive than that, implying longer timescales of stellar evolution. Within the SD scenario, the delay time of a SN Ia (i.e, the time from progenitor formation to explosion) is mostly dictated

by the main-sequence life time of the less massive, non-degenerate companion, since Roche-Lobe filling can first occur at the end of the secondary's core hydrogen burning (Kippenhahn & Weigert, 1967). During the subsequent accretion phase it would require only several Myr for the primary to reach $M_{\rm Ch}$, as mass transfer is possible only in a narrow range of rates ($\sim 10^{-7} M_\odot\,{\rm yr}^{-1}$; Tornambé & Piersanti 2005; Nomoto et al. 2007). If this rate is exceeded, hydrogen from the secondary is accumulated faster on the primary's surface than it can be processed to He and heavier elements. Depending on the model, this either quickly leads to a common-envelope phase, or to the presence of a non-negligible shell of hydrogen surrounding the WD at the moment of explosion, which would leave a footprint in SN-Ia spectra, contrary to what is observed. Too low a mass-transfer rate, on the other hand, would cause the WD to undergo Nova explosions, resulting in a net mass loss rather than a gain. In the DD scenario, the delay time is determined by the main-sequence life time of the less massive constituent of the binary system, and the actual merger time scale. The latter is set by the low efficiency of angular-momentum loss of the orbiting WDs by gravitational-wave emission, and highly sensitive to the initial separation of the WDs (Greggio, 2005). For initially wide WD-pairs, long delay times are expected.

Attempts have been made to determine the delay-time distribution of SNe Ia by evaluating the SN-Ia rate as a function of redshift, host-galaxy radio properties and colours (Mannucci, Della Valle & Panagia, 2006). The results favour a bimodal distribution, with some SNe Ia descending from rather short-lived ($\lesssim 100$ Myr) progenitor systems (the prompt component), and another (tardy) component with delay times up to 10 Gyr. Whether this complex distribution withstands critical tests, and whether the two components may arise from different progenitor systems (e.g., SD and DD), is still the subject of debate.

1.2.5 Own work

In Chapter 4 of this thesis, I present the data analysis and basic spectral modelling of the Type Ia SN 2005bl, which is fainter than 'normal' SNe Ia by about 1.5 to 2 mag, and very similar to the prototypical underluminous SN 1991bg in its spectroscopic and photometric properties (fast LC decline, no secondary maximum in the near-IR LCs, optical spectra with prominent O I and Ti II features). Thus, SN 2005bl offered the opportunity to address a number of issues connected to the subclass of 91bg-alikes.

The most fundamental question is surely whether or not 91bg-like and normal-luminosity SNe Ia originate from the same progenitor and explosion channel, the smaller amount of ^{56}Ni with all its consequences being the only

discriminating parameter. As will be shown in Chapter 4, a final conclusion cannot be obtained, but a number of arguments in favour of each scenario is provided. A common scenario for all SNe Ia is supported by the existence of objects with properties intermediate between those of SNe 2005bl or 1991bg, and normal-luminosity SNe Ia. Hence, it is unclear where the exact boundary would have to be located, should 91bg-like objects really descend from a separate population or have different explosion mechanisms. Moreover, underluminous SNe also obey a LC-width vs. luminosity relation, yet with a steeper slope than ordinary SNe Ia.

On the other hand, spectral modelling of SN 2005bl suggests differences which reach beyond a reduced amount of ^{56}Ni. The Cr and Ti content of the spectra is enhanced, and in contrast to the pre-maximum spectra of ordinary SNe Ia in which IMEs are most abundant, the early spectra of SN 2005bl suggest a dominance of unburned C and O. Furthermore, the density structure commonly used in these models, which gives good results when fitting ordinary SNe Ia, fails to reproduce the positions and widths of most absorption lines in SN 2005bl. While SNe Ia in general occur in all types of host galaxies, underluminous SNe Ia are strongly concentrated in early-type (E, S0) hosts, again lending support to a different progenitor system. At the same time, in our synthetic spectra we find a remarkably low abundance of Fe, about an order of magnitude lower than expected for a precursor with solar metallicity. This may indicate that underluminous SNe Ia are produced by a very old stellar population, having long delay times.

So, this work on SN 2005bl provides at least some good arguments which may help solving the puzzle of the nature of the 91bg-like class of SNe Ia. With more detailed modelling of these data in the future, chances are fair that a definite statement on the progenitors and explosion mechanisms can be made.

1.3 Stripped-envelope core-collapse supernovae

Contrary to Type Ia SNe which are thermonuclear explosions of WDs, Type Ib and Ic SNe are thought to descend from much more massive progenitors undergoing core collapse. The energy source is hence the gravitational binding energy of the newly formed compact remnant (a neutron star or a black hole), and not nuclear binding energy as in the case of SNe Ia. It is now commonly accepted that Type II, IIb, Ib and Ic SNe form one family of events, with an increasing fraction of their envelopes lost prior to explosion. The significant mass loss of Type Ib and Ic progenitors could have its origin in strong stellar winds during LBV (luminous blue variable) and WR (Wolf-Rayet) phases, but also in mass transfer to a possible binary companion.

1.3.1 Explosion mechanisms

As in Type II SNe, the underlying explosion mechanism in SNe Ib and Ic is the gravitational collapse of the Fe core that massive stars ($\gtrsim 8M_{\odot}$) have developed at the end of their regular lives. The final stages of the evolution of these stars and the core collapse itself happen on very short timescales, so that the star's outer envelope is in fact decoupled from the processes in the interior. Hence, the H and He layers have no influence on most of the explosion mechanism, making the following discussion valid for the entire sequence from Type II to Type Ic SNe. CC-SN models have recently been reviewed by Woosley & Janka (2005), Janka et al. (2005), Mezzacappa (2005), Buras et al. (2006) and Janka et al. (2007).

Since Fe has the highest binding energy per nucleon, burning to elements beyond Fe would consume rather than release energy, and does not take place in hydrostatic nucleosynthesis conditions. Therefore, the Fe core is not supported by radiation pressure from inside, as would be the case if further burning went on in the centre. Once the it has grown to about the Chandrasekhar mass, its inwards-directed gravitational forces can no longer be balanced by the degeneracy pressure of the electrons, and gravitationally driven core collapse sets in. Strong neutronisation reactions take place ($e^- + p \rightarrow n + \nu_e$), leading to the production of a large number of neutrinos, which are trapped since their diffusion timescale exceeds the collapse timescale. The collapse is not halted before nuclear matter density is reached and repulsive nuclear forces come into play. At this stage, the equation of state abruptly turns stiff, preventing further collapse and initiating an outwards-directed shock wave by core bounce.

However, simulations show that a prompt explosion fails. After some propagation, the shock stalls, as it loses too much energy by disintegrating the matter passing while falling in onto the newly formed proto-neutron star. Some sort of retarded shock revival is hence necessary to produce successful explosions. From state-of-the-art numerical simulations (which, however, still fail to produce robust explosions), the most promising mechanism of shock revival is neutino heating. Neutrinos, initially trapped inside the proto-NS, are released on diffusion timescales, and on their way outwards a small fraction of them deposits energy in the region just below the standing shock by charged-current reactions. This region is thus heated, and may re-energise the shock sufficiently to disintegrate the stellar envelope. Typically an energy of 10^{53} erg is released in a core collapse SN, 99% of it in neutrinos. Given this enormous neutrino flux, the importance of a precise treatment of the neutrino transport and reactions in numerical simulations is evident (Janka et al., 2005; Buras et al., 2006), despite their tiny interaction cross-sections. In particular, full Boltzmann neu-

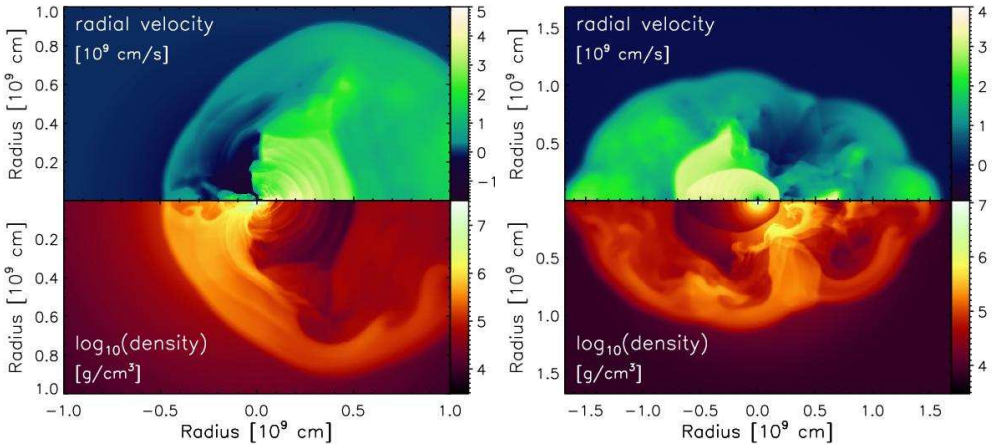

FIGURE 1.8— Two CC-models showing strong convection with dominant $l = 1$ mode in the neutrino-heated region below the shock, at 1 s after SN shock formation. Neutron-star recoil velocities of -350 km s^{-1} and $+520$ km s^{-1} are obtained for the left and right model, respectively (from Scheck et al. 2004).

trino transport is required, since at the given densities neither the diffusion nor the free-streaming approximations can be applied.

Alternatives to this 'standard' neutrino-driven mechanism would be an explosion triggered by large-scale fluid instabilities or by the effects of strong magnetic fields. Fluid instabilities are known to occur and deform the standing shock wave. Large-scale, low-mode ($l = 1, 2$) convection in the neutrino-heated region below the shock leads to strong anisotropies and a bipolar pulsation of the shock, and may aid significantly to the explosion (Scheck et al. 2004, 2006 and Fig. 1.8). The 'Stationary Accretion Shock Instability' (SASI), a low-mode (predominantly $l = 1$) perturbation of the accretion shock discovered by Blondin, Mezzacappa & DeMarino (2003), acts in a very similar manner. With low-mode convection or SASI, bipolar explosions can be produced even in the absence of rotation, and observed neutron-star kicks can be reproduced (Janka et al., 2005). Burrows et al. (2006, 2007) proposed another acoustic instability which might lead to explosions without the need of neutrino heating. Whether this 'advective-acoustic cycle' can be an alternative to neutrino-driven explosions, is currently debated (Janka et al., 2007). Magnetohydrodynamic (MHD) effects are expected to play an important role whenever rotation is strong. In these cases an MHD-jet will likely form, leading to strongly aspherical, bipolar explosions.

While the neutrino-heating mechanism is still favoured for the majority of CC-SNe (Burrows, 2005), different models have been suggested to account for

GRBs and the SNe connected to them, as they have to explain not only an energetic SN (subrelativistic ejecta), but also the highly relativistic jet which produces the prompt γ-ray emission and the afterglow. The proposed models include collapsars (Woosley, 1993; MacFadyen & Woosley, 1999), millisecond magnetars (Wheeler, Yi, Höflich & Wang, 2000; Lyutikov & Blackman, 2001; Drenkhahn & Spruit, 2002) and supranovae (Vietri & Stella, 1998). These models have in common that magnetic or MHD effects are supposed to produce the relativistic jet by extracting energy from strongly rotating neutron stars (magnetar model) or black holes (collapsar model), or from accretion disks around newly formed black holes (collapsar and supranova models). A comprehensive review of GRB-SN models is given by Woosley & Bloom (2006).

1.3.2 Observational facts

As in Type Ia SNe, the light curves of stripped-envelope core-collapse SNe are powered by the radioactive decay of ^{56}Ni and (subsequently) ^{56}Co. This clearly distinguishes them from Type II SNe, where the recombination of the previously ionised H envelope gives the largest contribution to the luminosity during the plateau phase. Accordingly, the principal morphology of SN Ib/c light curves is not dissimilar to that of SNe Ia (basically consisting of a peak and a radioactive tail, Fig. 1.4), with the notable exception that they lack the secondary maximum in the near-IR bands which characterises most thermonuclear explosions (cf. Section 1.2.2).

A fairly precise description of the behaviour of all Type I SNe is provided by an analytic model by Arnett (1982), where the effective photon diffusion time $\tau_{\rm m}$, which determines the width of the bolometric light-curve peak, is given by

$$\tau_{\rm m} \propto \kappa_{\rm opt}^{1/2} M_{\rm ej}^{3/4} E_{\rm kin}^{-1/4}, \tag{1.2}$$

where $\kappa_{\rm opt}$ is some mean opacity for optical photons, $M_{\rm ej}$ the ejecta mass and $E_{\rm kin}$ the explosion energy (cf. also Chapter 5.6.2). In thermonuclear explosions of $M_{\rm Ch}$-WDs, $M_{\rm ej} = M_{\rm Ch}$ and also $E_{\rm kin}$ is fixed within close margins. However, the amount of NSE-material synthesised in the explosion varies, and so does the opacity which is dominated by these elements. Differences in the LC widths of SNe Ia are hence governed by different values of $\kappa_{\rm opt}$.

The progenitors of stripped-envelope CC-SNe are much more diverse. In particular, they can have vastly different masses at the time of explosion, and the explosion energy can vary by more than one order of magnitude. The mass of the compact remnant can also be quite different (NS or BH). Accordingly, the LC width of these objects is mostly determined by the combination of $M_{\rm ej}$ and $E_{\rm kin}$, while differences in $\kappa_{\rm opt}$ are of minor importance. Since the ejecta

mass, the explosion energy and the amount of ^{56}Ni do not seem to correlate in CC-SNe, no relation between light-curve shape and peak luminosity has yet been found for SNe Ib/c. With observed absolute peak magnitudes from ~ -16 to -20, these objects are hence of little use as cosmological distance indicators.

The early spectra of Type Ic SNe are characterised by features of Ca II (H&K and the near-IR triplet), O I λ7774, Na I D, Mg II λ4481, Fe II blends, Si II λ6355 and often C II λ6580 (Filippenko, 1997). However, the latter two identifications are sometimes debated, since Ne I λ6402 and Hα would yield absorptions in the same part of the spectrum (Branch et al., 2006b). While no clear identification of He is possible in SN-Ic spectra (see Chapter 5.5.3 and Valenti et al. 2007b), a series of He I lines is *the* characteristic feature of SNe Ib, whose spectra otherwise closely resemble those of SNe Ic (Fig. 1.1).

In 1997 and the following years, a class of SNe Ic with exceptionally broad and strongly blended spectral features has been discovered (Garnavich et al., 1997a; Galama et al., 1998), requiring a large kinetic energy and a very shallow density gradient within the ejecta. In this thesis I refer to these objects as broad-lined (BL-) SNe Ic, but other expressions have also been used in the literature, including the term 'hypernova'. One is well advised to care about a proper nomenclature in this particular case (see also Chapter 5.1), since hypernovae were originally defined to be highly energetic SNe Ic with $E_{\rm kin} \gtrsim 10^{52}$ erg. While indeed all hypernovae seem to be broad-lined, some BL-SNe have a rather small ejecta mass and hence too low a kinetic energy to qualify as hypernovae.

Contrary to SNe Ia whose nebular spectra are dominated by [Fe] and [Co] lines, stripped CC-SNe at late phases are characterised by emission lines of lighter elements. [O I] $\lambda\lambda$6300, 6364 is often particularly pronounced, but [Ca II] $\lambda\lambda$7291, 7323, [O II] $\lambda\lambda$7320, 7330, the Ca II near-IR triplet and Mg I] λ4571 can be almost equally strong (Filippenko, 1997). In hypernovae, however, also Fe emission lines can reach a considerable strength (Mazzali et al., 2001). Differences between SNe Ib and Ic can no longer be discerned at those epochs.

1.3.3 The SN-GRB connection

Though hypothesised long before (Colgate, 1968), the firm connection between a GRB and a SN could not be established before 1998, when SN 1998bw was found in the error circle of the nearby GRB 980425 (Galama et al., 1998). This event and several more thereafter proved that at least some long-duration GRBs are associated with SN explosions, suggesting core collapse in massive stars as the common mechanism for both. Observations and modelling of SN 1998bw soon revealed that it was an extremely energetic object, with broad-lined, heavily blended spectra, a peak luminosity of ~ -19, an ejecta mass of $10 M_\odot$ and

an isotropic kinetic energy of $\sim 3 \times 10^{52}$ erg (Galama et al., 1998; Nakamura et al., 2000; Patat et al., 2001). In fact, it was in the context of SN 1998bw that the term 'hypernova' was first employed for a SN. Late-time observations of SN 1998bw showed broad Fe emission lines and a narrower, sharply peaked [O I] $\lambda\lambda 6300, 6364$ feature, inconsistent with spherically symmetric ejecta (Mazzali et al., 2001), but in good agreement with a jet-like explosion geometry as expected for GRB-related SNe (Paczyński, 1998a,b; MacFadyen & Woosley, 1999; Woosley & Bloom, 2006).

Other GRB-SNe discovered in the following years resembled SN 1998bw in almost every detail, and a simple picture seemed to emerge: normal-energetic SNe Ic ($E_{\rm kin} \sim 10^{51}$ erg, not too broad spectral lines, moderate luminosity) without GRB-connection on the one hand, and GRB-related hypernovae with at least ten times the explosion energy, broad lines and high luminosity on the other hand. An opening angle of the relativistic jet of a few degrees implies that only in a few percent of all GRBs an observer would be inside the cone where the γ-ray signal can be detected, while a possible associated SN would be seen from all directions. Taking this effect into account, it appeared possible that every long-duration GRB might be connected with a SN.

By now it is known that this picture was too simple. First, a number of SNe Ic have been discovered (one of them is presented in Chapter 5 of this thesis) which feature explosion energies intermediate between normal-energetic SNe Ic and hypernovae, are very diverse in their appearance (some broad-lined, others not), and are apparently not connected to GRBs. The latter can be inferred from the non-detection or faintness of these objects at radio wavelengths, where GRB-jets emit strongly.[3] Another supernova, SN 2006aj, was undoubtedly associated with the X-ray flash (XRF) of 2006 February 18 (XRFs are supposed to be 'soft' GRBs), and shows all spectroscopic characteristics of a BL-SN Ic (Pian et al., 2006). However, the short rise time of its light curve suggests an ejecta mass much smaller than in SN 1998bw, and the same accounts for the explosion energy. In fact, SN 2006aj turned out to be just slightly more energetic than ordinary SNe Ic (Mazzali et al., 2006). Finally, fairly nearby long-duration GRBs have been found not to be associated with a SN brighter than $\mathrm{M} \sim -14$, corresponding to the ejection of $\sim 10^{-3} M_\odot$ of ^{56}Ni (Gehrels et al., 2006; Fynbo et al., 2006; Della Valle et al., 2006; Gal-Yam et al., 2006). This ultimately casts doubts on the generally favoured explosion mechanisms. As a bottom line, the exact link between SNe and GRBs is not yet fully understood. One could also say it is more open than ever.

[3] Note that the radio signal of a GRB can be observed even if the jet does not point to the observer and no γ-ray emission is detected.

1.3.4 Asphericity of the ejecta

Two different methods exist to probe the geometry of SN ejecta: spectroscopy during the nebular phase (which is expensive in terms of telescope time), and spectropolarimetry (which is more expensive). Owing to the low intrinsic polarisation level of SNe (few percent at most), even with 10 m-class telescopes spectropolarimetry is feasible only for the most nearby objects close to their peak brightness. Therefore, spectropolarimetry provides insight into the geometry of outer layers above the photosphere around maximum light, whereas the inner parts of the ejecta, which are closest to the site of the core collapse and should carry the strongest imprint thereof, practically cannot be accessed in this way. Studying the emission-line profiles in nebular spectra, when the ejecta are transparent and the emissivity is roughly proportional to the density of the emitting material, is hence the way to go.

The question of the ejecta geometry of stripped-encvelope CC-SNe has just recently gained new attention, as it is closely related to the GRB-connection of some SNe Ic. Standard GRB models predict an ejection of ^{56}Ni-rich material along a polar, likely MHD-driven jet at rather high velocity, while oxygen-rich material, in an onion-shell structure initially located further outwards, is concentrated towards the equator and ejected at lower velocity. A parametrised jet-model has proven to be well suited to reproduce the characteristics of the nebular spectra of SN 1998bw, in particular the sharply peaked [O I] $\lambda\lambda 6300, 6364$ line, and Fe lines broader than those of O (Mazzali et al., 2001; Maeda et al., 2002).

If such a geometry is generic for GRB-SNe, one may ask what all those SNe look like which are observed from larger viewing angles relative to the jet. Assuming a jet opening angle of a few degrees, simple geometrical considerations show that these events, in which no GRB can direcly be observed, should be up to one order of magnitude more frequent than confirmed GRB-SNe. According to the models of Maeda et al. (2002), the [O I] $\lambda\lambda 6300, 6364$ becomes double-peaked for viewing angles close to 90°, as the oxygen distribution then resembles a doughnut (with a central void), viewed sideways (Fig. 1.9). Such a line profile has in fact been observed in the BL-SN 2003jd (Mazzali et al., 2005b), but the radio-non-detection of SN 2003jd casts doubts on its association with a GRB (Soderberg et al., 2006).

That asphericity and clumpiness can be present in the ejecta of CC-SNe is a long-known fact (see, e.g., Matheson et al., 2000). However, recent studies (cf. Maeda et al. 2008, Modjaz, Kirshner & Challis 2008 and Chapter 6 of this thesis) suggest that even strong large-scale asymmetries are nothing special, but a ubiquitous property of SNe Ib/c, thus lending support to explosion

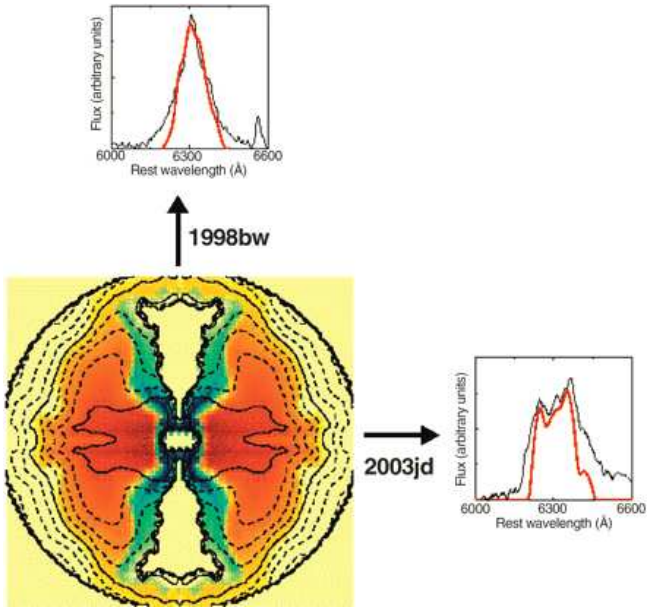

FIGURE 1.9— Ejecta distribution in Maeda et al.'s (2002) parametrised jet-model for GRB-SNe. Blue and green colours stand for Fe-group material, red for oxygen. The resulting [O I] $\lambda\lambda 6300, 6364$ profiles for different viewing angles are also shown (from Mazzali et al. 2005b).

mechanisms which naturally generate such asphericities, most notably the SASI mechanism. Double-peaked [O I] $\lambda\lambda 6300, 6364$ profiles are not limited to BL- or highly energetic SNe. The opposite rather seems to hold: they are quite rare among BL-SNe Ic (Chapter 6.5.2).

1.3.5 Own work

In Chapter 5 extensive optical and near-IR observations of the Type Ic SN 2004aw are presented. SN 2004aw is not broad-lined, but using Arnett's (1982) relations its slow light-curve evolution in combination with reasonably large ejecta velocities suggests a larger-than-average ejecta mass and kinetic energy, making SN 2004aw a possible link between normal, low-energy SNe Ic and hypernovae. With $M_{V,\mathrm{max}} \sim -18$, SN 2004aw may be somewhat more luminous than most other SNe Ic, but does not reach the brightness of those SNe which host a GRB. The nebular [O I] $\lambda\lambda 6300, 6364$ line profile of SN 2004aw exhibits a narrow line core which resembles that of SN 1998bw, indicating considerable asphericity.

Its extended data set makes SN 2004aw one of the best-studied SNe Ic ever, allowing a number of issues related to the heterogeneity of this class to

be addressed. For instance, through the non-detection of He I $\lambda 2.058\,\mu$m in a near-IR spectrum, a tight upper limit can be placed on the presence of He in the ejecta. This suggests that also the prominent feature at $1.04\,\mu$m in the same spectrum is not mainly He I $\lambda 1.083\,\mu$m (which is the strongest line of He I in the optical to near-IR regime), but rather dominated by C I lines, with maybe some contribution from He I. This is in agreement with the conclusion which Valenti et al. (2007b) obtained for the carbon-rich Type Ic SN 2007gr, but in contradiction to earlier suggestions for SNe Ic based on optical spectra or the $1.04\,\mu$m line alone (Filippenko et al., 1995a; Clocchiatti et al., 1996).

The second project about stripped-envelope CC-SNe presented in Chapter 6 is dedicated to an in-depth study of their ejecta geometry by analysing the profiles of nebular emission lines. Since this work is intended to be representative and of statistical significance, as large a sample of objects as possible is evaluated, making use of spectra already published in the literature, previously unpublished spectra from the Padova-Asiago SN archive, and spectra newly acquired through dedicated programmes. A total of 98 spectra of 39 different objects turns this into the biggest observational study ever conducted on late-phase spectra of stripped-envelope CC-SNe.

We fit the [O I] $\lambda\lambda 6300, 6364$ feature with multiple Gaussians (this choice is motivated in Section 6.3.1), trying to identify its principal components. In doing so, the doublet nature of the feature is automatically accounted for by assuming the low-matter-density limit for the intensity ratio of its two constituents. Evaluating the best-fit parameters, we try to identify recurrent patterns and to organise the objects within classes. Linking these classes to the actual ejecta geometries is not trivial, and in some cases the solution is degenerate. Nevertheless, for individual objects as well as for the entire statistical sample some interesting results are obtained. Potentially spherical SNe Ib/c seem to be relatively rare, making up just over 50% of the sample under the most optimistic assumptions, and significantly less than 50% with a more realistic treatment. Asphericity is hence a ubiquitous feature of this whole class. Symmetric double-peaked [O I] profiles, as one would expect for jet-SNe viewed sideways, are too rare to believe that a majority of the numerous objects with sharply peaked [O I] lines should be jet-SNe viewed along the jet axis. In many objects the [O I] feature exhibits randomly shifted secondary peaks or shoulders, interpreted as blobs of matter ejected in arbitrary directions. The mass contained in these blobs and their velocities can be quite large, making momentum conservation a challenge. We suggest that the observed configurations could correspond to strongly anisotropic models as presented by Scheck et al. (2004), Scheck et al. (2006) and Kifonidis et al. (2006), where neutron-star recoils provide momentum compensation.

In spectra taken earlier than ~ 200 d after maximum light, we systematically find blueshifted [O I] $\lambda\lambda 6300, 6364$ lines, most convincingly explained by residual opacity in the central region of the ejecta, which acts to shade the receding parts that otherwise give rise to the redshifted emission. Hence, it is only after some 200 d that the spectra have turned fully nebular, and attention has to be paid if earlier spectra are to be analysed or modelled.

In conclusion, the two projects about stripped-envelope core-collapse SNe, though quite different in their approach, both highlight the diversity that these objects exhibit. I am convinced that especially the ejecta geometry will attract more attention in the future, since it may influence essentially all relevant SN properties from the LC shape to the peak luminosity, and since it is a key feature to explore the SN-GRB connection.

2

Data acquisition and processing

Supernovae radiate a large fraction of their energy in the optical and near-IR regime. From an observational point of view, this is a lucky coincidence, as the Earth's atmospheric windows at these wavelengths permit ground-based observations, enabling both a more efficient SN search and more intensive and regular follow-up observations than would be possible from space, not speaking about the costs of respective space missions. All the observations included in this thesis were consequently made in the optical and near IR (3000–25 000 Å).

In this chapter some basic requirements concerning the data acquisition, mostly rooted in the nature of SNe as transient objects, are discussed (Section 2.1), and the instruments used to observe the SNe in this thesis are briefly presented (Section 2.2). Moreover, the techniques of photometric and spectroscopic data reduction are explained (Section 2.3).

2.1 Data acquisition

While Chapter 6 of this thesis mostly makes use of archival data or data already published in the literature, Chapters 4 and 5 are based on data newly obtained during an extensive observational campaign conducted by the European Supernova Collaboration (ESC)[1], a European Research Training Network (RTN) founded to study the Physics of Type Ia SNe. Following the strategy to observe in great depth a few objects rather than sparsely a big number, the aim was to get daily high signal-to-noise (S/N) optical photometric and spectroscopic observations before and around maximum light, a more relaxed sampling during the following weeks, and a few more observations in the neb-

[1] http://www.mpa-garching.mpg.de/∼rtn/

ular phase, when the SN ejecta are optically thin. A good temporal sampling is particularly important during the earliest phases after the explosion, when the spectral evolution is fast. A large number of early spectra is a requirement for sophisticated modelling techniques such as abundance tomography (Stehle et al., 2005). Whenever possible, the intensive optical follow-up was complemented by sporadic observations in the near IR.

Given that the occurrence of a SN is unpredictable, most of these observations could not be scheduled in visitor mode or regular service mode on fixed dates. Instead, to have maximum flexibility and be able to react quickly, Target-of-Opportunity (ToO) observations were the preferred modus operandi. Because of instrumental scheduling constraints, and to minimise the bad-weather risk, a large number of telescopes / instruments at different observatories spread all over the world were used to collect the data. Moreover, to fill possible gaps and intensify the sampling during important phases, a-posteriori collaborations with the Carnegie-Supernova-Project (CSP)[2] team (for SN 2005bl, Chapter 4) and the Berkeley Supernova Group (for SN 2004aw, Chapter 5) were initiated. As detailed in Chapter 2.3.2, the downside of this strategy was the increased effort necessary to homogenise the photometry from various sources.

2.2 Telescopes and instrumentation

In the following, we will briefly describe the main technical specifications of the different instrumental configurations used for the observations of the SNe presented in Chapters 4 and 5 of this thesis.

WHT + PFIP The 4.2 m William Herschel Telescope (WHT) at the Roque de los Muchachos Observatory, La Palma (Spain), equipped with the Prime Focus Camera (PFIP), was used for imaging with *UBVRI* Bessell filters. PFIP consists of two E2V 2k×4k CCDs, giving a scale of 0.24 arcsec/pixel and a field of view of 16.2×16.2 arcmin^2. The readout noise (RON) is 4.2 e^-, the conversion factor (gain) 0.9 e^-/ADU.
http://www.ing.iac.es/Astronomy/instruments/pfip/

TNG + DOLORES DOLORES (Device Optimized for the LOw RESolution) is installed at the Nasmyth B focus of the 3.58 m Telescopio Nazionale Galileo (TNG) on La Palma (Spain). The detector is a Loral thinned and back-illuminated 2048×2048 CCD. The scale is 0.275 arcsec/pixel (pixel size 15 μm), which yields a field of view of 9.4×9.4 arcmin^2. The conversion factor is 0.97 e^-/ADU, the RON $\sim 9\,e^-$. The instrument allows imaging as well as spectroscopic observations. We used Bessell *UBVRI* filters

[2] http://www.csp1.lco.cl/∼cspuser1/PUB/CSP.html

and the low-resolution grisms LR-B (3000–8800 Å, dispersion 2.8 Å/pixel) and LR-R (4470–10360 Å, dispersion 2.9 Å/pixel).
http://www.tng.iac.es/instruments/lrs/

TNG + NICS Equipped with NICS (Near Infrared Camera Spectrometer), the TNG was used to collect near-IR imaging and spectroscopy. The NICS detector is a Rockwell 1024×1024 HgCdTe Hawaii array, yielding an image scale of 0.25 arcsec/pixel and a field of view of 4.2×4.2 arcmin^2. The conversion factor is $8\,e^-$/ADU, the read noise $24\,e^-$. Imaging was performed in JHK' filters, while for spectroscopy an Amici prism (0.8–2.5 μm, dispersion 30–100 Å/pixel) was used as disperser.
http://www.tng.iac.es/instruments/nics/

NOT + ALFOSC Imaging and spectroscopy was obtained at the 2.56 m Nordic Optical Telescope (NOT) on La Palma (Spain) equipped with ALFOSC (Andalucia Faint Object Spectrograph and Camera). ALFOSC contains an E2V42-40 2k×2k back-illuminated CCD with 13.5 μm pixels, yielding a scale of 0.19 arcsec/pixel and a field of view of 6.3×6.3 arcmin^2. A gain of $0.726\,e^-$/ADU and a RON of $3.2\,e^-$ have been specified. Photometry was performed in *UBVRI* Bessell filters, while for spectroscopy the grism #4 (3200-9100 Å, dispersion 3.0 Å/pixel) was used.
http://www.not.iac.es/instruments/alfosc/

LT + RATCAM Imaging data were obtained with the optical RATCAM CCD Camera of the 2.0 m robotic Liverpool Telescope (LT) on La Palma (Spain). The CCD is a 2048×2048 pixel E2V CCD42-40, with a pixel size of 13.5 μm, a scale $\sim$ 0.135 arcsec/pixel and a field of view of 4.6×4.6 arcmin^2. The gain is $2.72\,e^-$/ADU, the RON $< 5\,e^-$. Sloan *ugriz* and Bessell BV filters were used.
http://telescope.livjm.ac.uk/Info/TelInst/Inst/RATCam/

Calar Alto 3.5 m Telescope + OMEGA 2000 OMEGA 2000, mounted at the prime focus of the 3.5 m Telescope at Calar Alto Observatory (located in Sierra de Los Filabres, Andalucía, Spain), offers wide-field (15.4×15.4 arcmin^2) near-IR imaging in JHK' filters. The Rockwell 2k×2k Hawaii-2 HgCdTe detector with 18 μm pixels yields an image scale of 0.45 arcsec/pixel, has a RON of $32\,e^-$ and a gain of $4.15\,e^-$/ADU.
http://www.caha.es/CAHA/Instruments/O2000/index.html

Calar Alto 2.2 m Telescope + CAFOS CAFOS, (Calar Alto Faint Object Spectrograph) mounted at the 2.2 m Telescope of the Calar Alto Observatory (Spain), is a focal-reducer instrument that allows imaging and

spectroscopic observations. Its 2048×2048 SITe#1d CCD has a pixel size of 24 μm, yielding an image scale of 0.53 arcsec/pixel, and a circular unvignetted field of view of 16 arcmin diameter. The gain is 2.3 e^-/ADU, the RON 5.06 e^-. Johnson *UBVRI* filters and the low-resolution grisms B-200 (range 3200–7000 Å, dispersion 4.4 Å/pixel) and R-200 (range 6300–11000 Å, dispersion 4.2 Å/pixel) were used for the observations.
http://www.caha.es/CAHA/Instruments/CAFOS/

Asiago-Ekar Copernico Telescope + AFOSC The 1.82 m Telescope of the Cima Ekar Observatory is located near Asiago, Italy. AFOSC (Asiago Faint Object Spectrograph and Camera) is equipped with a Tektronix TK1024 thinned back-illuminated 1024×1024 CCD, featuring a pixel size of 24 μm, an image scale of 0.473 arcsec/pixel, and a field of view of 8.1×8.1 arcmin^2. Gain and RON are 1.86 e^-/ADU and 9.6 e^-. For the photometry Johnson *BVR* and a Gunn *i* filter were used; spectroscopic observations were performed with the grisms #2 (3720–10200 Å, dispersion 15.67 Å/pixel) and #4 (3500–8450 Å, dispersion 4.99 Å/pixel).
http://www.oapd.inaf.it/asiago/2000/2300/2310.html

Loiano 152 cm Telescope + BFOSC The 1.52 m Loiano Telescope with a Ritchey-Chretien optical design is located near Bologna (Italy). BFOSC (Bologna Faint Object Spectrograph and Camera) contains an E2V 1340×1300 CCD camera with a scale of 0.58 arcsec/pixel, a pixel size of 20 μm, and a field of view of 13.0×12.6 arcmin^2. A conversion factor of 2.13 e^-/ADU and a RON of 1.73 e^- are specified. The observations were made with a set of *BVRI* Johnson filters.
http://www.bo.astro.it/loiano/152cm.html

Wendelstein 0.8 m Telescope + MONICA The Wendelstein 0.8 m Telescope atop the Wendelstein in the Bavarian Alps, Germany, contributed imaging observations obtained with the MOnochromatic Image CAmera MONICA. The detector is a thinned, back-illuminated, AR-coated 1024×1024 CCD with 24 μm pixel size, yielding a field of view of 8.5×8.5 arcmin^2 with a sampling of 0.5 arcsec/pixel (gain = 3.36 e^-/ADU, RON = 8 e^-). Bessell *B* and *I*, a Roeser *BV* and a Roeser *R*2 filter were used.
http://www.wendelstein-observatorium.de/monica/monica_en.html/

Keck I + LRIS The 10.0 m Keck I Telescope atop Mauna Kea, Hawaii (USA), was used for spectroscopic observations with the Low Resolution Imaging Spectrometer (LRIS), a double-beam spectrograph mounted at the Cassegrain focus. The blue arm is equipped with two 2k×4k Marconi

CCDs of 15 μm pixel size (gain = 1.5 e^-/ADU, RON = 4 e^-, plate scale 0.135 arcsec/pixel), and a 400 l/mm grating was used (dispersion 1.07 Å/pixel). On the red arm, a similar 400 l/mm grating yielded a dispersion of 1.92 Å/pixel, owing to the larger pixel size (24 μm, plate scale 0.215 arcsec/pixel) of the Tektronix 2k×2k detector (gain = 2.0 e^-/ADU, RON = 6–7 e^-). Both arms together allow a wavelength coverage from 3200 to 10 000 Å.
http://www2.keck.hawaii.edu/inst/lris/

UKIRT + UIST The 3.8 m United Kingdom Infra-Red Telescope is a dedicated IR facility located on Mauna Kea, Hawaii (USA). Equipped with UIST we used it in spectroscopic mode with the low-resolution *HK* grism (1.4–2.5 μm, R = 500). The detector is a 1024×1024 Aladdin II InSb array, with a conversion factor of 15 e^-/ADU.
http://www.jach.hawaii.edu/UKIRT/instruments/uist/uist.html

Shane Reflector + KAST The Lick Observatory Shane 3 m Reflector on Mount Hamilton, California (USA) is equipped with KAST, a double spectrograph designed to obtain simultaneous red/blue spectra. Both arms use UV-flooded Reticon 1200×400 devices with 27 μm pixels. The gain is 3.9 e^-/ADU, the read noise 6.5 e^- and 8.3 e^- for the blue and red side, respectively. The grism gm600 on the blue side (3300–5520 Å, dispersion 1.85 Å/pixel) and the grating grt300 on the red side (3800–11 0000 Å, dispersion 4.60 Å/pixel) were used.
http://mthamilton.ucolick.org/techdocs/telescopes/Shane/

KAIT + CCD camera The Katzman Automatic Imaging Telescope (KAIT) at Lick Observatory atop Mount Hamilton (California) is an entirely robotic 0.76 m telescope dedicated to the search and follow-up monitoring of supernovae. It is equipped with a 500×500 Peltier-cooled, back-illuminated CCD camera. The pixel size of 24 μm yields a scale of 0.8 arcsec/pixel and a field of view of 6.8×6.8 arcmin^2. Gain is 3.8 e^-/ADU, RON = 9 e^-. A set of Bessell *BVRI* filters was used.
http://astro.berkeley.edu/∼bait/kait.html

ESO VLT UT1 + FORS2 FORS2, the FOcal Reducer/low dispersion Spectrograph 2 mounted at the 8.2 m ESO Very Large Telescope (VLT) UT1 at Cerro Paranal, Chile, contains a mosaic of two 2k×4k MIT CCDs with 15 μm pixel size, a read-out noise of 2.7 e^-, and a conversion factor of 0.70 e^-/ADU. The pixel scale is 0.25 arcsec/pixel, the unvignetted field of view 6.8×6.8 arcmin^2. Bessell B and R filters and the grism

300V+GG435 order separation filter (wavelengths range 4450-8650 Å, dispersion 1.7 Å/pixel) have been used for the observations.
http://www.eso.org/instruments/fors2/

Las Campanas 2.5 m du Pont Telescope + WFCCD Spectroscopic observations were obtained with the 2.5 m Irénée du Pont Telescope at Las Campanas Observatory (Chile), equipped with the Wide Field Re-imaging CCD Camera WFCCD. Its Tek#5 2048×2048 CCD (24 μm pixels, gain = 1.0 e^-/ADU, RON = 5.6 e^-) yields dispersions of 3 and 4 Å/pixel with the Blue and Red grisms, respectively. A total wavelength coverage from 3800 to 9325 Å was achieved with this setup.
http://www.lco.cl/telescopes-information/irenee-du-pont/instruments/

Las Campanas 1.0 m Swope Telescope + CCD The 1.0 m Swope Telescope of Las Campanas Observatory, Chile, was used for optical observations with the Direct CCD Camera and a set of Sloan *ugri* and Bessell *BV* filters. The SITe#3 2048×3150 CCD (15 μm pixels) yields a field of view of 14.8×22.8 arcmin^2 at a scale of 0.435 arcsec/pixel (gain = 2.5 e^-/ADU, RON = 6.6 e^-).
http://www.lco.cl/telescopes-information/henrietta-swope/instruments

2.3 m SSO Telescope + DBS / imager The 2.3 m Telescope of the Siding Spring Observatory (Australia) hosts a Double Beam Spectrograph (DBS) equipped with two SITe 1752×532, ST-D06AB, thinned, back-illuminated, AR-coated, 15 μm pixel devices, labelled CCD #7 and CCD #9 (associated with the DBS-B and DBS-R arm, respectively). The RON is about 6 e^-, the gain $\sim$1 e^-/ADU. A separate optical imager was equipped with a SITe 1024×1024 thinned CCD with 24 μm pixels (#11, available until October 2004), with 0.59 arcsec/pixel, a 6 arcmin in diameter circular field of view, gain = 1 e^-/ADU and RON = 6 e^-. Both spectra and imaging (in Bessell *UBVRI* bands) were obtained.
http://www.mso.anu.edu.au/observing/telescopes/2.3m.php

2.3 Data reduction

The SN observations were processed using standard routines in IRAF[3] (Massey, 1997). The photometric measurements were performed using dedicated software developed by the Padova-Asiago SN Group within the IRAF environment.

[3] IRAF is distributed by the National Optical Astronomy Observatories, which are operated by the Association of Universities for Research in Astronomy, Inc, under contract with the National Science Foundation.

2.3.1 Pre-reduction

The first aim of data processing consists of removing any instrumental signature (due to the detector or the telescope) from the raw frames. This involves the following steps:

Bias subtraction. The bias level is an electronic offset added to the signal of the CCD to ensure that the Analogue-to-Digital Converter (ADC) always receives a positive value. The ADC samples the charge accumulated in a CCD pixel and returns a digital value. This value is proportional to the number of electrons detected in the pixel and is measured in Analogue-to-Digital Units (ADUs). The ratio between ADUs and the number of electrons is known as gain. It is common practice to create a 'master bias' image from the average of several bias images (frames obtained with exposure times of 0 seconds and the shutter closed) in order to improve the statistics, reduce the random noise and remove cosmic rays. The master bias is subtracted from all other frames.

Overscan correction. This is a second-order correction to account for possible changes in the bias level during the night (triggered, e.g., by temperature variations). To determine this effect, the mean bias level of each image is measured in the 'overscan' region (a stripe of a few columns/rows at the edge of the CCD, not exposed to light) and removed from the whole frame.

Trimming. Once the overscan correction is done, the respective columns/rows and other peripheral regions of the frame, which are often affected by irregular response and degraded, can be cut off, keeping only the area meaningful for a scientific analysis.

Flatfielding. Multiplicative pixel-to-pixel variations of the CCD sensitivity caused by transmissivity variations of the CCD coating, dust on the chip or the filter, and vignetting of the telescope optics, are corrected through division by flatfields. Imaging flatfields are obtained by pointing the telescope at a uniformly illuminated screen inside the telescope dome (domeflats) or, better, the sky at twilight (skyflats). Since the CCD response is wavelength-dependent, and since different filters have different blemishes, flatfield exposures are required in all the bands used for the scientific frames. In order to increase the signal-to-noise (S/N) and to remove artefacts such as cosmic rays or stars (in the case of skyflats), a number of flats are median-combined to obtain a master flat. Besides the tasks already mentioned, spectroscopic flatfields are required to reduce the 'fringing', an

interference pattern which occurs in thinned CCDs when the wavelength of monochromatic night-sky emission lines is similar to the thickness of the chip. Spectroscopic flats are obtained with an internal quartz lamp. As an additional processing step they are normalised along the dispersion axis to remove large-scale gradients owing to the system response, and keep only small-scale pixel-to-pixel sensitivity variations and the fringing.

2.3.2 Photometry

The photometric observations of our objects were obtained with a number of instruments equipped with broad-band Bessell *UBVRI* or Sloan *ugriz* filters. Typically, the observations consisted of short exposures at early times and dithered multiple exposures at late epochs. In the latter case, all images with the same filter were first geometrically aligned (registered) and then combined to produce a single deep image.

Because of the high and variable background emission in the near IR, and the limited linearity regime of near-IR detectors, observations in the JHK' bands were always made in form of multiple short exposures. Median-combined without registration these dithered images yielded a sky image with all astronomical sources removed. This sky image was subsequently subtracted from all individual frames before their registration and combination. While the basic reduction (background determination and subtraction, combination of dithered images) was always performed manually in order to have the best possible control over changes in the sky emission, a dedicated software (SNAP[4]) was used to correct cross-talking and field distortions in the NICS frames.

Measurement techniques and magnitude estimates

A major complication in SN photometry is separating the light from the SN itself from the underlying galaxy at the SN position. Poor subtraction of the background light can produce large errors in the light-curve shapes and colours. This is a particular concern at late times when the SN light fades. But also the SN location within its host galaxy (in the outskirts or close to the nucleus or a prominent spiral arm) and the seeing have an influence on the quality of the SN photometry. Depending on these circumstances, different photometric techniques were applied. When the SN signal was high and clearly dominated over any background sources, the SN magnitudes were typically measured using

[4]Written by F. Mannucci,
http://www.arcetri.astro.it/∼filippo/snap/

the Point Spread Function[5] fitting method, while in the case of a very complex background and at late phases, when the SN magnitude is comparable to that of the background features, preference was given to the template-subtraction technique.

PSF-fitting technique. This method consists of building up a PSF by fitting the 2D stellar profiles of isolated, unsaturated stars in the field, and measuring the SN magnitudes by scaling the PSF to obtain the best match with the actual SN profile. The host-galaxy background is fitted by low-order polynomials in a vicinity of the SN, and subtracted before the SN magnitudes are determined. For this purpose the Padova SN Group developed SNOOPY (SuperNOvaPhotometrY), a package originally designed by F. Patat and later implemented in IRAF by E. Cappellaro. It is based on DAOPHOT. The PSF-fitting technique is usually employed when the SN is projected on a fairly smooth background, when its luminosity largely exceeds that of the surroundings, or when no pre-explosion host-galaxy images are available to apply template subtraction.

In Fig. 2.1 an example of the application of SNOOPY to early-time observations of SNe 2004aw (Chapter 5) and 2005bl (Chapter 4) is shown.

Template-subtraction technique. This technique is mandatory when the SN exploded in a complex region, e.g. close to the host-galaxy nucleus, H II regions or spiral arms, and in general when the SN is faint. It consists of removing the host-galaxy contribution by subtracting a reference frame acquired when the supernova was not present, before or long after its explosion (Filippenko et al., 1986). This requirement is often a limitation for the applicability of the method. Ideally, the templates should be obtained with the same telescope and with similar seeing as the scientific image that contains the SN. Since this is typically not possible, a number of operations are required before a difference image can be obtained. The first step is a geometrical registration of target and template in order to correct for different pixel scale, spatial orientation and position within the frame. After that, the image with better seeing is degraded by Gaussian smoothing to match the PSF of the poorer-seeing image, and both frames are scaled to the same intensity of non-variable sources. Finally, the template image is subtracted from the SN frame. All these steps were performed with the template-subtraction program

[5]The Point Spread Function or PSF is the 2D function which describes the light distribution of a point source on the detector after passing through the earth's turbulent atmosphere and the telescope optics.

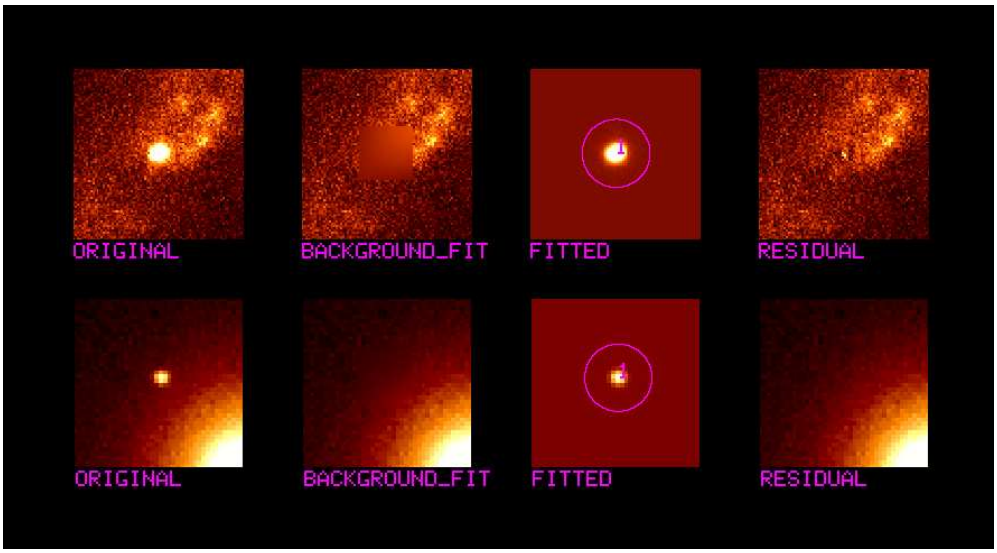

FIGURE 2.1— PSF-fitting SN photometry with SNOOPY, demonstrated for two quite different cases. SN 2004aw (top row) is projected on an arc of the host galaxy, which is a complicated background to fit. In contrast, the background in the vicinity of SN 2005bl (bottom row) varies smoothly. From left to right the original image, the fit of the background, the fitted SN PSF and the residuals after SN subtraction are displayed.

SVSUB, written by S. Valenti and based on ISIS (Alard, 2000). Ideally the resulting frame is flat except for variable objects in the field (the SN, variable stars), asteroids and artificial satellites. In reality, saturated stars, cosmic rays, hot pixels and bad columns leave undesired residuals in the background-subtracted images.

At this point, the instrumental magnitude of the SN can be measured in the galaxy-subtracted image using aperture photometry (e.g. with the IRAF task IMEXAMINE) or PSF-fitting photometry (SNOOPY is an integral part of the SVSUB package). An example of the template-subtraction technique is shown in Fig. 2.2, where a template taken $\sim$1 yr after the explosion is subtracted from an early-time image of SN 2005bl. The SN is clearly visible in the difference image, along with residuals of the brightest stars and some cosmic rays.

Both techniques (PSF-fitting and template subtraction) were used to obtain the photometric results presented in this work. For SN 2004aw (see Chapter 5) template subtraction was applied only to images observed with the KAIT telescope, which suffered from rather poor pixel scale and seeing, hence not allowing

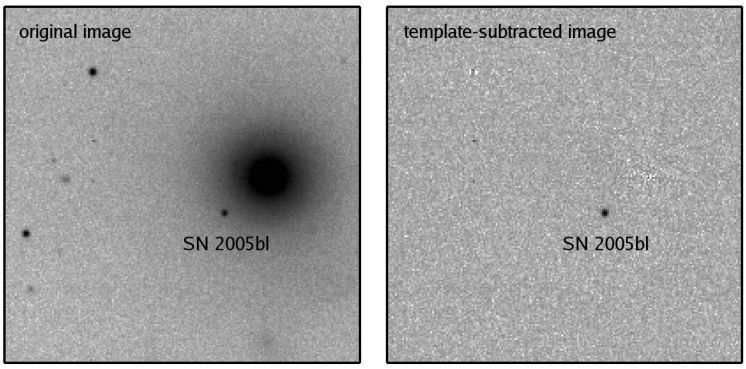

FIGURE 2.2— Template-subtraction technique, shown for an R-band image of SN 2005bl. *Left:* original image containing the SN, the host galaxy and several stellar sources. *Right:* After template subtraction only the SN is left.

a good separation of SN and host-galaxy light in the original images. To this aim, templates were obtained 266 to 270 d after the B-band maximum, when the SN had largely faded from visibility. They were taken with the same telescope (KAIT) and under variable seeing conditions, thus facilitating the subtraction. However, the SN had not entirely faded away at that epoch, which caused a flux over-subtraction. This was corrected by subtracting from the KAIT templates the SN flux measured in nearly simultaneous (day +258) TNG observations, which had better quality and seeing than those acquired with KAIT. Depending on epoch and filter, the correction thus derived ranged from 0.02 to 0.10 mag.

Although the host-galaxy background at the projected site of SN 2005bl (Chapter 4) seemed to be smooth, we applied the template-subtraction technique in order to eliminate any possible contamination from the host galaxy, a justified concern given the dimness of the SN. For this purpose we acquired templates in $BVRI$ with CAFOS mounted on the Calar Alto 2.2 m Telescope on UT 2006 March 28, and in $uBVgri$ with the Las Campanas 2.5 m du Pont Telescope from UT 2006 April 3 to 30, about one year after the explosion when the SN had faded from visibility. For the z band no templates were available, and the measurements were performed with ordinary background-fitting PSF photometry in SNOOPY. A check in the $BVRI$ bands showed a good agreement between the two methods. Therefore, we are confident that also our z-band photometry is sufficiently reliable.

Basic calibration

The instrumental magnitudes obtained with either method, defined as -2.5 times the logarithm of the counts in the source, are normalised to a reference exposure time of 1 s and corrected for the atmospheric extinction via

$$\mathrm{m}^*_\lambda = \mathrm{m}_{\lambda,\mathrm{instr}} + 2.5\ \log(t_{\mathrm{exp}}) - k_\lambda X_\lambda \tag{2.1}$$

where $\mathrm{m}_{\lambda,\mathrm{instr}}$ and m^*_λ are the instrumental and normalised magnitudes in the filter λ, respectively, t_{exp} is the exposure time, k_λ the atmospheric extinction coefficient depending on the telescope site, season and filter, and X_λ the airmass.

Since SNe are variable objects, each observation is unique and has to be used regardless of the ambient conditions. In order to calibrate the photometry obtained in non-photometric nights, a number of isolated, non-variable stars in the SN field are selected to be used as local standards. These are calibrated by comparison with optical (Landolt, 1992; Smith et al., 2002) or NIR (Hunt et al., 1998) standard fields during photometric nights. The Landolt-field observations also allow us to determine the colour terms, which are used to report the stars' magnitudes to a well-defined photometric system, correcting for deviations in actual passbands at the telescopes. In detail, for each night and instrumental configuration, the observation of the Landolt fields provides a system of colour equations of the form:

$$\mathrm{m}_{\lambda,\mathrm{std}} - \mathrm{m}^*_\lambda = \mathrm{ZP}_\lambda + \mathrm{ct}_{\lambda\lambda'}\left(\mathrm{m}_{\lambda,\mathrm{std}} - \mathrm{m}_{\lambda',\mathrm{std}}\right) \tag{2.2}$$

where λ and λ' are different, typically adjacent filters, $\mathrm{m}_{\lambda,\mathrm{std}}$ is the standard apparent magnitude of a star in the photometric reference system, and m^*_λ its normalised instrumental magnitude. The photometric zero point ZP_λ and the colour term $\mathrm{ct}_{\lambda\lambda'}$ characterise the instrumental configuration, and can be determined if the stars in the standard field encompass a sufficiently large range of colours. Once all zero points and colour terms are known, Eq. 2.2 can be applied to the SN field, solving for the apparent magnitudes $\mathrm{m}_{\lambda,\mathrm{std}}$ of the local standards and the SN itself. Eq. 2.2 then defines an implicit, coupled system of colour equations for the different filters. In non-photometric nights this step is iterated adjusting the zero points, until the magnitudes of the local sequence stars have converged to the values calibrated before on photometric nights.

In the near IR, Eq. 2.2 was replaced by a mere zero-point adjustment, since the observed NIR standard fields contained too few stars (or stars comprising too small a range of colours) to be suitable for a reliable estimate of the colour terms with respect to the standard JHK' system (Bessell & Brett, 1988; Wainscoat & Cowie, 1992).

Correction to standard photometric bands: S-correction

In principle, as described above Eq. 2.2 provides an estimate of the SN magnitudes. However, while this method works well for stars with their predominant blackbody continuum, it is known to be vastly imperfect for SNe with their line-dominated spectra. Hence, when calibrated through colour equations, photometric data obtained with different instruments may be systematically inconsistent, resulting in light curves with significant scatter.

Suntzeff (2000), Stritzinger et al. (2002), Krisciunas et al. (2003), Pignata (2004) and Pignata et al. (2004) have shown that with a more sophisticated treatment called 'S-correction' it is possible to overcome these problems and obtain very homogeneous SN photometry. The essence of the method is that, if the spectral energy distribution (SED) of the object and the response curves of the instruments used for the observations are both accurately known, the magnitudes can be reported to any well-defined photometric system by means of synthetic photometry. Following the implementation of Pignata (2004), the colour-term correction of Eq. 2.2 is replaced by

$$\mathrm{m}_{\lambda,\mathrm{std}} - \mathrm{m}^{*}_{\lambda} = \mathrm{ZP}_{\lambda} + S\text{-corr}_{\lambda} \tag{2.3}$$

where $S\mathrm{corr}_{\lambda}$ is the S-correction term, i.e., the difference between the synthetic SN magnitude obtained using the standard passband ($\mathrm{m}_{\lambda,\,\mathrm{syn},\,\mathrm{std}}$) and that using the actual instrumental passband ($\mathrm{m}_{\lambda,\,\mathrm{syn},\,\mathrm{instr}}$):

$$\begin{aligned} S\text{-corr}_{\lambda} &= \mathrm{m}_{\lambda,\,\mathrm{syn},\,\mathrm{std}} - \mathrm{m}_{\lambda,\,\mathrm{syn},\,\mathrm{instr}} \\ &= -2.5\,\log \int_0^{\infty} F(\lambda)\; S_{\mathrm{std}}(\lambda)\; \mathrm{d}\lambda + \mathrm{ZP}_{\lambda,\,\mathrm{syn},\,\mathrm{std}} \\ &\quad +2.5\,\log \int_0^{\infty} F(\lambda)\; S_{\mathrm{instr}}(\lambda)\; \mathrm{d}\lambda + \mathrm{ZP}_{\lambda,\,\mathrm{syn},\,\mathrm{instr}} \end{aligned} \tag{2.4}$$

In this equation $F(\lambda)$ is the flux of the SN as a function of wavelength, $S_{\mathrm{std}}(\lambda)$ and $S_{\mathrm{instr}}(\lambda)$ are the standard and instrumental passbands, and $\mathrm{ZP}_{\lambda,\,\mathrm{syn},\,\mathrm{std}}$ and $\mathrm{ZP}_{\lambda,\,\mathrm{syn},\,\mathrm{instr}}$ are the different zero points derived from synthetic photometry of Vega.

In order to determine the instrumental passband $S_{\mathrm{instr}}(\lambda)$, the following terms are taken into account:

$$S_{\mathrm{instr}}(\lambda) = T(\lambda) \cdot QE(\lambda) \cdot A(\lambda) \cdot M(\lambda) \cdot L(\lambda) \tag{2.5}$$

where $T(\lambda)$ is the filter transmission function, $QE(\lambda)$ the detector quantum efficiency, $A(\lambda)$ the continuum atmospheric transmission profile, $M(\lambda)$ the mirror reflectivity function and $L(\lambda)$ the lens throughput. Obtaining $S_{\mathrm{instr}}(\lambda)$

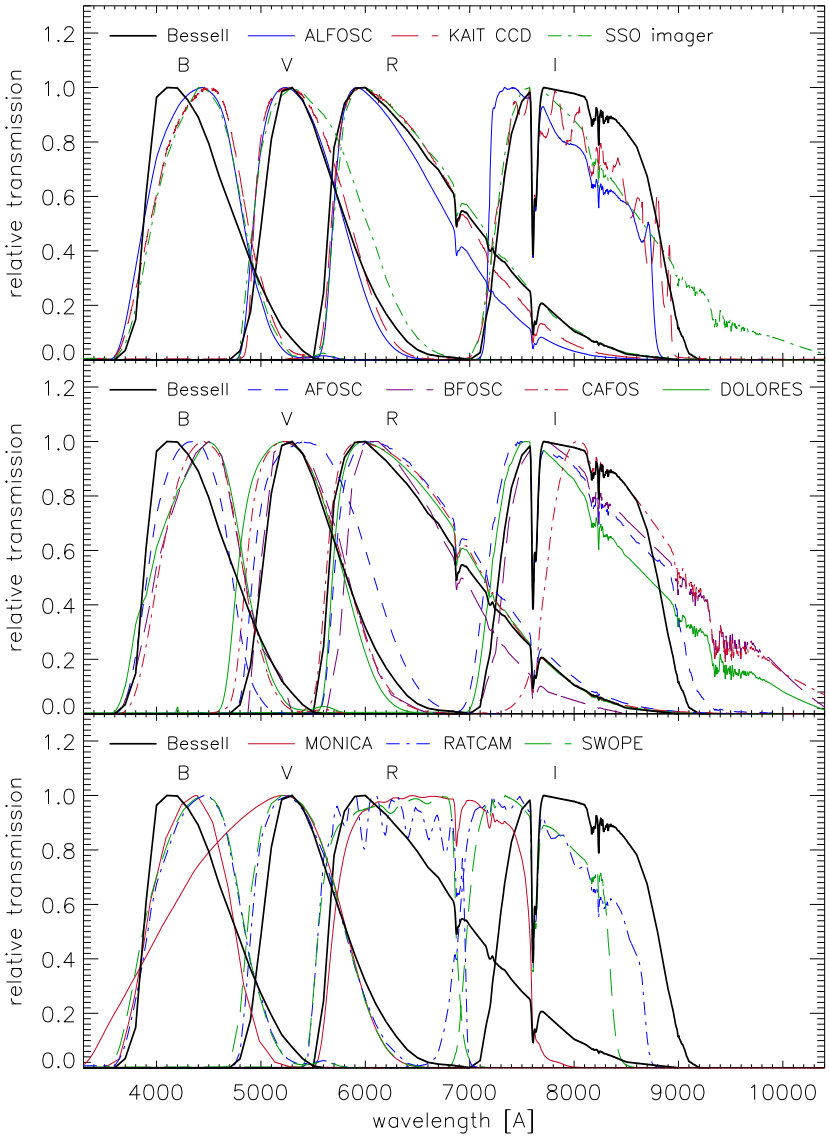

FIGURE 2.3— Instrumental *BVRI* / *ri* passbands used for the observations of SNe 2004aw and 2005bl. The standard Bessell (1990) curves are also displayed in the figure for comparison.

can be challenging, since not for all facilities the necessary information is fully available. In Fig. 2.3 the reconstructed *BVRI* passbands of most instruments used for the follow-up observations of SNe 2005bl (Chapter 4) and 2004aw (Chapter 5) are shown along with the standard Bessell (1990) curves.

Obviously, an S-correction can only be derived for epochs where SN spectra are available, and for bands which are fully covered by these spectra. The latter limited the S-correction to the $BVRI$ bands, as most spectra did not extend to the U and $zJHK'$ bands. The former requirement, on the other hand, prevented an S-correction at phases later than +50 d for SN 2005bl, and later than +40 d (B and V) or +60 d (R and I) for SN 2004aw. To fill gaps in the early-time spectroscopic coverage of SN 2005bl, several spectra of SNe 1991bg (Filippenko, 1992; Leibundgut et al., 1993; Turatto et al., 1996) and 1999by (Garnavich et al., 2004), artificially reddened and redshifted to match those of SN 2005bl, were used.

Transformation to zero redshift: K-correction

In order to compare the intrinsic properties of objects at different redshifts, one has to apply a so-called 'K-correction', which accounts for the fact that at different redshift the photometric bands sample different parts of the emitted spectrum. While the K-correction was generally omitted in the case of SN 2004aw (Chapter 5) because of its relative proximity, it was applied to the data of the more distant SN 2005bl (Chapter 4). For this SN, in computing the S-correction the spectra were shifted in order to account also for the K-correction. Since the same restrictions as before apply also here, a K-correction was only derived for the $BVRI$ bands and for data earlier than +50 d.

Photometric errors

Uncertainties in the instrumental photometry (via PSF-fitting or template subtraction) were estimated by adding artificial stars with the same magnitude and profile as the SN at positions close (within a few arcsec) to that of the SN, and applying the same measurement procedure as before to each of these (artificial-star experiment). The *rms* of the so-derived magnitudes served as estimate of the measurement error ($\mathrm{err_{art}}$).

For the calibration error we adopted, for each night and each filter, the uncertainty in the photometric zero point ($\mathrm{err_{ZP}}$), i.e., the *rms* of the local sequence stars' deviations from their calibrated values.

The final error of the SN magnitudes is then calculated as the quadratic sum of measurement error, calibration error, and in case an error associated with the S-correction:

$$\mathrm{err_{total}} = \sqrt{\mathrm{err_{art}^2} + \mathrm{err_{ZP}^2} + \mathrm{err_{S\text{-}corr}^2}} \tag{2.6}$$

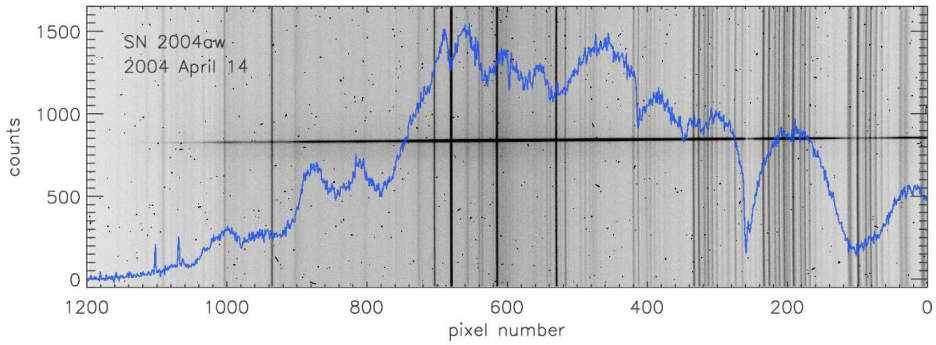

FIGURE 2.4— Two-dimensional spectroscopic image of SN 2004aw taken on 2004 April 14 with CAFOS (shown as negative). The dispersion axis is horizontal, the spatial axis (i.e., the slit orientation) vertical. The central horizontal trace is the SN, vertical lines are the monochromatic atmospheric night-sky emission lines. The numerous small dots are cosmic-ray hits. Overplotted in blue is the extracted, background-subtracted 1D spectrum which results from APALL.

2.3.3 Spectroscopy

All two-dimensional spectroscopic frames were first de-biased and flat-fielded (Chapter 2.3.1), before an optimal, variance-weighted extraction (Horne, 1986; Massey, Valdes & Barnes, 1992) was performed to obtain 1D spectra out of the 2D frames. To this aim, the location of the SN was identified in a slice along the spatial / slit direction of the 2D frames, and an extraction aperture was determined to sum up the counts inside. Background regions were selected on both sides of the aperture to subtract background or foreground flux from the host galaxy and atmospheric night-sky emission lines, and the SN aperture was traced along the dispersion direction to compensate an imperfect alignment of grism and CCD. All these steps were performed using the IRAF routine APALL (see Fig. 2.4).

Wavelength calibration was accomplished with the help of arc-lamp exposures (e.g. He-Ne, Cu-Ar, Hg-Cd) obtained with the same instrumental configuration and the telescope still pointing at the SN to avoid a change of the dispersion solution by telescope flexure. In these spectra the emission lines were identified and a polynomial dispersion function was fitted, yielding a pixel-to-wavelength transformation which thereafter was applied to the spectra of the SN and a flux standard. Whenever arc-lamp exposures were not available, the night-sky emission lines in the SN exposure itself were used. In our low-resolution spectra, the accuracy of the wavelength calibration was typically

1–2 Å throughout the useful spectral range.

The instrumental response functions required for flux calibration were determined from observations of spectrophotometric standard stars from the lists of Oke (1990), Hamuy et al. (1992) or Hamuy et al. (1994), whose fluxes are tabulated. Whenever no standard had been observed, the sensitivity curve obtained on a different night with the same instrumental configuration was used. An atmospheric extinction correction was applied using extinction coefficients tabulated for each observatory.

Errors in the absolute flux calibration can arise from global slit losses (when either the SN or the standard star are not perfectly centred in the slit) or non-photometric conditions. Most spectra were obtained with the slit oriented along the parallactic angle (i.e., perpendicular to the horizon) in order to minimise differential slit losses due to atmospheric refraction (Filippenko, 1982), which would otherwise affect the relative flux calibration of the spectra (in most cases causing a flux deficit in the blue part). Depending on the instrument / grism combination used, second-order overlap can also result in an erroneous relative flux calibration. For configurations where this effect was strong, the affected parts of the spectra were either disregarded, or corrected by dedicated software (for ALFOSC + grism #4; Stanishev 2007).

To check the calibration, the spectroscopic fluxes were transformed into magnitudes by integrating the spectra convolved with Bessell (1990) filter functions. Whenever necessary, the spectral fluxes were adjusted to match the contemporaneous photometry.

Broad telluric features (molecular absorption bands from H_2O and O_2 in the earth's atmosphere) were identified in the spectra of the standard stars and removed. Dividing by the original standard-star spectra, a correction function was derived, which was used to remove the telluric absorptions in the SN spectra. Finally, spectra of similar quality obtained during the same night were combined to increase the S/N; if the wavelength range of these spectra was different, they were averaged in their overlap region.

In 2005, (i.e., affecting the observations of SN 2005bl), the DOLORES CCD suffered from strong charge-transfer-efficiency problems. As a consequence, it was not possible to remove the night-sky emission in the TNG spectra cleanly. A pattern of negative and positive residuals was left, in some places coinciding with spectral features of the SN, thus limiting the reliability of any kind of line-depth measurements. To mitigate this problem, the lines affected were fitted with polynomials, excluding from the fit the regions of strongest residuals, and then the depth was determined in the polynomial curves.

Most reduction steps for the two IR spectra were identical to the optical case described above. After the usual pre-reduction steps, the dithered spectra

were pairwise subtracted to remove the night-sky emission. After that, the SN traces were optimally extracted, scaled to the flux level of the spectrum with the highest S/N (assuming that this suffered the least flux loss), and then combined. Wavelength calibration was performed using arc-lamp exposures (UIST) or a tabulated dispersion function relating pixel number to wavelength (NICS). Removal of telluric features and a rough flux calibration were accomplished with the help of telluric standard stars of spectral type A0 and F4V for NICS and UIST, respectively. In order to construct the sensitivity curves containing both instrumental response and atmospheric absorption, the A0 star was compared to Vega, and the F4V spectrum to that of the Sun. The final flux calibration was accomplished with respect to the contemporaneous SN photometry, and a constant correction factor was sufficient to provide satisfactory agreement. Finally, the two IR spectra taken during the same night were averaged in their overlap region.

Thermonuclear Supernovae

3

The European Supernova Collaboration

Studying a SN all the way from the earliest stages, as soon as possible after the explosion (although a delay of a few days typically cannot be avoided), to the nebular phase (starting, for Type Ia SNe, some 100 d after the explosion) is of great importance, since, owing to the fast expansion of the ejecta, the photosphere recedes as time goes on, exposing deeper and deeper layers of the SN ejecta. A time series of SN spectra can hence be considered a tomographic scan through the ejecta, providing clues on their composition as a function of depth, their temperature structure and expansion velocities. With this motivation in mind, the European Supernova Collaboration (ESC) was founded in 2002. One of its main goals was to observe about a dozen of nearby objects, collect some of the best data sets ever, and increase significantly the number of both very early ($\lesssim -10$ d) and very late SN Ia spectra available worldwide, thus providing an excellent basis for profound analyses and modelling. Since a major part of the work included in this thesis originated from observations carried out by the ESC, this chapter is devoted to reviewing the basic ideas behind this collaboration, giving a brief description of the targeted SNe, and summarising the main results derived from these observations so far.

3.1 The concept

The ESC was a joint effort of several European (+ an Australian) institutions, aiming at understanding the physics underlying Type Ia SNe. Neither observations nor theory can achieve this goal alone. Therefore, a comprehensive approach was chosen for the ESC, with observations and modelling

working hand in hand. Some of the groups involved mainly concentrated on observational programmes and tried to provide some of the best data sets ever obtained for SNe Ia, other groups performed state-of-the-art numerical simulations of the progenitor evolution and the explosions themselves, and again others provided the essential connection between these two worlds by means of radiative-transfer calculations. Note that the latter can be employed in two directions, simulating what the observable characteristics of a certain explosion model would be, or trying to constrain the models by iterating the input parameters of the radiative-transfer calculation until the observed data are matched. Both ways have been followed by the ESC.

3.2 SNe studied by the ESC

Between 2002 and 2006, the ESC studied 16 SNe in detail, 15 SNe Ia and one SN Ic which had initially been misclassified (Chapter 5.1). During this period, the ESC more than doubled the number of SNe Ia with spectra taken more than a week before maximum or having a good spectroscopic coverage in the infrared. The ESC targets generally had recession velocities < 6000 km s^{-1} (the relative proximity was one of the ESC's formal selection criteria), and only for SN 2005bl (see Chapter 4) an exception was made owing to the peculiarities found in its earliest spectrum. Here a brief overview of all these SNe is given, describing the data sets and concentrating on the individual objects' peculiarities.

SN 2002bo was the first SN observed by the ESC, and also one of the most thoroughly studied during the pre-maximum phase. The spectroscopic coverage reaches back to day -13, making the first spectrum of SN 2002bo one of the earliest ever obtained for a SN Ia. The moderately extinguished SN is an intermediate decliner [$\Delta m_{15}(B) = 1.13$], and features unusually high ejecta velocities (inferred from the Doppler shift of Si II λ6355) at early epochs. Almost daily spectroscopy until few days after maximum laid the basis for applying a novel modelling technique called abundance tomography, which entails a stratified chemical composition above the photosphere, with the radial extents of the abundance shells (and hence the compositional resolution) being determined by the temporal offsets between the observed spectra (cf. Section 3.3). This modelling was presented by Stehle et al. (2005), while most of the data were published by Benetti et al. (2004b). Some late-time data still await their publication (Elias-Rosa et al. in prep.)

SN 2002cv exploded in the same galaxy as SN 2002bo, and was discovered in the course of the 2002bo follow-up observations. Without this coin-

cidence, SN 2002cv might have been discovered later or even completely missed, since, lying behind a prominent dust lane, the SN was heavily obscured and detectable only at wavelengths redwards of ~ 6000 Å. Its high extinction (more than 9 mag in the V band) made this SN an ideal object to study the properties of the foreground dust, e.g., the total-to-selective-extinction ratio R_V. In fact, an R_V significantly smaller than for 'standard' dust in the Milky Way was found, indicating a smaller average dust grain size than in most parts of our Galaxy. The data of SN 2002cv were analysed and published by Elias-Rosa et al. (2008).

SN 2002dj is in many respects a clone of SN 2002bo, having very similar light-curve decline rates and spectroscopic characteristics, including the high ejecta velocities early on. The main difference is the smaller host-galaxy reddening, which of course is not an intrinsic SN property. The data are presented by Pignata et al. (2008).

SN 2002er is a somewhat faster decliner [$\Delta m_{15}(B) = 1.33$] than SNe 2002bo and 2002dj, but still in the 'normal' range for SNe Ia. Showing no evident spectrophotometric peculiarities, SN 2002er can be regarded as template SN for $\Delta m_{15}(B) \sim 1.3$. It is also the first ESC SN (and among the first worldwide) for which the sophisticated S-correction technique (see Chapter 2.3.2) was applied to calibrate the photometry obtained with many different instruments, reporting it to the Bessell standard photometric system. The photometry of SN 2002er was reduced and analysed by Pignata et al. (2004), while the observed spectra and basic spectral modelling were presented by Kotak et al. (2005).

SN 2003cg was the second ESC target with particularly strong dust extinction in the host galaxy. Like SN 2002cv it was located behind a prominent dust lane, but this time the extinction was less extreme, so that SN 2003cg could be studied also at bluer wavelengths. Again, a lower-than-average value of R_V was inferred, suggesting a fine grain structure of the dust. Apart from its extinction, SN 2003cg appears to be a normal SN Ia with $\Delta m_{15}(B) = 1.25$ and moderate ejecta velocities. Of particular interest is its excellent photometric and spectroscopic coverage in the near IR and a first photometric detection as early as 18 d before B-band maximum. The 2003cg data and synthetic spectra were presented by Elias-Rosa et al. (2006).

SN 2003du is a comparatively slow decliner [$\Delta m_{15}(B) = 1.02$], and has one of the best data sets of all ESC SNe, with the earliest optical spectrum taken

13 d before maximum light. Prominent high-velocity features (HVFs) of Ca and Si are present in the pre-maximum spectra. Suffering from virtually no dust extinction, the estimates on absolute magnitudes and colours of this SN are particularly reliable. The reduction and interpretation of the 2003du data was accomplished by Stanishev et al. (2007b).

SN 2003gs is an underluminous, rapidly-declining [$\Delta m_{15}(B) > 1.7$] 91bg-like SN Ia, discovered close to maximum light. The optical data are being analysed by Stanishev et al. (in prep.), whereas the extended set of near-IR observations will be discussed by Kotak et al. (in prep.).

SN 2003kf 's most important peculiarity is its lack of peculiarities, which makes this SN an ideal template for what is referred to as 'normal' SN Ia. This role is also justified by its extraordinary spectroscopic coverage in the optical, almost daily observations being available from 8 d before maximum onwards. Actually, SN 2003kf is a slightly slower-than-average decliner [$\Delta m_{15}(B) = 1.01$], similar to SN 2003du. High-velocity features of Ca are visible in early spectra. The complete data set is presented and analysed by Salvo (2006) and Salvo et al. (2008).

SN 2004aw was initially classified as peculiar, 91T-like Type Ia SN, and therefore selected for follow-up observations by the ESC. In the course of these observations, the spectrophotometric evolution revealed that SN 2004aw was of Type Ic rather than Type Ia. Since already a lot of data had been collected at that moment, the ESC decided to carry on with the observations, providing one of the best data sets ever obtained for a SN Ic. Besides being of high scientific value by itself, the case of SN 2004aw also raised questions about a possible contamination of high-z SN Ia samples with SNe of different types. The data of SN 2004aw, published by Taubenberger et al. (2006), are extensively discussed in Chapter 5 of this thesis.

SN 2004dt is another SN Ia with particularly good spectroscopic coverage before maximum light. Overall high ejecta velocities are found in the earliest spectra, and almost daily pre-maximum spectroscopy makes it possible to follow in great detail the evolution of the prominent HVFs of Si and Ca. While the optical spectroscopy of SN 2004dt and some synthetic spectra were presented by Altavilla et al. (2007), the optical photometry of this intermediate decliner [$\Delta m_{15}(B) = 1.22$] and the near-IR data still await their publication (Pignata et al. in prep., Taubenberger et al. in prep.)

SN 2004eo turns out to be an interesting target, since its $\Delta m_{15}(B)$ of 1.46 makes it a comparatively fast decliner, yet still much slower than the members of the underluminous, 91bg-like class. In fact, SNe Ia with $\Delta m_{15}(B)$ between 1.4 and 1.8 are rare. Studying such intermediate objects can potentially provide answers to the question of where the difference in 91bg-like SNe comes from, and whether they are a separate population or just the tail of the distribution of 'normal' SNe Ia. These and other issues were addressed by Pastorello et al. (2007b) when presenting the extended ESC data set of SN 2004eo, ranging from day −11 to +345 with respect to maximum light in B, and featuring the densest photometric coverage (both in the optical and near-IR) of all ESC SNe.

SN 2005W was discovered about 10 d before maximum light, and followed by the ESC for some 50 d before it disappeared behind the sun. HVFs of Ca are clearly discernable in the early spectra. The data of SN 2005W are currently being reduced and analysed, and will be presented by Kerzendorf et al. (in prep.).

SN 2005bl is the second underluminous, 91bg-like SN Ia within the ESC sample [$\Delta m_{15}(B) = 1.93$]. For this property, and for the detection of carbon lines in the earliest spectra, SN 2005bl was selected as a target even though it did not fulfil the ESC's formal selection criteria in terms of distance. Despite not being particularly early in absolute terms, SN 2005bl's first spectra and photometric points are among the earliest ever obtained for a 91bg-like SN, and its carbon signature (a few percent in mass above the photosphere at day −6, as inferred from synthetic spectra) is unprecedented within this class. The complete data set of SN 2005bl and elementary spectral modelling have been published by Taubenberger et al. (2007), and form the body of Chapter 4 of this thesis.

SN 2005cf is another standard Type Ia SN [$\Delta m_{15}(B) = 1.12$] with excellent spectrophotometric coverage down to day −12 in the optical, and a nice set of early near-IR spectra. Like SN 2004dt it shows strong high-velocity components in Ca and Si lines at early phases, but unlike 2004dt the expansion velocities inferred for the photospheric components are rather low. Its excellent coverage and rather 'normal' properties make SN 2005cf an ideal template for $\Delta m_{15}(B) \sim 1.1$-SNe. The photometric data and bolometric light-curve modelling were presented by Pastorello et al. (2007a), whereas the early-time optical spectra were analysed by Garavini et al. (2007). Near-IR spectra and nebular data are still to be published (Taubenberger et al. in prep., Elias-Rosa et al. in prep.).

SN 2005hk is undoubtedly the most peculiar Type Ia SN observed by the ESC. Being very similar to SN 2002cx, it is characterised by hot pre-maximum spectra whose features are reminiscent of those seen in over-luminous 91T-like SNe Ia. However, SN 2005hk is underluminous, and the velocity inferred from the lines' Doppler shifts are lower by almost a factor 2 compared to SN 1991T, suggesting an underenergetic explosion. At later phases the spectra are dominated by permitted Fe II lines, which even holds after more than one year when the ejecta of normal SNe Ia are largely transparent. At these phases, the lines of SN 2005hk are extremely narrow, with a *fwhm* of ~ 600 km s^{-1}. The excellent ESC data set of SN 2005hk, starting 9 d before maximum light, is presented by Stanishev et al. (2007a and in prep.).

SN 2006X was the last ESC target, and the third one with significant extinction within the host galaxy. From the variability of narrow absorption features visible in high-resolution spectra, Patat et al. (2007) concluded that a snall fraction of the extinguishing dust was circumstellar and hence related to the SN progenitor system. The ESC acquired a first spectrum of SN 2006X 11 d before maximum light, and surveyed the SN evolution all the way into the nebular phase. As in SNe 2002cv and 2003cg, the dust properties deviate from the average Galactic ones, R_V being significantly smaller ($R_V = 1.56$). The intrinsic SN properties are also intriguing, Ca features being unusually pronounced and all lines being extremely broad and blueshifted in early spectra, suggesting high ejecta velocities and a shallow density gradient. The ESC data of SN 2006X will be presented by Elias-Rosa et al. (in prep.).

3.3 Generic results

Going beyond the specific analysis of individual SNe, a number of results with more universal character were obtained making use of ESC data. Most of them are based on an analysis of SN spectra, and the extraordinary spectral data base of the ESC provided an ideal starting point for investigations of that sort. The studies referred to in this section include the attempt to explain the main spectrophotometric sequence among SNe Ia by a different extension of the NSE-dominated region of the ejecta at the expense of intermediate-mass elements ('Zorro' diagnostics, Mazzali et al. 2007c), the search for a second parameter relevant for the diversity of SNe Ia beyond the well-known $\Delta m_{15}(B)$-relation (Benetti et al., 2005), and the identification of high-velocity features as a ubiquitous property among SNe Ia (Mazzali et al., 2005d,c). The establishment of abundance tomography as a powerful way to infer the ejecta composition as a

function of radius (Stehle, 2004; Stehle et al., 2005), and the systematic study of dust properties in highly-extinguished SNe (Elias-Rosa et al., 2006; Elias-Rosa, 2007; Elias-Rosa et al., 2008) should also be mentioned in this context.

High-velocity features (HVFs). Although the first HVFs in SNe Ia had been reported earlier on (Hatano et al., 1999; Li et al., 2001b; Wang et al., 2003; Gerardy et al., 2004a; Mazzali et al., 2005c), Mazzali et al. (2005d) for the first time performed a systematic study based on a large set of early-time spectra, many of them obtained by the ESC. They found that virtually all SNe Ia show evidence of HVFs in the Ca near-IR triplet at sufficiently early epochs, but that their appearance varies a lot from object to object. There are differences in the strength of the HVFs and the time of their fading. Some SNe show HVFs only in the Ca II lines, while in others more lines are affected (especially Si II, see Fig. 3.1; Altavilla et al. 2007; Garavini et al. 2007; Stanishev 2007). What is more, in some SNe the Ca II HVFs form a separate detached, strongly blueshifted feature, whereas in others they are blended with the photospheric component to a single wide trough.

A pure abundance enhancement of Ca and Si at high velocities has been discussed by Mazzali et al. (2005c), but considered unlikely, since extreme conditions with 90% Si and 10% Ca at $v > 20\,000$ km s^{-1} would be necessary to reproduce the observed strength of the HVFs with 1D synthetic spectra. Instead, or in addition to an abundance enhancement, an increased density at high velocities was suggested (Gerardy et al., 2004a; Mazzali et al., 2005c). This could have its origin in interaction with circumstellar material as originally suggested by Gerardy et al. (2004a), but also in an aspherical 3D structure of the ejecta with fast-moving dense blobs (Mazzali et al., 2005c). The latter scenario would also give an explanation for high polarisation degrees found in the HVFs of SNe 2001el (Wang et al., 2003), 2002bf and 2004dt (Leonard et al., 2005; Wang et al., 2006), since the absorption in the blobs does not remove light uniformly, but selectively from certain areas of the SN, thus breaking spherical symmetry and generating polarisation.

Second parameter. Most of the observed differences in SN Ia properties have their origin in different amounts of synthesised ^{56}Ni, as this not only determines the peak luminosity through its γ-ray deposition (see Arnett 1982) but also the light-curve shape, in particular the width of the light-curve peak, through its opacity. To be precise, the opacity is determined by the sum of ^{56}Ni and stable NSE elements rather than the ^{56}Ni alone (Mazzali

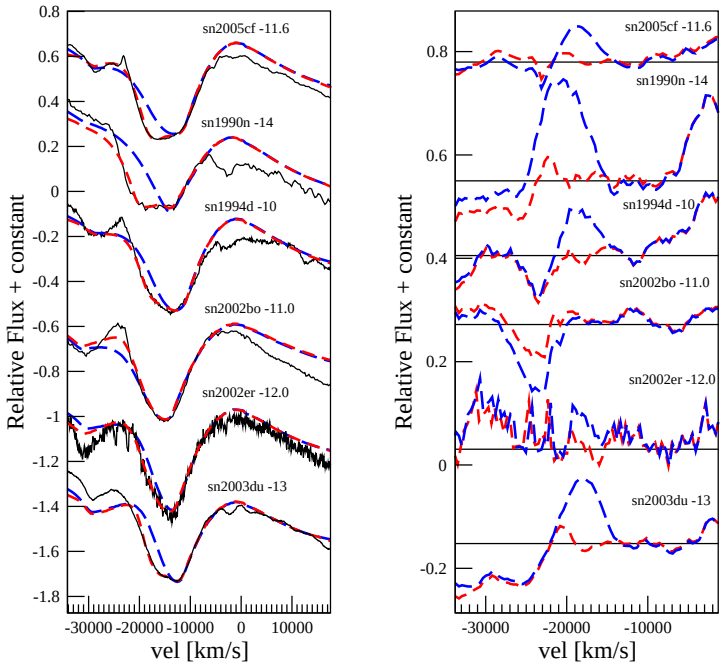

FIGURE 3.1— High-velocity features in the Si II λ6355 lines of a number of SNe Ia at very early phases. The left panel shows the observed line profiles (solid black lines), and SYNOW[2] fits with (dashed red lines) and without (dashed blue lines) high-velocity Si II. The residuals of the fits are shown in the right panel (from Garavini et al. 2007).

et al., 2007b), but this is a higher-order correction. Hence, to first-order precision SNe Ia form a one-parameter family, the peak luminosity being determind by the light-curve decline rate, measured as $\Delta m_{15}(B)$ (Phillips, 1993; Phillips et al., 1999), stretch factor s (Perlmutter et al., 1997) or Multicolor Light-Curve Shape (MLCS) parameter Δ (Riess et al., 1996).

However, more detailed studies reveal that SNe Ia with the same $\Delta m_{15}(B)$ are *not* all the same. Even disregarding peculiar objects such as SNe 2002cx (Li et al., 2003; Jha et al., 2006a), 2005hk (Phillips et al., 2006; Stanishev et al., 2007a; Sahu et al., 2007), 1999ac (Garavini et al., 2005; Phillips et al., 2006) or 2000cx (Li et al., 2001a; Candia et al., 2003), there is still significant diversity in their spectroscopic appearance, suggesting the presence of (at least) one more relevant parameter. Searching for a possible second parameter, Benetti et al. (2005) compared a large

[2] SYNOW is a simple, parameterised code for SN synthetic spectroscopy. See Fisher (2000) for code details.

sample of SNe Ia and found differences in the evolution of the ejecta velocities. Plotting the post-maximum velocity gradient $\dot{v}$, as inferred from the blueshift of Si II λ6355, against $\Delta m_{15}(B)$, Benetti et al. (2005) showed that SNe Ia are clustered into three groups, dubbed High-Velocity-Gradient (HVG), Low-Velocity-Gradient (LVG) and FAINT SNe. HVG SNe include mostly intermediate decliners with $\dot{v} > 70$ km s^{-1} d^{-1}, LVG SNe slow and intermediate decliners with $\dot{v} < 60$ km s^{-1} d^{-1}, whereas FAINT SNe show a large range of velocity gradients but are separated by a large $\Delta m_{15}(B) \gtrsim 1.7$. Independently, Branch et al. (2006a, 2007a,b) found another way to divide SNe Ia into four groups, mostly congruent with those of Benetti et al. (2005), but with the LVG SNe subdivided into 'core-normal' and 'shallow-silicon' SNe, the latter being characterised by weak Si II features before and around maximum light owing to their high temperatures. SN 1991T (Filippenko et al., 1992a; Phillips et al., 1992; Ruiz-Lapuente et al., 1992; Mazzali et al., 1995) would be the prototype of this class.

Whether or not the observed spectroscopic diversity has an impact on the peak luminosity and increases the scatter in the Hubble diagram if not corrected properly, is not yet fully investigated. It is also unclear whether there is a dependence on metallicity, which would result in SNe Ia properties evolving with cosmic time, and could introduce systematic errors in the Hubble diagram. One may speculate that the influence on the bolometric or *uvoir* light curves should be small, but that the narrower filter light curves could be more strongly affected by spectroscopic differences. Further investigation is definitely needed if precision SN cosmology is desired.

'Zorro' disgnostics. Roughly dividing SN ejecta, from the deepest to the outermost layers, into radial shells dominated by stable NSE elements (^{58}Ni, ^{54}Fe), radioactive ^{56}Ni, IMEs and unburned material (C, O), Mazzali et al. (2007c) found that all SNe Ia possess fairly similar amounts of stable NSE material, while the ratio of ^{56}Ni to IMEs can vary by more than one order of magnitude. This result is condensed in the so-called 'Zorro' plot (it carries its name for its characteristic shape, an inverted 'Z'; see Fig. 3.2). Within the 'Zorro' analysis, all SNe Ia are assumed to descend from Chandrasekhar-mass progenitors, so that the total ejecta mass is constant. A variety of methods were employed to determine the boundaries between the regions of different composition: the masses of ^{56}Ni and stable NSE material were determined modelling nebular spectra. This yielded an estimate of the boundaries between stable NSE material and

^{56}Ni, and between ^{56}Ni and IME elements. On the other hand, the lowest and highest velocities measured in the Si II λ6355 line in the observed spectra served as estimate for the inner and outer extension of the IME shell. The inner IME boundary thus derived was shown to be in good agreement with the outer extension of the NSE-dominated region. To mitigate the influence of high-velocity features, which may have a strong impact on the blueshift of the Si II line in early spectra, but can be created by very little high-velocity material (thus not being representative), the Si II line velocities were evaluated only after maximum light, and extrapolated to day -18 using a polynomial of order ≤ 2.

This treatment is arguably a weak point of the 'Zorro' analysis. First of all, the extrapolation over 18 d of possibly rapid evolution is already quite uncertain. But also the idea that the velocity range encompassed by the minimum of the Si II λ6355 line should be a measure of the extension of the IME-dominated shell is an assumption which is not necessarily true, and which has not been veryfied with the help of synthetic early-time spectra. In fact, at least for underluminous SNe Ia spectral modelling suggests the outer boundary of the IME-rich region to be much further inwards than proposed by the 'Zorro' analysis (see Mazzali et al. 1997, Taubenberger et al. 2007 and Chapter 4.7.4 of this thesis).

What has also been shown by Mazzali et al. (2007c) is that the total amount of NSE elements (i.e., stable plus radioactive nuclei) correlates more tightly with $\Delta m_{15}(B)$ than ^{56}Ni does, indicating that the opacity is determined by the abundance of Fe-group elements rather than by the temperature of the ejecta. Since still the peak luminosity is given by ^{56}Ni, the amount of stable NSE material could be a parameter responsible for some of the observed scatter in the SN Ia Hubble diagram.

Abundance tomography is a modelling technique developed by Stehle (2004), which relies on a dense spectroscopic coverage during early phases of the SN evolution. It is based on the 1D Monte-Carlo spectrum synthesis code of Mazzali (2000)[3], modified to include a stratified composition above the photosphere. Each spectrum available defines one abundance zone. A denser spectroscopic coverage hence results in a better compositional resolution of this method. What makes the application of this technique demanding is the fact that the outcome of the calculation for a certain spectrum depends on the parameters of all earlier spectra. Since a con-

[3] A brief description of the basic concepts of this code is given in Chapter 4.6.1 of this thesis.

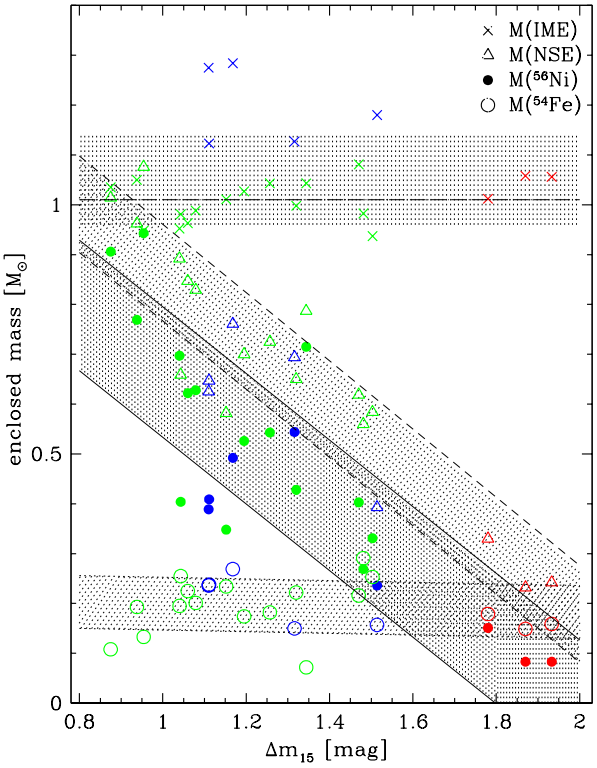

FIGURE 3.2— 'Zorro' diagram, analysing the distribution of the principal isotopic groups in a sample of SNe Ia. The enclosed mass of different burning products is plotted vs. $\Delta m_{15}(B)$. Open circles refer to stable ^{54}Fe and ^{58}Ni; solid circles to ^{56}Ni, and open triangles to the sum of these. Crosses show the mass enclosed inside the IME layer, i.e., the total mass burned. Using the methods discussed in the text, the amount of ^{54}Fe and ^{58}Ni in the SN core appears roughly constant irrespective of luminosity. On the contrary, ^{56}Ni determines the luminosity and correlates with $\Delta m_{15}(B)$. The mass enclosed by IMEs is inferred to be similar for all SNe of the sample, and the explosion energy seems constant (from Mazzali et al. 2007c).

sistent fit of the entire series from the first spectrum to beyond maximum light is required, it may at some point be necessary to return to an earlier spectrum and modify its fit parameters to improve the results for subsequent spectra.

The capability of abundance tomography to determine the chemical stratification within the SN ejecta has been demonstrated by Stehle et al. (2005) modelling the ESC data set of SN 2002bo. Their result resembles the com-

position stratification of the standard W7 explosion model (Nomoto et al., 1984) in gross terms, but shows important differences in detail. Most significantly, the radial extension of different chemical species is less confined in the 02bo model than in W7 (see Fig. 3.3), IMEs and unburned material reaching to lower velocities and NSE elements found also further outside. This is indicative of strong mixing in SN 2002bo, in agreement with what modern 3D hydrodynamic models predict, especially for deflagrations (see e.g. Röpke et al. 2007).

Dust properties. Foreground dust cannot be regarded an intrinsic SN property.[4] Nevertheless, studying the dust properties is an important subject also and especially in the context of SN research, since the amount of dust extinction is often the largest uncertainty in the calibration of the absolute SN magnitudes and colours, limiting the precision which can be achieved with SNe Ia in cosmological measurements.

If, on the other hand, a SN data set is good enough (in particular, a broad wavelength coverage from the optical / near-UV to the near IR is essential), the homogeneity of SNe Ia in terms of (decline-rate-corrected) peak luminosity and colour evolution provides a unique opportunity to study the properties of the extinguishing material. By comparing a number of colour indices of an extinguished SN with the values expected for unextinguished objects, a Cardelli, Clayton & Mathis (1989) extinction law can be fitted to the data and the selective-to-total-extinction ratio $R_V = A_V/E(B-V)$ can be determined. Since R_V is directly related to the average grain size of the dust particles, this approach provides insight into the dust structure. If different dust properties can be established in a vicinity of the SN or in different galactic environments (dust lanes, ...), a lot can be learned about the dust production mechanisms at work.

Pioneering studies in this field have been conducted by Elias-Rosa (2007) and Elias-Rosa et al. (2006, 2008 and in prep.) using the ESC data of three highly extinguished SNe Ia. A common property of these objects and also other reddened SNe studied in similar detail (Krisciunas et al., 2006; Pozzo et al., 2006) is a value of R_V typically between 1 and 2, significantly lower than the canonical 3.1 inferred on average for dust in the Milky Way (Seaton, 1979; Savage & Mathis, 1979). This holds for SNe which are visibly located behind a dust lane (e.g., SN 2002cv, Elias-Rosa

[4] This statement refers to pre-existing dust, since dust newly formed within the SN ejecta has so far only been found in core-collapse SNe at very late phases, cf. Danziger et al. (1989) and Lucy et al. (1989), but also Smith et al. (2007). Pre-existing circumstellar dust, however, at least provides clues on the SN progenitor system by which it was produced.

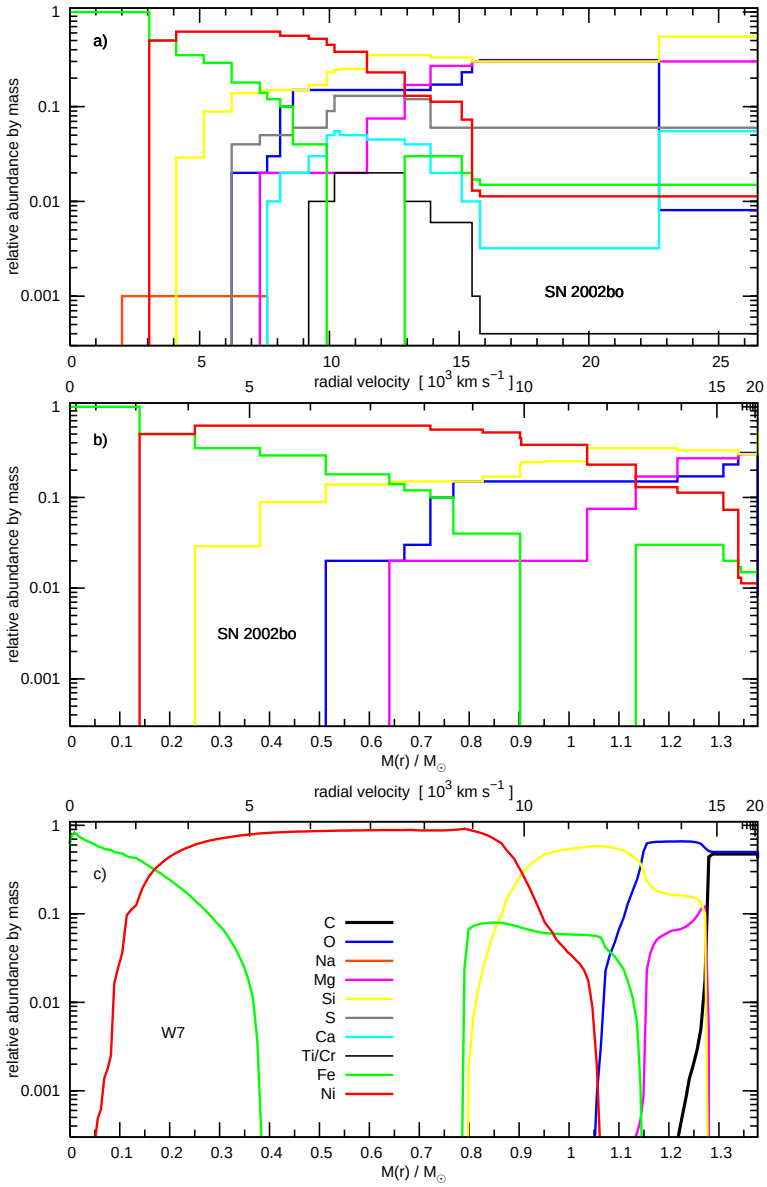

FIGURE 3.3— Abundance stratification of SN 2002bo from tomography. *Top panel:* all elements included. *Middle panel:* only O, Mg, Si, Fe and ^{56}Ni displayed. *Bottom panel:* W7 deflagration model abundances for comparison. A larger degree of mixing in SN 2002bo than in the W7 model is suggested (from Stehle et al. 2005).

et al. 2008; SN 2003cg, Elias-Rosa et al. 2006) as well as for objects where no such dust lane is evident and at least some fraction of the extinction comes from circum-SN dust (SN 2006X; Patat et al. 2007, Wang et al. 2007, Elias-Rosa et al. in prep.).

4

The underluminous Type Ia Supernova 2005bl

In this chapter, already published by Taubenberger et al. (2007), optical observations of one ESC target, the Type Ia supernova 2005bl in NGC 4070, are presented in detail. The photometric evolution of this SN is characterised by rapidly-declining light curves [$\Delta m_{15}(B)_{\rm true} = 1.93$] and red colours at peak and soon thereafter. With $M_{B,\rm max} = -17.24$ the SN is underluminous, similar to the peculiar SNe 1991bg and 1999by. This similarity also holds for the spectroscopic appearance, the only remarkable difference being the likely presence of carbon in pre-maximum spectra of SN 2005bl. A comparison study among underluminous SNe Ia is performed, based on a number of spectrophotometric parameters. Previously reported correlations of the light-curve decline rate with peak luminosity and $\mathcal{R}$(Si) are confirmed, and a large range of post-maximum Si II λ6355 velocity gradients is encountered. 1D synthetic spectra for SN 2005bl are presented, which confirm the presence of carbon and suggest an overall low burning efficiency with a significant amount of leftover unburned material. Also, the Fe content in pre-maximum spectra is very low, which may point to a low metallicity of the precursor. Implications for possible progenitor scenarios of underluminous SNe Ia are briefly discussed.

4.1 Introduction

The history of underluminous SNe Ia is a typical example of the ever-recurring pattern in which knowledge about nature is accumulated. Usually, in the beginning there is the observation of a phenomenon, followed by a successful theoretical explanation. However, as further experiments or observations are carried out in order to confirm the newly developed theoretical ideas, often an ever higher degree of diversity and ever more exceptions from

the simple rules are found the closer the subject of interest is studied. The need for refined and more complex theories to obtain a realistic description of the involved processes becomes evident.

In the case of SNe Ia, first a class of cosmic explosions apparently similar in absolute luminosity ('standard candles') and spectroscopic appearance was identified. These events were explained as the disruptions of white dwarfs which had accreted matter until they reached their stability limit close to the Chandrasekhar mass ($M_{\rm Ch}$). However, in 1991 the paradigm of SN Ia homogeneity had to be relaxed a lot. This was triggered by the discovery of two peculiar SNe Ia, which thereafter served as prototypes of newly-defined SN Ia subclasses with distinct spectrophotometric properties. One of these, SN 1991T (Filippenko et al. 1992a; Phillips et al. 1992; Ruiz-Lapuente et al. 1992; Mazzali et al. 1995), was up to 0.6 mag brighter than average SNe Ia, and characterised by a hot early-time spectrum with strong Fe III features and weak or absent Si II and S II lines. The other one, SN 1991bg (Filippenko et al., 1992b; Leibundgut et al., 1993; Ruiz-Lapuente et al., 1993; Turatto et al., 1996; Mazzali et al., 1997) was even more deviant, with low ejecta velocities and a cool spectrum dominated by intermediate-mass-element (IME) lines and particularly strong O I and Ti II. Moreover, it had unusually red colours at early phases, and was underluminous by about 2 mag at peak (hereafter we will refer to such an appearance as 91bg-like). Hence, quasi instantaneously the luminosity range of SNe Ia had increased to a factor of ten between the brightest and the faintest objects, proving that they were *no* standard candles. However, two years later Phillips (1993) realised a tight correlation between peak luminosity and decline rate in the B band. This relation and revised versions of it (e.g. Phillips et al. 1999) turned SNe Ia into standardisable candles, and hence made them an extremely useful tool for precision cosmology[1].

In the following years, several more 91bg-like SNe Ia were discovered, but the available data set grew less rapidly than for ordinary SNe Ia. From the results of the Lick Observatory Supernova Search (LOSS) and the Beijing Astronomical Observatory Supernova Survey (BAOSS), Li et al. (2001a) estimated that about 16 % of all SNe Ia are of the 91bg-like variety. This may still be an underestimate, as their low intrinsic luminosity makes 91bg-like SNe prone to Malmquist bias; nevertheless Li et al. (2001a) estimated this effect to be negligible in their sample. Statistical studies (Hamuy et al., 1996a, 2000; Howell, 2001) have shown that SNe Ia occur in all host-galaxy types, but revealed a

[1]Several years later even more peculiar objects such as SN 2002cx (Li et al., 2003) were discovered which did not obey the Phillips relation, showing that not *all* SNe Ia are standardisable.

correlation between SN decline rate and host morphology, with a clear tendency for 91bg-like SNe to be associated with early-type hosts and hence old stellar populations.

While the single-degenerate (SD) Chandrasekhar-mass model has survived as the favoured scenario for the normal and indeed rather homogeneous SNe Ia, a number of alternative models have been suggested for the 91bg-like subclass. Ideas include double-degenerate (DD) explosions of merging white dwarfs, sub-Chandrasekhar-mass explosions triggered by detonation of the accreted helium layer (cf. Hillebrandt & Niemeyer 2000 for a review), and deflagrations in strongly rotating white dwarfs, where the turbulent propagation of the flame front is suppressed by the differential rotation (Pfannes, 2006). Still, the notion that 91bg-like SNe are – in terms of the underlying explosion model – no different from ordinary SNe Ia, and that the only discriminating parameter is the mass of synthesised ^{56}Ni, has supporters in the SN Ia community. No conclusive evidence for any of these ideas has been found so far.

In this chapter of my thesis the data set of SN 2005bl obtained by the ESC is presented, complemented by additional data taken by the Carnegie Supernova Project (CSP). Since these observations are among the earliest ever obtained for a 91bg-like SN, they may help to better constrain possible progenitor and explosion models. The observations and techniques applied for data reduction and calibration are discussed in Section 4.2. In Section 4.3 we estimate the distance of SN 2005bl and the extinction along the line of sight. Sections 4.4 and 4.5 are devoted to the analysis of the light curves and spectra, respectively. Results of 1D spectrum synthesis calculations are presented in Section 4.6, and a comparison with other underluminous SNe Ia is performed in Section 4.7, where we also discuss the impact of SN 2005bl on our picture of SN Ia explosions. A short summary of the main results is given in Section 4.8.

4.2 Observations

SN 2005bl ($z = 0.024$) was discovered in the course of the Lick Observatory Supernova Search programme (LOSS) with the Katzman Automatic Imaging Telescope (KAIT) on UT 2005 April 14.34 and 15.36 at unfiltered magnitudes of 18.8 and 18.3, respectively (Shimasaki & Li, 2005). The SN was not detected on images obtained with the same setup on UT 2005 March 11.33 to a limiting magnitude of 19.5. Based on spectra taken with the Las Campanas 2.5 m du Pont Telescope (+ WFCCD spectrograph) and the Fred Lawrence Whipple Observatory 1.5 m Telescope (+ FAST), SN 2005bl was classified as SN Ia, probably belonging to the 91bg-like variety given the similarity of the spectra with those of SN 1999by a few days before maximum light (Morrell et al.,

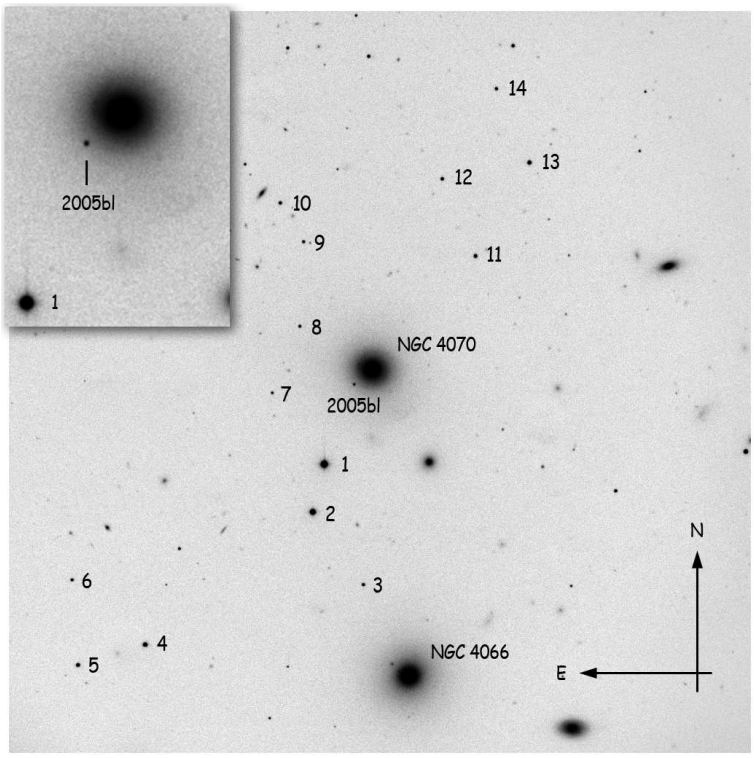

FIGURE 4.1— R-band image of the SN 2005bl field taken with the Calar Alto 2.2 m Telescope + CAFOS on UT 2005 May 14. The field of view is 9 × 9 arcmin^2, and the local sequence stars are indicated. In the upper-left corner a twice-enlarged blow-up of the SN and its host galaxy is shown.

2005; Gallagher et al., 2005a). The SN is located in the elliptical galaxy NGC 4070 (de Vaucouleurs morphological type −4.9; LEDA[2]), projected on a region of steep yet smooth background variation (Fig. 4.1). Details on the SN and host-galaxy properties are summarised in Table 4.1.

Although SN 2005bl was too distant to fulfil the formal selection criteria of the ESC, optical follow-up observations were performed owing to the peculiarities found in our first spectrum, obtained almost at the same time as the classification spectra by other groups. However, given the dimness of the SN, an intensive coverage as for other ESC targets was out of reach. In particular, the early part of the light curves was not well sampled owing to bad weather and scheduling constraints. At the same time, the CSP collaboration started

[2]Lyon-Meudon Extragalactic Database, http://leda.univ-lyon1.fr/
[3]NASA / IPAC Extragalactic Database, http://nedwww.ipac.caltech.edu/

TABLE 4.1— Properties of SN 2005bl and its host galaxy.

NGC 4059 / NGC 4070[a]		
α	12h 04m 11.43s	1
δ	$+20°24'37''.7$	1
redshift	0.02406 ± 0.00008	2
recession velocity v	7213 ± 24 km s^{-1}	2
$v^b_{\rm Virgo}$	7330 ± 28 km s^{-1}	2
$v^c_{\rm CMB}$	7534 ± 33 km s^{-1}	2
distance modulus μ^d	35.10 ± 0.09 mag	2
apparent corr. B magnitude	13.75 ± 0.15	1
morphological type[e]	E, -4.9	1
Galactic reddening $E(B-V)$	0.028 mag	3
SN 2005bl		
α	12h04m12.32s	4
δ	$+20°24'24''.8$	4
offset from galaxy centre	$13''.9$ E, $11''.2$ S	4
host reddening $E(B-V)$	0.17 ± 0.08 mag	5
$\Delta {\rm m}_{15}(B)_{\rm true}$	1.93 ± 0.10	5
JD$_{\rm max}$ in U	$2\,453\,481.4 \pm 0.3$	5
JD$_{\rm max}$ in B	$2\,453\,482.6 \pm 0.3$	5
JD$_{\rm max}$ in V	$2\,453\,484.9 \pm 0.3$	5
JD$_{\rm max}$ in R	$2\,453\,485.9 \pm 0.3$	5
JD$_{\rm max}$ in I	$2\,453\,487.0 \pm 0.3$	5
JD$_{\rm max}$ in g	$2\,453\,483.0 \pm 0.3$	5
JD$_{\rm max}$ in z	$2\,453\,487.0 \pm 3.0$	5
$U_{\rm max}$	19.14 ± 0.18	5
$B_{\rm max}$	18.68 ± 0.04	5
$V_{\rm max}$	17.87 ± 0.03	5
$R_{\rm max}$	17.55 ± 0.03	5
$I_{\rm max}$	17.38 ± 0.04	5
$g_{\rm max}$	18.20 ± 0.07	5
$z_{\rm max}$	17.77 ± 0.12	5
M$_{U,{\rm max}}$	-16.91 ± 0.43	5
M$_{B,{\rm max}}$	-17.24 ± 0.34	5
M$_{V,{\rm max}}$	-17.85 ± 0.27	5
M$_{R,{\rm max}}$	-18.06 ± 0.23	5
M$_{I,{\rm max}}$	-18.10 ± 0.18	5
M$_{g,{\rm max}}$	-17.55 ± 0.29	5
M$_{z,{\rm max}}$	-17.67 ± 0.20	5

[a] The galaxy is listed twice in the NGC catalogue.
[b] v corrected for Local-Group infall onto Virgo cluster.
[c] v corrected to the CMB reference frame.
[d] From $v_{\rm CMB}$, using $H_0 = 72$ km s^{-1} Mpc^{-1}.
[e] Numerical code according to de Vaucouleurs.

1: LEDA; 2: NED[3]; 3: Schlegel, Finkbeiner & Davis 1998;
4: Puckett & Langoussis 2005; 5: this work

TABLE 4.2— Bessell *UBVRI* (top) and Sloan *griz* (bottom) magnitudes of the local sequence stars in the field of SN 2005bl (Fig. 4.1).

ID	U	B	V	R	I
1	15.207 ± 0.022	14.786 ± 0.013	13.952 ± 0.014	13.502 ± 0.010	13.080 ± 0.013
2	16.387 ± 0.022	15.931 ± 0.012	15.048 ± 0.014	14.510 ± 0.011	14.011 ± 0.012
3	18.340 ± 0.019	18.633 ± 0.021	18.110 ± 0.016	17.767 ± 0.013	17.385 ± 0.012
4		18.154 ± 0.014	16.658 ± 0.020	15.665 ± 0.021	14.792 ± 0.017
5		17.464 ± 0.009	16.962 ± 0.027	16.621 ± 0.007	16.269 ± 0.012
6		19.132 ± 0.014	18.220 ± 0.015	17.690 ± 0.018	17.247 ± 0.010
7	19.274 ± 0.017	19.488 ± 0.020	18.979 ± 0.014	18.629 ± 0.008	18.272 ± 0.015
8	19.538 ± 0.022	19.396 ± 0.021	18.659 ± 0.019	18.251 ± 0.013	17.824 ± 0.017
9	18.656 ± 0.049	18.924 ± 0.016	18.454 ± 0.018	18.115 ± 0.020	17.834 ± 0.018
10		20.035 ± 0.020	18.640 ± 0.022	17.532 ± 0.014	16.260 ± 0.022
11	18.355 ± 0.049	18.267 ± 0.013	17.539 ± 0.021	17.104 ± 0.015	16.687 ± 0.011
12		18.346 ± 0.014	17.873 ± 0.020	17.510 ± 0.016	17.196 ± 0.011
13		18.278 ± 0.011	17.206 ± 0.017	16.509 ± 0.018	15.893 ± 0.025
14		19.083 ± 0.013	18.198 ± 0.023	17.666 ± 0.013	17.193 ± 0.020

ID	g	r	i	z
1				13.386 ± 0.013
2				14.295 ± 0.024
3				17.710 ± 0.074
4	17.174 ± 0.222			
5				
6	18.563 ± 0.216	17.949 ± 0.013	17.661 ± 0.031	
7	19.133 ± 0.143	18.831 ± 0.014	18.660 ± 0.015	18.526 ± 0.035
8	18.931 ± 0.173	18.452 ± 0.013	18.239 ± 0.013	18.096 ± 0.030
9				18.112 ± 0.040
10				
11	17.591 ± 0.253	17.306 ± 0.011	17.059 ± 0.012	16.965 ± 0.014
12	17.812 ± 0.266	17.705 ± 0.011	17.558 ± 0.022	
13	17.454 ± 0.265	16.741 ± 0.011	16.327 ± 0.011	
14	18.465 ± 0.243	17.914 ± 0.011	17.629 ± 0.026	

their follow-up of SN 2005bl, focussing mainly on the photometric evolution near maximum light. Hence, the two data sets were almost perfectly complementary.

A precise description of the instruments used for the observations can be found in Chapter 2.2. The data reduction and calibration was performed as detailed in Chapter 2.3, including, for the imaging observations, the calibration of local standard stars in the SN field (see Table 4.2 and Fig. 4.1), the sub-

traction of host-galaxy templates acquired about a year after the SN explosion, and the application of an S- and K-correction to report the magnitudes to the standard Bessell (1990) photometric system (for $BVRI$). Observations with the Sloan (Fukugita et al., 1996) r and i filters at the Liverpool and Swope telescopes were transformed to Bessell R and I magnitudes through S-corrections, but – like the g and z data – additionally reported in their native system applying colour-term corrections only. To convert the Swope u-band data to the Bessell system, transformation formulae (Jordi, Grebel & Ammon, 2006; Zhao & Newberg, 2006) were employed. All relevant instrumental response curves are reported in Fig. 2.3, and it is evident that some of them, most notably the MONICA V filter which is actually a Roeser BV filter, deviate strongly from the standard prescription, thus complicating a reliable calibration of the SN magnitudes.

The final SN magnitudes in the Bessell $UBVRI$ bands and their uncertainties are reported in Table 4.3. An S- and K-correction, separately reported in Table 4.4, has been applied to these magnitudes except for the U-band data and any data later than +50 d. The colour-term calibrated Sloan $griz$ magnitudes of SN 2005bl are listed in Table 4.5. Details of the spectroscopic observations of SN 2005bl are reported in Table 4.6.

4.3 Distance, extinction and host-galaxy properties

Like most 91bg-like SNe Ia (Gallagher et al., 2005b), SN 2005bl exploded in an early-type host, the elliptical galaxy NGC 4070. Other prominent examples are SN 1991bg itself and SN 1997cn in elliptical hosts (Filippenko et al., 1992b; Leibundgut et al., 1993; Turatto et al., 1996, 1998), and SN 1998de whose host galaxy was of type S0 (Modjaz et al., 2001).[4] Since early-type galaxies are assumed to have experienced no significant star formation over long times, this behaviour might be indicative of 91bg-like SNe Ia originating from an old stellar population. Even if one allows for some more recent star formation in elliptical galaxies (e.g. triggered by mergers or interaction), the relative paucity of 91bg-like SNe in late-type, actively star-forming galaxies clearly disfavours young or intermediate-aged stellar progenitors or progenitor systems.

A widely accepted paradigm for elliptical galaxies is that they have only little interstellar gas and dust (but see Patil et al. 2007 for a more sophisticated picture). This is consistent with the negligible host-galaxy extinction found in SNe 1991bg, 1997cn and 1998de. However, recent mergers or interaction may alter this picture, as exemplified by the radio galaxy Centaurus A, the host of

[4] SN 1999by (Garnavich et al., 2004) was hosted by NGC 2841, a spiral galaxy, but with the spectral appearance of an elliptical galaxy (Gallagher et al., 2005b).

TABLE 4.3— S- and K-corrected Bessell magnitudes of SN 2005bl.[a]

JD[b]	Epoch[c]	U	B	V	R	I	Telescope	Seeing[d]
476.61	−6.0	19.591 ± 0.114	19.364 ± 0.022	18.950 ± 0.030	18.776 ± 0.024	18.599 ± 0.045	SWO	1.41
477.63	−5.0	19.389 ± 0.117	19.135 ± 0.022	18.695 ± 0.029	18.523 ± 0.023	18.402 ± 0.038	SWO	1.34
478.66	−3.9	19.237 ± 0.134	18.955 ± 0.022	18.461 ± 0.029	18.290 ± 0.022	18.120 ± 0.036	SWO	1.68
479.64	−3.0		18.818 ± 0.029	18.307 ± 0.031	18.116 ± 0.030	17.948 ± 0.043	SWO	1.57
479.68	−2.9			18.393 ± 0.042	18.120 ± 0.030	17.883 ± 0.034	TNG	1.47
480.65	−1.9	19.151 ± 0.144	18.766 ± 0.025	18.150 ± 0.029	17.883 ± 0.028	17.770 ± 0.038	SWO	1.44
481.61	−1.0	19.185 ± 0.174	18.709 ± 0.027	18.052 ± 0.030	17.798 ± 0.022	17.650 ± 0.036	SWO	1.45
483.62	1.0	19.235 ± 0.203	18.682 ± 0.040	17.899 ± 0.030	17.636 ± 0.026	17.513 ± 0.039	SWO	1.54
484.65	2.1	19.296 ± 0.291	18.733 ± 0.042	17.839 ± 0.031	17.526 ± 0.043	17.414 ± 0.045	SWO	1.52
485.39	2.8		18.872 ± 0.036	17.887 ± 0.051	17.563 ± 0.035	17.361 ± 0.051	LT	0.84
489.32	6.7			18.172 ± 0.280			WD	1.89
489.59	7.0	20.248 ± 0.152	19.472 ± 0.031	18.146 ± 0.027	17.692 ± 0.021	17.416 ± 0.035	SWO	1.84
490.52	7.9	20.640 ± 0.155	19.653 ± 0.026	18.194 ± 0.025	17.781 ± 0.025	17.435 ± 0.044	LT	0.81
490.60	8.0	20.640 ± 0.163	19.687 ± 0.023	18.258 ± 0.028	17.791 ± 0.022	17.456 ± 0.038	SWO	1.34
491.51	8.9		19.824 ± 0.046	18.296 ± 0.048	17.845 ± 0.027		WD	1.60
491.57	9.0	20.620 ± 0.140	19.834 ± 0.022	18.359 ± 0.029	17.836 ± 0.026	17.477 ± 0.039	SWO	1.37
493.35	10.8			18.553 ± 0.028	17.959 ± 0.025	17.503 ± 0.031	LOI	2.41
498.38	15.8				18.551 ± 0.045	17.805 ± 0.052	LT	0.95
500.51	17.9			19.258 ± 0.184	18.722 ± 0.041		WD	2.38
502.38	19.8				18.807 ± 0.034	18.192 ± 0.063	LT	0.70
503.35	20.8		20.912 ± 0.073	19.334 ± 0.040	18.960 ± 0.023		WD	1.55
503.35	20.8		20.893 ± 0.133	19.429 ± 0.046	18.965 ± 0.074	18.361 ± 0.059	Ekar	2.57
504.49	21.9				19.035 ± 0.035	18.325 ± 0.057	LT	0.67
505.49	22.9		20.936 ± 0.050	19.609 ± 0.069	19.180 ± 0.045	18.474 ± 0.064	Caha	1.29
506.41	23.8		21.052 ± 0.081	19.597 ± 0.037	19.216 ± 0.028	18.571 ± 0.035	Caha	1.91

TABLE 4.3— *continued.* S- and K-corrected Bessell magnitudes of SN 2005bl.[a]

JD[b]	Epoch[c]	U	B	V	R	I	Telescope	Seeing[d]
510.53	27.9			19.693 ± 0.119			WD	1.70
511.36	28.8			19.687 ± 0.092	19.530 ± 0.045		WD	1.70
512.55	29.9		21.168 ± 0.176	19.847 ± 0.063	19.480 ± 0.036	18.874 ± 0.051	SWO	1.56
516.48	33.9				19.877 ± 0.073		WD	1.78
518.43	35.8			20.044 ± 0.068	20.020 ± 0.042		WD	1.52
519.40	36.8		21.421 ± 0.075	20.031 ± 0.042	19.925 ± 0.055	19.310 ± 0.096	LT	1.01
520.44	37.8		21.407 ± 0.124	20.205 ± 0.055	20.002 ± 0.045		WD	2.07
521.39	38.8			20.122 ± 0.040	20.009 ± 0.036	19.358 ± 0.094	LT	0.96
524.42	41.8		21.379 ± 0.097	20.141 ± 0.069	20.159 ± 0.071		WD	1.40
538.38	55.8			20.685 ± 0.168			WD	1.75
548.41	65.8			20.984 ± 0.280	21.183 ± 0.347		WD	2.15

[a] No S- and K-correction applied in the U band and to any data after +50 d.
[b] JD − 2 453 000.00
[c] Epoch in days with respect to the B-band maximum JD 2 453 482.6 ± 0.5.
[d] Seeing in arcsec averaged over all filter bands.

SWO = Las Campanas 1.0 m Swope Telescope + CCD
TNG = 3.58 m Telescopio Nazionale Galileo + DOLORES
LT = 2.0 m Liverpool Telescope + RATCAM
WD = 0.8 m Wendelstein Telescope + MONICA
LOI = 1.52 m Loiano Telescope + BFOSC
Ekar = Asiago 1.82 m Telescope + AFOSC
Caha = Calar Alto 2.2 m Telescope + CAFOS SiTe

TABLE 4.4— Amount of S- and K-correction contained in the magnitudes reported in Table 4.3. No S- and K-correction has been applied to the U-band data.

JD[a]	Epoch[b]	B	V	R	I	Tel.[c]
476.6	−6.0	−0.020	0.030	0.033	0.147	SWO
477.6	−5.0	−0.038	0.029	0.044	0.177	SWO
478.7	−3.9	−0.028	0.011	0.045	0.162	SWO
479.6	−3.0	−0.054	0.011	0.044	0.151	SWO
479.7	−2.9		0.123	0.193	0.252	TNG
480.7	−1.9	−0.032	0.007	0.022	0.093	SWO
481.6	−1.0	−0.062	−0.003	0.043	0.110	SWO
483.6	1.0	−0.078	−0.044	0.088	0.102	SWO
484.7	2.1	−0.099	−0.042	0.048	0.085	SWO
485.4	2.8	−0.077	−0.002	0.136	−0.054	LT
489.3	6.7		0.137			WD
489.6	7.0	−0.113	−0.039	0.187	0.060	SWO
490.5	7.9	−0.116	−0.034	0.166	−0.042	LT
490.6	8.0	−0.128	−0.065	0.213	0.049	SWO
491.5	8.9	−0.233	−0.034	0.074		WD
491.6	9.0	−0.142	−0.074	0.190	0.035	SWO
493.4	10.8		−0.029	0.027	−0.018	LOI
498.4	15.8			0.126	−0.105	LT
500.5	17.9		−0.064	0.096		WD
502.4	19.8			0.096	−0.209	LT
503.4	20.8	−0.237	−0.065	0.074		WD
503.4	20.8	−0.166	−0.067	0.055	−0.017	Ekar
504.5	21.9			0.113	−0.220	LT
505.5	22.9	−0.201	−0.087	0.083	0.009	Caha
506.4	23.8	−0.207	−0.085	0.093	0.011	Caha
510.5	27.9		−0.292			WD
511.4	28.8		−0.286	0.062		WD
512.6	29.9	−0.150	−0.084	0.199	−0.218	SWO
516.5	33.9			0.078		WD
518.4	35.8		−0.037	0.082		WD
519.4	36.8	−0.125	−0.038	0.120	−0.304	LT
520.4	37.8	−0.196	−0.076	0.076		WD
521.4	38.8		−0.078	0.127	−0.304	LT
524.4	41.8	−0.191	−0.054	0.074		WD

[a] JD − 2 453 000.0
[b] Epoch in days with respect to the estimated B-band maximum JD 2 453 482.6 ± 0.5.
[c] See Table 4.3 for details.

TABLE 4.5— Sloan photometry of SN 2005bl. No S- and K-correction has been applied.

JD[a]	Epoch[b]	g	r	i	z
476.6	−6.0	18.976 ± 0.072	18.870 ± 0.015	18.845 ± 0.028	
477.6	−5.0	18.727 ± 0.070	18.608 ± 0.015	18.611 ± 0.015	
478.7	−3.9	18.530 ± 0.069	18.379 ± 0.015	18.352 ± 0.015	
479.6	−3.0	18.391 ± 0.075	18.211 ± 0.024	18.189 ± 0.028	
480.6	−2.0	18.279 ± 0.096	18.014 ± 0.015	18.054 ± 0.015	
481.6	−1.0	18.228 ± 0.073	17.916 ± 0.015	17.925 ± 0.015	
483.6	1.0	18.210 ± 0.075	17.735 ± 0.015	17.786 ± 0.015	
484.6	2.0	18.147 ± 0.077	17.666 ± 0.027	17.706 ± 0.024	
485.4	2.8	18.295 ± 0.115	17.669 ± 0.023	17.866 ± 0.051	17.769 ± 0.080
489.6	7.0	18.791 ± 0.070	17.779 ± 0.015	17.750 ± 0.015	
490.5	7.9		17.877 ± 0.025	17.870 ± 0.031	17.808 ± 0.039
490.6	8.0	18.992 ± 0.071	17.870 ± 0.015	17.809 ± 0.015	
491.6	9.0	19.145 ± 0.072	17.950 ± 0.015	17.853 ± 0.015	
498.4	15.8		18.676 ± 0.046	18.308 ± 0.092	18.113 ± 0.080
502.4	19.8		18.921 ± 0.039	18.760 ± 0.059	
504.5	21.9		19.138 ± 0.047	18.878 ± 0.077	18.548 ± 0.095
512.6	30.0	20.620 ± 0.110	19.562 ± 0.029	19.495 ± 0.037	
519.4	36.8		19.998 ± 0.071	19.982 ± 0.093	19.548 ± 0.165
521.4	38.8		20.073 ± 0.043	20.081 ± 0.100	19.680 ± 0.240

[a] JD − 2 453 000.0
[b] Epoch in days with respect to B-band maximum (JD = 2 453 482.6 ± 0.5).

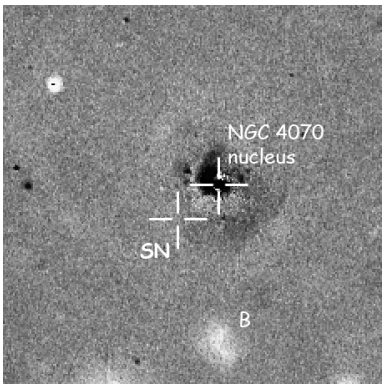

FIGURE 4.2— $B - R$ difference image of NGC 4070, constructed as described in the text. Dark shades in the figure correspond to red areas. The field of view is 2 × 2 arcmin^2; north is up, east to the left. Crosshairs mark the explosion site of SN 2005bl and the centre of NGC 4070. 'B' denotes a bluish patch, probably a companion galaxy of NGC 4070 (see discussion in the text).

TABLE 4.6— Journal of spectroscopic observations of SN 2005bl.

UT Date	JD[a]	Epoch[b]	Exposure	Airmass	Tel.	Grism	Range [Å]	Res. [Å][c]	Standards
05/04/16	476.6	−6.0	900 s × 3	1.54	DUP	blue	3800 – 9200	6	L745-46A, LTT7987
05/04/17	477.6	−5.0	2400 s	1.54	Caha	b200	3500 – 8800	10	BD+33 2642
05/04/19	479.6	−3.0	900 s × 3	1.54	DUP	blue	3700 – 9000	6	L745-46A, LTT7379
05/04/19	479.7	−2.9	1200 s	2.06	TNG	LR-R	5000 – 9750	11	Hz44
05/04/26	487.4	4.8	1500 s	1.09	TNG	LR-B	3300 – 8000	13	Feige 34
05/04/26	487.4	4.8	1500 s	1.15	TNG	LR-R	5000 – 9750	12	Feige 34
05/05/04	495.5	12.9	1500 s	1.04	TNG	LR-B	3500 – 8900	14	Feige 56
05/05/04	495.5	12.9	1500 s	1.08	TNG	LR-R	5000 – 9750	12	Feige 56
05/05/11	502.4	19.8	1500 s × 2	1.01	TNG	LR-B	3300 – 8000	14	Feige 66
05/05/11	502.4	19.8	2700 s × 2	1.14	Caha	r200	6200 – 9750	11	Feige 34
05/05/14	505.4	22.8	2400 s × 2	1.11	Caha	b200	3500 – 8800	14	BD+33 2642
05/05/24	515.6	33.0	1800 s	1.93	VLT	300V + GG435	4200 – 9600	9	LTT7987

[a] JD − 2 453 000.0
[b] Relative to B-band maximum (JD = 2 453 482.6 ± 0.5).
[c] Full-width at half maximum of isolated, unblended night-sky lines.

DUP = Las Campanas 2.5 m du Pont Telescope + WFCCD
Caha = Calar Alto 2.2 m Telescope + CAFOS SiTe
TNG = 3.58 m Telescopio Nazionale Galileo + DOLORES
VLT = ESO 8.2 m Very Large Telescope UT1 + FORS2

SN 1986G (Phillips et al., 1987). In this case, the SN lay behind a prominent dust lane, and consequently was strongly extinguished. In NGC 4070 no such dust lane is visible even in deep images, but SN 2005bl showed signs of extinction within its host galaxy, the most prominent being a narrow interstellar Na I D line in the spectra at the redshift of the host, with an equivalent width (EW) of 2.6 ± 0.3 Å.

Since elliptical galaxies lack H II regions with strong emission lines, their surface colours are good tracers of the internal dust distribution (Patil et al., 2007). Hence, to investigate the dust content in NGC 4070, we constructed a $B - R$ image of the galaxy from the templates obtained with CAFOS on UT 2006 March 28, following largely the prescription of Patil et al. (2007): after the usual pre-reduction, the B- and R-band images were spatially aligned, and the sky background was subtracted. The images were then scaled to contain the same flux inside an aperture of 45 arcsec around the centre of NGC 4070, and subtracted one from the other. The difference image is shown in Fig. 4.2. Both the centre of the galaxy and the position of SN 2005bl are marked. Dark shades correspond to redder areas, indicative of either dust or an intrinsically redder stellar population. A red region is present to the immediate east and north-east of the nucleus, and another more extended but less opaque arc to its south-west. This asymmetric surface-colour distribution suggests that there probably is dust in NGC 4070. However, at the exact position of SN 2005bl no major blue or red structures can be discerned, so that the dust obscuring the SN is probably too locally confined to be resolved.

Deep images of NGC 4070 reveal some deviation from a perfectly spherical or ellipsoidal shape (Fig. 4.3). This is an indication of fairly recent interaction, either with the galaxy 2MASX J12040831+2023280 about 1.3 arcmin to its south-west (labelled 'A' in Fig. 4.3), or with a small knot about 0.8 arcmin to its south (labelled 'B', and most easily seen as irregularly-shaped bright patch in the lower part of Fig. 4.2). Furthermore, in Fig. 4.3 a faint, broad bridge of luminous matter between NGC 4070 and its equally massive elliptical neighbour galaxy NGC 4066 can be detected.[5] The two galaxies are offset by about 3.74 arcmin, which corresponds to a projected distance of 114 kpc (for $H_0 = 72\,\mathrm{km\,s^{-1}\,Mpc^{-1}}$).

The exact amount of dust extinction towards SN 2005bl is quite difficult to determine, and it constitutes the main uncertainty in the calibration of the SN absolute magnitudes. The Galactic component is small, with a colour excess $E(B-V) \approx 0.03$ mag (Schlegel et al., 1998). However, as mentioned before,

[5]The situation is somewhat reminiscent of SN Ia 2005cf (Pastorello et al., 2007a), with the difference that this SN was directly located in the tidal bridge.

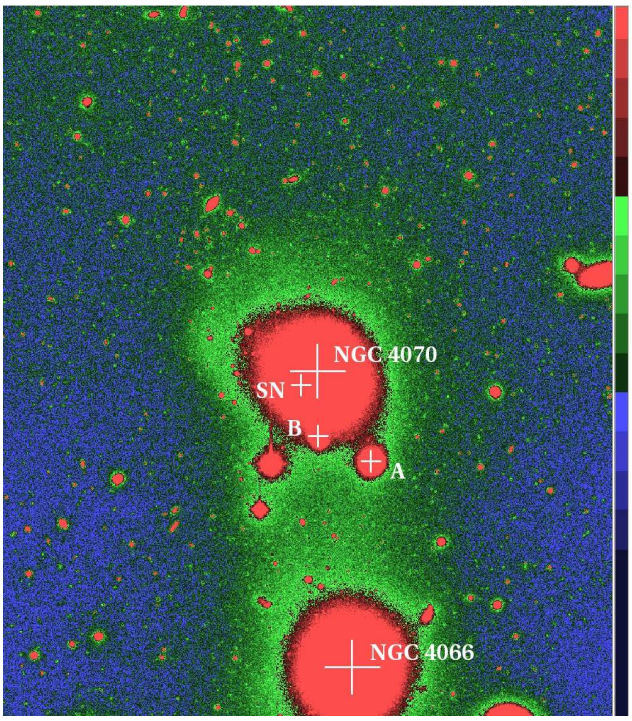

FIGURE 4.3— Deep 7.7×9.0 arcmin^2 exposure of NGC 4070 and its neighbour NGC 4066 obtained on UT 2006 March 28 with CAFOS. North is up, east to the left; brightness increases from blue over green to red. The distorted shape of NGC 4070 and the bridge of luminous matter connecting the two galaxies are discernible. 'A' and 'B' mark companion galaxies of NGC 4070.

the contribution of dust in the host galaxy is significant. With EW(Na I D)= 2.6 ± 0.3 Å and applying

$$E(B-V) \;=\; 0.16 \times \mathrm{EW(Na\,I\,D)}\,,$$

(Turatto, Benetti & Cappellaro, 2003), we obtain $E(B-V)_{\rm host} = 0.42 \pm 0.05$ mag. However, the lack of knowledge of the extinguishing material's gas-to-dust ratio makes this method very uncertain. Therefore, in the case of Type Ia SNe, alternative ways to determine the colour excess using the light and colour curves are usually preferred. Among the most well-known is the Lira (1995) relation, which assumes a uniform $B-V$ colour evolution of SNe Ia between 30 and 90 d after maximum (but see Wang et al. 2007 for a recent warning about the use of this method). Apparently, this relation seems to hold also for underluminous SNe Ia, which are characterised by much redder $B-V$ colours at maximum and soon thereafter. However, the decreasing quality of

the SN 2005bl photometry after +30 d and the lack of B-band observations later than +42 d, result in a relatively large range of colour excesses consistent with the Lira relation, from $E(B-V)_{\rm host} \approx 0.12$ to 0.25 mag.

Since SN 2005bl is an underluminous SN Ia with $\Delta {\rm m}_{15}(B)_{\rm true} = 1.93$ (cf. Section 4.4.1), SNe 1991bg and 1999by [$\Delta {\rm m}_{15}(B)_{\rm true} = 1.94$ and 1.90, respectively; cf. Section 4.7] are natural comparison objects. Despite their numerous similarities, the reddening-corrected colour curves of the two latter objects differ especially at early phases, SN 1991bg being $\sim$0.15 mag redder in $B-V$ than SN 1999by. This intrinsic colour difference directly propagates to an uncertainty in the inferred colour excess of SN 2005bl determined on the basis of such comparison. Matching the colours of SN 2005bl to SN 1991bg, we obtain $E(B-V)_{\rm host} \approx 0.13 \pm 0.05$ mag, whereas a comparison with SN 1999by yields $E(B-V)_{\rm host} \approx 0.29 \pm 0.05$ mag.

A study of the extinction law towards SN 2005bl, analogous to that presented by Elias-Rosa et al. (2006) and based on extracting an extinction curve from a comparison with coeval spectra of SNe 1991bg and 1999by, yields a host-galaxy colour excess of 0.22 ± 0.02 mag. Furthermore, no deviation of the total-to-selective-extinction parameter R_V from the canonical value of 3.1 as inferred from 'standard' dust in the Milky Way can be discerned.

For the rest of the discussion we assume $E(B-V)_{\rm host} = 0.17 \pm 0.08$ mag. This estimate is based solely on the study of the SN colours (giving the strongest weight to the comparison with SN 1991bg), and ignores the larger colour-excess estimate from the interstellar Na I D line, since the latter would result in too blue a colour and too high an absolute luminosity given SN 2005bl's spectrophotometric similarity to SNe 1991bg and 1999by. This choice of $E(B-V)_{\rm host}$, together with the foreground reddening of 0.03 mag, yields a total colour excess $E(B-V)_{\rm total} = 0.20 \pm 0.08$ mag and, adopting a standard Cardelli et al. (1989) reddening law with $R_V = 3.1$, a total B-band extinction along the line of sight of $A_B = 0.82 \pm 0.33$ mag.

With a recession velocity corrected to the CMB reference frame of 7534 ± 33 km s^{-1} (Table 4.1), NGC 4070 is well within the Hubble flow. Adopting $H_0 = 72$ km s^{-1} Mpc^{-1} (Freedman et al., 2001; Spergel et al., 2003), this corresponds to a distance of 104.6 Mpc and a kinematical distance modulus $\mu = 35.10$ mag, similar to that of the Coma Cluster. However, the latter is about $14^\circ 45'$ away (which, at the given distance, corresponds to 27 Mpc), excluding any physical association. Accounting for an uncertainty of 300 km s^{-1} arising from a possible peculiar motion of NGC 4070, we obtain $\mu = 35.10 \pm 0.09$ mag.

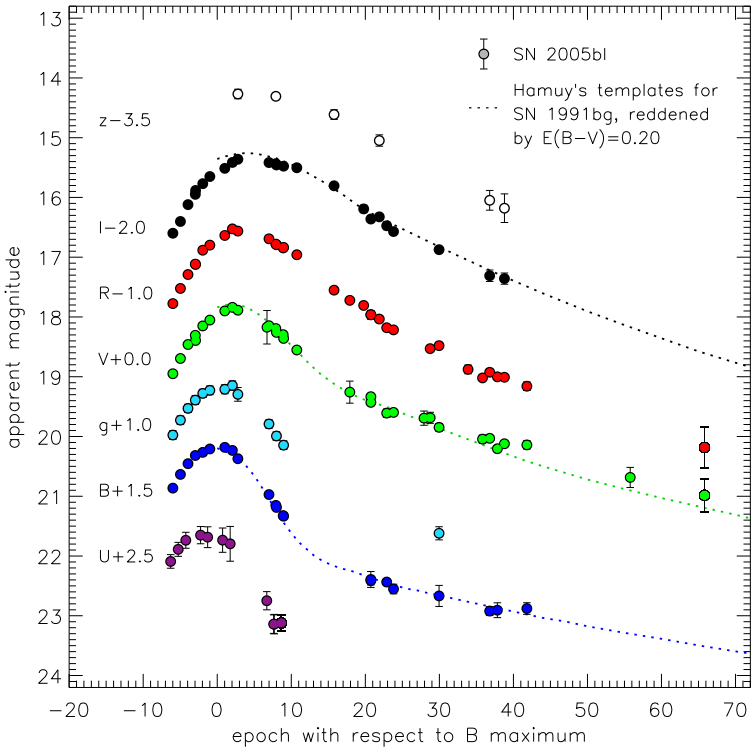

FIGURE 4.4— *UBVRI* Bessell and *gz* Sloan light curves of SN 2005bl. The *BVRI* data (Table 4.3) are *S*- and *K*-corrected except for the latest phases, while the *U*, *g* and *z* data (Tables 4.3 and 4.5) are not. Hamuy et al.'s (1996c) templates for SN 1991bg are shown for comparison (dotted lines).

4.4 Photometric evolution

4.4.1 Filtered light curves

The photometric observations of SN 2005bl are among the earliest ever obtained for a 91bg-like SN. In Fig. 4.4 we present the Bessell *UBVRI* and Sloan *gz* light curves, i.e. the data of Tables 4.3 and 4.5. *S*- and *K*-corrections have been applied to the *BVRI* bands. Also shown are *BVI*-templates constructed from SN 1991bg (Hamuy et al., 1996c), reddened by $E(B-V) = 0.20$ mag. These provide an excellent match to SN 2005bl.

Compared to normal-luminosity SNe Ia the light curves of SN 2005bl are characterised by a fast rise to and decline from the light-curve peak, especially in the blue bands. Moreover, in the *B* band the settling to the exponential tail (corresponding to the bend parameter t_b of Pskovskii 1984 and the intersection

parameter t_2^B as defined by Hamuy et al. 1996c) occurs at a remarkably early epoch, only about 15 d after maximum, as compared to 25–38 d for intermediate and slow decliners (Hamuy et al., 1996c). Consequently, the decline from the peak to the onset of the radioactive tail is only ~ 1.9 mag, less than in most SNe Ia with shallower initial decline.

The exact value of the Phillips (1993) decline rate parameter $\Delta m_{15}(B)$ is difficult to measure directly because of a gap in the light curves around +15 d. A polynomial fit including the B-band data up to one month past maximum yields $\Delta m_{15}(B) = 1.91$, and we adopt a conservative error of 0.10 to account for the fact that the fit around +15 d is not very well constrained. After correction for the mitigating effects of extinction (Phillips et al., 1999) this turns into an actual decline rate $\Delta m_{15}(B)_{\rm true} = 1.93 \pm 0.10$.

Besides the B band, differences with respect to normal-luminosity SNe Ia are most pronounced in the near-IR (I and z bands), where – like in other 91bg-like SNe – the secondary light-curve maximum is absent, and the main maximum is delayed with respect to that in B (JD 2 453 482.6 $\pm$ 0.5) by a couple of days rather than advanced. In general, the instance of peak brightness seems to be the more delayed the redder the band is. V-band maximum occurs 2.3 d after that in B, and those in R and I are delayed by 3.3 and 4.4 d, respectively (see Table 4.1), whereas in U the light-curve peak precedes that in B by about 1.0 d. For the z band the sparse photometric coverage does not allow for an exact determination of the time of maximum light, but it can be estimated to be similarly delayed as in R or I.

The absolute peak magnitudes of SN 2005bl (Table 4.1), calculated adopting the distance and extinction estimates presented in Section 4.3, reveal that the SN is underluminous by 1 to 2 mag in all filters compared to a canonical, $\Delta m_{15}(B)_{\rm true} = 1.1$ SN Ia, the difference being most pronounced in the blue bands.

4.4.2 Bolometric light curve

The differences in luminosity can clearly be seen in Fig. 4.5, where the quasi-bolometric light curve of SN 2005bl is compared to those of the other underluminous SNe Ia 1991bg, 1997cn, 1998de and 1999by (Filippenko et al., 1992b; Leibundgut et al., 1993; Turatto et al., 1996, 1998; Modjaz et al., 2001; Garnavich et al., 2004), and the intermediate decliner SN Ia 2004eo [$\Delta m_{15}(B)_{\rm true} = 1.46$, Pastorello et al. 2007b], which forms a bridge to canonical, normal-luminosity SNe Ia such as 2005cf [$\Delta m_{15}(B)_{\rm true} = 1.12$, Pastorello et al. 2007a]. The integrated optical light curves (see, e.g., Nomoto, Filippenko & Shigeyama 1990) were constructed in the following way: in a first step the U through I mag-

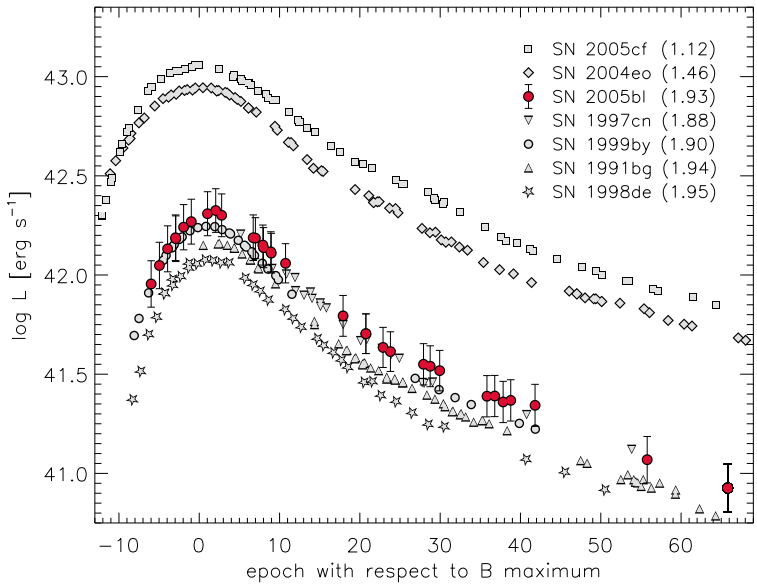

FIGURE 4.5— Quasi-bolometric light curves of SNe 2005bl, 1991bg, 1997cn, 1998de, 1999by, 2004eo and 2005cf, obtained by integrating the U-through-I-band fluxes (for the adopted distance and extinction parameters see Table 4.8 and Pastorello et al. 2007a,b). Error bars are shown for SN 2005bl only, and account for uncertainties in the photometric calibration, distance and extinction estimates. The $\Delta m_{15}(B)_{\rm true}$ of the SNe is given in parentheses.

nitudes were converted to monochromatic fluxes and the spectral energy distribution (SED) was interpolated linearly. The SED was then integrated over frequency, assuming zero flux at the integration limits, which are given by the blue edge of the U band and the red edge of the I band. Whenever no U-band observations were available, or the coverage of this band was incomplete, a correction derived from SN 1999by was applied to the analogously constructed B-through-I light curve. This method appeared more reliable than applying U-band corrections based on ordinary SNe Ia.

As Fig. 4.5 shows, 91bg-like SNe form a fairly homogeneous group in terms of bolometric light-curve shape and luminosity. Both their light-curve width and their luminosities distinguish them even from intermediate decliners such as SN 2004eo. SNe Ia with $\Delta m_{15}(B)_{\rm true} \sim 1.50$–$1.85$ (which are rare, cf. Section 4.7.1) would probably fall in the gap between SN 2004eo and the 91bg-like SNe. In Fig. 4.5 they are not included because their light-curve coverage is insufficient in some of the relevant bands. Within the 91bg-like group, SN 2005bl appears to be the brightest object ($\log L_{\rm max} = 42.31 \pm 0.11$), but the differences are mostly within the error bars, which for SN 2005bl are dominated by the

uncertainty in the host-galaxy extinction.

In the only rapidly-declining SN Ia with extended near-IR photometry, SN 1999by (Höflich et al., 2002; Garnavich et al., 2004)[6], the JHK bands contribute $\sim 25\,\%$ to the total bolometric flux around maximum, and $\sim 36\,\%$ after one month. The corresponding numbers measured for SN 2004eo are $\sim 16\,\%$ and $\sim 37\,\%$, respectively. This means that at early phases the near IR gives a larger contribution in the fast decliners than it does in intermediate and slow decliners, but that by +30 d the difference has vanished. Wavelength regions other than the optical and near-IR appear to contribute very little to the total bolometric flux in SNe Ia (Suntzeff, 1996; Contardo, Leibundgut & Vacca, 2000). Therefore, neglecting these regimes should not cause a significant underestimate of the true bolometric luminosity.

4.4.3 Colour evolution

Fig. 4.6 presents the time-evolution of the $U-B$, $B-V$, $V-R$ and $V-I$ colours of SN 2005bl. The good agreement with the colour curves of SN 1991bg (Hamuy et al., 1996c) also shown in the figure is evident. Except for the late $V-R$ points, all colour indices are > 0 throughout the investigated period, indicating that SN 2005bl – like other rapidly-declining SNe Ia – was a rather red event. In particular it was much redder at early phases than ordinary SNe Ia, which are characterised by a $B-V$ between 0.0 and -0.1 at maximum light. Remarkably, the evolution of SN 2005bl's various colour indices with time is very similar. From our first observations at -6 d on, all colours become monotonically redder until at least ~ 10 d after maximum, and almost simultaneously exhibit a red peak between +12 and +17 d, followed by a monotonic bluening which probably lasts beyond the end of our photometric coverage around +40 d. Such a high degree of similarity between different colour indices is not encountered in normal-luminosity SNe Ia (cf. Section 4.7.1).

4.5 Spectroscopic evolution

4.5.1 Spectra of SN 2005bl

The spectra of SN 2005bl presented in Fig. 4.7 cover the interval from 6 d before to 33 d after B-band maximum light, i.e., the photospheric phase and the early transition stages towards the nebular phase. During this entire period, the SN follows the evolution of other SNe Ia, in particular of the 91bg-like subclass. The

[6]SN 1991bg has been observed in JHK by Porter et al. (1992) (five epochs), but only the three epochs close to maximum light have been calibrated and published (Krisciunas et al., 2004)

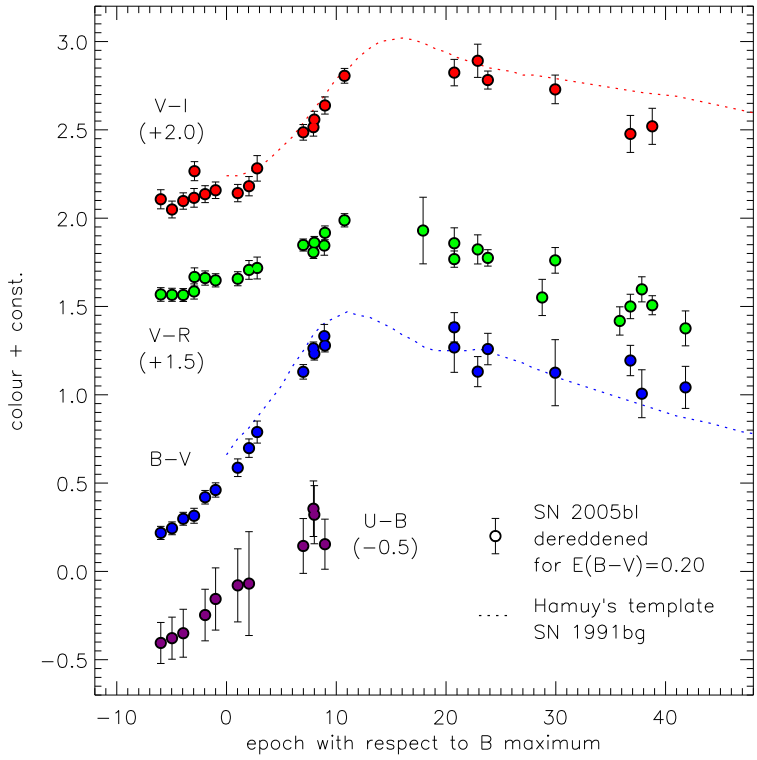

FIGURE 4.6— Time-evolution of the $U-B$, $B-V$, $V-R$ and $V-I$ colour indices of SN 2005bl. The curves have been reddening-corrected adopting a Cardelli et al. (1989) extinction law with $E(B-V) = 0.20$ mag and $R_V = 3.1$.

pre-maximum spectra have a blue continuum, with characteristic P-Cygni lines of Si II, S II, Ca II and Mg II superimposed. With respect to normal-luminosity SNe Ia, additional strong Ti II absorptions are visible, and the Si II λ5972 and O I λ7774 absorptions are more pronounced. Shortly after maximum light the blue flux decreases significantly, and also the S II and Si II λ5972 lines fade rapidly, and are no longer detectable two weeks after maximum. Si II λ6355 is, like most other photospheric lines, somewhat more persistent, and can still be discerned beyond +20 d. Na I D shows a trend opposite to that of Si and S, first being just visible as a shoulder in the blue wing of the Si II λ5972 line on day +5, but evolving to a distinct absorption feature by day +20. In the same period, Fe II emission lines start to dominate the spectrum.

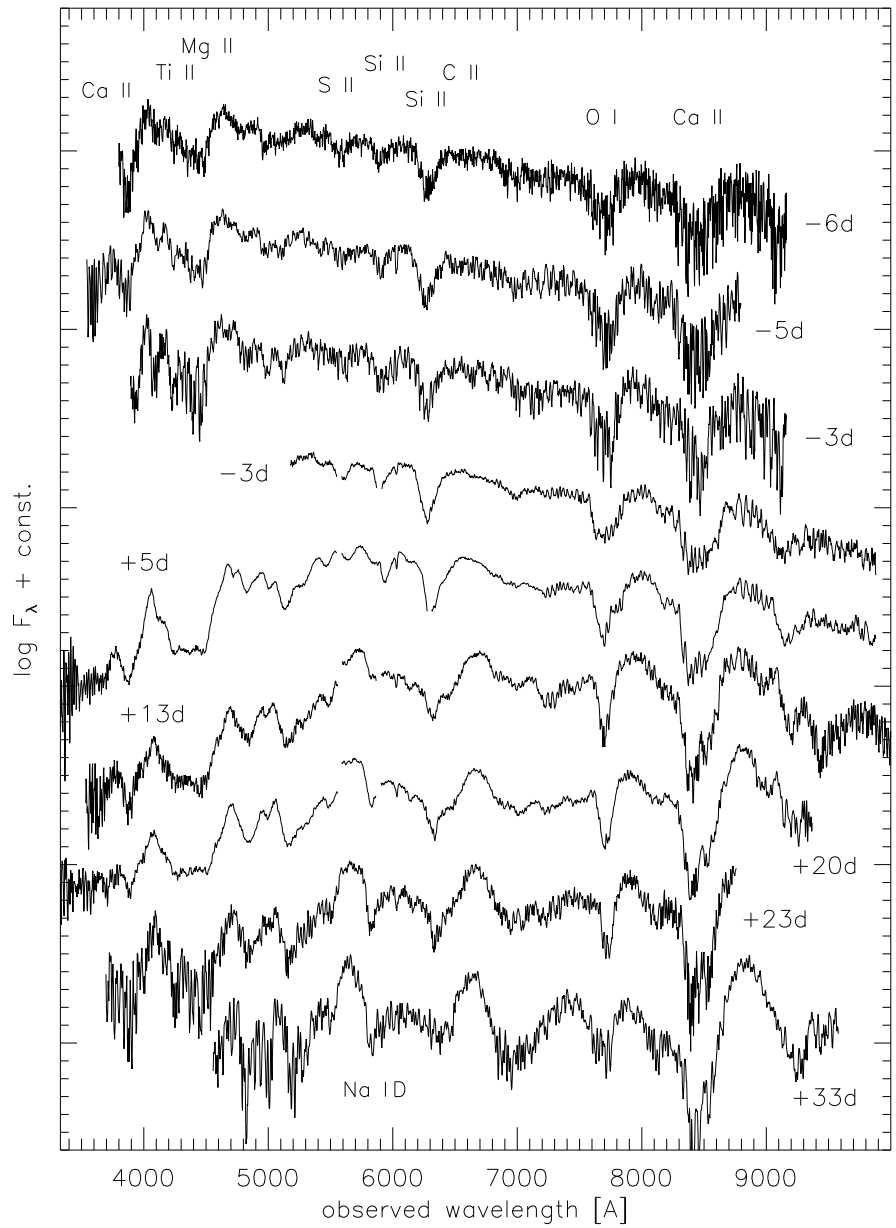

FIGURE 4.7— Time sequence of SN 2005bl spectra in the observer frame. The phases reported next to each spectrum are with respect to B-band maximum. The -3 d (blue part) and $+33$ d spectra have been smoothed using kernel sizes of 600 km s^{-1}. Gaps in the TNG spectra indicate the positions of the strongest night-sky residuals, which have been cut in order to avoid confusion with true SN or host-galaxy features (see Section 2.3.3 and Table 4.6).

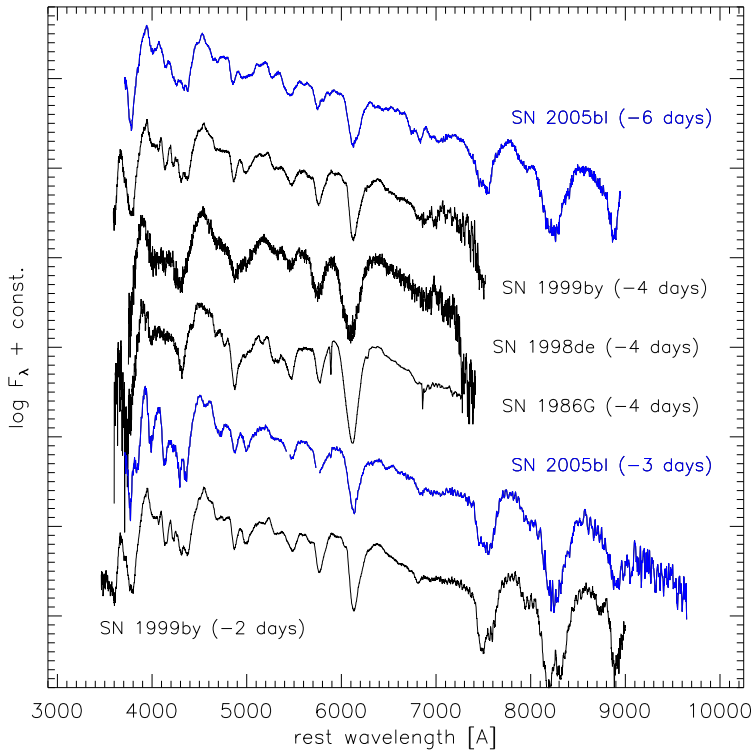

FIGURE 4.8— Comparison of pre-maximum spectra of underluminous SNe Ia. The spectra were reddening-corrected according to the $B-V$ colour excesses reported in Section 4.7. The -6 d spectrum and the blue part of the combined -3 d spectrum of SN 2005bl were boxcar smoothed using kernel sizes of 2300 and 3400 km s^{-1}, respectively.

4.5.2 Comparison with other underluminous SNe Ia

In Figs. 4.8 to 4.10 the spectra of SN 2005bl are compared with those of other underluminous SNe Ia at epochs of about -5 d, $+4$ d and $+30$ d, respectively. For illustration, a comparison with the spectra of the intermediate decliner SN Ia 2004eo [$\Delta m_{15}(B)_{\rm true} = 1.46$, Pastorello et al. 2007b] is made in Fig. 4.11. The figures show that 91bg-like SNe form a relatively homogeneous spectroscopic subclass, distinct from SNe Ia with normal luminosity and even from those with $\Delta m_{15}(B)_{\rm true}$ close to 1.5.

Already at -5 d (Fig. 4.8) the underluminous SNe Ia show evident Ti features between 4000 and 4400 Å, which are absent in SN 2004eo (Fig. 4.11) where this region is dominated by Si and Mg lines. At the same time Fig. 4.11 suggests that at -6 d the continuum temperatures are not too different, indicating that the strength of the Ti features in 91bg-like SNe may not be a

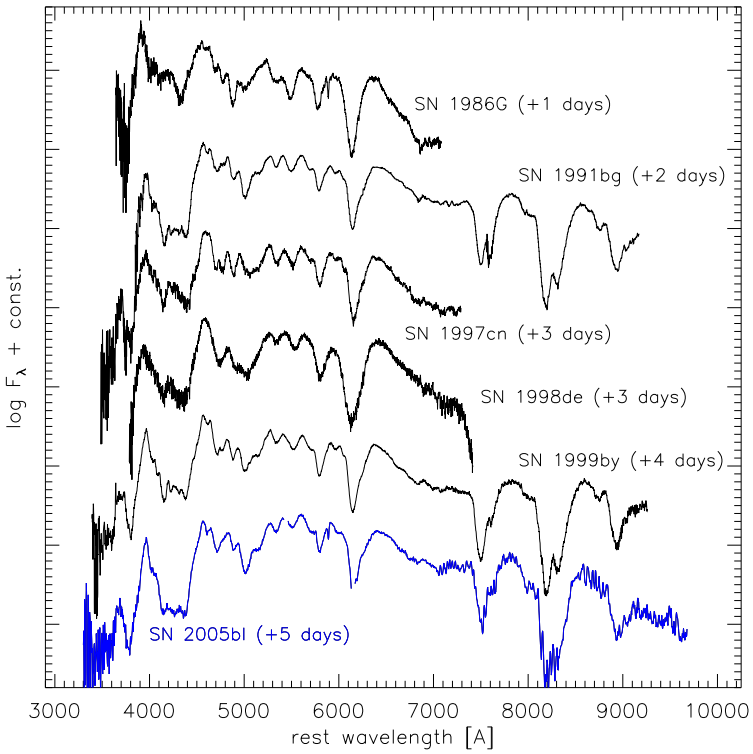

FIGURE 4.9— The same as Fig. 4.8, but some days after maximum light in B.

pure temperature effect but require a truly larger Ti abundance (see also Section 4.6.2). In SN 1986G (Phillips et al., 1987) the Ti lines are less pronounced than in SNe 1998de (Matheson et al., 2008), 1999by (Garnavich et al., 2004) and 2005bl, emphasising its transitional character between 'normal' and strictly 91bg-like SNe Ia. Also, the absolute depth of the Si II λ6355 line in SN 1986G resembles more that of SN 2004eo than those of SNe 1999by and 2005bl. The Si II lines and most other features of SN 1998de at day -5 are broader and at bluer wavelength than in the other SNe of the sample. The spectra of SNe 2005bl and 1999by are essentially identical, the only exception being the flux depletion in SN 2005bl redwards of the Si II λ6355 line at -6 and -5 d, which we attribute to C II λ6580 (see also Section 4.7.4). O I λ7774 is particularly pronounced in all underluminous SNe Ia for which the spectral region is covered.

By a few days after maximum light (Fig. 4.9) the spectra have evolved significantly with the continuum being much redder now, but the degree of homogeneity is still remarkably high. The Ti troughs in the blue are now fully

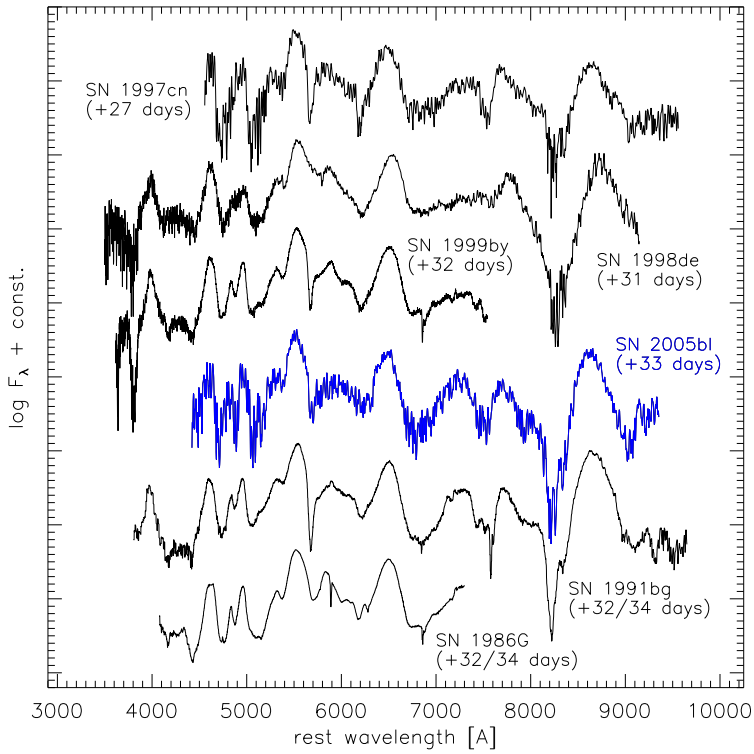

FIGURE 4.10— The same as Fig. 4.8, but 4–5 weeks after maximum light in B. The spectra of SNe 1997cn and 2005bl were smoothed using kernel sizes of 600 km s^{-1}.

developed, showing the characteristic flat bottom that distinguishes 91bg-like from other SNe Ia (Fig. 4.11). The W-shaped S II lines around 5500 Å are comparatively weak. Again SN 1986G takes an intermediate position, with the characteristic properties of the underluminous class being less pronounced than in the other objects shown in Fig. 4.9.

The spectra taken 4–5 weeks past maximum (Fig. 4.10) reveal that at those phases the transition to the nebular phase has already started. Emission lines of Fe-group elements are visible, but the pseudo-continuum has not yet vanished. Ca II, O I and the Ti trough are still prominent in absorption, while S II lines cannot be identified any longer. A characteristic feature of many 91bg-like SNe Ia at those epochs is the remarkably narrow Na I D absorption near 5700 Å. Especially in SNe 1991bg (Filippenko et al., 1992b; Leibundgut et al., 1993; Turatto et al., 1996), 1997cn (Turatto et al., 1998) and 1999by this line is very deep and distinct, while it is less pronounced in SNe 2005bl and, in particular, 1986G and 1998de (Modjaz et al., 2001), where also the narrow core is absent.

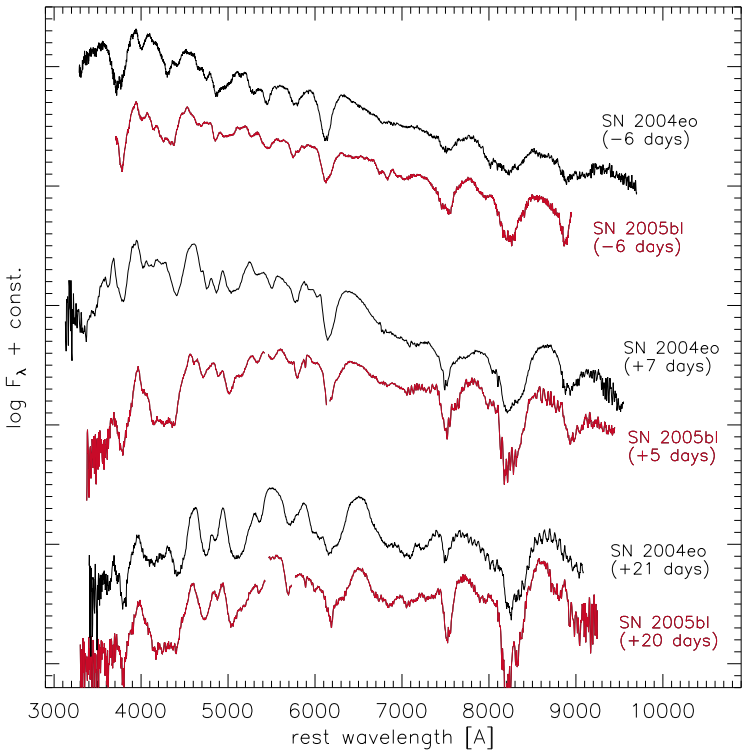

FIGURE 4.11— Spectroscopic comparison of SN 2005bl and the intermediate decliner SN 2004eo (Pastorello et al., 2007b) at three different epochs. The spectra of SN 2004eo have been dereddened for $E(B-V) = 0.109$ mag; the -6 d spectrum of SN 2005bl was smoothed using a kernel of 2300 km s^{-1}.

As already noted by Modjaz et al. (2001), SN 1998de deviates significantly from other 91bg-like SNe between 6800 and 7700 Å, exhibiting a relatively smooth continuum without strong O I λ7774 feature.

Unfortunately, no late-time spectra of SN 2005bl were obtained, so that it cannot be verified whether the distinct, broad nebular emission feature near 7300 Å, which characterises SN 1991bg and distinguishes it from ordinary SNe Ia at late epochs (Filippenko et al., 1992b; Turatto et al., 1996; Mazzali et al., 1997), is also present in SN 2005bl.

4.5.3 Ejecta velocities

Although ejecta velocities inferred from the blueshift of the absorption minima of P-Cygni lines suffer from a number of uncertainties (such as the typically strong line blending in SN Ia spectra), they do provide important information

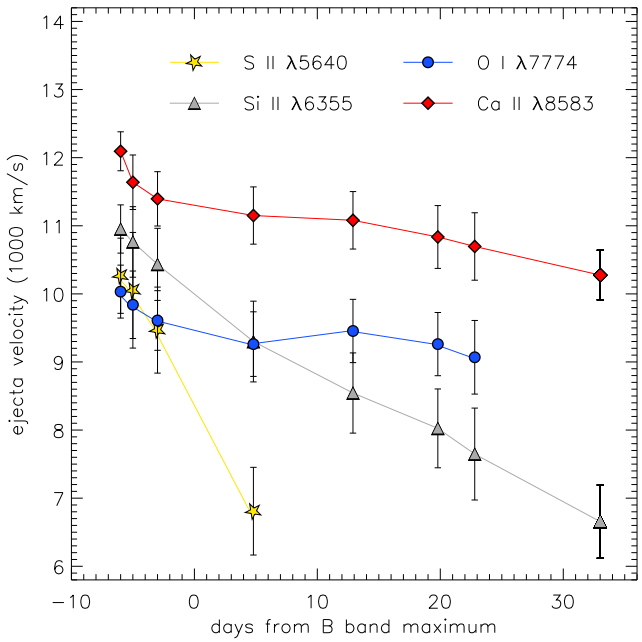

FIGURE 4.12— Expansion velocities of S II λ5640, Si II λ6355, O I λ7774 and the Ca II NIR-triplet as measured from the minima of the P-Cygni line profiles in SN 2005bl.

about the kinetic energy of the ejecta, and can be used as an observationally accessible parameter for comparison studies between different SNe. Furthermore, the range of velocities encompassed by different elements provides insight into the chemical stratification of the ejecta, and hence into nucleosynthesis conditions. This fact has recently been made use of in the Zorro diagnostics (Mazzali et al., 2007c). In SNe Ia, especially the Si II λ6355 has proved to be a suitable velocity indicator, since the line is usually well pronounced, fairly unblended and well visible over a relatively long period.

The Si line velocity in SN 2005bl (Fig. 4.12) evolves from $\sim 11\,000$ km s^{-1} at -6 d to ~ 6600 km s^{-1} at $+33$ d. At maximum light, it is about 10 000 km s^{-1}, which is low for a SN Ia. The velocity evolution of S II λ5640 resembles that of Si II, but the temporal decrease is steeper, and the absolute values are systematically lower by 500–2500 km s^{-1}, meaning that the line predominantly forms in deeper layers of the ejecta (note that the line is visible only until $+5$ d). The Ca II IR triplet, on the other hand, has higher velocities than Si II, and the difference increases from about 1000 km s^{-1} at -6 d to 3500 km s^{-1} at $+33$ d. This relatively shallow decrease in velocity means that Ca II lines mainly form well above the photosphere. Finally, O I λ7774 also exhibits a fairly constant

velocity of 9000–10 000 km s^{-1} during the entire period of our observations, but this result is not very robust as the feature may be substantially blended with Mg II λ7890.

4.6 Spectral modelling

A 1D Monte-Carlo spectrum synthesis code (Mazzali, 2000) was used to simulate the radiation-transport processes in the expanding ejecta of SN 2005bl. Basic assumptions include spherical symmetry, a Chandrasekhar-mass explosion, and an underlying density profile adopted from the W7 explosion model of Nomoto et al. (1984). No attempt was made to obtain better results altering these ingredients. Synthetic fits to four early-time spectra of SN 2005bl were obtained and are presented here, after a short introduction to the concept of the code and the underlying model.

4.6.1 Concept of the radiative transfer code

Only a brief outline is given here; for detailed descriptions of the code see Abbott & Lucy (1985), Mazzali & Lucy (1993), Lucy (1999) and Mazzali (2000), where the basic developments are documented.

The radiative transfer is performed above the photosphere, which is located at an adjustable radius $r_{\rm ph}$. Energy deposition from radioactivity is assumed to occur below the photosphere, from which a blackbody continuum is thought to be emitted. In the 'atmosphere' above, radiative equilibrium is supposed to hold. Photons interact with lines and scatter on free electrons, but no continuum formation is assumed (Schuster-Schwarzschild approximation). The underlying W7 density profile is scaled to match the epoch of each spectrum, assuming homologous expansion, i.e. $r = v\,t$ for each particle.[7] Element abundances are assumed to be homogeneous inside the envelope. They can be freely adjusted in order to match a given observed spectrum.

In our Monte Carlo calculation, radiation packets are followed from their emission at the photosphere through their interaction history, until they either escape or are reabsorbed at the photosphere. The code takes into account scattering processes (on atoms / ions and electrons) as well as photon branching (absorption in an atomic line and subsequent reemission in another). Line optical depths are calculated in the Sobolev approximation, applicable for fast-expanding atmospheres.

Ionisation and excitation conditions are calculated from the radiation-field statistics. This is done using approximate NLTE formulae (see references

[7] This is almost exact for our purposes, as the expansion is homologous already ~ 10 s after explosion onset (see e.g. Röpke 2005).

TABLE 4.7— Physical parameters of SN 2005bl inferred from synthetic spectra, assuming a rise time of 17 d in B. The mass fractions of selected elements are recorded, and solar photospheric abundances (Asplund, Grevesse & Sauval, 2005) are shown for comparison.

	−6.0 d	−5.0 d	−3.0 d	+4.8 d	Solar
t [a]	11.0 d	12.0 d	14.0 d	21.8 d	
$L_{\rm bol}$ [b]	1.24×10^{42}	1.56×10^{42}	2.06×10^{42}	2.56×10^{42}	
$v_{\rm ph}$ [c]	7500	7350	7100	6000	
$T_{\rm bb}$ [d]	10 620	10 790	10 670	9230	
X(C)	0.045	0.030	0.010	0.000	2.16×10^{-3}
X(O)	0.905	0.878	0.847	0.788	5.36×10^{-3}
X(Mg)	0.015	0.040	0.060	0.080	6.04×10^{-4}
X(Si)	0.025	0.037	0.060	0.090	6.66×10^{-4}
X(S)	0.006	0.009	0.013	0.020	3.24×10^{-4}
X(Ti)	3.7×10^{-4}	7.3×10^{-4}	1.4×10^{-3}	4.5×10^{-3}	2.79×10^{-6}
X(Cr)	3.7×10^{-4}	7.3×10^{-4}	1.4×10^{-3}	4.5×10^{-3}	1.66×10^{-5}
X(stable Fe)	1.0×10^{-4}	1.2×10^{-4}	4.0×10^{-4}	1.4×10^{-3}	1.15×10^{-3}
X(^{56}Ni) [e]	–	–	2.0×10^{-4}	2.5×10^{-3}	

[a] Time from explosion.
[b] Bolometric luminosity [erg s^{-1}].
[c] Photospheric velocity [km s^{-1}].
[d] Photospheric blackbody temperature [K].
[e] Mass fraction of ^{56}Ni and its decay products.

above), which in principle employ LTE radiative rates, but additionally take into account the dilution of the radiation field. Collision processes are neglected. A radiation temperature $T_{\rm R}$, determining radiative rates, is calculated in each zone of the envelope. As in Mazzali & Lucy (1993) it is chosen such that the mean frequency of the radiation field inside the zone matches that of a blackbody at $T_{\rm R}$. The matter state and the radiation field are iterated until sufficient convergence is achieved. Within this process, the temperature of the inner-boundary blackbody spectrum is adjusted in order to match the bolometric SN luminosity.

Finally, the emitted spectrum is recalculated solving the formal integral, employing source functions obtained from the packet statistics. This yields smooth spectra at relatively low packet numbers.

4.6.2 Model parameters & chemical composition

The basic parameters and composition inferred from the best-fitting synthetic spectra are reported in Table 4.7. In Fig. 4.13 these models are compared to the observed spectra, and line identifications for the −6 d spectrum are shown.

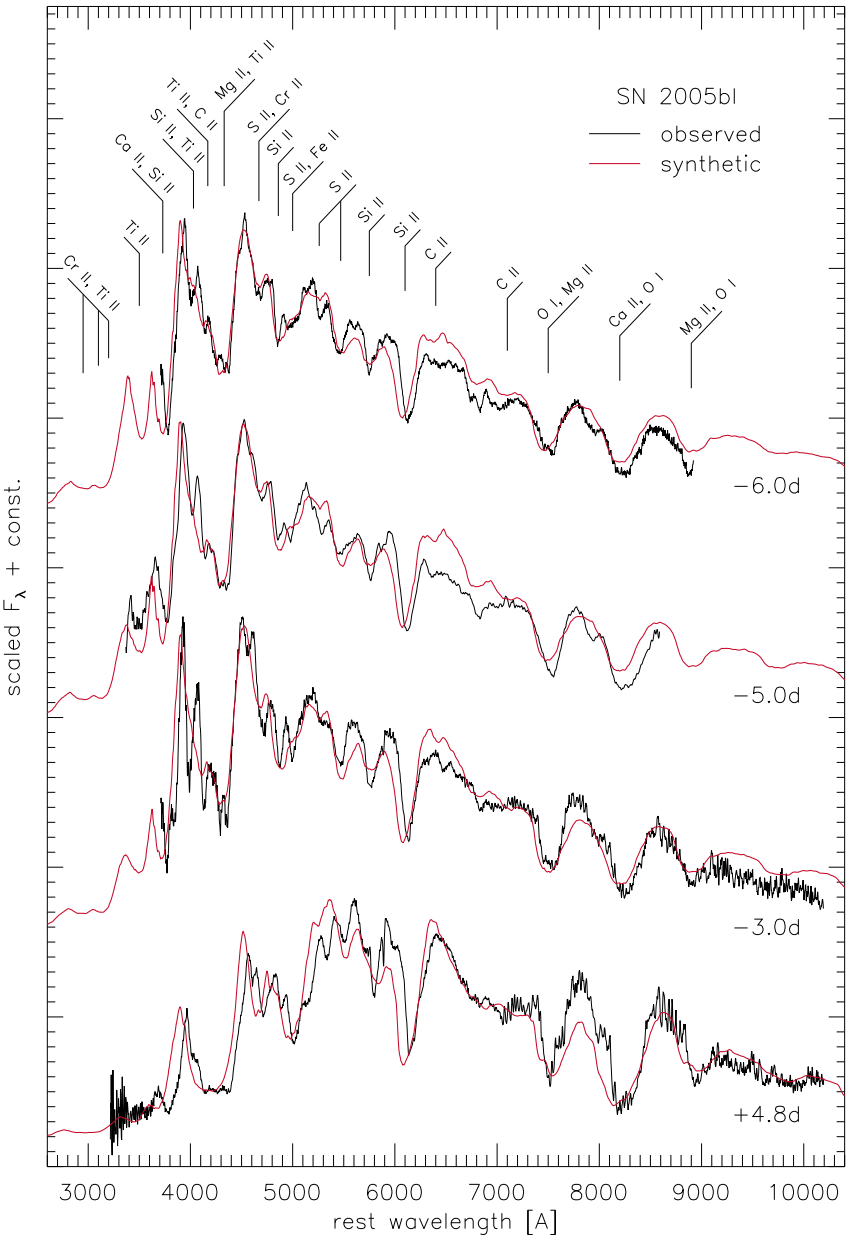

FIGURE 4.13— Synthetic fits to the SN 2005bl spectra at days −6.0, −5.0, −3.0 and +4.8. The observed spectra were smoothed with kernel sizes of 2300 $\mathrm{km\,s^{-1}}$ (−6.0 d) and 3400 $\mathrm{km\,s^{-1}}$ (−5.0 d and −3.0 d–blue part) for presentation. The values of relevant fit-parameters are summarised in Table 4.7. Atop the −6 d spectrum an identification of the most important lines is given.

A rise time to the B-band maximum of 17.0 d is assumed, slightly less than the fiducial value of ~ 19.5 d for normal-luminosity SNe Ia (Riess et al., 1999; Conley et al., 2006). This choice is discussed in Section 4.7.2.

While the overall shape of the continua is nicely matched and most features are well reproduced, the main shortcomings of the models are a flux excess in the emission component of Si II λ6355 at early times, and, more worrysome, a mismatch in the position of some lines. Additionally, many synthetic features are too broad and strongly blended, as they were in models for SN 1991bg (Mazzali et al., 1997). No substantial improvement is obtained reducing the photospheric velocity $v_{\rm ph}$, which indicates that the W7 density profile may not be perfectly suitable for 91bg-like SNe, and that a steeper density gradient may be required. With $v_{\rm ph} = 7500$ km s^{-1} 6 d prior to maximum light, the inferred photospheric velocity is significantly lower than in normal SNe Ia ($\sim 10\,000$ to 11 000 km s^{-1} at comparable epochs). By day +5, $v_{\rm ph}$ further decreases by about 1500 km s^{-1}. Singly and doubly ionised species dominate the ejecta. Especially the singly ionised species leave strong imprints on the spectra, as can be seen from the line identification in Fig. 4.13. In all spectra modelled here the heavy-element content is comparatively low, but Table 4.7 shows that it increases with time, indicating composition stratification in the ejecta.[8] At the higher velocities the ejecta are almost entirely made up of unburned material, whereas NSE elements are essentially absent. In particular, no Ni and Co, and only very little Fe are included in the -6 and -5 d models. After maximum light, IMEs and Fe-group elements become more abundant, but still less so than in normal-luminosity SNe Ia (cf., e.g., Stehle et al., 2005; Tanaka et al., 2007). Interestingly, Ti and Cr, whose abundances can be well constrained from the depth of the characteristic trough between 4000 and 4400 Å, appear to be more abundant than Ni, Co and Fe, yet another indication for explosion conditions which disfavour burning to NSE.

4.7 Discussion

In a number of works (e.g. Filippenko et al. 1992b; Leibundgut et al. 1993; Ruiz-Lapuente et al. 1993; Turatto et al. 1996; Mazzali et al. 1997; Turatto et al. 1998; Modjaz et al. 2001; Garnavich et al. 2004) 91bg-like SNe Ia have been studied and found to be different from normally luminous SNe Ia in several respects. Besides their lower luminosity, they have rapidly declining light curves

[8] For this reason it would be necessary to work with the stratified version of the code (Stehle et al., 2005) if accurate abundances were required. This reaches beyond the scope of the work presented here. Therefore, the composition reported in Table 4.7 reflects the overall trend, but the absolute numbers should be taken with caution.

which do not show the characteristic secondary maximum in the near-IR, cooler spectra with significant Ti II absorption troughs, low ejecta velocities and large values of $\mathcal{R}$(Si) (Nugent et al., 1995). Nevertheless, the light-curve width and peak luminosity of underluminous SNe Ia seem to obey a correlation (Garnavich et al., 2004), but not the same one as more ordinary SNe Ia. Also, 91bg-like SNe seem to fit smoothly into the Zorro plot (Mazzali et al., 2007c), where they represent the extremely ^{56}Ni-poor, IME-rich end of the SN Ia distribution (but see Section 4.7.4 for a revised picture). With the increasing number of well-observed objects of this class, it is interesting to revisit some of the aspects mentioned above and to investigate in more detail the degree of homogeneity, or rather diversity, that these SNe exhibit. In Tables 4.8 and 4.9 elementary information on our comparison sample of rapidly-declining SNe Ia is collected; selection criteria were a reasonably dense light-curve coverage starting at least around maximum light, and $\Delta m_{15}(B)_{\rm true} > 1.5$.

4.7.1 Photometric behaviour of underluminous SNe Ia

Here we focus on the photometric properties of underluminous SNe Ia, compare their light-curve shapes and colour indices, determine their peak absolute magnitudes, and investigate their decline-rate vs. luminosity relationship.

Light- and colour-curve morphology

Fig. 4.14 compares the B, V and I light curves of all the objects in Table 4.9, rescaled to coincide at maximum light.

SNe with $\Delta{\rm m}_{15}(B)_{\rm true} \sim 1.9$ (red symbols in Fig. 4.14), including SN 2005bl, show a single-peaked broad I-band light curve, whose maximum is delayed by a few days with respect to that in B. In contrast, the SNe with $\Delta{\rm m}_{15}(B)_{\rm true} \sim 1.5$ to 1.75 (green symbols) clearly have double-peaked I-band light curves, and, as in normal-luminosity SNe Ia, the first I-band peak precedes that of the B band (e.g. Hamuy et al. 1996c; Leibundgut 2000). These observations are in agreement with the results of Kasen (2006), who computed synthetic light curves with the SEDONA code, varying the mass of ^{56}Ni. His prediction is an ever smaller temporal offset of the first and secondary I-band maxima with decreasing SN luminosity, and the merging to a single broad peak for the most underluminous objects. The B-band light curves of the two groups (red and green symbols in Fig. 4.14) also exhibit noticeable differences in shape, probably influenced by the evolution of the Ti trough. 91bg-like SNe settle to the

[9]For SN 1986G the Cepheid measurement does not refer to the actual host galaxy Centaurus A, but to NGC 5253, which is a member of the same group (Ferrarese et al., 2000). It was adopted here for the lack of more reliable distance estimates.

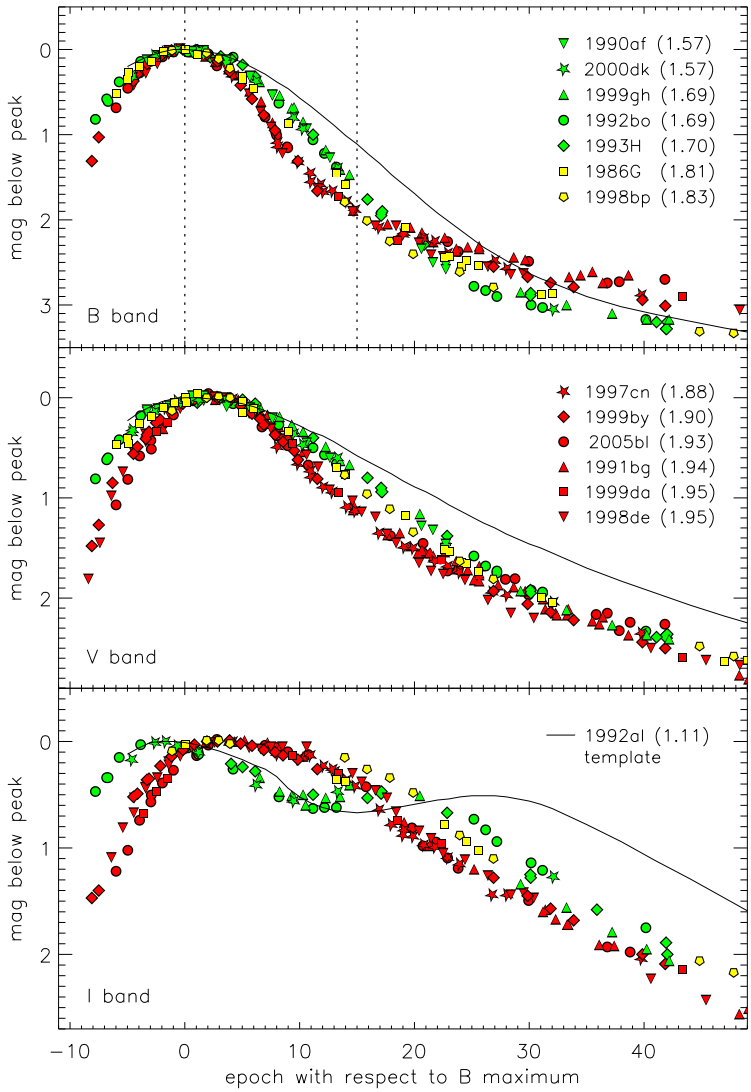

FIGURE 4.14— *BVI* light curves of the rapidly-declining SNe Ia of Table 4.9, normalised to their peak magnitudes. The $\Delta m_{15}(B)_{\rm true}$ of each SN is given in parentheses. Different symbol colours represent different decline rates [green: $1.50 < \Delta m_{15}(B)_{\rm true} < 1.75$; yellow: $1.75 \leq \Delta m_{15}(B)_{\rm true} < 1.85$; red: $\Delta m_{15}(B)_{\rm true} \geq 1.85$]. Light-curve templates of SN 1992al [$\Delta m_{15}(B)_{\rm true} = 1.11$, Hamuy et al. 1996c] are shown for comparison.

TABLE 4.8— Comparison sample of SNe Ia with $\Delta m_{15}(B)_{\rm true} > 1.5$, ordered by increasing $\Delta m_{15}(B)_{\rm true}$ – distances, colour excesses and host galaxies.

SN	$E(B-V)^a$	μ^b	host galaxy	morph.^{c}
1990af	0.07(0.06)	36.59(0.05)	*anonymous*	SB0
2000dk	0.07(0.03)	34.18(0.13)	NGC 382	E
1999gh	0.06(0.03)	32.82(0.25)	NGC 2986	E2
1992bo	0.03(0.03)	34.34(0.12)	ESO 352-57	$SB0_{pec}$
1993H	0.12(0.06)	35.07(0.09)	ESO 445-66	SBab(rs)
1986G	0.78(0.07)	27.61(0.11)	NGC 5128	$S0_{pec}$
	R_V=2.4^d			
1998bp	0.08(0.03)	33.13(0.22)	NGC 6495	E
1997cn	0.03(0.03)	34.25(0.13)	NGC 5490	E
1999by	0.02(0.03)	30.75(0.23)	NGC 2841	Sb
2005bl	0.20(0.08)	35.10(0.09)	NGC 4070	E
1991bg	0.08(0.06)	31.28(0.20)	NGC 4374	E1
1999da	0.06(0.03)	33.58(0.17)	NGC 6411	SA0
1998de	0.06(0.03)	34.06(0.14)	NGC 252	S0

[a] Total (Galactic + host-galaxy) colour excess.
[b] Distance modulus from Cepheids (SNe 1986G and 1999by; Ferrarese et al. 2000; Garnavich et al. 2004)[9], SBF and PNLF (SN 1991bg; Ferrarese et al. 2000; Tonry et al. 2001) or the host-galaxy recession velocity with respect to the CMB rest frame (NED) assuming $H_0 = 72\,{\rm km\,s^{-1}\,Mpc^{-1}}$ (other SNe). For the latter, an uncertainty of $300\,{\rm km\,s^{-1}}$ has been adopted to account for the galaxies' peculiar motions.
[c] Host-galaxy morphology (from LEDA).
[d] Spectropolarimetry (Hough et al., 1987) indicates $R_V = 2.4 \pm 0.13$ for the dust in Centaurus A, the host of SN 1986G. We adopted this value and propagated the assigned error to the uncertainty in the absolute magnitudes.

radioactive tail earlier, only $\sim 15\,{\rm d}$ after maximum light. Consequently, the drop in magnitude from the peak to the tail is smaller for these, although their initial decline is steeper. Thus, the B light curves of 91bg-like and 'normal' SNe Ia cannot be transformed into each other by employing a simple strech factor.

The only objects in the sample with $1.75 \leq \Delta{\rm m}_{15}(B)_{\rm true} < 1.85$ are SNe 1986G and 1998bp (yellow symbols). The light-curve morphology of these SNe seems to provide a link between the formerly defined groups. While the I band is still single-peaked with maybe a hint of a double peak, the luminosity drop from maximum to the radioactive tail in the B band resembles that of SNe with $\Delta{\rm m}_{15}(B)_{\rm true} < 1.75$. The existence of objects with such intermediate properties might support the idea of a common progenitor and explosion scenario for *all* SNe Ia. However, SN statistics tell us that objects

TABLE 4.9— Comparison sample of SNe Ia with $\Delta m_{15}(B)_{\rm true} > 1.5$, ordered by increasing $\Delta m_{15}(B)_{\rm true}$ – intrinsic SN properties.

SN	$\Delta m_{15}(B)_{\rm true}$	$M_{B,\rm max}$	$M_{V,\rm max}$	$\mathcal{R}(\rm Si)_{\rm max}$	$\dot{v}^a$	References
1990af	1.57(0.05)	−18.96(0.25)	−18.98(0.19)			H96a, H96b, P99
2000dk	1.57(0.09)	−18.84(0.18)	−18.83(0.17)			J06, VSNET
1999gh	1.69(0.05)	−18.60(0.30)	−18.73(0.28)			J06, VSNET
1992bo	1.69(0.05)	−18.61(0.17)	−18.59(0.15)			H96a, H96b, P99
1993H	1.70(0.10)	−18.57(0.25)	−18.73(0.20)	0.50(0.05)	73(8)	H96a, H96b, P99
1986G	1.81(0.07)	−17.76(0.32)	−18.03(0.26)	0.60(0.04)	68(4)	P87, P99, B05
1998bp	1.83(0.06)	−17.73(0.25)	−18.08(0.24)			G04, J06
1997cn	1.88(0.10)	−17.17(0.20)	−17.79(0.19)	0.68(0.07)	75(9)	T98, B05, J06
1999by	1.90(0.05)	−17.17(0.26)	−17.65(0.25)	0.69(0.05)	97(4)	T00, H01, V01, G04, VSNET
2005bl	1.93(0.10)	−17.24(0.34)	−17.85(0.27)	0.63(0.06)	99(9)	this work
1991bg	1.94(0.10)	−16.85(0.34)	−17.56(0.29)	0.66(0.05)	106(5)	F92, L93, T96, P99
1999da	1.95(0.10)	−16.98(0.22)	−17.65(0.20)			K01
1998de	1.95(0.09)	−16.74(0.19)	−17.43(0.17)	0.69(0.04)	146(3)	M01, J06

[a] Post-maximum decrease of the Si II λ6355 velocity in $\rm km\,s^{-1}\,d^{-1}$, see Benetti et al. (2005) and Section 4.7.3.

H96a = Hamuy et al. (1996a);
H96b = Hamuy et al. (1996b);
P99 = Phillips et al. (1999);
J06 = Jha et al. (2006a);
P87 = Phillips et al. (1987);
B05 = Benetti et al. (2005);
G04 = Garnavich et al. (2004);
T98 = Turatto et al. (1998);
T00 = Toth & Szabo (2000);
H01 = Howell et al. (2001);
V01 = Vinkó et al. (2001);
F92 = Filippenko et al. (1992b);
L93 = Leibundgut et al. (1993);
T96 = Turatto et al. (1996);
K01 = Krisciunas et al. (2001);
M01 = Modjaz et al. (2001);
VSNET = Variable Star Network

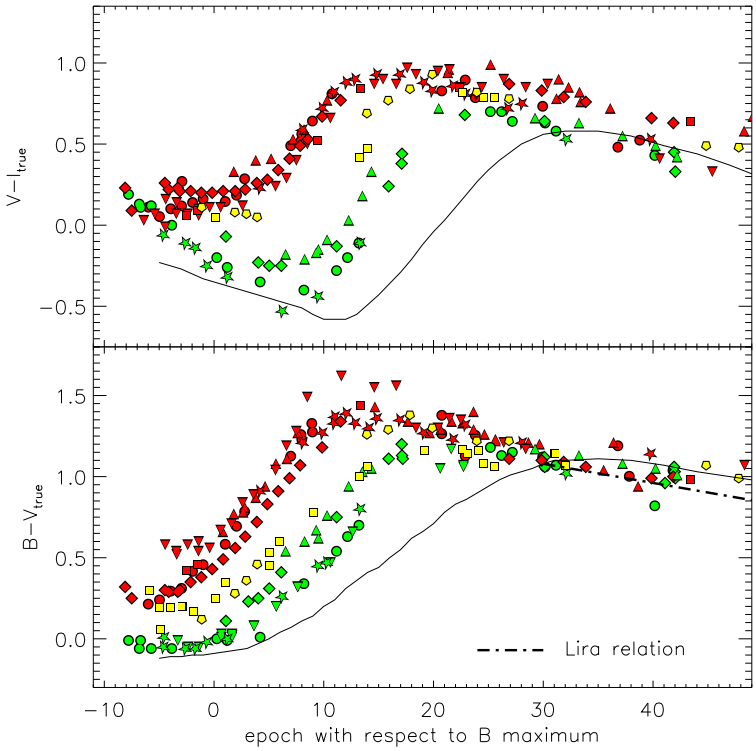

FIGURE 4.15— Evolution of the $B-V$ (top panel) and $V-I$ (bottom panel) colour indices of the rapidly-declining SN Ia sample of Table 4.9 plus SN 1992al. The symbols and colour coding are the same as in Fig. 4.14. The dash-dotted line in the lower panel represents the Lira (1995) relation, i.e. the uniform $B-V$ colour that all SNe Ia are supposed to exhibit between day +30 and +90.

with $\Delta m_{15}(B)_{\rm true} \approx 1.8$ are intrinsically rare.

Fig. 4.15 shows the reddening-corrected $B-V$ and $V-I$ colour curves of the same SNe as above. The differences in $B-V$ after +30 d are marginal, and all SNe obey the Lira (1995) relation within the uncertainties (note, however, that for the more strongly-reddened SNe 1986G and 2005bl the Lira relation was directly or indirectly used to infer the true extinction along the line of sight, making this a circular argument). On the contrary, the $B-V$ colour evolution around maximum light shows remarkable differences, the 91bg-like SNe Ia having a much redder colour at maximum [0.4 to 0.7 mag, compared to $\sim$0.0 mag for SNe Ia with $\Delta m_{15}(B)_{\rm true} < 1.75$]. Also, the peak $B-V$ colour is reached earlier in underluminous SNe, and is redder by $\sim$0.3 mag.

In $V-I$ the differences among the objects of Table 4.9 are even more

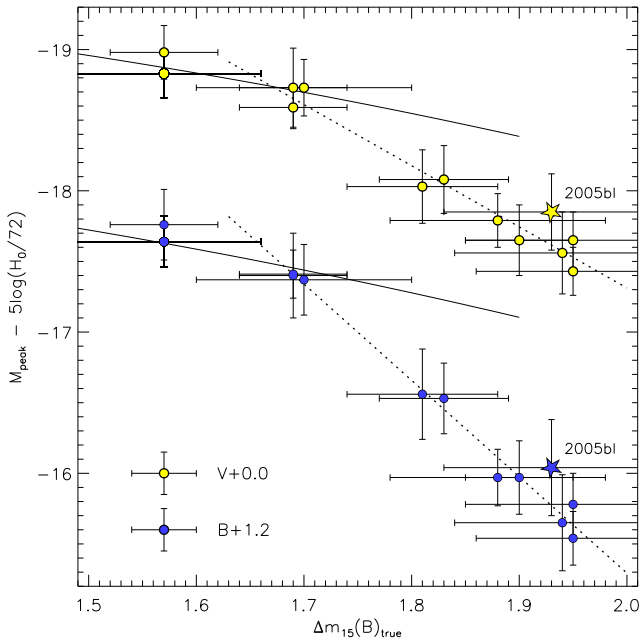

FIGURE 4.16— Peak absolute B- and V-band magnitudes of the SN sample of Table 4.9. The dotted lines are the best linear fits to the data with $\Delta m_{15}(B)_{\rm true} \geq 1.69$, characterised by slopes of 6.83 ± 0.32 and 4.33 ± 0.31 for B and V, respectively. The solid lines show the quadratic relation obtained by Phillips et al. (1999) for SNe Ia with $\Delta m_{15}(B)_{\rm true} < 1.70$.

pronounced. The $V-I$ colour index of SNe Ia with $1.50 < \Delta m_{15}(B)_{\rm true} < 1.75$ decreases from about 10 d before to 5–10 d after B-band maximum just like in all intermediate or slow decliners, then increases steeply, levelling off at ~ 20 d and again decreasing slowly thereafter. 91bg-like SNe, in contrast, do not show the initial bluening, but become redder from the very first available observations onwards. This behaviour continues until ~ 15 d past maximum, when the curves flatten and subsequently a soft bluening sets in. Evidently, the origin of the different $V-I$ evolution lies in the different delay of the main maximum and the presence or absence of the secondary maximum in the I band.

Absolute magnitudes & Phillips relation

Table 4.9 shows that the peak absolute magnitudes of the SNe with $\Delta m_{15}(B)_{\rm true} > 1.5$ span a wide range, from -16.74 to -18.96 in the B band. As Hamuy et al. (1996a), Phillips et al. (1999) and Garnavich et al. (2004) pointed out, also for these SNe the peak magnitudes correlate with $\Delta m_{15}(B)_{\rm true}$, but the dependence is steeper than for more slowly declining SNe Ia. Based only on

SNe with $\Delta\mathrm{m}_{15}(B)_{\mathrm{true}} \geq 1.69$, our best linear fits (Fig. 4.16) are given by

$$\begin{aligned} M_{B,\mathrm{peak}} &= -18.54 + 5\,\log(H_0/72) + 6.83\,[\Delta m_{15}(B)_{\mathrm{true}} - 1.7\,] \\ M_{V,\mathrm{peak}} &= -18.61 + 5\,\log(H_0/72) + 4.33\,[\Delta m_{15}(B)_{\mathrm{true}} - 1.7\,]\,. \end{aligned}$$

The slopes of 6.83 ± 0.32 and 4.33 ± 0.31 for the B and V bands are in excellent agreement with the results of Garnavich et al. (2004), and much steeper than what Hamuy et al. (1996a) find for SNe with $\Delta\mathrm{m}_{15}(B)_{\mathrm{true}} \leq 1.69$ (0.78 ± 0.17 and 0.71 ± 0.14 for B and V, respectively). Also the quadratic relation derived by Phillips et al. (1999) for SNe with $\Delta\mathrm{m}_{15}(B)_{\mathrm{true}} < 1.70$ provides a poor fit to the peak magnitudes of fast decliners.

4.7.2 The rise time of underluminous SNe Ia

Rise times of SNe Ia are important to constrain possible explosion models. In our synthetic spectra the rise time t_{r} determines the actual (scaled) density profile at a given epoch (cf. Section 4.6.1), and hence the matter density of the line-forming region. Here we report our attempts to estimate the rise time of 91bg-like SNe, in particular of SN 2005bl.

Photometric rise-time determination

Efforts have been made to measure SN-Ia rise times directly from a fit to their early-time light curves (Riess et al., 1999; Conley et al., 2006; Strovink, 2007). Depending on measurement details, these studies yield rise times of 17 to 20 d for fiducial $\Delta\mathrm{m}_{15}(B)_{\mathrm{true}} = 1.1$ SNe Ia. Furthermore, there seems to be a negative correlation between t_{r} and $\Delta\mathrm{m}_{15}(B)_{\mathrm{true}}$, faster decliners having shorter rise times. However, all these studies are based on samples of 'normal' SNe Ia with $\Delta\mathrm{m}_{15}(B)_{\mathrm{true}} \leq 1.5$, and it may be doubted whether the inferred trends can be extrapolated to 91bg-like SNe with $\Delta\mathrm{m}_{15}(B)_{\mathrm{true}} \approx 1.9$.

What makes these direct measurements so demanding is the need for high-quality early-time photometry, preferentially before day -10 (Riess et al., 1999), which to date is not available for any 91bg-like SN, including 2005bl. In order to constrain the rise times of this class of objects, it may be useful to consider the two 91bg-like SNe Ia with the earliest photometric data, SNe 1998de and 1999by. Both have a filtered light-curve coverage starting about one week before B-band maximum, complemented by earlier unfiltered measurements and some deep detection limits shortly before. For SN 1998de the earliest detection showing just 'a hint of the supernova' was on unfiltered CCD frames taken 12.3 d before B-band maximum (preceded by a non-detection down to a limiting magnitude of 19.0 five days earlier, Modjaz et al. 1998), thus providing at least a lower limit for the rise time. For SN 1999by, the earliest detection on

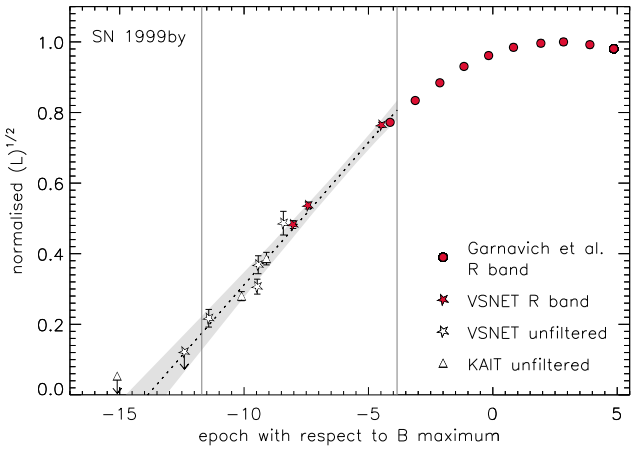

FIGURE 4.17— R-band / unfiltered early-time light curve of SN 1999by, plotted as $L^{1/2}$ vs. $t - t_{B_{\max}}$, and linear fit (dotted line) to the data up to day −4 (between the two thin vertical lines). Assuming $L \propto t^2$, the instance of explosion would be given by the intersection of the fit with $L^{1/2} = 0$ at −13.9 d. The grey-shaded region marks the 3-σ confidence bands of the linear fit. Caveats are discussed in the text.

unfiltered CCD frames dates back to day −11.4, showing the SN at only 5 ± 1 % of the peak R-luminosity (Arbour et al., 1999). Further detection limits constrain the SN luminosity to be less than ∼1.6 % of the peak value at −12.4 d, and less than ∼0.3 % at −15.1 d. Applying the method described by Riess et al. (1999) to these data, but using unfiltered and R-band points between −11.4 and −4.0 d for the fit (Fig. 4.17), a rise time to B-band maximum of $13.9^{+1.2}_{-1.1}$ dwould be inferred for SN 1999by, the errors being the 3-σ confidence levels of the fit combined with the uncertainty in determining the epoch of B-band maximum (Garnavich et al., 2004).

In this approach we disregarded a possible (and theoretically not unexpected) deviation from the early $L \propto t^2$-behaviour which is the basis of the Riess et al. analysis. If the synthesised ^{56}Ni is confined to the inner ejecta, which – at least for 91bg-like objects – is supported by the lack of Ni in the −6 and −5 d spectra of SN 2005bl (cf. Section 4.6.2), it should require some time for the photons to reach the photosphere and be released. This could result in an initial post-explosion phase with only very little brightening of the SN, before the observed steep rise of the light curve sets in. For this reason, the inferred value of 13.9 d might be considered a *lower limit* to the actual rise time of SN 1999by. Given the similarity in terms of light-curve shape, this result should provide a good indication also for the rise time of SN 2005bl.

The rise time addressed by spectral modelling

The rise time constitutes an important input parameter for our spectrum synthesis calculations. Since the colour of an observed spectrum has to be reproduced in a corresponding model, the photospheric temperature, which can be crudely approximated through the Stefan-Boltzmann law $L \propto v_{\rm ph}^2 t^2 T^4$, is confined to a limited range. Assuming a shorter rise time, the photospheric velocity thus usually has to be increased in order to keep the photospheric temperature constant. The line velocities in the synthetic spectrum then also tend to be larger.

Given the difficulties in observational rise-time determination, we created eight models with different rise times (12.5–25.0 d) for the earliest available spectrum of SN 2005bl (−6 d), where a change in $t_{\rm r}$ has the largest relative effect. Excluding models largely deviating from the observed spectrum yielded a range of acceptable rise times. For the models with $t_{\rm r} < 14.0$ d, we had to use photospheric velocities of $v_{\rm ph} > 10\,200$ km s^{-1}, which are incompatible with observed and measured (Fig. 4.12) O I and S II expansion velocities. Choosing rise times of 14.0–15.5 d, most weaker lines were fitted nicely, while in stronger lines such as Si II λ6355 or Ca II H&K there was still a lack of absorption at low velocity. While weaker lines mostly form near the photosphere, strong lines have considerable strength also in layers well above. Thus, their centroid typically shows a larger blueshift, and their emission, centred at the rest wavelength, is more pronounced. In order to decrease the flux in their red wings, $v_{\rm ph}$ had to be reduced to 5000–6000 km s^{-1}, corresponding to rise times of 22–20 d. The weaker features, however, then appeared at velocities too low in the synthetic spectrum.

The difficulty to match all line-velocities simultaneously points to some substantial shortcoming in our treatment of the SN ejecta. Stratifying the ejecta composition (Stehle et al., 2005) assuming only little Si and Ca at high velocity might cure some of the problems, as it could potentially remove the blue parts of the respective strong absorption lines and reduce their re-emission. Yet, we retained our uniform-abundance approach, because no observational data earlier than −6 d are available to constrain the additional parameters of a stratified-abundance model. Alternative explanations for the inconsistencies include a possible inadequacy of the W7 density structure, a deviation of the total ejected mass from $M_{\rm Ch}$, or 3D effects.

Nonetheless, based on our model sequence, we confidently exclude rise times shorter than 14 and longer than 22 d. For all spectral models discussed below we assumed a rise time of 17.0 d. This value is fully compatible with the lower limits observationally derived above. At the same time, it is slightly shorter

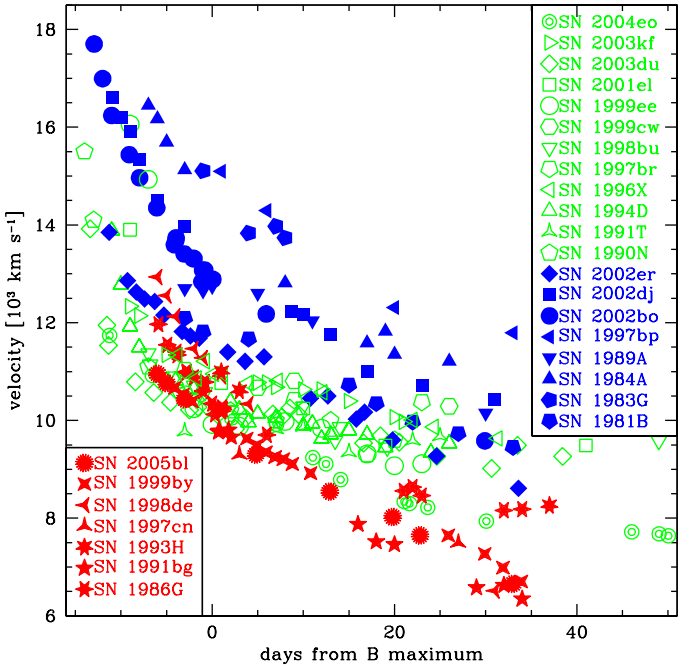

FIGURE 4.18— Velocity measured from the minimum of the Si II λ6355 line as a function of time. Open green symbols represent low-velocity-gradient (LVG) SNe, filled blue symbols high-velocity-gradient (HVG) SNe, and red starred symbols correspond to the FAINT SNe, as defined by Benetti et al. (2005). The values for HVG and LVG SNe are taken from the literature (Benetti et al., 2005; Pastorello et al., 2007b), while the data set for the FAINT class has been extended and in parts remeasured.

than what is favoured for $\Delta m_{15}(B)_{\rm true} = 1.1$-SNe, in agreement with the trend found for SNe Ia with $\Delta m_{15}(B)_{\rm true} \leq 1.5$ (e.g. Riess et al. 1999; Kasen & Woosley 2007).

4.7.3 Spectroscopic parameters

A spectroscopic comparison of SN 2005bl with other underluminous SNe Ia was performed in Section 4.5.2, in particular in Figs. 4.8–4.10. Here, we concentrate on parameters such as $\mathcal{R}$(Si) (Nugent et al., 1995) and $\dot{v}$ (the average daily rate of velocity decrease of Si II λ6355 between B-band maximum and either the time the Si II feature disappears or the last available spectrum, whichever is earlier; Benetti et al. 2005). With respect to Benetti et al. (2005), these

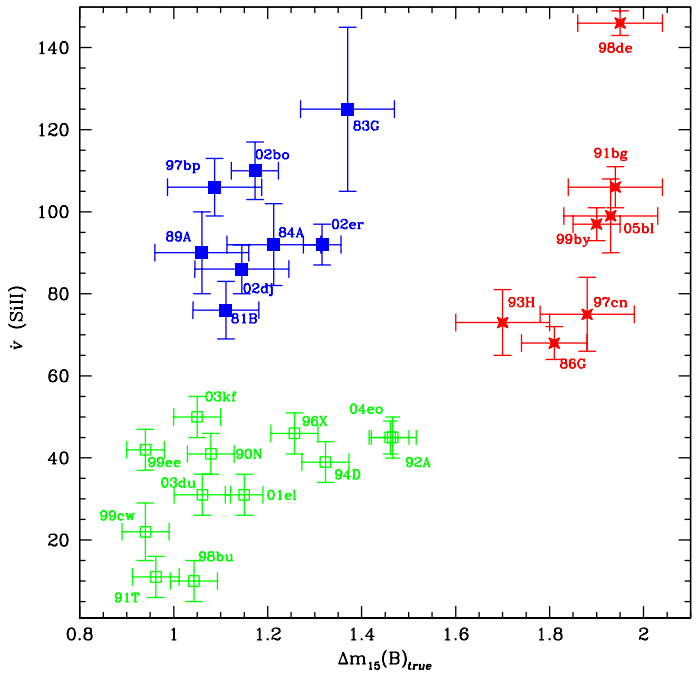

FIGURE 4.19— Si II λ6355 post-maximum velocity gradient $\dot{v}$ (Benetti et al. 2005) versus $\Delta m_{15}(B)_{\rm true}$. Filled blue squares are HVG SNe, open green squares LVG SNe, and filled red stars FAINT SNe.

parameters have been remeasured for some FAINT SNe using additional data, and SNe 1998de (Matheson et al., 2008) and 2005bl have been added.

Fig. 4.18 shows the velocity evolution of the Si II λ6355 line of SN 2005bl and a large set of comparison objects. Once more, SN 2005bl is extremely similar to SNe 1991bg, 1997cn and 1999by. Before maximum light, the Si velocities of these SNe are comparable to those of the slower members of Benetti et al.'s LVG group, but the velocity decrease is much faster. Hence, after maximum light, they have clearly the lowest expansion velocities. SN 1998de, photometrically nearly a twin of SN 2005bl, has noticeably higher expansion velocities at early phases. Whether this is caused by a high-velocity component (Mazzali et al., 2005d), by differences in the density structure, or by a higher kinetic energy is difficult to decide without detailed modelling. High-velocity features could provide a natural explanation for the observed differences without the need to change the explosion energetics. On the other hand the Si II λ6355 line of

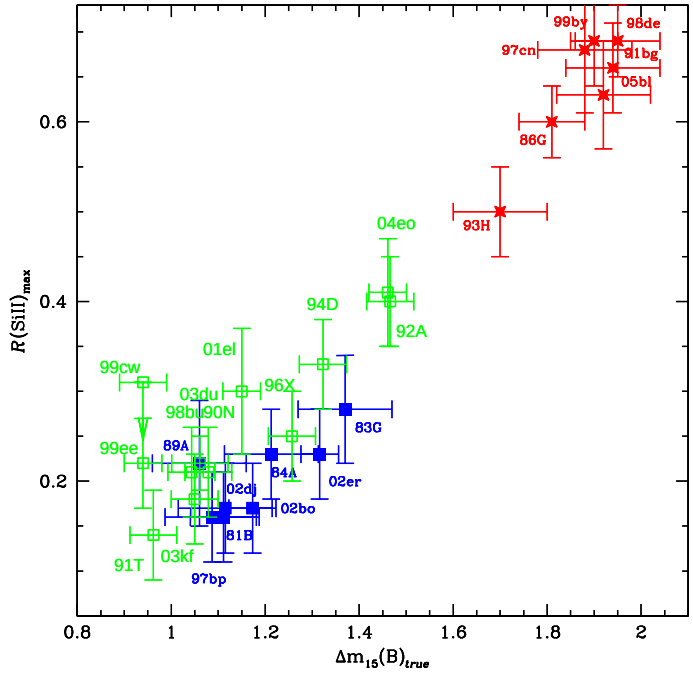

FIGURE 4.20— Si line-depth ratio $\mathcal{R}(\mathrm{Si})_{\max}$ (Nugent et al., 1995) as a function of SN decline rate $\Delta\mathrm{m}_{15}(B)_{\mathrm{true}}$. The strong correlation between these two parameters is evident. Symbols as in Fig. 4.19.

SN 1998de looks symmetric, and the velocities are higher than in other 91bg-like SNe not only at the earliest phases, but also near maximum light, when in most other SNe the high-velocity features have disappeared (Mazzali et al., 2005d; Garavini et al., 2007). Finally, the transitional SNe 1993H and 1986G have higher velocities than SN 2005bl and the other 91bg-like SNe (except SN 1998de), more similar to the LVG group. Their comparatively shallow post-maximum velocity decrease $\dot{v}$ (Benetti et al., 2005) also shows their proximity to LVG SNe.

In the $\dot{v}$ vs. $\Delta\mathrm{m}_{15}(B)_{\mathrm{true}}$ plane, FAINT SNe seem to form a separate cluster (Fig. 4.19). However, this impression may be caused by the lack of SNe with $\Delta\mathrm{m}_{15}(B)_{\mathrm{true}}$ between 1.5 and 1.7 in the Benetti et al. sample. Whether or not this gap is real is not easy to decide given the poor statistics for rapidly-declining SNe Ia. With respect to $\dot{v}$ alone, FAINT SNe are very heterogeneous, with values ranging from those typical of LVG SNe to the highest values ever

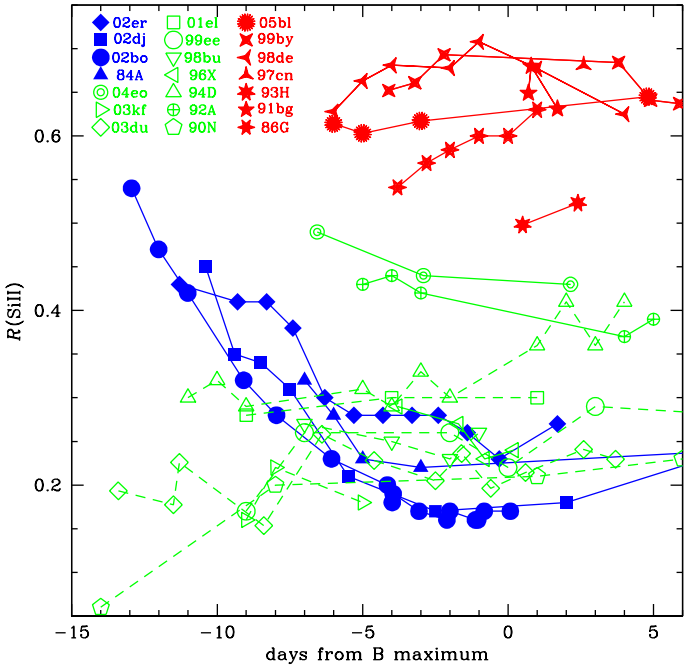

FIGURE 4.21— Time-evolution of the Nugent et al. (1995) ratio $\mathcal{R}$(Si) before and near maximum light. The same symbols as in Fig. 4.18 have been used. Interpolating lines between adjacent points have been drawn to guide the eye.

recorded in a SN Ia (for SN 1998de). The mean $\dot{v}$ of 95 ± 27 km s^{-1} d^{-1} (error statistical) is similar to that reported by Benetti et al. for HVG SNe (97 ± 16 km s^{-1} d^{-1}). Within the FAINT group there may be a tendency for higher $\dot{v}$ with larger $\Delta m_{15}(B)_{\rm true}$, but there are too few objects and their range in $\Delta m_{15}(B)_{\rm true}$ is too small to postulate a correlation.

Concerning $\mathcal{R}(\mathrm{Si})_{\rm max}$, the value of $\mathcal{R}$(Si) at B-band maximum, we confirm the observed trend of larger values for faster decliners (Fig. 4.20). The origin of this behaviour was the subject of a number of studies, as an explanation is not straightforward. Hachinger, Mazzali & Benetti (2006) have shown that the change in $\mathcal{R}(\mathrm{Si})_{\rm max}$ with $\Delta m_{15}(B)_{\rm true}$ is almost solely caused by a variation in the strength of the Si II λ5972 line, which is somewhat counter-intuitive as the excitation of this line should be favoured by higher temperatures. Garnavich et al. (2004) suggested that in underluminous SNe Ia the feature at $\sim$5800 Å might be dominated by Ti lines. However, from the synthetic spectra shown

in Section 4.6.2 we cannot confirm this option. Instead, Hachinger (2007) and Hachinger et al. (in prep.) demonstrate that the observed tendency is a combined ionisation and excitation effect, natural rather than unexpected.

The pre-maximum time-evolution of $\mathcal{R}$(Si), which was also used by Benetti et al. (2005) to distinguish between the LVG and HVG groups, cannot be studied equally well for the FAINT SNe because of the lack of sufficiently early data (more than 5 d before maximum). In fact, only before day −5 do LVG and HVG SNe show significant differences in their behaviour, $\mathcal{R}$(Si) decreasing with time for HVG SNe, and being constant or increasing slightly for LVG SNe. Near maximum light, the evolution seems to be fairly flat for all SNe Ia, including the FAINT SNe which merely exhibit larger absolute values of $\mathcal{R}$(Si) (see Fig. 4.21). However, especially the Si II λ5972 line may suffer from variable contributions of other elements, notably Na I D at later phases when the spectra become cooler. This limits the conclusive power of all studies related to the evolution of $\mathcal{R}$(Si) after maximum light, as already at day +5 Na I D is visible as a shoulder in the blue wing of the Si II λ5972 feature (cf. Section 4.5.1).

4.7.4 Element abundances from synthetic spectra

Spectrum synthesis calculations offer an insight into the chemical composition of the ejecta, making it possible to trace the nuclear reactions that took place during explosive burning. However, because of the limitations and possible shortcomings of the models mentioned in Section 4.6 (i.e., no abundance stratification, use of a Chandrasekhar-mass progenitor and of the W7 density distribution), the exact numbers in Table 4.7 should be taken with caution. Therefore, we confine ourselves to analysing clear trends, which should be robust with respect to refined models.

Unburned material, carbon detection

As for all rapidly-declining SNe Ia the spectrum of SN 2005bl is characterised by strong O I λ7774. The strength of this line is largely a temperature effect, as the comparatively low temperatures encountered in 91bg-like SNe Ia result in a fair fraction of neutral oxygen besides the singly ionised state which normally dominates the ejecta. Nevertheless, it also signals the presence of a significant amount of unburned material in the SN ejecta.[10] This is fully consistent with the often-anticipated low burning efficiency of these objects (from light curves and nebular spectra one can infer that the amount of synthesised ^{56}Ni

[10] In this section we refer to C and O as unburned, although – depending on the initial C-to-O ratio of the white dwarf – a significant fraction of the O may have been produced during the explosion by incomplete C burning.

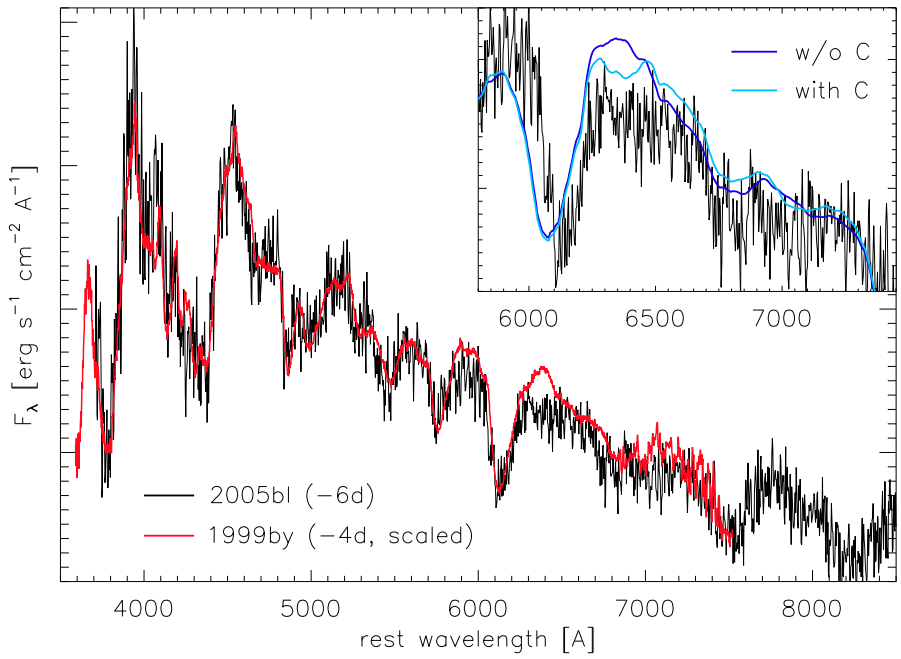

FIGURE 4.22— Identification of carbon in the spectra of SN 2005bl. A comparison of the −6 d spectrum of SN 2005bl and the −4 d spectrum of SN 1999by shows a flux deficit at 6400 Å in SN 2005bl, likely caused by C II λ6580. The insert shows synthetic spectra for day −6, one with the composition reported in Table 4.7 including 4.5% of C, the other without any C.

is $\sim 0.1\,M_\odot$, which is at most a quarter of that in normal-luminosity SNe Ia, Stritzinger et al. 2006). Direct information on the oxygen abundance is difficult to derive from synthetic spectra, since O I λ7774 is the only strong feature of this element at optical wavelengths, and is heavily saturated in all our models. Hence, moderate changes in the oxygen content have no impact on the strength of this feature. Additionally, our abundance estimate should be considered an upper limit, as, guided by nuclear reaction network calculations, we ascribe the entire mass without observable signatures to oxygen.

Applying this strategy, we find oxygen mass fractions ranging from $> 90\%$ at day −6 to $\sim 80\%$ at day +5. With a W7 density profile and photospheric velocities of 7500 and 6000 $\mathrm{km\,s^{-1}}$, about 50 and 60% of the ejecta mass are located above the photospheres at days −6 and +5, respectively. Hence, if a Chandrasekhar-mass explosion with W7 density profile provides an acceptable model for 91bg-like SNe Ia, at least the outer 50% of the ejecta of SN 2005bl and other members of this group are entirely dominated by unburned material.

These numbers are significantly different from the results obtained by modelling normal SNe Ia (cf., e.g., Stehle et al., 2005; Tanaka et al., 2007). They are also in disagreement with the picture sketched in the Zorro plot (Mazzali et al., 2007c), i.e. that all LVG and FAINT SNe Ia have about the same amount of unburned material, and that the observed spectrophotometric sequence among SNe Ia has its origin only in a variable ratio of ^{56}Ni to IMEs.

Another indication of the low burning efficiency in SN 2005bl is the likely detection of unprocessed carbon in its early spectra. Although the S/N of the -6 and -5 d spectra is low, a clear flux deficit redwards of the Si II λ6355 absorption can be discerned compared to coeval spectra of SN 1999by (Fig. 4.22).

Synthetic spectra enable us to investigate the effect of including different chemical species on this region. There are only few lines which could potentially contribute to the observed absorption.[11] Including hydrogen did not improve the model, since the resulting Hα absorption was at too short a wavelength, and Hα emission deteriorated the fit around 6500 Å. A clearly better match to the observed spectrum was obtained introducing carbon, as C II lines not only cropped the flux peak at 6400 Å through C II λ6580 (Fig. 4.22, insert), but also improved the fit in other regions, most notably around 7000 Å (through C II λ7234). Therefore, we consider the presence of a few percent of carbon in the ejecta at days -6 and -5 very likely.

The temperature and density conditions for carbon burning are more relaxed than those for oxygen burning, so that carbon is burned much more completely to heavier elements than oxygen. In fact, only in some – usually very early (~ -10 d) – optical spectra of SNe Ia have clear signatures of carbon ever been found (most prominently in SN 2006gz, Hicken et al. 2007; cf. also Branch et al. 2007a for an overview). None of these SNe was 91bg-like, although the lower burning efficiency in these objects might favour the presence of unprocessed carbon. The lack of spectra taken earlier than 5 d before maximum light may have so far prevented the detection of carbon. In SN 2005bl, however, we are confident that signatures of carbon are present less than one week before maximum. This constitutes one of the few detections of C II in SN Ia spectra at such a relatively late epoch; previous cases include SNe 1996X and 2006D (Thomas et al., 2007).

[11] Conversely, because of the relative lack of strong lines, the region around 6400 Å proved to be a preferential window for flux redistributed from shorter wavelengths to escape. All elements which create opacity in the blue and UV part of the spectrum (Fe-group elements, Ti, Cr, other metals) rather led to an increase of the 6400 Å flux excess in the model. This in turn yielded constraints on the metal abundance.

Abundance of Fe-group elements

The Fe-group abundance of SN 2005bl of $\sim 0.01\%$ at day -6 and $\sim 0.4\%$ at day $+5$ is about two orders of magnitude lower than in normal-luminosity SNe Ia at comparable epochs (see, e.g., Stehle et al. 2005; Kotak et al. 2005; Elias-Rosa et al. 2006; Altavilla et al. 2007; Tanaka et al. 2007). At a first glance this looks perfectly consistent with the low luminosity and hence the low production of ^{56}Ni and other NSE-elements in a 91bg-like SN Ia.

However, closer examination reveals that the Fe content of the pre-maximum models is significantly sub-solar. At -6 d the best-fitting model contains no Ni or Co, and only 0.010 % of stable Fe. Acceptable results were obtained with Fe abundances up to 0.025 %, but also without any Fe (see Fig. 4.23). Solar Fe abundances (the Fe mass fraction of the Sun's photosphere is about 0.115 %, Asplund et al. 2005) can safely be ruled out, as with this amount of Fe the quality of the fit deteriorates a lot around 5000 Å. Now, the Fe content deduced not only accounts for ^{54}Fe synthesised during the explosive burning (the ^{56}Ni decay chain has too long decay times to give a relevant contribution at these epochs), but also for Fe already present in the progenitor star before the explosion. Hence, a sub-solar Fe content of the precursor star might be inferred. On the other hand, SN 2005bl exploded in an elliptical galaxy, a presumably not metal-poor environment. If the chemical composition of the precursor did not deviate significantly from the average material in NGC 4070, it rather should have had a fairly high Fe abundance, and nuclear burning should have further enriched the ejecta with Fe-group elements, although this may be confined to the inner shells.

There may be two ways to explain the small amount of Fe required to fit the early-time spectra of SN 2005bl. One is to assume that Fe was not distributed homogeneously in the progenitor star, but concentrated towards the centre. A certain degree of gravitational settling of heavier elements can indeed be expected. Estimating whether or not this effect is sufficient to yield Fe abundances in accordance to those inferred from the synthetic spectra would require a model of gravitational diffusion inside the white dwarf, and accurate constraints on the mass accretion rate from the companion and the composition of the accreted material. Note, however, that assuming $v_{\rm ph} = 7500$ km s^{-1} and a W7 density profile (as we did in our model) the photosphere at day -6 is not located in the outermost layers, but half the way down the ejecta in mass coordinates.

Alternatively, the progenitor of SN 2005bl might have had a metallicity truly lower than the average metallicity of an elliptical galaxy. This could be explained if the progenitor was rather old (~ 10 Gyr), formed before the ISM

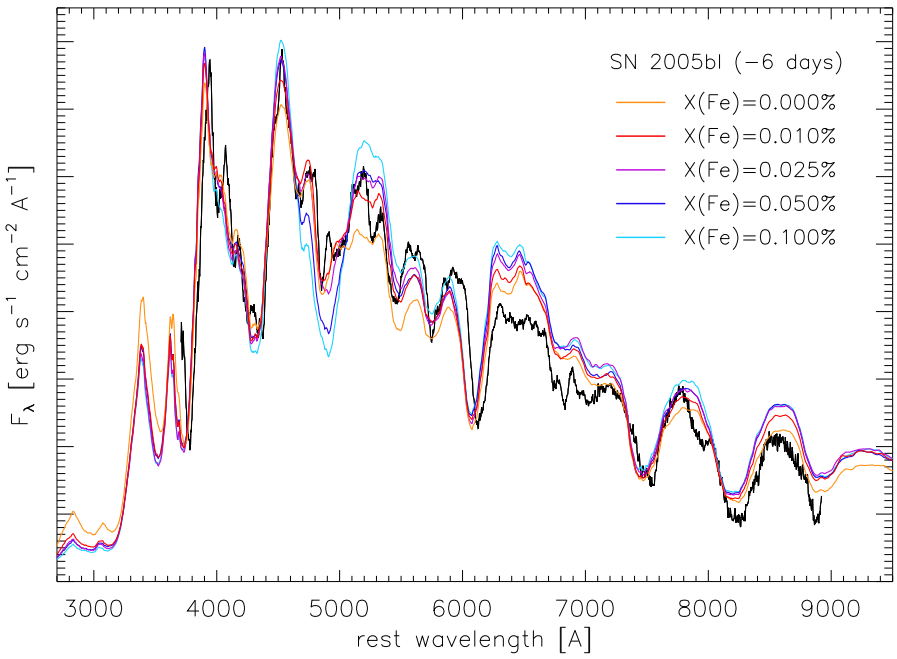

FIGURE 4.23— Sequence of synthetic spectra, varying the mass fraction of Fe between 0 to 0.1 % (the latter roughly represents solar Fe abundance). The observed but smoothed −6 d spectrum is shown in black. The parameters of the best-fitting spectrum [with X(Fe) = 0.01 %] are summarised in Table 4.7. The other spectra have been obtained by changing only the amount of stable Fe at the expense of O, the most abundant element, without attempting to optimise the fit by adapting other parameters. Hence, better fits might be feasible also for the models with X(Fe) ≠ 0.01 %.

in NGC 4070 was metal-enriched through recurrent cycles of stellar birth, mass loss and death. If this scenario held true, it would provide one of the first direct constraints on the lifetime of an individual SN Ia progenitor. Given the spectroscopic similarity of SN 2005bl to SNe 1991bg, 1997cn, 1998de and 1999by, and given that most of the latter SNe also exploded in early-type, supposedly metal-rich galaxies (see Table 4.8), this could point towards a very long-lived progenitor population for *all* underluminous, 91bg-like SNe Ia.

A speculation could be that 91bg-like SNe Ia descend from white-dwarf mergers (DD scenario). White-dwarf binary systems should meet the requirement of long lifetimes because of the low efficiency of angular-momentum loss through gravitational-wave emission. In fact, in a study of the delay-time distribution of SNe Ia, Greggio (2005) identified initially wide white-dwarf pairs as the only progenitor model whose delay-time distribution does not drop dramat-

ically beyond ~ 8 Gyr. Models of Kobayashi et al. (1998) lend further support to the DD scenario, as they predict that no SNe Ia should occur in SD systems for [Fe/H] ≤ -1, a limit which may be exceeded by SN 2005bl. Finally, from spectropolarimetric observations of SN 1999by Howell et al. (2001) inferred a degree of asphericity much higher than in ordinary SNe Ia. On this basis they identified rapidly rotating white dwarfs and merging white-dwarf binaries as the most promising progenitor candidates for 91bg-like SNe Ia. A different progenitor system with respect to ordinary SNe Ia (for which the SD scenario consisting of a white dwarf and a non-degenerate companion is favoured), including the possibility that the mass is different from $M_{\rm Ch}$, could account for observed differences in the photometric and spectroscopic properties of 91bg-like SNe.

4.8 Conclusions

We have presented and analysed optical photometric and spectroscopic data of the underluminous Type Ia SN 2005bl from one week before to two months after maximum light in B. In this entire interval the evolution of SN 2005bl is substantially different from that of slow or intermediate decliners, but very similar to that of the prototypical fast decliners SNe 1991bg and 1999by. At peak, SN 2005bl appears slightly more luminous than the latter, but the difference is marginal and within the error bars, which for SN 2005bl are dominated by uncertainties in the amount of host-galaxy extinction. With respect to quantities like the $\Delta {\rm m}_{15}(B)_{\rm true}$ of 1.93, the ejecta velocities inferred from the minimum of the Si II λ6355 line, and temperature indicators such as $\mathcal{R}$(Si) or the time-evolution of various colour indices, SN 2005bl is in fact – within the measurement uncertainties – a clone of SNe 1991bg and 1999by.

We confirm that $\Delta {\rm m}_{15}(B)_{\rm true}$ is a good luminosity indicator also for underluminous SNe Ia, with a steeper dependence of the peak magnitudes on $\Delta {\rm m}_{15}(B)_{\rm true}$ than for slow and intermediate decliners. From linear fits we obtain $\frac{{\rm d(M_{peak})}}{{\rm d}[\Delta {\rm m}_{15}(B)_{\rm true}]} = 6.83 \pm 0.32$ and 4.33 ± 0.31 for the B and V band, respectively, considering objects with $\Delta {\rm m}_{15}(B)_{\rm true} \geq 1.69$.

We conducted an analysis analogous to that of Benetti et al. (2005), focussing on the behaviour of the FAINT subclass and trying to identify trends within this group. In addition to the SNe in Benetti et al. we not only added the measurements of SN 2005bl, but also included SN 1998de (Modjaz et al., 2001; Matheson et al., 2008) and updated some numbers on the basis of better data availability. We find a correlation between $\Delta {\rm m}_{15}(B)_{\rm true}$ and $\mathcal{R}({\rm Si})_{\rm max}$, nicely extending the observed linear trend among HVG and LVG SNe to larger decline rates. Because of the lack of early data, the time-evolution of $\mathcal{R}$(Si) at phases where differences between the LVG and HVG groups become evident

cannot be investigated. The Si II line velocities of FAINT SNe are mostly similar to those of LVG SNe near maximum light, but significantly lower a few weeks later. There is a large dispersion in post-maximum velocity gradients $\dot{v}$ within the FAINT class, with numbers comparable to those of HVG SNe, but exceeding their range in both directions.

Synthetic spectra for SN 2005bl at four epochs before and soon after maximum light have been computed using a 1D Monte Carlo code. Despite uncertainties and shortcomings such as the poorly-constrained rise time, the possible inadequacy of the W7 density profile for 91bg-like SNe Ia, and the fact that computations were performed without chemical stratification, a number of interesting results were obtained. The presence of carbon in the -6 and -5 d spectra, indicated by a visual comparison with SN 1999by at similar epoch, was confirmed, and an overall low burning efficiency was established. NSE elements, but also IMEs, are significantly less abundant than in ordinary SNe Ia; instead, most of the ejecta above 6000 km s^{-1} are made of oxygen, and are hence either unburned or the result of highly incomplete carbon burning. Furthermore, in the -6 and -5 d spectra only traces of Fe are found, one order of magnitude less than expected for unprocessed material with solar composition. Possible implications of this low metallicity on the nature of the progenitor were discussed in Section 4.7.4.

It is presently very difficult to decide whether 91bg-like SNe Ia form a separate group, distinct from ordinary SNe Ia and possibly descending from different progenitors or explosion mechanisms, or whether they are just the extreme end of a continuous distribution of objects, with their characteristic appearance owing to lower temperatures in conjunction with a different chemical composition, both caused by the overall low burning efficiency. To tackle this problem will require a new statistical analysis similar to that of Benetti et al. (2005) once a bigger sample of rapidly-declining SNe Ia will be available, and more detailed spectral modelling of the data sets already published.

Stripped-envelope core-collapse Supernovae

5

SN 2004aw: Diversity in Type Ic Supernovae

Optical and near-infrared observations of the Type Ic supernova 2004aw are presented in this chapter, obtained from day -3 to day $+413$ with respect to the B-band maximum. The photometric evolution is characterised by a comparatively slow post-maximum decline of the light curves. The peaks in redder bands are significantly delayed relative to the bluer bands, the I-band maximum occurring 8.4 days later than that in B. With an absolute peak magnitude of -18.02 in the V band the SN can be considered fairly bright, but not exceptional. This also holds for the U through I bolometric light curve, where SN 2004aw has a position intermediate between SNe 2002ap and 1998bw. Spectroscopically SN 2004aw provides a link between a normal-energetic Type Ic SN like SN 1994I and the group of broad-lined SNe Ic. The spectral evolution is rather slow, with a spectrum at day +64 being still predominantly photospheric. The shape of the nebular [O I] $\lambda\lambda 6300, 6364$ line indicates a highly aspherical explosion. Helium cannot be unambiguously identified in the spectra, even in the near-infrared. Using an analytical description of the light curve peak we find that the total mass of the ejecta in SN 2004aw is $3.5-8.0\,M_\odot$, significantly larger than in SN 1994I, although not as large as in SN 1998bw. The same model suggests that about $0.3\,M_\odot$ of ^{56}Ni has been synthesised in the explosion. No connection to a GRB can be firmly established. The content of this chapter has already been published by Taubenberger et al. (2006).

5.1 Introduction

Historically, only a subdivision of supernovae into Type II (with hydrogen lines in the spectra) and Type I (without hydrogen) was known (Minkowski, 1941). The sample of Type I SNe was dominated by SNe Ia and

known to be quite homogeneous in its spectrophotometric appearance. Objects deviating in their spectral features (e.g., by the absence of a strong Si II λ6355 line) or absolute luminosity were simply called 'Type I peculiar' (Wheeler & Levreault, 1985; Uomoto & Kirshner, 1985). It was not before the mid 1980s that the advances in detector technology and the increasing SN sample made fundamental differences among Type I SNe evident. Elias et al. (1985) suggested a subdivision into SNe Ia (thermonuclear) and SNe Ib which, at that time, encompassed the modern Type Ib and Ic classes, and were correctly attributed to core-collapse explosion of envelope-stripped massive progenitors (Filippenko & Sargent, 1986; Gaskell et al., 1986; Harkness et al., 1987; Filippenko, 1988). An important contribution to this process was provided by late-phase observations of the nearby SNe 1985F and 1983N (Filippenko & Sargent, 1986; Gaskell et al., 1986), whose spectra were dominated by forbidden lines of [O I], [Ca II] and Mg I] rather than the [Fe II] lines known to be characteristic of the nebular spectra of the normal Type I(a) SN 1972E (Kirshner & Oke, 1975). Later, a further subdivision into SNe Ib and SNe Ic was introduced by Filippenko et al. (1990), after Wheeler et al. (1987) had noticed the variety of He line strengths among the objects constituing the former SN Ib class.

However, over the subsequent years only a few observational efforts were made to further constrain the nature and properties of Type Ib/c SNe. Exceptions were SN 1987M (Filippenko et al., 1990; Nomoto et al., 1990; Jeffery et al., 1991; Swartz et al., 1991), SN 1990U, SN 1990aa, and SN 1991A (Filippenko, 1992; Gómez & López, 1994), and especially SN 1994I (e.g. Filippenko et al., 1995a; Richmond et al., 1996) whose spectrophotometric evolution was studied in great detail at various frequencies. For some other SNe Ic, like SN 1983V (Clocchiatti et al., 1997) and SN 1990B (Clocchiatti et al., 2001), extensive data sets were obtained, but their publication took some time and coincided with the new boom in SN Ic research, which set in with the discovery of SN 1997ef (Garnavich et al., 1997a,b,c; Iwamoto et al., 2000; Mazzali et al., 2000) and SN 1998bw (Galama et al., 1998; Patat et al., 2001). These objects showed extremely broad spectral features owing to an unusually high kinetic energy of their ejecta, and therefore were labelled as 'hypernovae'. Also, the collection of SN Ib/c spectra published by Matheson et al. (2001) and efforts to model spectra of SNe Ib/c by Branch et al. (2002) and Elmhamdi et al. (2006) might be considered expressions of the new enthusiasm in this field.

In the following years, several more broad-lined SNe Ic (hereafter BL-SNe) were discovered. Unfortunately, a specific and generally accepted definition of the term 'hypernova' could not be established; instead, several different definitions were used in parallel, creating considerable confusion. Probably the most commonly adopted definition is that of Nomoto et al. (2003, 2005) and Mazzali

et al. (2005a), who refer to hypernovae as core-collapse SNe with a total kinetic energy of the ejecta larger than 10^{52} erg, about an order of magnitude larger than in ordinary SNe Ic like SN 1994I. However, others use hypernova as a synonym for a jet-induced SN connected to a GRB as predicted by the collapsar model (Paczyński, 1998a,b; MacFadyen & Woosley, 1999). In addition, a classification based on observationally accessible quantities such as the width of spectral features (Mazzali et al., 2002; Pandey et al., 2003a) or the luminosity (Brown et al., 2000) can be found in the literature. Because of this ambiguity, we avoid the use of the term hypernova and rather concentrate on the observable discrimination of SNe Ic into normal-velocity and broad-lined events on the basis of spectra obtained near the time of optical maximum brightness.

Some of the SNe Ic discovered so far could be linked to GRBs, while for the majority there is apparently no association. Thus far, the precise mechanism connecting GRBs with SNe is not fully understood. In particular, it is not clear how the occurrence of a GRB accompanying a SN explosion could be inferred, if the former is directed away from the observer, so that neither γ-rays nor X-rays are detected. Given the relatively small number of well-observed SNe Ic or BL-SNe to date, every additional object with good photometric and spectroscopic coverage may help to improve the picture of stripped-envelope core-collapse SNe and their relation to GRBs. This is the context of the observing campaign conducted on SN 2004aw.

SN 2004aw ($z = 0.0163$) was discovered independently by Boles & Itagaki (2004) on UT 2004 March 19.85 and 20.51, respectively. After an initial classification as a SN Ia (Matheson, Challis & Kirshner 2004; Benetti et al. 2004a), it was reclassified as a SN Ic (Filippenko et al., 2004). The SN is located at $\alpha = 11\mathrm{h}\,57\mathrm{m}\,50.25\mathrm{s}$ and $\delta = +25°15'55\farcs1$, in the outskirts of NGC 3997, a barred spiral (SBb) galaxy and multiple system (LEDA). Van den Bergh, Li & Filippenko (2005) note that NGC 3997 is a merger system of two spiral galaxies showing tidally deformed spiral arms.

After discovery and classification, the European Supernova Collaboration and the Berkeley Supernova group started follow-up observations in the optical and infrared at various telescopes. We present the entire set of data obtained for SN 2004aw in Section 5.2. In Section 5.3 we estimate the distance of SN 2004aw and the extinction along the line of sight toward it. Sections 5.4 and 5.5 are devoted to the analysis of the light curves and spectra, respectively. Conclusions are drawn and their impact on the connection between ordinary SNe Ic, BL-SNe, and GRBs is discussed in Section 5.6, followed by a short summary in Section 5.7. Synthetic light curves and spectra will be presented in separate papers (Deng et al. in prep.; Baklanov et al. in prep.).

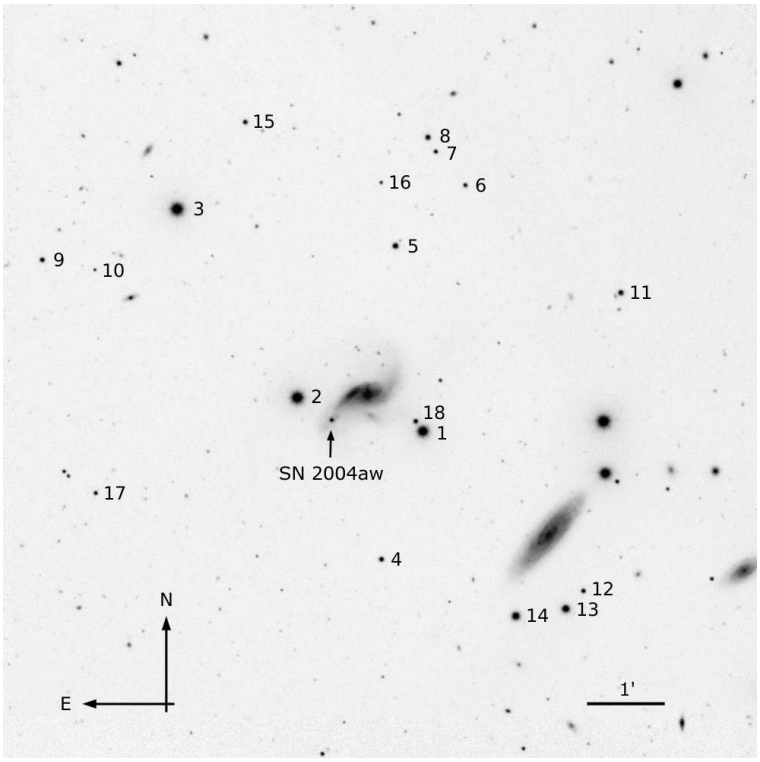

FIGURE 5.1— J band image of the SN 2004aw field taken with the Calar Alto 3.5 m Telescope + OMEGA 2000 on UT 2004 April 6. The local sequence stars are marked.

5.2 Observations

5.2.1 Photometric observations

Imaging observations of SN 2004aw were acquired from 3 days before to almost 1 year after maximum light (which in B occured on JD $2\,453\,088.4 \pm 0.5$), with dense sampling during the first 2 months. The data were reduced and calibrated as explained in Chapter 2.3.2, including the calibration of a sequence of stars in the field of the SN (cf. Fig. 5.1 and Table 5.1) as photometric reference, template subtraction for all KAIT images, and the measurement of the SN magnitudes employing the PSF-fitting technique.

IR photometry in the JHK' bands was also obtained. The observations range from approximately 10 to 29 days after maximum light. The photometric reference stars were the same as for optical wavelengths, complemented by four additional red stars (Fig. 5.1 and Table 5.1).

To compensate for instrumental response curves deviating from the stan-

TABLE 5.1— Magnitudes of local sequence stars in the field of SN 2004aw (Fig. 5.1).[a]

ID	U	B	V	R	I	J	H	K'
1		13.67 ± 0.01	13.01 ± 0.01	12.64 ± 0.01	12.40 ± 0.01			
2		13.43 ± 0.01	12.67 ± 0.01	12.27 ± 0.01	11.99 ± 0.01			
3		13.62 ± 0.01	12.71 ± 0.02	12.21 ± 0.01	11.79 ± 0.01			
4	20.77 ± 0.04	19.44 ± 0.01	18.09 ± 0.01	17.20 ± 0.01	16.38 ± 0.01	15.27 ± 0.06	14.68 ± 0.05	14.53 ± 0.04
5	19.85 ± 0.04	18.48 ± 0.01	17.17 ± 0.02	16.30 ± 0.03	15.55 ± 0.02	14.58 ± 0.08	13.94 ± 0.07	13.85 ± 0.09
6		20.47 ± 0.03	18.93 ± 0.02	17.93 ± 0.02	16.91 ± 0.01	15.74 ± 0.04	15.12 ± 0.08	15.03 ± 0.06
7	17.61 ± 0.04	17.77 ± 0.02	17.27 ± 0.01	16.95 ± 0.02	16.64 ± 0.02	16.23 ± 0.03	15.93 ± 0.07	16.00 ± 0.05
8		19.93 ± 0.01	18.41 ± 0.01	17.34 ± 0.02	16.19 ± 0.02	14.95 ± 0.04	14.34 ± 0.05	14.23 ± 0.06
9	17.06 ± 0.05	17.22 ± 0.03	16.68 ± 0.02	16.28 ± 0.03	15.93 ± 0.03	15.52 ± 0.03	15.21 ± 0.03	15.22 ± 0.04
10	21.00 ± 0.06	19.98 ± 0.06	19.04 ± 0.02	18.44 ± 0.02	17.94 ± 0.05			
11	19.24 ± 0.05	18.11 ± 0.04	16.95 ± 0.03	16.28 ± 0.03	15.75 ± 0.04	14.81 ± 0.04	14.22 ± 0.04	14.15 ± 0.03
12	18.04 ± 0.02	17.82 ± 0.01	17.08 ± 0.01	16.70 ± 0.02	16.30 ± 0.02	15.64 ± 0.04	15.32 ± 0.03	15.24 ± 0.06
13	16.38 ± 0.02	15.66 ± 0.02	14.76 ± 0.01	14.30 ± 0.02	13.88 ± 0.02	13.16 ± 0.02	12.80 ± 0.04	12.77 ± 0.03
14	18.91 ± 0.02	17.63 ± 0.01	16.13 ± 0.02	15.16 ± 0.01	14.18 ± 0.02			
15						15.48 ± 0.03	14.90 ± 0.05	14.76 ± 0.04
16						16.95 ± 0.04	16.37 ± 0.08	16.29 ± 0.11
17						16.09 ± 0.02	15.48 ± 0.08	15.39 ± 0.05
18						15.37 ± 0.04	14.73 ± 0.05	14.60 ± 0.05

[a]The optical data for stars 4 to 14 were obtained on 9 photometric nights using CAFOS, DOLORES, and PFIP, while stars 1, 2, and 3 were calibrated with KAIT images relative to the rest of the sequence. In the near-IR, all nights were used to calibrate the stars.

TABLE 5.2— IR photometry of SN 2004aw.[a]

Date	JD −2 453 000	Epoch[b] (days)	J	H	K'	Tel.	Seeing[c] (arcsec)
04/04/02	98.6	10.2	15.98±0.06	15.78±0.06	15.65±0.08	TNG	0.96
04/04/06	102.6	14.2	15.88±0.03	15.79±0.06	15.64±0.07	Caha	1.35
04/04/07	103.6	15.2	15.87±0.06	15.80±0.06	15.72±0.06	Caha	1.06
04/04/13	109.4	21.0	15.92±0.03	15.86±0.04	15.72±0.07	Caha	0.96
04/04/21	117.4	29.0	16.25±0.09	15.99±0.14	15.95±0.13	TNG	0.96

[a] The magnitudes are not corrected for interstellar extinction.
[b] Epoch with respect to the estimated B-band maximum JD 2 453 088.4 ± 0.5.
[c] Average seeing of all filters.

TNG = Telescopio Nazionale Galileo + NICS
Caha = Calar Alto 3.5 m Telescope + OMEGA 2000

dard Bessell (1990) passbands, an S-correction was applied to the optical data between maximum light and +36 d (B and V bands) or +57 d (R and I bands). While the corrections were mostly small in the V and R filters, they were more significant in B and I, improving the coherence of the light curves in these bands.

The final apparent magnitudes for SN 2004aw are reported in Tables 5.2 (near IR) and 5.3 (optical), together with their uncertainties, computed as the sum in quadrature of the measurement errors of the instrumental SN magnitudes and the error associated with the photometric zero point of the night.

5.2.2 Spectroscopic observations

The spectroscopic observations of SN 2004aw are reported in Table 5.4. Before the SN started its transition to the nebular phase at ~ 2 months from maximum light, its evolution was densely sampled at optical wavelengths. During the nebular phase, the SN was recovered and three additional spectra were taken at phases between 236 and 413 d after maximum. Moreover, 29 d after maximum light two IR spectra were obtained. The one taken with the TNG/Amici prism covers the full wavelength range from the I through K bands, but has extremely low resolution (*fwhm* of night-sky lines $\approx 60 - 200$ Å). The other, taken at UKIRT, has rather poor S/N.

5.3 Distance and Extinction

This section deals with two aspects that turn out to represent the largest source of uncertainty in the absolute calibration of the SN 2004aw data. Neither

TABLE 5.3— Optical photometry of SN 2004aw.[a]

UT Date	JD −2 453 000	Epoch[b] (days)	U	B	V	R	I	Telescope	Seeing[c] (arcsec)
04/03/21	85.8	−2.6		18.12±0.04	17.47±0.04	17.19±0.04	16.97±0.05	KAIT	2.24
04/03/23	87.8	−0.6		18.08±0.03	17.36±0.04	17.07±0.02	16.77±0.03	KAIT	2.64
04/03/24	88.8	0.4		18.06±0.12	17.32±0.11	16.97±0.06	16.78±0.11	KAIT	2.58
04/03/24[d]	89.4	1.0	18.18±0.06	18.07±0.06	17.29±0.04	17.01±0.04	16.71±0.04	TNG	1.38
04/03/26	90.9	2.5			17.31±0.03	16.93±0.06	16.63±0.04	KAIT	2.69
04/03/28	92.8	4.4		18.38±0.07	17.32±0.04	16.91±0.04	16.60±0.04	KAIT	3.90
04/03/28	93.1	4.7	18.38±0.11	18.24±0.06	17.31±0.03	16.87±0.03	16.52±0.02	SSO	2.62
04/03/29	93.8	5.4		18.39±0.04	17.35±0.04	16.92±0.04	16.54±0.04	KAIT	2.44
04/03/29	94.1	5.7	18.55±0.05	18.35±0.05	17.37±0.06	16.91±0.04	16.54±0.07	SSO	2.20
04/03/29	94.5	6.1		18.42±0.11	17.44±0.06	16.99±0.06	16.54±0.06	Ekar	3.16
04/03/30	94.8	6.4		18.43±0.10	17.33±0.06	16.91±0.07	16.53±0.07	KAIT	2.48
04/03/30	95.5	7.1		18.52±0.10	17.38±0.06	16.88±0.04	16.43±0.05	WD	1.57
04/03/30	95.5	7.1			17.43±0.16		16.54±0.06	NOT	0.75
04/03/31	95.8	7.4		18.53±0.08	17.43±0.06	16.92±0.03	16.54±0.04	KAIT	2.32
04/03/31	96.5	8.1	18.95±0.09	18.58±0.04	17.32±0.05	16.85±0.04	16.40±0.05	NOT	0.96
04/04/01	96.8	8.4		18.56±0.12	17.44±0.05	16.95±0.04	16.56±0.05	KAIT	3.08
04/04/01	97.4	9.0		18.81±0.08	17.34±0.08	16.88±0.03	16.42±0.03	WD	1.82
04/04/07	102.8	14.4			17.69±0.06	17.04±0.04	16.58±0.04	KAIT	2.44
04/04/07	103.3	14.9		19.14±0.05	17.71±0.05	17.07±0.05	16.59±0.05	Caha	1.34
04/04/07[d]	103.5	15.1	19.81±0.18	19.25±0.08	17.73±0.11	17.04±0.05	16.56±0.10	TNG	1.93
04/04/09	104.8	16.4		19.25±0.07	17.82±0.03	17.10±0.05	16.65±0.03	KAIT	2.24
04/04/12	107.8	19.4		19.47±0.11	18.02±0.15	17.26±0.05	16.71±0.05	KAIT	2.74
04/04/12	108.3	19.9		19.49±0.06	17.97±0.03	17.23±0.03	16.71±0.03	Caha	1.47
04/04/13[d]	109.6	21.2		19.54±0.11	18.01±0.04	17.27±0.04	16.74±0.04	Caha	1.91
04/04/14[d]	110.4	22.0		19.60±0.03	18.07±0.03	17.33±0.04	16.77±0.05	Caha	1.14
04/04/16	111.8	23.4		19.67±0.12	18.15±0.05	17.41±0.04	16.88±0.03	KAIT	2.84
04/04/17	113.4	25.0		19.77±0.15	18.22±0.07	17.49±0.06	16.93±0.05	Caha	3.70
04/04/18	114.5	26.1	20.81±0.08	19.95±0.04	18.30±0.03	17.55±0.03		NOT	0.86
04/04/20	116.4	28.0	20.91±0.06	19.96±0.06	18.35±0.03	17.61±0.03	17.00±0.03	NOT	0.69

TABLE 5.3— *continued.* Optical photometry of SN 2004aw.[a]

UT Date	JD −2 453 000	Epoch[b] (days)	U	B	V	R	I	Telescope	Seeing[c] (arcsec)
04/04/20	116.4	28.0		19.99±0.05	18.42±0.04	17.65±0.03	17.03±0.04	Caha	1.09
04/04/21	117.4	29.0		20.17±0.15	18.44±0.05	17.67±0.07	17.03±0.07	Ekar	2.30
04/04/21	117.5	29.1		20.02±0.05	18.46±0.04	17.68±0.04	17.05±0.05	Caha	1.57
04/04/22	118.6	30.2		20.04±0.09	18.47±0.07	17.71±0.07	17.08±0.04	Caha	2.92
04/04/23[d]	119.4	31.0		20.09±0.09	18.52±0.06	17.74±0.04	17.12±0.05	Caha	1.84
04/04/24	119.8	31.4		20.05±0.11	18.57±0.07	17.78±0.05	17.15±0.05	KAIT	2.46
04/04/24[d]	120.5	32.1	20.88±0.14	20.14±0.05	18.58±0.04	17.80±0.03	17.13±0.03	Caha	1.35
04/04/25[d]	121.5	33.1		20.20±0.07	18.64±0.03	17.83±0.03	17.16±0.04	Caha	1.30
04/04/29	124.8	36.4		20.49±0.43	18.86±0.20	17.99±0.06	17.29±0.08	KAIT	3.18
04/05/04	129.8	41.4		20.37±0.41	18.75±0.11	18.05±0.08	17.33±0.06	KAIT	2.68
04/05/06[d]	132.5	44.1	21.43±0.13	20.53±0.06	18.97±0.04	18.15±0.02	17.52±0.04	TNG	1.05
04/05/09	134.8	46.4		20.47±0.19	19.01±0.09	18.25±0.08	17.53±0.06	KAIT	2.54
04/05/11[d]	137.4	49.0	21.44±0.13	20.63±0.07	19.09±0.03	18.29±0.02	17.62±0.03	WHT	1.38
04/05/13	138.7	50.3		20.51±0.17	19.05±0.08	18.31±0.06	17.59±0.06	KAIT	2.20
04/05/13	139.4	51.0		20.65±0.11	19.16±0.05	18.32±0.04		Ekar	2.06
04/05/20	145.7	57.3			19.15±0.07	18.44±0.05	17.77±0.09	KAIT	2.08
04/05/27	152.7	64.3			19.32±0.16	18.63±0.10	17.81±0.10	KAIT	2.18
04/06/03	159.7	71.3			19.33±0.25	18.57±0.12	17.91±0.08	KAIT	2.68
04/12/06	346.7	258.3	> 23.3	23.45±0.34	22.70±0.37	21.26±0.23	20.84±0.12	TNG	1.43
05/03/06	436.7	348.3		> 24.0		22.27±0.44		VLT	1.76

[a] The magnitudes are S-corrected, but not corrected for interstellar extinction.
[b] Epoch with respect to the estimated B-band maximum JD 2 453 088.4 ± 0.5.
[c] Average seeing of all filters.
[d] Night used to calibrate a local sequence.

KAIT = 0.76 m Katzman Automated Imaging Telescope + CCD; TNG = 3.58 m Telescopio Nazionale Galileo + DOLORES; SSO = Siding Spring Observatory 2.3 m Telescope + imager; Ekar = Asiago 1.82 m Telescope + AFOSC; WD = 0.8 m Wendelstein Telescope + MONICA; NOT = 2.5 m Nordic Optical Telescope + ALFOSC; Caha = Calar Alto 2.2 m Telescope + CAFOS SiTe; WHT = 4.2 m William Herschel Telescope + PFIP; VLT = ESO 8.2 m Very Large Telescope + FORS2

TABLE 5.4— Spectroscopic observations of SN 2004aw.

Date	JD −2 453 000	Epoch[a] (days)	Airmass	Telescope	Grism / Grating	Range (Å)	Resolution[b] (Å)	Standards
04/03/24	89.4	1.0	1.21	TNG-D	LR-B + LR-R	3200 – 9200	12	Feige56
04/03/28	93.0	4.6	1.83	SSO	grt300 + grt316	3650 – 9000	5	Feige56, Cd329927
04/03/29	94.0	5.6	1.85	SSO	grt300 + grt316	3650 – 9000	5	Feige56, L745-46
04/03/29	94.5	6.1	1.26	Ekar	gm 4	3800 – 7700	24	
04/03/31	96.5	8.1	1.01	NOT	gm 4	3500 – 8900	14	Feige67
04/04/07	103.5	15.1	1.01	TNG-D	LR-B + LR-R	3500 – 9400	14	Hd93521
04/04/13	109.5	21.1	1.06	Caha	b200 + r200	3550 – 9200	10	Feige66
04/04/14	110.5	22.1	1.04	Caha	b200 + r200	3500 – 9600	10	Feige66
04/04/18	114.5	26.1	1.21	NOT	gm 4	3650 – 8900	13	
04/04/20	116.4	28.0	1.12	Caha	b200 + r200	3500 – 9400	10	Feige66
04/04/21	116.8	28.4	1.01	UKIRT	gm *HK*	13700 – 24500	34	BS4501 (F4V)
04/04/21	117.4	29.0	1.16	TNG-N	Amici prism	7500 – 25000	60-200	AS24-0 (A0)
04/04/21	117.4	29.0	1.26	Ekar	gm 4	3800 – 7700	24	Bd+332642
04/04/22	118.4	30.0	1.26	Ekar	gm 2	5200 – 9400	75	Bd+332642
04/04/27	123.5	35.1	1.26	Caha	b200	3800 – 8650	12	Feige66
04/05/06	132.4	44.0	1.05	TNG-D	LR-R	4950 – 9400	11	Feige56
04/05/12	137.8	49.4	1.21	Lick	gm600 + grt300	5200 – 9600	5/11	Feige34, HD84937
04/05/25	151.4	63.0	1.54	Ekar	gm 2	5200 – 9200	75	
04/05/27	152.8	64.4	1.45	Lick	grt600	4000 – 6650	8	HD84937
04/11/14	324.1	235.7	1.50	Keck	gm400 + grt400	3750 – 9300	6	Feige34, Bd+174708
04/12/08	348.8	260.4	1.08	TNG-D	LR-B	3800 – 7950	15	GD140
05/05/11	501.8	413.4	1.04	Keck	gm400 + grt400	5450 – 9200	6	Feige34, HD84937

[a] Relative to B-band maximum (JD = 2 453 088.4).
[b] Full-width at half maximum of isolated, unblended night-sky lines.

TNG-D = 3.58 m Telescopio Nazionale Galileo + DOLORES; TNG-N = 3.58 m Telescopio Nazionale Galileo + NICS; SSO = Siding Spring Observatory 2.3 m Telescope + DBS; NOT = 2.5 m Nordic Optical Telescope + ALFOSC; Caha = Calar Alto 2.2 m Telescope + CAFOS SiTe; Ekar = Asiago 1.82 m Telescope + AFOSC; UKIRT = 3.8 m United Kingdom Infrared Telescope + UIST; Lick = Shane 3 m Reflector + KAST; Keck = Keck 10 m Telescope + LRIS

Cepheid distances nor other similarly precise distance measurements are available for NGC 3997, the host galaxy of SN 2004aw. Therefore, the redshift is the only indicator of its distance. LEDA reports a recession velocity of 4769 km s^{-1} inferred mainly from radio measurements, which increases to 4906 km s^{-1} when a correction for the Local-Group infall onto the Virgo cluster is applied. The recession velocities of the other members of the small galaxy cluster to which NGC 3997 belongs show only little dispersion (approximately $\pm$250 km s^{-1} around an average Local-Group infall corrected value of 4700 km s^{-1}). Thus, assuming 500 km s^{-1} as an upper limit for the peculiar motion seems conservative, and we adopt this value for the uncertainty in determining the distance from the Hubble law. Using $v_{\rm rec} = 4906$ km s^{-1} and $H_0 = 72$ km s^{-1} Mpc^{-1}, this implies a distance modulus of $\mu = 34.17 \pm 0.23$ mag.

The uncertainty associated with the amount of extinction must be considered the dominant source of error in the calibration of the SN 2004aw data. Based on our current knowledge from a very limited set of well-observed nearby objects, SNe Ic have very heterogeneous observed properties. Hence, in contrast to SNe Ia (e.g. Phillips et al., 1999) and to a certain degree also SNe IIP (Hamuy et al., 2003; Pastorello, 2003), it is not possible to infer the amount of reddening from light curves or colour curves of SNe Ic, so that (apart from spectral modelling) the only possibility of getting an estimate of the extinction along the line of sight towards SN 2004aw is by relating the equivalent width (EW) of the interstellar Na I D lines in the spectrum to the colour excess. This procedure suffers from the entirely unknown composition of the dust, and in particular the unconstrained gas-to-dust ratio of the extinguishing material. In addition, the lines might be saturated, which is impossible to be verified in low-resolution spectra.

For SN 2004aw we find a moderately strong Na I D line at the redshift of the host galaxy, and in some high-S/N spectra a weak line at its rest wavelength is also visible. The equivalent widths were determined to be 2.17 ± 0.11 Å and 0.65 ± 0.03 Å, respectively (errors are only statistical). Using

$$E(B-V) \;=\; 0.16 \times \mathrm{EW(Na\,I\,D)} \tag{5.1}$$

(Turatto et al., 2003), this implies a reddening $E(B-V) = 0.35 \pm 0.02$ mag in NGC 3997, and a Galactic reddening of $E(B-V) = 0.10 \pm 0.01$ mag. The value for the Galactic contribution is inconsistent with the colour excess of $E(B-V) = 0.021$ mag reported by Schlegel et al. (1998) for the direction towards NGC 3997. The discrepancy could either be attributed to small-scale variations in the dust distribution of the Milky Way, to scatter in the Turatto et al. relation, or to a measurement error owing to the weakness of the line.

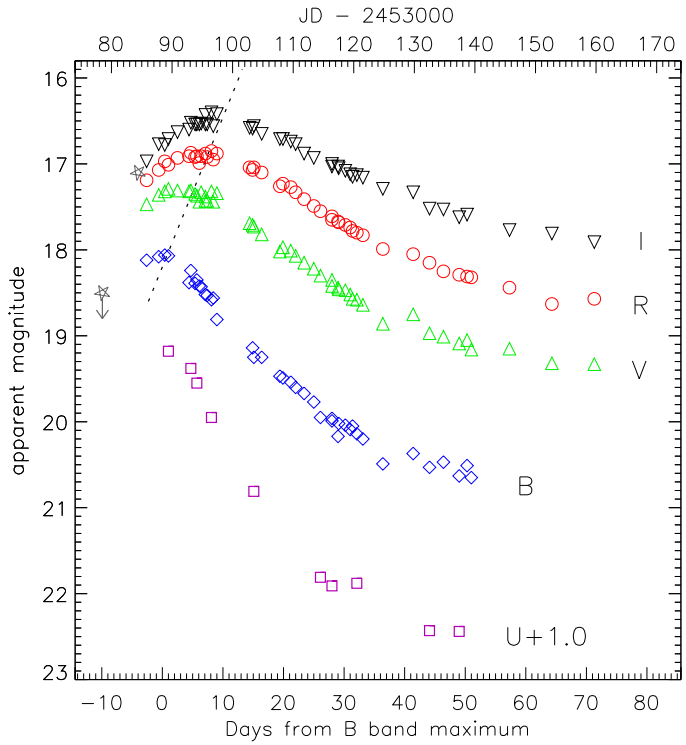

FIGURE 5.2— *UBVRI* light curves of SN 2004aw from −3 to +71 d from B-band maximum (JD 2 453 088.4 ± 0.5). In addition, two unfiltered measurements (open starred symbols) made by amateur astronomers are shown: T. Boles reports a magnitude of 17.1 for JD 2 453 084.4 (discovery) and K. Itagaki provides a detection limit of 18.5 for JD 2 453 078.5 (Boles & Itagaki, 2004). The dotted line roughly connects the maxima of the B through I bands.

Since we consider this last option to be the most likely, we adopt the Galactic reddening of Schlegel et al., which yields a total reddening along the line of sight of 0.37 mag. With a value of 3.1 typically assumed for $R_V = A_V/E(B-V)$ (for a more detailed discussion see, e.g., Cardelli et al. 1989; O'Donnell 1994; Riess et al. 1996; Phillips et al. 1999; Elias-Rosa et al. 2006) we obtain $A_V = 1.15$ mag and $A_B = 1.52$ mag. We conservatively assume a total uncertainty in our estimate of the $B - V$ colour excess of 25% or 0.10 mag.

5.4 Light curves

5.4.1 Optical light curves

Fig. 5.2 shows the *UBVRI* light curves of SN 2004aw before the seasonal gap. In addition to the results from our monitoring campaign, an unfiltered mea-

surement provided by T. Boles and the prediscovery limit of K. Itagaki (Boles & Itagaki, 2004) are included in the figure. The SN maximum is covered in all bands except U. The post-maximum decline in the blue bands is much faster than that in the redder ones. The latest points in Fig. 5.2 (approximately from day +45 on) mark the onset of the radioactive tail of the light curve. Unfortunately, several of these magnitudes are uncertain owing to the very poor S/N (see errors reported in Table 5.3).

Fig. 5.3 shows the complete light curves of SN 2004aw, including the data points obtained at late phases. For comparison the light curves of SNe 1998bw (Galama et al., 1998; McKenzie & Schaefer, 1999; Patat et al., 2001; Sollerman et al., 2002) and 2002ap (Foley et al., 2003; Yoshii et al., 2003; Tomita et al., 2006) are also displayed in the figure, shifted individually to match SN 2004aw at peak. During the radioactive tail, one complete *UBVRI* set of observations was taken 258 d past maximum at TNG, and in B and R the SN was observed again 348 d past maximum at the VLT under poor seeing conditions (for details see Table 5.3). Since no template is available for these observations, the non-isolated position of SN 2004aw limits the precision of our late-time photometry. The SN is not visible in the TNG U-band image and in the VLT B-band image, so that only limits can be derived.

In Table 5.5 the most important photometric properties of SN 2004aw are reported. One of them is the clear delay of maximum light in the red with respect to the bluer bands, which is highlighted by a dotted line in Fig. 5.2. Between the maxima in the B and I bands, for instance, there is an offset of 8.4 days. Fig. 5.3 reveals that the early B-band light curve of SN 2004aw (until $\sim$40 days after the B-band maximum) overlaps with that of SN 1998bw. The U band seems to fade slightly faster (very similar to SN 2002ap), while in the redder bands the decline of SN 2004aw is slower than that of SN 1998bw. Even with measurement uncertainties of up to 0.4 mag (see Table 5.3), the late-time light curves of SN 2004aw shown in Fig. 5.3 seem to deviate from those of the other two SNe. Measured relative to the peak, SN 2004aw appears between 0.4 mag (B band) and 0.9 mag (R band) more luminous than SN 1998bw at day +258, and a comparison with SN 2002ap yields similar results. This can be interpreted either as a measurement error due to a possible underlying compact source of light in the host galaxy, or as a real effect, making SN 2004aw a very slowly declining SN. The fact that even in the nebular spectra taken at similar epochs (Table 5.4), almost no trace of an underlying stellar continuum or narrow Hα emission can be detected (see Section 5.5.1), indicates that the galaxy background at the site of SN 2004aw is smooth enough to be properly subtracted. Hence, we tend to believe in our measurements and think that SN 2004aw truly declines more slowly than SNe 1998bw and 2002ap.

TABLE 5.5— Main photometric parameters of SN 2004aw.[a]

	U	B	V	R	I
Apparent peak mag	18.18 ± 0.15[b]	18.06 ± 0.04	17.30 ± 0.03	16.90 ± 0.03	16.53 ± 0.03
Absolute peak mag[c]	-17.79 ± 0.56[b]	-17.63 ± 0.48	-18.02 ± 0.39	-18.14 ± 0.34	-18.18 ± 0.28
Extinction [mag]	1.80 ± 0.49	1.52 ± 0.41	1.15 ± 0.31	0.87 ± 0.24	0.54 ± 0.15
JD of peak[d]		$2\,453\,088.4 \pm 0.5$	$2\,453\,091.1 \pm 0.4$	$2\,453\,095.0 \pm 0.4$	$2\,453\,096.8 \pm 0.8$
peak relative to B [d]		0.0	$+2.7 \pm 0.6$	$+6.6 \pm 0.6$	$+8.4 \pm 0.9$
Decline rate β[e]	10.28 ± 0.60	6.96 ± 0.16	4.64 ± 0.12	3.20 ± 0.12	2.16 ± 0.12
Tail decline rate[f]		1.35 ± 0.18	1.74 ± 0.22	1.36 ± 0.14	1.53 ± 0.09
Δm_{15}^{g}	1.62 ± 0.25[b]	1.09 ± 0.04	0.62 ± 0.03	0.41 ± 0.03	0.34 ± 0.03

	$(U-B)_0$	$(B-V)_0$	$(V-R)_0$	$(R-I)_0$	$(V-I)_0$
Colour at $B_{\max}$	-0.16 ± 0.16[b]	0.35 ± 0.05	0.02 ± 0.04	-0.03 ± 0.04	-0.01 ± 0.04

[a] A distance modulus $\mu = 34.17$ mag (LEDA, but $H_0 = 72$ km s^{-1} Mpc^{-1}) and a colour excess $E(B-V) = 0.37$ mag were adopted.
[b] Calculated using the earliest data point in the U band, which is estimated to be within 2 days from maximum.
[c] Values corrected for interstellar extinction.
[d] Based on a polynomial fit and overplotted light curves of other SNe Ic.
[e] Average decline rate in the time interval 5–30 days past B-band maximum (in mag/100 d).
[f] Average decline rate in the time interval 60–300 days past B-band maximum (in mag/100 d).
[g] Decline in magnitudes within 15 days from peak.

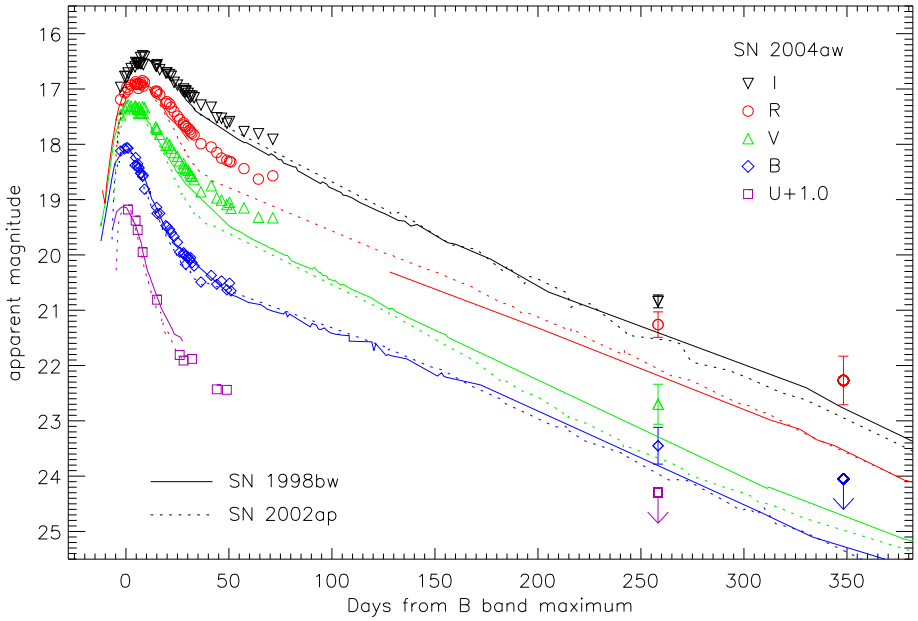

FIGURE 5.3— Late-time light curves of SN 2004aw compared to SN 1998bw (McKenzie & Schaefer, 1999; Patat et al., 2001) and SN 2002ap (Foley et al., 2003; Yoshii et al., 2003; Tomita et al., 2006). The latter two have been shifted in time and magnitude to match SN 2004aw at maximum. The data suggest a comparatively slow decline of SN 2004aw.

5.4.2 Near-IR light curves

To date our knowledge of the behaviour of SNe Ic in the near-IR is very limited. Only a few objects have ever been observed in the IR, and in most cases the coverage is rather poor. IR photometry at more than ~ 5 epochs is available only for SN 2002ap (Nishihara et al., 2002; Yoshii et al., 2003). Given the paucity of IR observations, even our modest IR dataset of SN 2004aw may shed some light on the behaviour of SNe Ic in this wavelength range.

As mentioned in Section 5.2.1, no colour corrections were applied to calibrate the JHK' magnitudes of SN 2004aw presented in Table 5.2. This is a considerable source of uncertainty; moreover, the sparse sampling makes it difficult to check the self-consistency of the light curves, as can be seen in Fig. 5.4. The H and K' light curves show a relatively flat behaviour with only a slight decline (≤ 0.3 mag) in the interval from +10 to +30 days. The J band seems to peak at about day +17, but we cannot exclude that because of lacking colour corrections the calibration error of some points is actually larger than

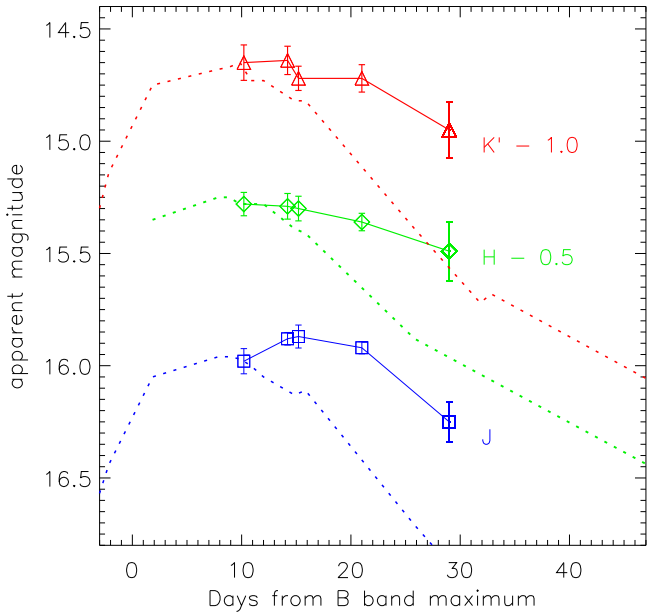

FIGURE 5.4— JHK' light curves of SN 2004aw. For comparison the JHK light curves of SN 2002ap are also displayed (dotted lines, Yoshii et al., 2003). A global shift, besides the one mentioned in the figure for each band, has been applied to the data of SN 2002ap to roughly match SN 2004aw at +10 days.

that reported in Table 5.2. During the time interval covered by our near-IR photometry, all optical bands show a significant decline, from about 0.6 mag in the I band to 1.7 mag in the U band. The different behaviour of the optical and the near-IR bands in this phase is responsible for the strongly increasing contribution of the near-IR to the total bolometric flux, which is discussed in Section 5.4.4.

To date SN 2002ap is the only SN Ic with good temporal coverage of the near-IR bands at early phases (Nishihara et al., 2002; Yoshii et al., 2003), making a systematic comparison of SNe Ic in this regime difficult. At least between day +10 and day +30, SN 2002ap and SN 2004aw show substantial differences in their evolution, as can be seen in Fig. 5.4. While SN 2004aw exhibits an almost plateau-like behaviour, the JHK' light curves of SN 2002ap fade with rates similar to the optical bands, ranging from 0.75 to 1.0 mag within these 20 days. Given the fairly similar optical light curves of these two SNe, the differences in the near-IR are a surprising result.

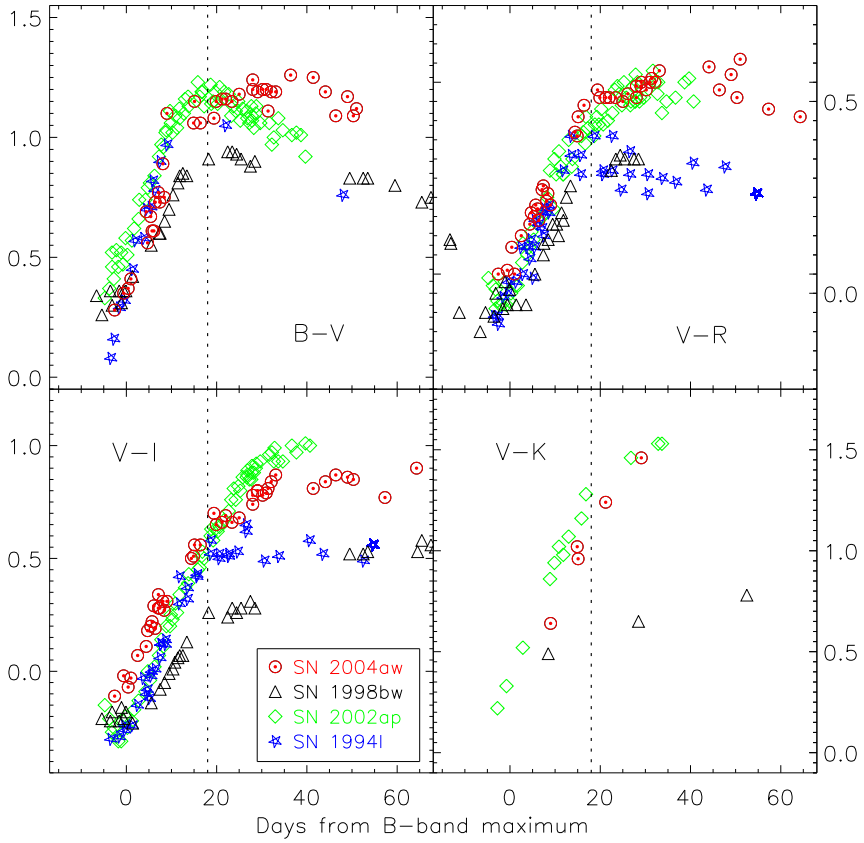

FIGURE 5.5— Colour evolution of SNe 2004aw, 1998bw, 2002ap, and 1994I. The curves have been dereddened according to the values reported in Section 5.4.4 [in particular $E(B-V) = 0.30$ mag for SN 1994I] and shifted in time to match the B-band maximum of SN 2004aw. The vertical dotted lines at +18 days mark the epoch suggested to be used for dating SNe Ic (see Section 5.4.3).

5.4.3 Colour evolution

Fig. 5.5 presents the evolution of the intrinsic $B-V$, $V-R$, and $V-I$ colours for SNe 2004aw, 1998bw, 2002ap, and 1994I. The extinction values reported in Sections 5.3 and 5.4.4 were used to deredden the colour curves. Starting before maximum light, the colours of all objects become monotonically redder for more than 2 weeks. Later on, the differences among the different objects become more distinct.

The $B-V$ colours of SN 1994I and SN 2002ap are reddest at about +15 to +20 days, and then become bluer again. This also holds for SN 1998bw,

although here the evolution after the red peak is much slower. In contrast, in SN 2004aw this epoch marks the onset of a plateau of fairly constant $B-V$ colour lasting at least until +50 days. During this plateau phase SN 2004aw is typically 0.3 to 0.4 mag redder than SN 1998bw. The $V-R$ colour evolution of SN 2004aw and SN 2002ap is very similar, whereas SN 1994I becomes increasingly bluer after day +18. SN 1998bw shows the bluest $V-R$ colour until +15 days, but the subsequent behaviour cannot be evaluated due to lack of information in the R band after +30 days. At +30 days, SN 2004aw and SN 2002ap are redder by $\sim$0.2 mag than SN 1994I and SN 1998bw. Finally, SN 2004aw shows the reddest $V-I$ colour until day +18. After this epoch, SN 1998bw and SN 2004aw still become redder, but with a reduced slope. SN 2002ap takes another 10 days to reach this inflection point, while the $V-I$ colour of SN 1994I remains constant between +20 and +50 days. At +30 days there is a clear colour separation between the objects with a $V-I$ of 0.3, 0.5, 0.8, and 0.9 mag for SN 1998bw, SN 1994I, SN 2004aw, and SN 2002ap, respectively.

In all the colours, SN 1998bw appears to be bluer than SN 2002ap and SN 2004aw during the entire post-maximum phase. After day +20, the same holds for SN 1994I, but in this case this may be due to contamination from blue stars in the host galaxy (see also Section 5.5.2). Remarkably, the SNe of our sample all show a peak or a change in the slope of their colour curves at about 15 to 20 days after B-band maximum. If the generality of such behaviour can be confirmed using a significantly larger sample of well-monitored SNe Ic, this may provide an interesting, extinction-independent new tool to determine the phase of SNe Ic and BL-SNe when maximum light was missed by not more than a few days.

5.4.4 Absolute magnitudes, bolometric light curve

In order to compare the absolute peak magnitudes, the values reported in the literature should first be homogenised with respect to the treatment of distance and extinction. Whenever available, we preferred a Cepheid distance modulus. When a kinematical distance modulus had to be used, it was computed using the host-galaxy recession velocity corrected for the Local-Group infall onto the Virgo cluster and $H_0 = 72$ km s^{-1} Mpc^{-1}. In most cases, extinction estimates from the original papers were adopted, but for SN 1994I a more recent result provided by Sauer et al. (2006) was used.

Comparing the absolute magnitudes, SN 2004aw seems to be a fairly bright, but not outstanding object. Type Ic SNe exhibit peak magnitudes in the V band from about -17 to beyond -19 (see, e.g., Richardson, Branch & Baron 2006). With $M_V = -19.13$ [Galama et al. 1998; $\mu = 32.76$ mag, $E(B{-}V) = 0.06$ mag],

the BL-SN 1998bw is one of the brightest core-collapse SNe ever observed. The broad-lined SN 2002ap, on the other hand, is comparatively faint at maximum with $M_V = -17.35$ [Sharina, Karachentsev & Tikhonov 1996; Foley et al., 2003; Yoshii et al., 2003; $\mu = 29.46$ mag, $E(B-V) = 0.09$ mag], and with $M_V = -17.14$ the BL-SN 1997ef is not very luminous either [Garnavich et al. 1997a,b,c; Mazzali et al. 2002; $\mu = 33.54$ mag, $E(B-V) = 0.04$ mag]. The peak absolute magnitudes of the so-called 'normal' SNe Ic seem to cover a similarly wide range. SN 1994I peaks at $M_V = -17.62$ [Richmond et al. 1996; Sauer et al. 2006; $\mu = 29.60$ mag, $E(B-V) = 0.30$ mag], SN 1999ex reaches -17.58 [Stritzinger et al. 2002; $\mu = 33.28$ mag, $E(B-V) = 0.30$ mag], and SN 1992ar may even have $M_V < -20$ (Clocchiatti et al., 2000). SN 2004aw ($M_V = -18.02 \pm 0.39$) is a bit brighter than SN 1994I (and probably also the average of all SNe Ic), but not exceptionally luminous.

We have constructed a 'quasi-bolometric light curve' (see, e.g., Nomoto et al., 1990) of SN 2004aw in the following way: first the U through I magnitudes were converted into monochromatic fluxes and the spectral energy distribution (SED) was interpolated linearly. Then the SED was integrated over frequency, assuming zero flux at the integration limits, which are given by the blue edge of the U band and the red edge of the I band. In Fig. 5.6(a) we compare the bolometric curve of SN 2004aw with those of SN 1998bw, SN 2002ap and SN 1994I. We note a wide spread in peak luminosities, with SN 1998bw being the brightest object and SN 2004aw intermediate. The differences in the decline rates observed in different bands are clearly reproduced in the bolometric light curves.

Taking into account the contribution of the JHK' bands (see Section 5.4.2 and Table 5.2) makes a significant difference in the bolometric light curves, as can be seen in Fig. 5.6(b). Between +10 days and +30 days the near-IR contribution increases from $\sim 31\%$ to $\sim 45\%$, demonstrating that a considerable portion of the bolometric flux is released in these bands. Unfortunately, no near-IR photometry is available for epochs earlier than +10 days or later than +30 days, so that the corrections to the U-through-I light curve cannot be obtained for all phases. Yoshii et al. (2003) estimated that in SNe Ic, wavelength regions other than the optical and near-IR contribute much less than 10% to the total bolometric flux. Therefore, ignoring the contribution from these frequencies does not lead to a significant underestimate of the true bolometric luminosity.

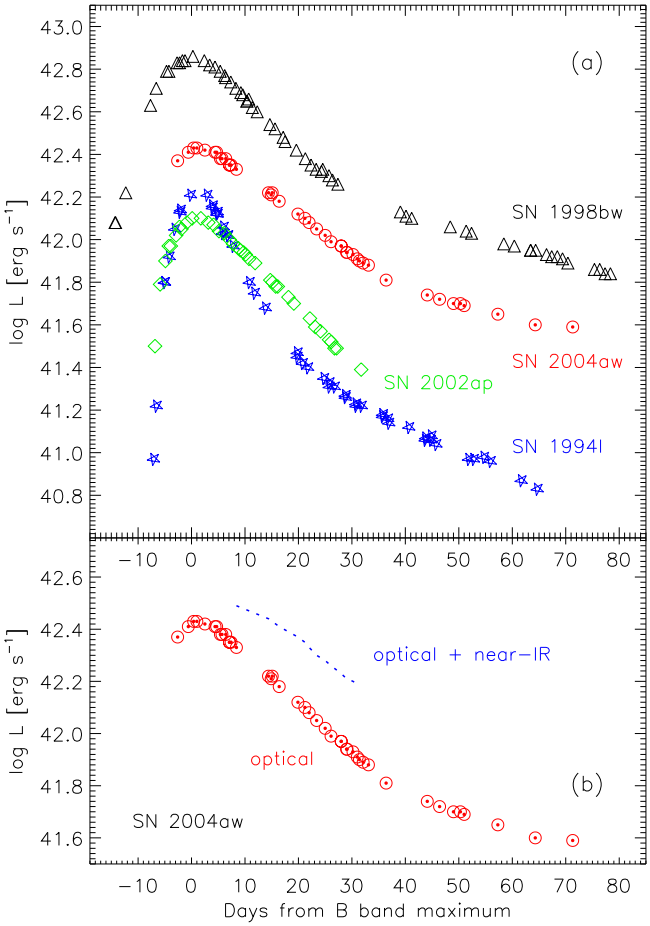

FIGURE 5.6— (a) Quasi-bolometric light curves of SN 2004aw, SN 1998bw, SN 2002ap, and SN 1994I, computed including the U-band through I-band fluxes. The distance and extinction values reported in Section 5.4.4 have been adopted.
(b) Comparison of the quasi-bolometric light curves of SN 2004aw with (dotted line) and without the contribution of the JHK' bands. For phases earlier than +10 days and later than +30 days no near-IR photometry is available.

5.5 Spectral evolution

5.5.1 Sequence of optical spectra

The spectroscopic evolution of SN 2004aw from maximum light to +65 days is densely covered. During this period a continuum is present in all the spectra, so that the photospheric phase lasts for at least two months from maximum. However, after approximately one month the emission component of the Ca II

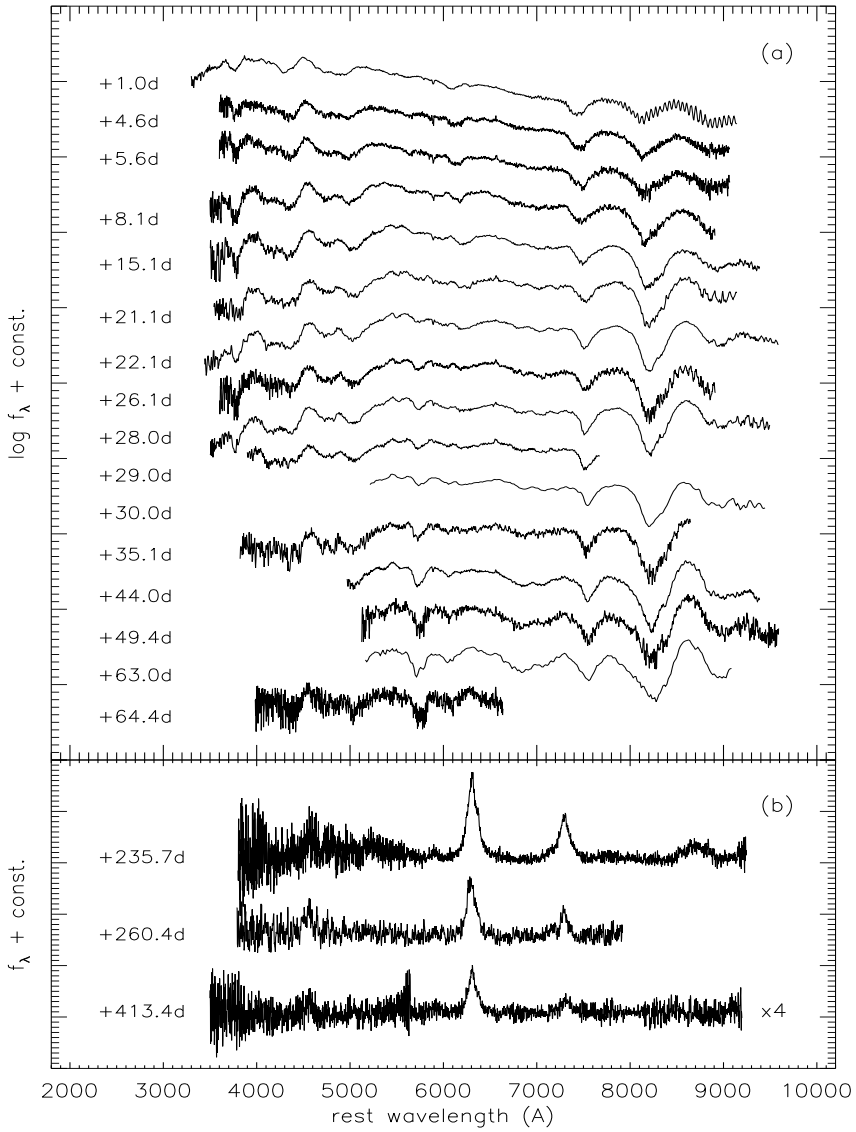

FIGURE 5.7— Spectroscopic evolution of SN 2004aw. Epochs are with respect to B-band maximum (JD = 2 453 088.4). The spectra were checked against the photometry, transferred to the SN rest frame assuming a recession velocity of 4900 km s^{-1} (inferred from a faint host-galaxy Hα line visible in most spectra), and dereddened assuming $E(B-V) = 0.37$ mag.
(a) Series of photospheric spectra from maximum light to about 2 months later (logarithmic scaling). The day +5.6 spectrum is a combination of two spectra taken within half a day.
(b) Nebular spectra, plotted linearly. For better clarity the day +413 spectrum was scaled up by a factor of 4. The increased noise in this spectrum around 5500 Å marks the overlap region of the blue and red channels of Keck/LRIS, with low signal in both of them.

near-IR triplet starts to grow, and in the last two spectra of this sequence first hints of forbidden O I and Ca II emission lines become visible, marking the onset of the transition to the nebular phase. In addition, three entirely nebular spectra at epochs between 236 and more than 400 days past maximum have been obtained. The complete spectroscopic evolution is presented in Fig. 5.7.

The first spectrum of this sequence, obtained one day after B-band maximum, is characterised by a blue continuum and P-Cygni features of Ca II (H&K and the near-IR triplet), O I λ7774, Fe II blends, and Mg II λ4481. Also, Si II λ6355 and possibly C II λ6580 and Na I D can be seen. He I λ5876 might be blended with Na I D, although other optical He I lines cannot be detected. During the first week after maximum (covered by the first four spectra) the evolution is significant. Within a few days the flux in the blue part decreases dramatically, the Ca II near-IR triplet becomes stronger, and the absorption troughs centred at 4200 Å and 4800 Å develop the characteristic "W"-shaped profile that is observed in many Type I SNe around and after maximum.

Later on the spectra evolve more slowly, and during the following month the main changes consist of a further suppression of the flux in the blue, an increasing strength of the emission component of the Ca II near-IR triplet, and an increasingly distinct Na I D absorption. The Si II line, on the other hand, disappears (Clocchiatti et al. 1997 mentioned the possibility that it might be filled by the emerging [O I] $\lambda\lambda$6300, 6364 emission lines). Toward the end of our early-time follow-up, approximately 65 days after maximum, SN 2004aw still shows a well-developed continuum, with only hints of the characteristic nebular emission lines superimposed.

About 170 days later (at a phase of +236 days) the continuum has entirely disappeared, and the spectrum is dominated by forbidden emission lines of [O I] $\lambda\lambda$6300, 6364 and [Ca II] $\lambda\lambda$7291, 7323, possibly blended with [O II] $\lambda\lambda$7320, 7330. Emissions of the Ca II near-IR triplet, Mg I] λ4571 and blended [Fe II] lines near 5000 Å are also visible. While the weak feature near 6000 Å could be a residual of Na I D, the faint emission line near 4000 Å can tentatively be attributed to [S II] λ4069. The peaks of both [O I] $\lambda\lambda$6300, 6364 and [Ca II] $\lambda\lambda$7291, 7323 / [O II] $\lambda\lambda$7320, 7330 are sharp and show a narrow core. Between 236 and 413 days past maximum only minor changes occurred, the most obvious being the disappearance of the permitted emission of the Ca II near-IR triplet. The strength of the [Ca II] relative to [O I] also declines.

5.5.2 Comparison to optical spectra of other SNe Ic

The spectral evolution of SN 2004aw is consistent with that of other Type Ic SNe. However, the spectroscopic variety among the members of this class is

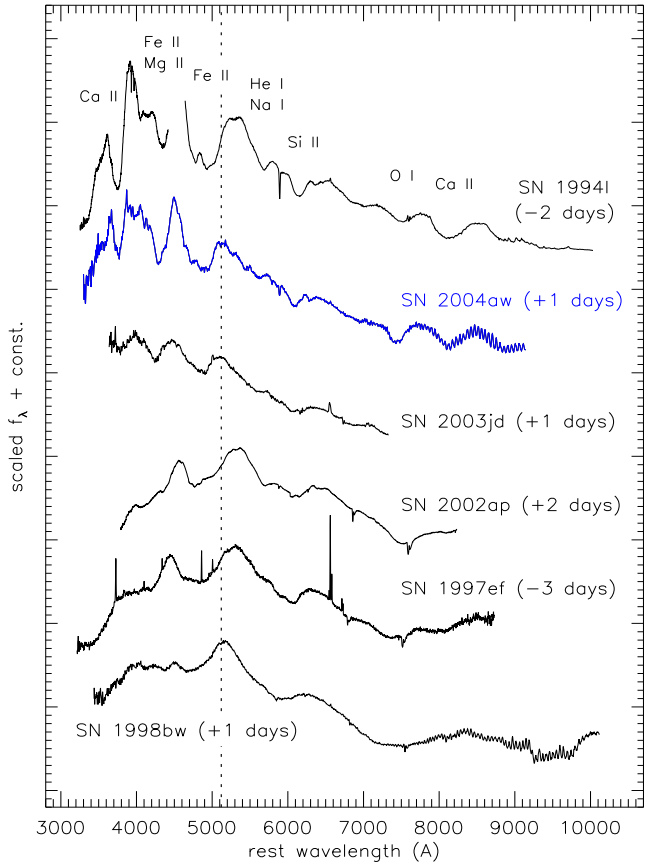

FIGURE 5.8— Comparison of spectra of SNe Ic close to maximum light. The spectra have been dereddened assuming $B - V$ colour excesses of 0.30 mag for SN 1994I (Sauer et al., 2006), 0.37 mag for SN 2004aw, 0.14 mag for SN 2003jd (Valenti et al., 2007a), 0.04 mag for SN 1997ef (only Galactic extinction, Schlegel et al., 1998), 0.09 mag for SN 2002ap (Yoshii et al., 2003), and 0.06 mag for SN 1998bw (Galama et al., 1998). The order of plotting suggests increasing ejecta velocities from top to bottom.

large, especially when also the broad-lined supernovae are taken into account. It is the aim of this section to examine the differences among SNe Ic with particular attention to SN 2004aw.

Figs. 5.8 to 5.10 show a comparison of the spectra of SN 2004aw with those of SN 1994I (Filippenko et al., 1995a) and the BL-SNe 1998bw (Patat et al., 2001), 2002ap (Kawabata et al., 2002; Foley et al., 2003), 1997ef (Mazzali et al., 2000; Matheson et al., 2001), and 2003jd (Valenti et al., 2007a) at maximum light, 2 weeks later, and 6 to 9 weeks past maximum, respectively. At all 3

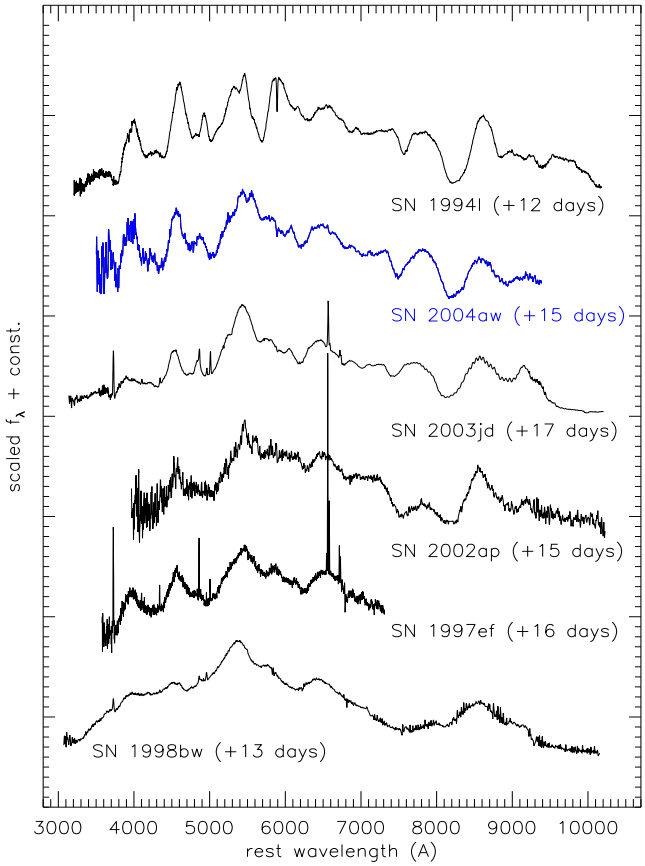

FIGURE 5.9— The same as Fig. 5.8, but 2 weeks after maximum light.

epochs SN 1998bw is an outstanding object, exhibiting comparatively broad and shallow features and strong line blending due to a large amount of ejected material at extremely high velocities. SNe 2002ap and 1997ef (and to a lesser degree SN 2003jd) are similar to SN 1998bw at early epochs (Fig. 5.8), but then evolve towards more typical (i.e., SN 1994I-like) Type Ic spectra (see Fig. 5.10). Compared with SNe 1994I and 2004aw around maximum light, SNe 1998bw, 1997ef and 2002ap show a clear flux deficit shortward of $\sim$5000 Å due to strong line blanketing. Worth mentioning is also the difference in the exact position of the broad emission feature lying between 5000 Å and 5500 Å in all maximum-light spectra. In SNe 2004aw, 2003jd and 1998bw its peak is located at $\sim$5120 Å (indicated by a vertical line in Fig. 5.8), whereas in SNe 1994I, 1997ef and 2002ap it is shifted by about 200 Å to the red.

By +12 days (see Fig. 5.9) Na I D (possibly blended with He I, see Filippenko

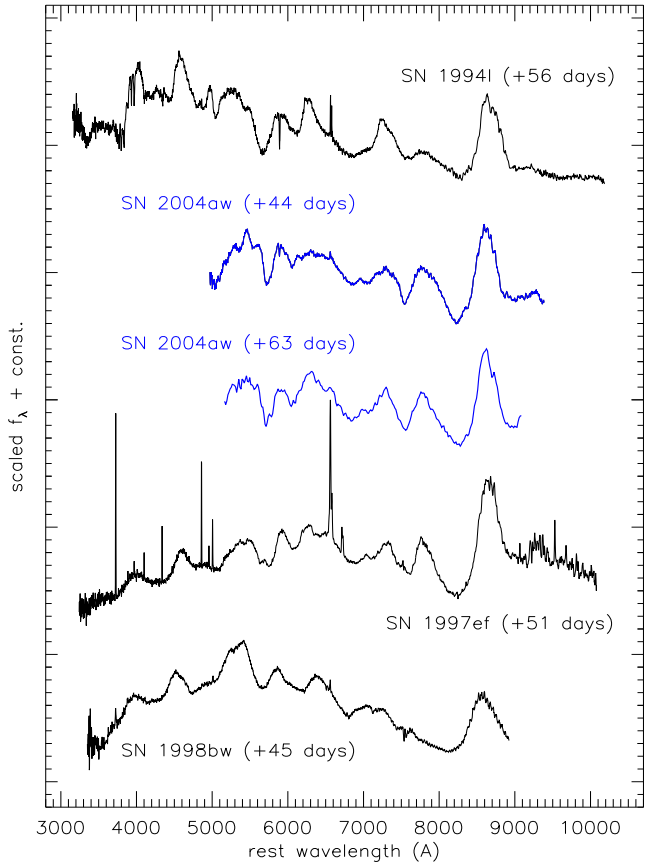

FIGURE 5.10— The same as Fig. 5.8, but 6 to 9 weeks after maximum light.

et al. 1995a; Clocchiatti et al. 1996) is one of the dominant features in the spectrum of SN 1994I, while it is still rather weak in all the other objects in the figure. At similar epoch it is also weak in SNe 1983V (Clocchiatti et al., 1997) and 1987M (Filippenko, Porter & Sargent, 1990) which are not shown here. Moreover, the emerging nebular emission features of [O I] $\lambda\lambda 6300, 6364$ and [Ca II] $\lambda\lambda 7291, 7323$ are clearly seen in SN 1994I at +56 days, while at best only a hint of them can be detected in the spectra of the other SNe at comparable phases (see Fig. 5.10). This suggests that SN 1994I underwent a relatively fast spectral evolution.

The spectrum of SN 2004aw shows similarities to both SN 1994I and the group of moderate BL-SNe represented by SNe 1997ef, 2002ap, and 2003jd. At maximum (Fig. 5.8) the width of the lines of SN 2004aw is well matched by SN 1994I and is significantly smaller than in all BL-SNe except SN 2003jd.

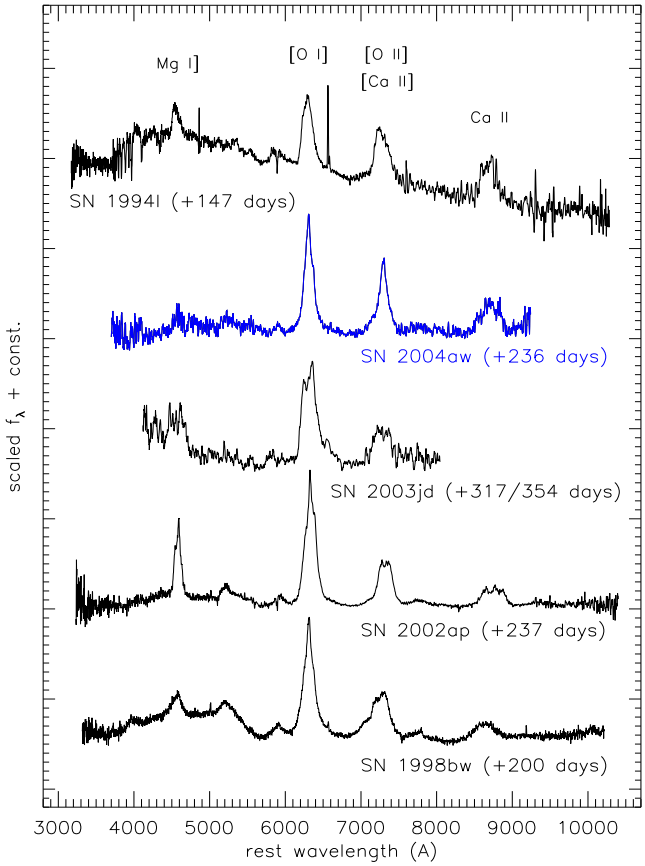

FIGURE 5.11— The same as Fig. 5.8, but 5 to 12 months after explosion. The spectrum of SN 2004aw was smoothed with a box size of 10 Å. The spectrum of SN 2003jd is a combination of two spectra taken 317 and 354 days after maximum, respectively. SN 1994I is heavily contaminated by light from the underlying galaxy.

However, SN 2004aw does not follow the fast evolution of SN 1994I, and hence at later times (Figs. 5.9 and 5.10) it bears a closer resemblance to the spectra of the BL-SNe 2003jd and 1997ef. Also, the Na I D feature is much weaker than in SN 1994I at all epochs.

All nebular spectra in Fig. 5.11 have in common that [O I] $\lambda\lambda 6300, 6364$ is the strongest feature. However, the shape of this feature reveals important differences: in SNe 2004aw, 1998bw, and 2002ap the line has a sharp, narrow core, whereas in SN 1994I its top is somewhat rounded. In SN 2003jd the feature even exhibits a double-peaked structure. The impact that these differences have on our picture of the explosions is discussed in Section 5.6, and in greater depth

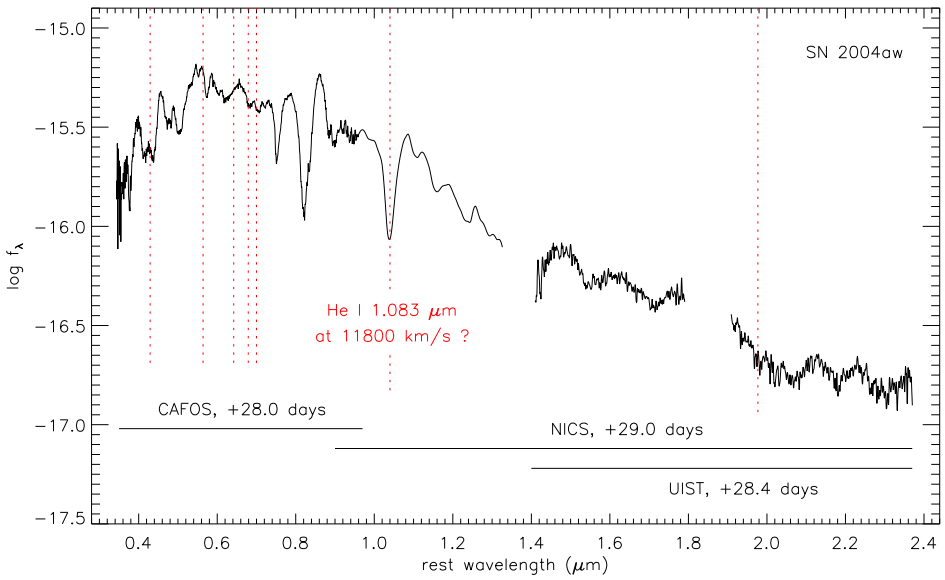

FIGURE 5.12— Combined optical and near-IR spectrum of SN 2004aw taken four weeks after B-band maximum. In the bottom of the figure the ranges of the three individual spectra are indicated. Vertical dotted lines indicate the expected position of strong He I features for an expansion velocity of 11800 km s^{-1}.

in Chapter 6. In SN 2004aw, the [Ca II] $\lambda\lambda 7291, 7323$ / [O II] $\lambda\lambda 7320, 7330$ emission shows a sharp peak, in contrast to the other SNe where the top of this feature is flat or rounded. Mg I] $\lambda 4571$ is particularly strong in SN 2002ap, and rather weak in SN 2004aw. The [Fe II] lines near 5000 Å are more prominent in SN 1998bw than in other SNe of this sample.

5.5.3 Near-IR spectroscopy: Identification of He I lines?

Not many SNe Ic have been followed spectroscopically in the near IR. Besides SN 2004aw, only for a few other objects are the data public: SN 1999ex (which is an object intermediate between Type Ib and Ic; Hamuy et al., 2002), the highly energetic BL-SN 1998bw (Patat et al., 2001), and the low-velocity Type Ic SN 2007gr (Valenti et al., 2007b). However, near-IR spectroscopy may turn out to be a powerful tool for investigating important properties of the progenitor stars of stripped-envelope core-collapse SNe. Although it is commonly accepted that SNe Ic originate from massive stars that have lost most of their H and He envelope, several questions (e.g., concerning the exact mechanism of mass loss) are yet unresolved. Some of these issues may be effectively addressed by a

possible detection of He in the spectra of SNe normally classified as Type Ic. Since the He I features in the near-IR are much stronger than those in the optical regime, IR spectroscopy may play a key role.

Fig. 5.12 shows a combination of an optical and two IR spectra of SN 2004aw 29 days past maximum, covering the spectral range $0.35-2.40$ μm. Among the most prominent features is an absorption at 1.04 μm. The origin of this absorption, which is also seen in other SNe Ic, has been the subject of some debate. For SN 1994I this feature was originally attributed to He I (Filippenko et al., 1995a; Clocchiatti et al., 1996). However, Baron et al. (1999) disfavoured an identification with He I because it would require other optical lines from this ion to show up in the spectrum as well, which is not seen. Millard et al. (1999) discussed alternative origins for this feature such as Si I and C I, based on line identifications with the parametrised spectrum synthesis code SYNOW.

Sauer et al. (2006) found that the absorption might be caused by a mix of some He I and C I. A consistent treatment of He I requires nonthermal excitation and ionisation processes by fast electrons, created by Compton scattering of γ-ray photons, to be taken into account. Without those processes, the excitation of He I at the temperatures present in the ejecta is too low to cause any significant absorption (Lucy, 1991). Sauer et al. (2006) use a simple estimate of these excitations by increasing the optical depth in He I by hand. Although this method does not provide a self-consistent description of the formation of the helium lines, their estimate shows that it is unlikely that He I alone can form such a broad absorption without showing a trace of other lines of this ion.

Contrary to SN 1994I, where no observation of the IR wavelength bands is available, SN 2004aw provides the opportunity to place a tighter constraint on the contribution of the He I 1.083 μm line to the 1.04 μm absorption, because the presence of significant amounts of He I should be detectable in the infrared through the 2.058 μm line. The position of all strong He I lines at a velocity of $11800\,\mathrm{km\,s^{-1}}$ is indicated in Fig. 5.12 by vertical dotted lines. There is no clear detection of a line at ~ 1.98 μm, which provides strong evidence that the contribution of He I to the 1.04 μm absorption must indeed be small. In contrast to other helium lines, the wavelength region of this strong IR line is not crowded with lines from other ions. Mazzali & Lucy (1998) studied the formation of the proposed He I line in the spectra of the Type Ia SN 1994D using a full non-LTE description of this ion including the nonthermal excitations. They found that He I 2.058 μm clearly showed up as the second strongest line in their model spectra. Therefore, a detection should be possible if He I alone was responsible for the 1.04 μm feature. Based on IR observations of SNe 2000ew, 2001B, and 2002ap, Gerardy et al. (2004b) reached a similar conclusion.

Patat et al. (2001) dealt with the formation of the near-IR He I features

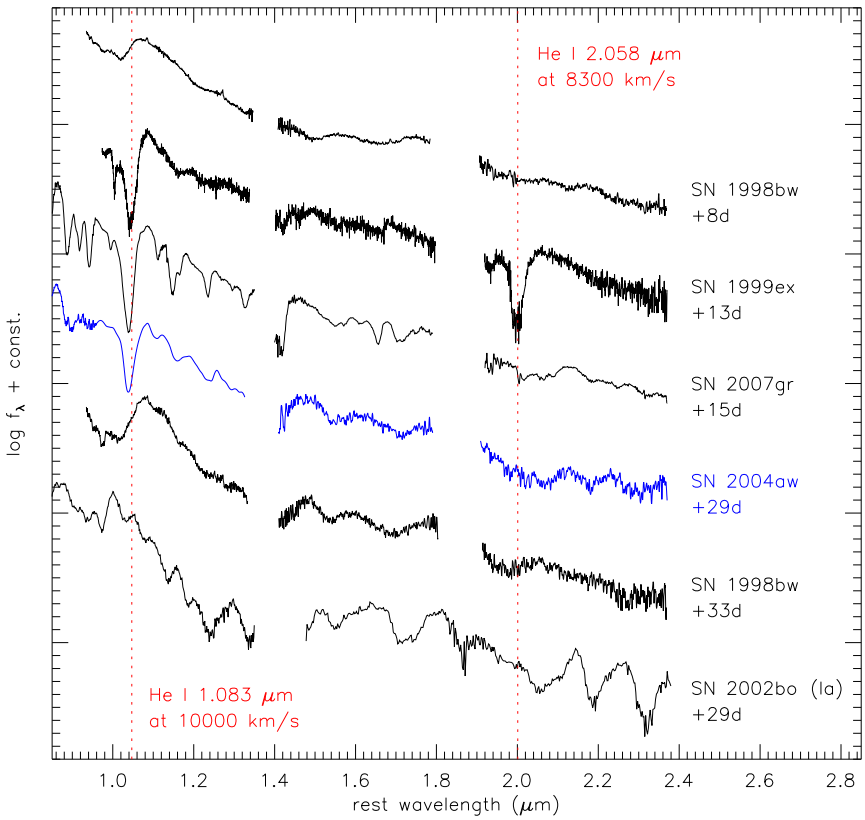

FIGURE 5.13— Near-IR spectra of SNe 2004aw (Type Ic), 1999ex (Type Ib/c), 2007gr (Type Ic), 1998bw (BL-SN), and 2002bo (Type Ia) at epochs from 1 to 5 weeks after B-band maximum. The minima of two pronounced He I features in SN 1999ex are marked by vertical dotted lines. References are in the text.

in great detail, including a discussion of factors (intrinsic line strengths, level populations, non-thermal excitation, resonance scattering enhancement of the He I 1.083 μm line) which may influence the ratio of the EWs of He I 2.058 μm to He I 1.083 μm (hereafter $\mathcal{R}_{\rm He}$). They concluded that a $\mathcal{R}_{\rm He}$ of less than 1 was not unexpected, consistent with a putative detection of He I in the near-IR spectra of SN 1998bw at an observed line width ratio of $\sim 1/3$.

However, values of $\mathcal{R}_{\rm He}$ close to 1 seem to be feasible, as confirmed by SN 1999ex, an intermediate case between SN Ib and SN Ic with weak He I lines visible in the optical part of the spectrum. For this SN three near-IR spectra were obtained by Hamuy et al. (2002). The latest one, at an epoch of 13 days after B-band maximum, is shown in Fig. 5.13, together with the spectrum of

SN 2004aw at +29 days, two spectra of the BL-SN 1998bw (Patat et al., 2001) and one of the Type Ia SN 2002bo (Benetti et al., 2004b). The spectrum of SN 1999ex is the only one in which the lines near 1.04 μm and 2.00 μm are almost equally pronounced, suggesting $\mathcal{R}_{\rm He} \approx 1$ if the 1.04 μm absorption is purely He I, or $\mathcal{R}_{\rm He} > 1$ if also other elements contribute to it. In SN 2004aw only the feature at 1.04 μm is visible, which could be interpreted in two ways. The feature being predominantly formed by He I would require basic physical conditions near the photosphere to be substantially different from SN 1999ex in order to explain the much lower value of $\mathcal{R}_{\rm He} \approx 0$. Models clearly disfavour this option (see Mazzali & Lucy, 1998). Alternatively, the physical conditions are similar, but the 1.04 μm absorption in SN 2004aw is mainly formed by ions other than He I. More recently, the same conclusion was drawn by Valenti et al. (2007b), who found that in synthetic spectra of SN 2007gr the 1.04 μm feature was almost entirely reproduced by C I. The presence of C I was necessary to improve the fit in other parts of the near-IR spectrum, and thus established independent of the 1.04 μm line. Together with the lack of other He I features at 5700 Å and 2.00 μm, this convinced Valenti et al. (2007b) that He was not the main constituent of the 1.04 μm feature in SNe Ic.

Apart from the overall narrower features (SN 2007gr is even more extreme in that respect), the near-IR spectrum of SN 2004aw is quite similar to that of SN 1998bw at a comparable epoch. This especially holds for the H band. However, in the K band SN 2004aw is somewhat reminiscent of SNe Ia, although all features are much less pronounced than those in SN 2002bo. Based on near-IR spectra of the Type Ia SN 1999ee at similar epochs, Hamuy et al. (2002) attributed this group of bumps to blends of iron-group elements. By contrast, the few near-IR spectra of SNe Ib/c available so far seem to be clearly dominated by intermediate-mass elements, even during the nebular phase (Oliva, 1987; Gerardy et al., 2004b).

5.5.4 Ejecta velocities

Though already partially discussed in the previous sections, it is worth taking a more detailed and quantitative look at the expansion velocities of different chemical species in SN 2004aw. All velocities have been determined by fitting a Gaussian profile to the absorption component of the P-Cygni features in the redshift-corrected spectra and measuring the blueshift of the minimum. The outcome of this procedure is a rough estimate of the expansion velocities of the shells where the individual lines predominantly form. The main caveat of this method is the fact that most features are actually blends of several lines, especially when the ejecta velocities are high. In that case, a shift of

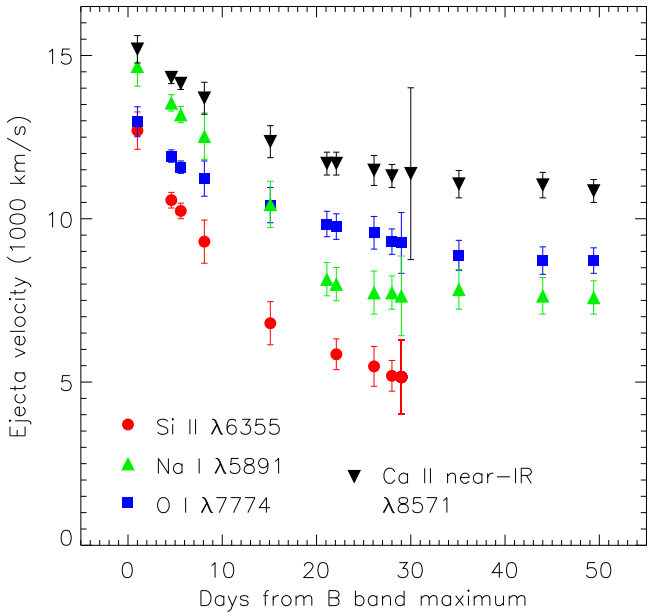

FIGURE 5.14— Velocity evolution of different spectral lines of SN 2004aw.

the absorption minimum with time could also be produced by a change in the relative strength of different lines contributing to the same feature, and hence does not need to be connected to real velocity evolution due to a receding photosphere.

Fig. 5.14 shows the velocity evolution of Si II λ6355, Na I D, O I λ7774, and the Ca II near-IR triplet in SN 2004aw. At all epochs Si II has the lowest and Ca II the highest expansion velocities. The velocities of O I and Na I D are intermediate and always similar to each other, but Na I D shows a faster decline in the early phases until 20 days past maximum. However, for this line possible contamination with He I λ5876 has to be considered. This may be particularly important at maximum and soon after when the feature is generally weak, and could partially be responsible for the apparently different velocity evolution at early times.

5.6 Discussion

In Section 5.4.1 and Fig. 5.2 we noted that the delay of maximum light in the red with respect to bluer bands is one of the remarkable properties of SN 2004aw. The offset of 8.4 days between the B-band and I-band maximum (Table 5.5) is significantly longer than observed not only in the 'prototypical'

Type Ic SN 1994I (1.88 days; Richmond et al. 1996), but also in the Type Ib/c SN 1999ex (6.1 days; Stritzinger et al. 2002) and the BL-SNe 1998bw (3.5 days; Galama et al. 1998) and 2002ap (5.59 days; Foley et al. 2003).

Light curves of all SNe Ic have in common that neither a plateau with constant luminosity as in SNe IIP, nor a rebrightening and secondary maximum in the near-IR bands as in SNe Ia, is present. Nevertheless, their exact shape, and in particular the early decline rate, varies a lot. Some authors have proposed a bimodal distribution (e.g. Clocchiatti, 1995; Clocchiatti et al., 2000, and references therein), dividing Type Ic SNe into slow and fast decliners. Accordingly, SNe 1987M (Filippenko et al., 1990) and 1994I (Yokoo et al., 1994; Tsvetkov & Pavlyuk, 1995; Richmond et al., 1996) are representatives of the rapidly declining group, whereas SNe 1983V (Clocchiatti et al., 1997) and 1990B (Clocchiatti et al., 2001), the Type Ib/c SN 1999ex (Stritzinger et al., 2002), and the BL-SNe 1998bw (Galama et al., 1998; McKenzie & Schaefer, 1999; Patat et al., 2001; Sollerman et al., 2002), 2002ap (Foley et al., 2003; Pandey et al., 2003b; Yoshii et al., 2003; Tomita et al., 2006), 1997ef (Garnavich et al., 1997a,b,c; Mazzali et al., 2004), and 1997dq (Mazzali et al., 2004) belong to the class of slow decliners. However, Fig. 5.15, which compares the light curves of SN 2004aw with those of other SNe Ic, suggests instead that a continuous distribution of decline rates might be a more appropriate description, SN 1987M and 1994I representing the extreme fast end (see also figs. 4 and 6 of Richardson et al. 2006 for a larger sample).

SN 2004aw is one of the slowest decliners of all SNe Ic, slower than SN 1998bw and SN 2002ap. Only SN 1997ef and SN 1997dq (the latter is not included in Fig. 5.15) fade even more slowly, with a decline rate in the radioactive tail that follows the radioactive decay of ^{56}Co, indicating little or no γ-ray escape (Mazzali et al., 2004). On the other hand, the much faster decline of SN 1994I in all bands is apparent, and quantitatively demonstrated by its larger Δm_{15} [$\Delta m_{15}(B) = 2.07$ for SN 1994I versus 1.09 for SN 2004aw; see Richmond et al. (1996) and Table 5.5]. Since the width of the light-curve peak is, assuming the same kinetic energy per unit mass for the two SNe, closely related to the ejecta mass (the SN with higher ejecta mass declining more slowly), the comparison of SNe 2004aw and 1994I suggests that the progenitor of SN 2004aw was significantly more massive than that of SN 1994I. We address this topic in more detail in Section 5.6.2.

Interestingly, the strongly different decline rates of the light curves have no direct impact on the colour evolution of the four SNe included in Fig. 5.5. The differences between these objects, emphasised in Section 5.4.3, appear rather random, and no correlation between the light-curve decline rates and either the absolute values of the colours or their time evolution can be established.

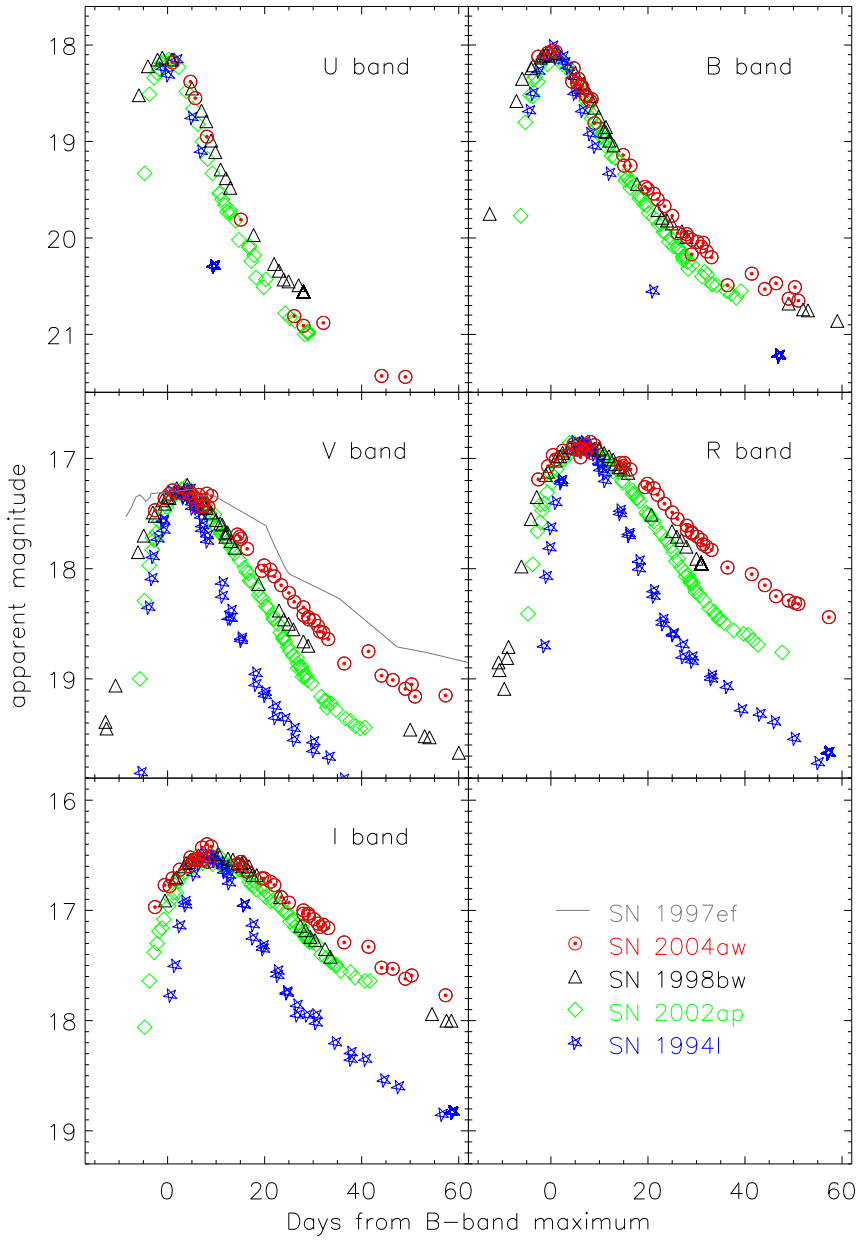

FIGURE 5.15— Light curves of SN 2004aw compared with those of SNe 1998bw, 2002ap, 1994I, and 1997ef (see text for references). As in Fig. 5.3, the latter have been shifted in time and magnitude to match SN 2004aw at maximum.

In general, diversity seems to be characteristic of SNe Ic. Correlations between observable parameters – if they exist – are subtle and hence difficult to establish from the small sample of objects available to date. For example, from the bolometric light curves in Fig. 5.6(a) we find no simple correlation between the brightness at peak and the decline rate as in Type Ia SNe (e.g. Phillips et al., 1999). Furthermore, we have no evidence that the expansion velocity of the ejecta and the peak luminosity of a Type Ic SN are related, i.e., BL-SNe might generally be no brighter than 'normal' SNe Ic. It is true that SN 1998bw not only has extremely high ejecta velocities, but also is one of the most luminous core-collapse SNe ever found. However, as seen in Section 5.4.4, SNe 2002ap and 1997ef are comparatively faint and at peak even less luminous than the normal low-velocity SNe 1994I, 1999ex, and 2004aw.

A comparison of SNe 1994I and 1997ef could lead to the conclusion that the speed of the spectroscopic evolution of a SN Ic and the decline rate of its light curves might be somehow related. SN 1994I shows rapidly fading light curves and a comparatively fast spectral evolution (see Fig. 5.15 and Section 5.5.2), while in SN 1997ef a very slow light-curve decline comes along with an unusually persistent continuum in the spectra (Mazzali et al., 2004). However, in the Type Ic SN 1990B (Clocchiatti et al., 2001) slowly declining light curves meet a fast spectroscopic evolution, burying almost any hope for a useful correlation.

In Section 5.5.2 we showed that from a spectroscopic point of view SN 2004aw shares properties with both the group of so-called 'normal' SNe Ic (e.g., SNe 1983V, 1990B, and of course 1994I) and the moderate BL-SNe 1997ef, 2002ap and especially 2003jd. This intermediate position – together with the wide variety of characteristics among BL-SNe themselves – gives rise to the question of whether BL-SNe actually form a distinct subclass, or if it is more appropriate to think of a continuity of properties from ordinary low-velocity SNe Ic to the most powerful events like SN 1998bw.

An idea to explain the origin of the observed diversity has been to assume that broad-lined SNe are highly aspherical, jet-driven events (some of them connected to a GRB), while ordinary SNe Ic represent more spherical explosions (Mazzali et al., 2005b). In order to verify this picture, the examination of nebular spectra is of particular interest, as they provide an insight into the innermost layers of the ejecta and the geometry of the explosion (see also Chapter 6). Mazzali et al. (2005b) discuss what GRB-related SNe may look like when they are observed from directions almost perpendicular to the jet, so that the burst itself is not visible. Their prediction is that SNe seen along the jet axis have a narrow, sharp, single-peaked [O I] $\lambda\lambda 6300, 6364$ and strong and comparatively broad [Fe II] emission features, while if viewed off axis the [Fe II] feature

should be narrower and weaker, and the [O I] double-peaked. Finally, spherical explosions without a jet should produce a nebular [O I] line with a flat or rounded top.

As can be seen from Fig. 5.11, SN 1998bw fits well into the scenario of a GRB-SN viewed fairly along the jet axis, consistent with the detection of the spatially and temporally coincident GRB 980425. SN 2003jd exhibits a double-peaked [O I] line, indicating that it might be a GRB-SN viewed well off axis (Mazzali et al. 2005b, but see also Soderberg et al. 2006). With its rounded tops of the emission peaks, SN 1994I is traditionally considered to be a more spherical explosion. However, the detailed analysis in Chapter 6 of this thesis reveals a more complex scenario also for this object. SN 2002ap and SN 2004aw show the same sharp [O I] line core as SN 1998bw, but in both cases no GRB was detected. Following the arguments of Maeda et al. (2002), Mazzali et al. (2007b), and Tomita et al. (2006), the observed line profiles require both explosions to be strongly asymmetric, but maybe the jet was too strongly contaminated by baryons to trigger a GRB (Tominaga et al., 2004). However, this still does not explain the completely different kinetic energy per unit mass in the outer ejecta of SN 2004aw and SN 2002ap, as indicated by the significantly different line widths at early phases.

5.6.1 Search for an associated GRB

In order to probe the possible association of SN 2004aw with a GRB the data of the Interplanetary Network (IPN[1]) of high-energy satellites (see, e.g., Hurley et al. 1999) were examined in the period UT March 2 to 17, i.e. from about 7 to 22 days prior to maximum light in B. At that time the IPN involved six spacecraft (Konus-Wind, HETE, Mars Odyssey, RHESSI, RXTE, and INTEGRAL), securing nearly isotropic coverage and almost 100% duty cycle.

A total of seven confirmed GRBs (i.e., events observed by at least two experiments, and having GRB characteristic), plus three unconfirmed events (observed by a single instrument, but likely being genuine GRBs and not particle-induced events) were identified (K. Hurley, private communication). For six out of these ten candidates the localisation through triangulation was sufficiently precise to exclude a spatial association with SN 2004aw. For the remainder (two confirmed and two unconfirmed bursts) there was at best a very coarse localisation (excluding only 30 to 85% of the sky). Within this limited accuracy the four events are all consistent with SN 2004aw, although the probability that this is by chance is very large.

Hence, the result of the search remains rather inconclusive, as an association

[1] http://www.ssl.berkeley.edu/ipn3/

of SN 2004aw with a GRB can be neither firmly established nor definitely excluded. Assuming that none of the unconfirmed GRBs was associated with SN 2004aw, a rough upper limit of $10^{-6}\,\mathrm{erg\,cm^{-2}}$ can be set on the fluence of a possible accompanying GRB in the energy range 25 – 150 keV. However, depending on the spectrum and time history of the burst, the fluence threshold could vary by an approximate factor of 5 in either direction.

It should be noted that SN 2004aw was not detected at radio wavelengths in images taken about half a year after the explosion (A. Soderberg, *private communication*), disfavouring an association with a GRB.

5.6.2 Mass of the ejecta

In order to roughly estimate the total mass of the ejecta of SN 2004aw, we make use of an analytical description of the peak of the light curve developed by Arnett (1982). The model assumes spherical symmetry, a homologous expansion, no mixing of ^{56}Ni, a constant optical opacity κ_{opt}, radiation-pressure dominance, and the applicability of the diffusion approximation for photons, which restricts it to early phases when the density is sufficiently high to make the ejecta optically thick. In this model the time evolution of the SN luminosity is given by

$$L(t) = \varepsilon_{\mathrm{Ni}}\, M_{\mathrm{Ni}}\; e^{-x^2} \int_0^x 2z\, e^{-2zy+z^2} dz, \tag{5.2}$$

where $x \equiv \frac{t}{\tau_{\mathrm{m}}}$, $y \equiv \frac{\tau_{\mathrm{m}}}{2\tau_{\mathrm{Ni}}}$, and $\varepsilon_{\mathrm{Ni}} = \frac{Q_{\mathrm{Ni}}}{m_{\mathrm{Ni}}\,\tau_{\mathrm{Ni}}}$.
Here Q_{Ni} is the energy release per ^{56}Ni decay (1.73 MeV, not accounting for neutrinos, for which the environment is optically thin), and τ_{Ni} is the e-folding time of the ^{56}Ni decay (8.77 d). The effective diffusion time τ_{m} determines the width of the peak of the bolometric light curve and is given by

$$\tau_{\mathrm{m}} \;=\; \left(\frac{2}{\beta c}\,\frac{\kappa_{\mathrm{opt}} M_{\mathrm{ej}}}{v_{\mathrm{sc}}}\right)^{1/2} \;\propto\; \kappa_{\mathrm{opt}}^{1/2}\, M_{\mathrm{ej}}^{3/4}\, E_{\mathrm{kin}}^{-1/4}, \tag{5.3}$$

where v_{sc} is the velocity scale of the homologous expansion and β is an integration constant. Given a certain light-curve shape (i.e., a certain value of τ_m), Eq. 5.3 allows for a family of photometrically degenerate models with different combinations of M_{ej} and E_{kin}. By specifying E_{kin} or, alternatively, the velocity of the ejecta, this degeneracy can be broken, and an estimate of the total ejecta mass becomes feasible. For our mass estimate we make use of Eq. 5.3 and compare SN 2004aw to SN 1994I, for which the relevant parameters are well known from detailed modelling (Nomoto et al., 1994). We do not consider any differences in the mean optical opacities κ_{opt}.

TABLE 5.6— Comparison of absolute magnitudes, kinetic energy, ejecta mass and Ni mass of SNe Ic.[a]

SN	M_V (mag)	$E_{\rm kin}/10^{51}$erg	$M_{\rm ej}/M_\odot$	$M_{\rm Ni}/M_\odot$	references
1994I	−17.62	1	0.9	0.07	N94,R96
2004aw	−18.02	3.5–9.0	3.5–8.0	0.25–0.35	this paper
2002ap	−17.35	4	3	0.08	M02,F03,T06
1997ef	−17.14	19	9.5	0.16	M00,M04
1998bw	−19.13	30	10	0.70	G98,N00

[a] For all SNe except SN 2004aw, the values for kinetic energy, ejecta mass, and nickel mass have been inferred from light curve and spectral models.

N94 = Nomoto et al. 1994;
R96 = Richmond et al. 1996;
M02 = Mazzali et al. 2002;
F03 = Foley et al. 2003;
T06 = Tomita et al. 2006;
M00 = Mazzali, Iwamoto & Nomoto 2000;
M04 = Mazzali et al. 2004;
G98 = Galama et al. 1998;
N00 = Nakamura et al. 2000

The comparison to SN 1994I starts from the observation that the ejecta velocities of these two objects are quite similar ($v_{\rm sc,04aw} \approx v_{\rm sc,94I}$), but that the widths of the bolometric light curves are significantly different. Taking $\tau_{\rm m}$ as the time from peak of the bolometric light curve to the moment when the luminosity is equal to $1/e$ times the peak luminosity (which corresponds to a decline of 1.1 mag), we find that $\tau_{\rm m,04aw}/\tau_{\rm m,94I} \approx 2$–3 (the large uncertainty arises from the unknown effect of the bolometric corrections when considering also the near-IR bands). Assuming $v_{\rm sc,04aw} \approx v_{\rm sc,94I}$, Eq. 5.3 yields

$$M_{\rm ej,04aw} \approx M_{\rm ej,94I} \left(\frac{\tau_{\rm m,04aw}}{\tau_{\rm m,94I}} \right)^2 \approx 4\text{–}9 \times M_{\rm ej,94I}. \qquad (5.4)$$

With $M_{\rm ej,94I} = 0.9\,M_\odot$ (Nomoto et al., 1994) the range of ejecta masses for SN 2004aw turns out to be 3.5–8.0 $M_\odot$. The corresponding kinetic energy, computed via $v_{\rm sc,04aw} \approx v_{\rm sc,94I}$ with $E_{\rm kin,94I} \approx 1.0 \times 10^{51}$erg (Nomoto et al., 1994), would range from 3.5 to 9.0×10^{51}erg. If instead $M_{\rm ej,94I} = 1.2\,M_\odot$ as suggested by Sauer et al. (2006) was adopted, both the inferred ejecta mass and the kinetic energy of SN 2004aw would increase by about 30%.

Hence, this comparison suggests an ejecta mass for SN 2004aw of at least 3.5 $M_\odot$. This value is substantially larger than that found for SN 1994I, and

even larger than that for the BL-SN 2002ap (for a comparison of explosion properties see Table 5.6). At the same time the kinetic energy is less enhanced with respect to SN 2002ap, consistent with the ejecta velocities in SN 2004aw being significantly lower than those in SN 2002ap.

Eq. 5.2 can also be utilised to estimate the mass of ^{56}Ni synthesised in the explosion. For this purpose the formula was resolved for $M_{\rm Ni}$ and evaluated at the time of peak brightness. The effective diffusion time $\tau_{\rm m}$ was determined as described above, and for L the value from our quasi-bolometric (U-through-I) light curve was adopted. To account for the necessary corrections to the true bolometric luminosity and to ensure that the zero-point of the Arnett (1982) relation is properly fixed, we repeated these steps for SNe 1994I, 1998bw, and 2002ap, and introduced an additional factor of 1.1 in Eq. 5.2 that enabled us to better reproduce the Ni masses reported in Table 5.6 for these objects. What we finally find for SN 2004aw is a ^{56}Ni mass of about $0.30 \pm 0.05\,M_{\odot}$, well above the average for core-collapse supernovae.

Given the comparatively high ejecta mass and Ni production in SN 2004aw, it is interesting to discuss which physical parameters of the progenitor star are crucial for accelerating the ejecta to the high velocities observed in BL-SNe. If we assume that the ejecta mass is correlated with the total mass of the progenitor star just before core collapse (which is surely true if the compact remnant is a neutron star with a strict upper mass limit), then the progenitor of SN 2004aw was probably more massive than that of SN 2002ap. But even if the possibility of black hole formation in at least one of the two objects is taken into account, the probability that fall-back of matter is sufficiently strong to invert the progenitor mass versus ejecta mass relation is low. This almost certainly rules out the progenitor mass as the only criterion for producing broad-lined SNe. Since BL-SNe are supposed to be highly aspherical jet-like explosions, it is plausible that the angular momentum of the progenitor star (or the progenitor system in case of a binary) will also play an important role (see e.g. Woosley & Heger, 2006, and references therein).

5.7 Summary and Outlook

We have presented a comprehensive set of optical and near-IR data of the Type Ic SN 2004aw. The light curves of this object, both in the optical and the IR, show a peak broader than that observed in most SNe Ic so far. Also, the decline during the radioactive tail is rather slow, suggesting an enhanced trapping of

γ-rays with respect to the majority of SNe Ic. Both findings require a relatively large ejecta mass, which in the previous section was determined to be 3.5–8.0 $M_{\odot}$. With absolute peak magnitudes of ~ -18 in the optical bands, SN 2004aw seems to be a bit brighter than the average of all SNe Ic, but still more than 1 mag less luminous than the very bright BL-SN 1998bw. The optical spectra show the typical lines found in most SNe Ic. Line blending is similar to that seen in spectra of SN 1994I and much weaker than in the BL-SNe, owing to normal ejecta velocities. The spectroscopic evolution is rather slow, making the moderate BL-SNe 1997ef and 2003jd a better match than SN 1994I a few weeks past maximum. The nebular [O I] $\lambda\lambda 6300, 6364$ line shows a sharp, narrow core, as would be expected for a highly aspherical explosion. Unfortunately, no final conclusion can be drawn concerning a possible association with a GRB. The detection of He also remains controversial, but we can at least say that in SN 2004aw the feature observed at 1.04 μm cannot be He alone.

With the physical parameters computed in the previous section, SN 2004aw proves to be a fairly massive and energetic representative of the SN Ic class. About 0.3 $M_{\odot}$ of synthesised ^{56}Ni is a large amount for a core-collapse SN, and both ejecta mass and total kinetic energy are a factor of 4 to 9 larger than in the prototypical Type Ic SN 1994I. This makes SN 2004aw one of the most energetic normal-velocity SNe Ic ever observed, lying in a parameter region so far almost exclusively populated by some BL-SNe.

These properties also confirm that the various definitions of 'hypernova' mentioned in Section 5.1 are not equivalent. We do believe that SN 2004aw was a highly aspherical explosion, but the ejecta velocities were normal and the total kinetic energy was fairly high, though still below 10^{52} erg. However, the latter also holds for SN 2002ap (see Table 5.6), which is by some authors referred to as hypernova owing to its high ejecta velocities and SN 1998bw-like spectra near maximum light (see e.g. Mazzali et al., 2002; Pandey et al., 2003a).

What we believe to see in both normal and broad-lined SNe Ic is a continuous range of relevant physical parameters such as ^{56}Ni mass, ejecta mass and kinetic energy. A wide variety of combinations of these parameters seems to be realised in Nature, giving rise to the tremendous diversity in the Type Ic SN subclass.

6

Nebular emission-line profiles of Type Ib/c Supernovae – implications for the ejecta geometry

It is the aim of the project presented in this chapter to constrain the ejecta geometry of stripped-envelope CC-SNe from late-phase spectroscopy. Nearly 100 nebular spectra, several previously unpublished, form the basis of this investigation. Integral part of this work is a multi-parameter Gauss-fitting of the [O I] $\lambda\lambda 6300, 6364$ feature in all spectra, with the position, *fwhm* and intensity of the $\lambda 6300$ Gaussian being free parameters, and the $\lambda 6364$ Gaussian being added accordingly to account for the doublet nature of the [O I] feature. On the basis of the best-fit parameters, an attempt is made to organise the objects within morphological classes, concluding that even under optimistic assumptions at most 59% of all SNe Ib/c may be spherical. Jet-models do not seem to be universally applicable either, as we find too few symmetric double-peaked [O I] profiles predicted to be a consequence thereof. In some SNe, the [O I] line exhibits randomly shifted secondary peaks or shoulders, interpreted as blobs of matter ejected at high velocity. This might be the outcome of SASI-driven explosions with neutron-star recoils assuring momentum conservation. At phases earlier than ~ 200 d, a systematic blueshift of the [O I] $\lambda\lambda 6300, 6364$ line centroids can be discerned. Residual opacity in the ejecta provides the most convincing explanation of this phenomenon, photons emitted on the rear side of the SN being scattered or absorbed on their way through the ejecta. Once modified to account for the doublet nature of the oxygen feature, the profile of Mg I] $\lambda 4571$ often resembles that of [O I] $\lambda\lambda 6300, 6364$, suggesting negligible contamination from other lines and confirming that O and Mg are similarly distributed within the ejecta.

6.1 Introduction

That stripped-envelope core-collapse explosions are not necessarily spherically symmetric has been known for a long time, at least since extensive late-time observations of the Type IIb SN 1993J (Spyromilio, 1994; Matheson et al., 2000) became available. Owing to its proximity and a declination which made it circumpolar from northern observatories, this object could be followed without interruption throughout the nebular phase for more than 1000 d (Matheson et al., 2000). The profiles of SN 1993J's nebular emission lines showed plenty of fine-structure, interpreted as clumpiness of the ejected material (Matheson et al., 2000).

After SN 1993J several years passed before the geometry of SN Ib/c ejecta moved again into the focus of scientific interest. This was triggered by the discovery of SN 1998bw inside the error circle of the nearby γ-ray burst GRB 980425, under circumstances that made a by-chance association highly unlikely (Galama et al., 1998). Together with subsequent examples of SN-GRB associations (see e.g. Ferrero et al. 2006 for an overview) this suggested that at least some SNe Ib/c may be powered by the same engine as long-duration GRBs, and that their ejecta may show strong large-scale asphericity along an axis defined by the GRB-jet. Indeed, the nebular spectra of SN 1998bw exhibited properties (with iron emission lines being broader than those of oxygen) which could not be explained within the framework of spherical symmetry (Mazzali et al., 2001; Maeda et al., 2002). Instead, a model with Fe-rich material ejected along the jet axis at high velocity, and lower-velocity O forming approximately a torus perpendicular to this axis, was proposed. From this geometry a strong viewing-angle dependence of the nebular line profiles was predicted (Maeda et al., 2002). In particular, a double-peaked profile of O lines should be observed for the same model viewed from a direction perpendicular to the jet.

Such a profile was first observed in SN 2003jd (Mazzali et al., 2005d), providing an important step towards a coherent picture. However, whether or not such large-scale asphericity is found only in SNe Ic connected with a GRB (which, to our current understanding, can only be a few percent), and how large the degree of asphericity in 'normal' SNe Ib/c actually is, are still subject of debate. For instance, Maeda et al. (2008) recently studied a sample of nebular spectra of 18 stripped-envelope CC-SNe and found a large fraction of double-peaked [O I] $\lambda\lambda 6300, 6364$ line profiles, consistent with about half of all SNe Ib/c being strongly aspherical, or all of them moderately. Similarly, Modjaz et al. (2008) analysed late-time spectra of 10 stripped core-collapse SNe, finding several with double-peaked lines and concluding that asphericity is ubiquitous in all these events, not only the hyperenergetic ones.

In this chapter we conduct a similar study, but based on a larger sample of SNe, considering virtually all nebular SN Ib/c spectra we could find in the literature, complemented by previously unpublished spectra from the Asiago Supernova Archive and recent observations carried out at the ESO Very Large Telescope (VLT). The work is organised as follows: in Section 6.2 we present the entire SN sample, discuss the selection criteria for spectra to be included, and present in more detail those spectra which were previously unpublished. Section 6.3 concentrates on the link between the ejecta geometry and observed line profiles, motivates the choice to focus on the [O I] $\lambda\lambda 6300, 6364$ feature, addresses the complications arising from its doublet nature, and introduces the fitting procedure employed to gain insight into the ejecta morphology. The results of this fitting are analysed in Sections 6.4 and 6.5, trying to find an explanation for the mean blueshifts of the line's centroids at phases $\lesssim 200$ d, and presenting an attempt to divide the objects into different classes on the basis of the best-fit parameters. Individual objects with interesting line profiles are more deeply looked at in Section 6.6, while Section 6.7 extends the discussion to the profile of Mg I] $\lambda 4571$, found to be similar to that of [O I] in most objects. Finally, a brief summary of the main results is given in Section 6.8.

6.2 The sample of SN Ibc spectra

The idea behind this work was to compare a large set of late-time spectra of stripped-envelope CC-SNe, concentrating on what can be learned about the ejecta geometry by studying the profiles of nebular emission lines, in particular [O I] $\lambda\lambda 6300, 6364$ (the motivation to focus on this line is given in Section 6.3). Contrary to other works on this subject (e.g. Mazzali et al. 2005d; Maeda et al. 2006, 2008) we intended to study the line profiles by a simple analytical fitting procedure (for details cf. Section 6.3), since modelling with a nebular spectrum synthesis code would have been too time-consuming to be carried out for the desired large number of spectra. Furthermore, modelling would have required decent information on the peak luminosity and early-time light-curve shape to constrain the synthesised mass of ^{56}Ni, the total ejecta mass and the explosion energetics, and would have relied on a proper absolute flux calibration of the nebular spectra. Only very few of the objects studied here would have fulfilled all these requirements, thus reducing the sample significantly.

Nebular emission features in SNe Ib/c typically start to emerge about two months past maximum light, but at that epoch the photospheric contribution is still strong. For this reason we decided to include in our sample only spectra which were taken more than ~ 90 d after maximum light in the blue bands, which, assuming typical rise times, corresponds to 100 or 110 d after explosion.

Evidently, this criterion required a fairly precise knowledge of the SN phase. For most SNe this information was available or could be reconstructed from the discovery history and classification remarks reported in IAU-circulars. In exception to this rule, spectra of three SNe were included whose phases were not so well constrained. For SN 1995bb (Matheson et al., 2001) no direct information on the age was available, but its spectrum was decidedly nebular. The same accounts for the later two out of three spectra of SN 1990aj, while the first one in this series appears rather peculiar and may still show some photospheric features, but was included for completeness.[1] Finally, a spectrum of SN 2005N was dated to be ~ 90 d past maximum light by cross-correlation with a large set of comparison spectra using the PASSPARTOO code (Harutyunyan et al., 2008). Besides the constraints on the phase, also spectra with insufficient signal-to-noise ratio (S/N) in the wavelength region of interest were rejected.

6.2.1 The full sample

Applying the previously mentioned selection criteria, our full sample consists of 39 SNe with 98 nebular spectra in total. It contains almost all suitable spectra up to the year 2004 that could be found in the literature (asserting no claim for completeness), complemented by previously unpublished spectra from the Asiago Supernova Archive (ASA, Barbon et al. 1993) and selected spectra obtained through dedicated programmes after 2004. The observations thus span the entire era of SN CCD spectroscopy, reaching back to 1984, when with SN 1983N maybe the first nebular spectrum of a SN Ib/c ever was obtained. The full catalogue of spectra studied in this work is presented in Table 6.1, complemented by additional information on the SN classifications and host-galaxy properties.

6.2.2 Previously unpublished spectra

Our sample contains 30 nebular SN Ib/c spectra of 18 objects not previously published elsewhere, most of them taken in the course of the ESO-Asiago SN monitoring programme in the 1990s (Turatto, 2000) or through dedicated VLT programmes from 2004 onwards. Several different telescopes and instruments have been used for these observations. Details are summarised in Table 6.2.

The previously unpublished spectra are presented in Fig. 6.1. They have been optimally extracted using standard tasks in IRAF or MIDAS, wavelength

[1] On the basis of this spectrum, SN 1990aj is sometimes referred to as Type Iac SN, for the simultaneous presence of strong [Fe], [O I] and [Ca II] lines, normally characteristic of either SN Ia or SN Ic late-time spectra (Turatto, 2003).

TABLE 6.1— List of SNe Ib/c included in the sample.

SN	Type	Host galaxy	Morphology[a]	$v^b_{\rm rec}$	Redshift	Date	Epoch[c]	Reference
1983N	Ib	NGC 5236	SBc	554 ± 119	0.0018(04)	1984/03/01	226 ± 5	Gaskell et al. 1986
1985F	Ib/c	NGC 4618	SBm	544 ± 59	0.0018(02)	1985/03/19	280 ± 4	Filippenko & Sargent 1986
1987M	Ic	NGC 2715	SABc	1216 ± 132	0.0041(04)	1988/02/09	141 ± 7	Filippenko et al. 1990
						1988/02/25	157 ± 7	Filippenko et al. 1990
1988L	Ic	NGC 5480	Sc	1963 ± 100	0.0065(03)	1988/07/17	90 ± 12	Matheson et al. 2001
						1988/09/15	149 ± 12	Matheson et al. 2001
1990B	Ic	NGC 4568	Sbc(M)	2255 ± 153	0.0075(05)	1990/04/19	91 ± 2	Clocchiatti et al. 2001
						1990/04/30	102 ± 2	Matheson et al. 2001
1990I	Ib	NGC 4650A	S0/a(M)	2880 ± 99^d	0.0096(03)	1990/07/26	90 ± 2	Elmhamdi et al. 2004
						1990/12/21	237 ± 2	Elmhamdi et al. 2004
						1991/02/20	298 ± 2	Elmhamdi et al. 2004
1990U	Ic	NGC 7479	SBbc	2525 ± 162	0.0084(05)	1990/10/20	100 ± 12	Matheson et al. 2001
						1990/10/24	104 ± 12	Gómez & López 1994
						1990/11/23	134 ± 12	Asiago archive
						1990/11/28	139 ± 12	Matheson et al. 2001
						1990/12/12	153 ± 12	Matheson et al. 2001
						1990/12/20	161 ± 12	Asiago archive
						1991/01/06	178 ± 12	Matheson et al. 2001
						1991/01/12	184 ± 12	Gómez & López 1994
1990W	Ib/c	NGC 6221	SBc	1481 ± 126	0.0049(04)	1991/02/21	183 ± 3	Asiago archive
						1991/04/21	242 ± 3	Asiago archive
1990aa	Ic	MCG+05-03-016	Sb	5032 ± 108	0.0168(04)	1991/01/12	130 ± 7	Gómez & López 2002
						1991/01/23	141 ± 7	Matheson et al. 2001
1990aj	Ib/c$_{pec}$	NGC 1640	SBb(R)	1604 ± 64^d	0.0053(02)	1991/01/29	140 ± 50	Asiago archive
						1991/02/22	164 ± 50	Asiago archive
						1991/03/10	180 ± 50	Matheson et al. 2001
1991A	Ic	IC 2973	SBcd	3232 ± 84	0.0107(03)	1991/03/22	99 ± 10	Gómez & López 1994
						1991/04/07	115 ± 10	Matheson et al. 2001
						1991/04/16	124 ± 10	Gómez & López 1994
						1991/06/08	177 ± 10	Gómez & López 1994
1991L	Ib/c	MCG+07-34-134	Sc(M)	9186 ± 200^d	0.0306(07)	1991/06/08	121 ± 20	Gómez & López 2002
1991N	Ic	NGC 3310	SABb(R)	1071 ± 80	0.0036(03)	1991/12/14	274 ± 15	Matheson et al. 2001
						1992/01/09	300 ± 15	Matheson et al. 2001

TABLE 6.1— *continued.* List of SNe Ib/c included in the sample.

SN	Type	Host galaxy	Morphology[a]	$v^b_{\rm rec}$	Redshift	Date	Epoch[c]	Reference
1993J	IIb	NGC 3031	Sab	-140 ± 192^d	-0.0001(06)	1993/10/19	205 ± 3	Barbon et al. 1995
						1993/11/19	236 ± 3	Barbon et al. 1995
						1993/12/08	255 ± 3	Barbon et al. 1995
						1994/01/17	295 ± 3	Barbon et al. 1995
						1994/01/21	299 ± 3	Barbon et al. 1995
						1994/01/22	300 ± 3	Barbon et al. 1995
						1994/03/25	362 ± 3	Barbon et al. 1995
						1994/03/30	367 ± 3	Barbon et al. 1995
1994I	Ic	NGC 5194	Sbc(M)	493 ± 70	0.0016(02)	1994/07/14	97 ± 1	Filippenko et al. 1995a
						1994/08/04	118 ± 1	Filippenko et al. 1995a
						1994/09/02	147 ± 1	Filippenko et al. 1995a
1995bb	Ib/c	anonymous	S/Irr	1626 ± 250	0.0054(08)	1995/12/17	nebular	Matheson et al. 2001
1996D	Ic	NGC 1614	SBc(M)	4531 ± 167	0.0151(06)	1996/09/10	214 ± 10	Asiago archive
1996N	Ib	NGC 1398	SBab(R)	1396 ± 214	0.0047(07)	1996/10/19	224 ± 7	Sollerman et al. 1998
						1996/12/16	282 ± 7	Sollerman et al. 1998
						1997/01/13	310 ± 7	Sollerman et al. 1998
						1997/02/12	340 ± 7	Sollerman et al. 1998
1996aq	Ib	NGC 5584	SABc	1675 ± 83	0.0056(03)	1997/02/11	176 ± 4	Asiago archive
						1997/04/02	226 ± 4	Asiago archive
						1997/05/14	268 ± 4	Asiago archive
1997B	Ic	IC 438	SABc(R)	2919 ± 144	0.0097(05)	1997/09/23	262 ± 5	Asiago archive
						1997/10/11	280 ± 5	Asiago archive
						1998/02/02	394 ± 5	Asiago archive
1997X	Ic	NGC 4691	SB0/a	1072 ± 47	0.0036(02)	1997/05/10	103 ± 5	Gómez & López 2002
						1997/05/13	106 ± 5	Asiago archive
1997dq	Ic	NGC 3810	Sc	993 ± 114^d	0.0033(04)	1998/05/30	217 ± 10	Asiago archive
						1998/06/18	236 ± 10	Matheson et al. 2001
1997ef	BL-Ic	UGC 4107	Sc	3452 ± 63	0.0115(02)	1998/09/21	287 ± 3	Matheson et al. 2001
1998bw	BL-Ic	ESO184-G82	SBbc	2445 ± 135	0.0082(05)	1998/09/12	126 ± 1	Patat et al. 2001
						1998/11/26	201 ± 1	Patat et al. 2001
						1999/04/12	337 ± 1	Patat et al. 2001
						1999/05/21	376 ± 1	Patat et al. 2001
1999cn	Ic	MCG+02-38-043	Sab	6502 ± 235	0.0217(08)	2000/04/08	297 ± 5	Asiago archive
1999dn	Ib	NGC 7714	SBb(M)	2744 ± 74	0.0091(02)	2000/09/01	375 ± 5	Asiago archive
2000ew	Ic	NGC 3810	Sc	1049 ± 114	0.0035(04)	2001/03/17	112 ± 12	Asiago archive

TABLE 6.1— *continued.* List of SNe Ib/c included in the sample.

SN	Type	Host galaxy	Morphology[a]	$v^b_{\rm rec}$	Redshift	Date	Epoch[c]	Reference
2002ap	BL-Ic	NGC 628	Sc	657 ± 22^d	0.0022(01)	2002/06/09	123 ± 1	Foley et al. 2003
						2002/06/18	132 ± 1	Foley et al. 2003
						2002/07/12	156 ± 1	Foley et al. 2003
						2002/08/09	185 ± 1	Foley et al. 2003
						2002/10/01	237 ± 1	Foley et al. 2003
						2002/10/09	245 ± 1	Foley et al. 2003
						2002/10/14	250 ± 1	Asiago archive
						2002/11/06	274 ± 1	Foley et al. 2003
						2003/01/07	336 ± 1	Foley et al. 2003
						2003/02/27	386 ± 1	Foley et al. 2003
2003jd	BL-Ic	MCG-01-59-021	SABm	5654 ± 78	0.0188(03)	2004/09/11	317 ± 1	Mazzali et al. 2005d
						2004/10/18	354 ± 1	Mazzali et al. 2005d
2004aw	Ic	NGC 3997	SBb(M)	4900 ± 118	0.0163(04)	2004/11/14	236 ± 1	Taubenberger et al. 2006
						2004/12/08	260 ± 1	Taubenberger et al. 2006
						2005/05/11	413 ± 1	Taubenberger et al. 2006
2004gt	Ic	NGC 4038	SBm(M)	1424 ± 133	0.0047(04)	2005/05/24	160 ± 5	Asiago archive
2005N	Ib/c	NGC 5420	Sb	4885 ± 198^d	0.0163(07)	2005/01/21	88 ± 30	Harutyunyan et al. 2008
2006F	Ib	NGC 935	Sc(M)	4270 ± 180	0.0142(06)	2006/11/16	312 ± 7	Maeda et al. 2008
2006T	IIb	NGC 3054	SBb(R)	2560 ± 182	0.0085(06)	2007/02/18	371 ± 2	Maeda et al. 2008
2006aj	BL-Ic	anonymous	late spiral	9845 ± 250	0.0328(08)	2006/09/19	204 ± 1	Mazzali et al. 2007c
						2006/11/27	273 ± 1	MPA data base
						2006/12/19	295 ± 1	MPA data base
2006gi	Ic	NGC 3147	Sbc	2820 ± 178^d	0.0094(06)	2007/02/10	148 ± 5	Asiago archive
2006ld	Ib	UGC 348	SABd(R)	4168 ± 41	0.0139(01)	2007/07/17	280 ± 4	MPA data base
						2007/08/06	300 ± 4	MPA data base
						2007/08/20	314 ± 4	MPA data base
2007C	Ib	NGC 4981	SBbc(R)	1766 ± 116	0.0059(04)	2007/05/17	131 ± 4	MPA data base
						2007/06/20	165 ± 4	MPA data base
2007I	BL-Ic	anonymous	late spiral	6445 ± 250	0.0215(08)	2007/06/18	165 ± 6	MPA data base
						2007/07/15	192 ± 6	MPA data base

[a] Classification according to LEDA.
[b] Recession velocity in $\mathrm{km\,s^{-1}}$, inferred from narrow Hα; error from 'vmaxg' (LEDA).
[c] Epoch in days from B-band maximum light; photometry of SN 1985F from Tsvetkov (1986).
[d] Heliocentric recession velocity from NED (no Hα visible in the spectra).

TABLE 6.2— Instrumental details of previously unpublished spectra.

SN	Date	Instrumental setup
1990U	1990/11/23	ESO 3.6m + EFOSC + B300 + R300
	1990/12/20	ESO 3.6m + EFOSC + B300
1990W	1991/02/21	ESO 3.6m + EFOSC + B300 + R300
	1991/04/21	ESO 3.6m + EFOSC + B300 + R300
1990aj	1991/01/29[a]	ESO 2.2m + EFOSC2 + gr1
	1991/02/22[a]	ESO 3.6m + EFOSC + B300 + R300
1996D	1996/09/10	ESO 1.5m + B&C + gt15
1996aq	1997/02/11	ESO 3.6m + EFOSC + R300
	1997/04/02[b]	ESO 1.5m + B&C + gt15
	1997/05/14	ESO 2.2m + EFOSC2 + gr1 + gr5
1997B	1997/09/23	ESO 2.2m + EFOSC2 + gm5
	1997/10/11	Danish 1.54m + DFOSC + gr5
	1998/02/02[a]	ESO 3.6m + EFOSC2 + gr6
1997X	1997/05/13	ESO 2.2m + EFOSC2 + gr1 + gr5
1997dq	1998/05/30	ESO 3.6m + EFOSC2 + B300N + R300N
1999cn	2000/04/08	ESO 3.6m + EFOSC2 + gr11
1999dn	2000/09/01	ESO 3.6m + EFOSC2 + gr12
2000ew	2001/03/17	Danish 1.54m + DFOSC + gm4
2002ap	2002/10/14	SSO 2.3m + DBS
2004gt	2005/05/24	VLT-U1 + FORS2 + 300V
2006aj	2006/11/27	VLT-U1 + FORS2 + 300V + 300I
	2006/12/19	VLT-U1 + FORS2 + 300V
2006gi	2007/02/10	NOT 2.56m + ALFOSC + gm4
2006ld	2007/07/17	VLT-U1 + FORS2 + 300V
	2007/08/06	VLT-U1 + FORS2 + 300V
	2007/08/20	VLT-U1 + FORS2 + 300V
2007C	2007/05/17	VLT-U1 + FORS2 + 300V
	2007/06/20	VLT-U1 + FORS2 + 300V + 300I
2007I	2007/06/18	VLT-U1 + FORS2 + 300V + 300I
	2007/07/15	VLT-U1 + FORS2 + 300V

[a] Already shown by Turatto (2003).
[b] Already shown by Valenti et al. (2007a).

calibrated with respect to arc lamps, and flux calibrated using instrumental response curves obtained from spectrophotometric standard stars observed in the same nights. The spectra unanimously show [O I] $\lambda\lambda 6300, 6364$ as one of their strongest features, complemented by other lines typical of SNe Ib/c at late phases, most notably [Ca II] $\lambda\lambda 7291, 7323$ / [O II] $\lambda\lambda 7320, 7330$, Mg I] $\lambda 4571$, a multitude of blended [Fe II] lines in the region 4000 to 5000 Å, and the Ca II near-IR triplet. In spectra taken less than 150 d after maximum a contribution from photospheric lines and a weak pseudo-continuum can also be discerned.

SN 2006aj is peculiar in a sense that the emission feature around 7400 Å is not dominated by [Ca II] $\lambda\lambda 7291, 7323$, but by [Ni II] $\lambda 7380$ (Maeda et al., 2007; Mazzali et al., 2007c). The extremely narrow [O I] $\lambda\lambda 6300, 6364$ emission

features on top of an unusually broad line basis are also remarkable. As already noted by Turatto (2003), the earliest available spectrum of SN 1990aj is highly peculiar, showing Fe lines at a strength otherwise only found in late-time spectra of thermonuclear SNe. Unfortunately, nothing is known about this SN's early spectral evolution, as it was already in the nebular phase when it was discovered. The only information available is that it was not detected in repeated observations of R. Evans' visual SN search to a limiting magnitude of 15 throughout 1990 (McNaught, 1991), suggesting that it either was no brighter than ~ -17 at maximum or had a rather narrow light-curve peak.

Even considering only this subsample of unpublished objects, a variety of different profiles of the [O I] $\lambda\lambda 6300, 6364$ feature, but also most other nebular emission lines, can be found. The possibilities range from rounded tops as for SNe 1997B and 1997X over sharply peaked lines (SNe 1990aj, 2006aj) to double-peaked (SNe 1996aq, 2000ew, 2004gt) and even more complex, multi-peaked profiles (SN 2006ld).

6.3 Fitting the oxygen line

[O I] $\lambda\lambda 6300, 6364$ is one of the dominant and most characteristic features of nebular spectra of stripped-envelope CC-SNe, and maybe the most useful to study the ejecta geometry, in particular the degree of asphericity. Compared to the multitude of forbidden Fe lines found mostly at bluer wavelength and to the [Ca II] / [O II] feature around 7300 Å, [O I] $\lambda\lambda 6300, 6364$ is – except for being a doublet itself – largely isolated and unblended. In contrast to the weaker Mg I] $\lambda 4571$ it lies in a region which is covered by almost all late-time spectra, and where the sensitivity of most spectrographs is at a maximum, allowing for a relatively good S/N. Furthermore, oxygen is the most abundant element in the ejecta of stripped-envelope CC-SNe, thus telling more about the overall geometry than the distribution of a minor species like Ca.

In this section we aim at describing the method we used to collect information on the geometry of the ejected oxygen, which involves the characterisation of the expected line profile, the development of a suitable parametrisation, and the actual procedure applied to infer the best-fitting parameters for each single spectrum.

6.3.1 Expected line profiles

In completely transparent SN ejecta the profile of a forbidden emission line is determined by the spatial distribution of the emitting material (emissivity $\propto$ density), but also the distribution of ^{56}Co, the daughter nucleus of ^{56}Ni, whose radioactive decay provides the γ-rays needed to populate the line's upper level

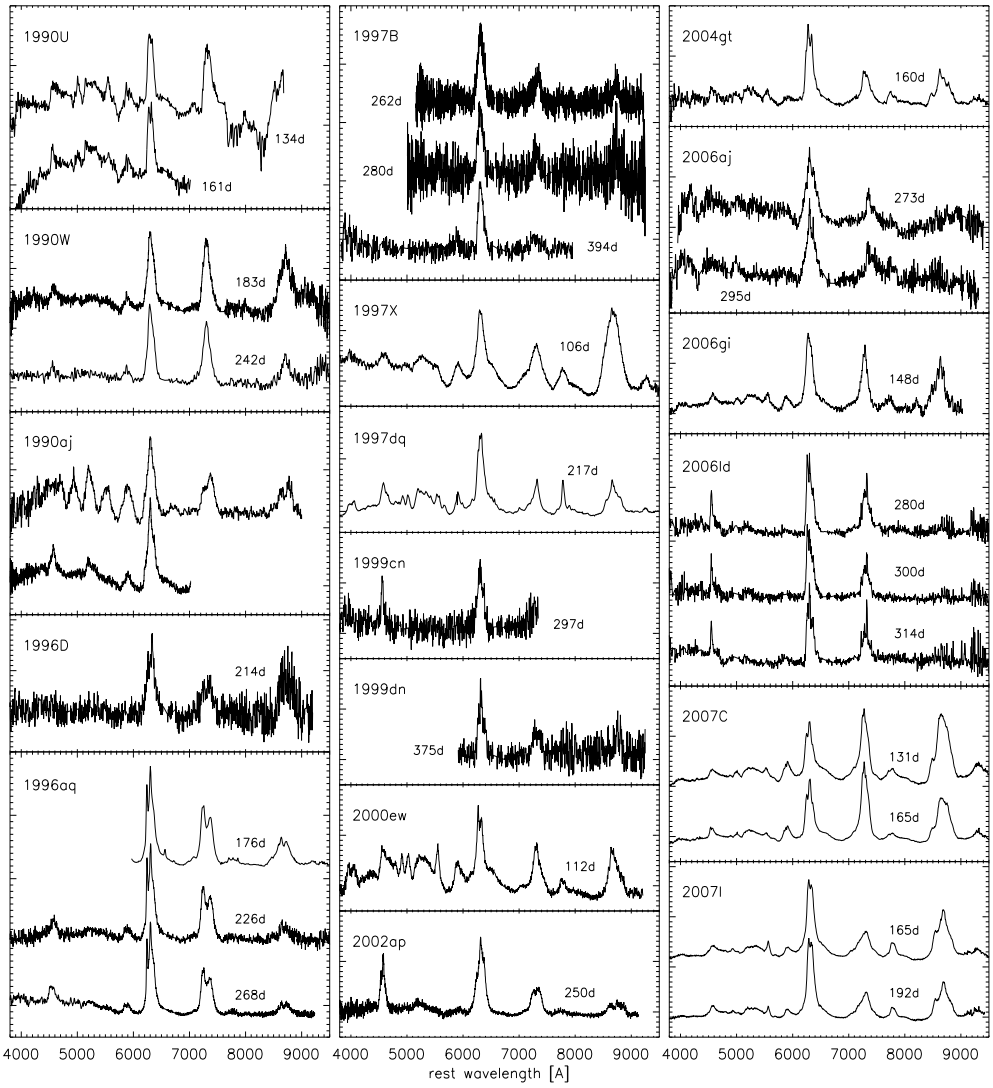

FIGURE 6.1— Previously unpublished spectra of our sample (cf. Table 6.2). All spectra are shown at their rest wavelength inferred (whenever possible) from narrow interstellar Hα lines. Overly strong continuum slopes and narrow host-galaxy emission features have been removed for presentation purposes.

(Fransson & Chevalier, 1987, 1989). The latter dependence would vanish only if the spatial distributions of Co and the emitting species were similar. For the oxygen doublet this is usually not fulfilled, since Co and O are abundant in different regions of the ejecta, and only mixed to some degree through hydrodynamic instabilities. However, for a spherically symmetric explosion the assumption that the [O I] $\lambda\lambda 6300, 6364$ line profile mainly depends on the oxygen distribution should not be too bad; only the line may be somewhat more strongly peaked, since the Co has lower expansion velocities and is hence confined to the inner parts of the ejecta. The larger the degree of asphericity, the stronger is probably the influence of the spatial distribution of ^{56}Co. However, even in the most aspherical, jet-like explosions such as 1998bw and 2003jd detailed modelling (Mazzali et al., 2005d; Maeda et al., 2006) reveals that the profile of the [O I] feature mainly reflects the geometry of the oxygen-rich part of the ejecta, and not so much that of Co which provides the excitation.

To predict line profiles for a spherically symmetric case, we start with the simplified assumption that the emission is isotropic in the co-moving frame (cmf) and proportional to the overall matter density (this is a fair approximation for oxygen, which is the most abundant element in stripped-envelope CC-SN ejecta). It is thus described by an isotropic cmf emissivity:

$$\eta_{\nu,\mathrm{cmf}}(\mathbf{r}) \equiv \left(\frac{\delta P}{\delta V\, \delta\nu}\right)_{\mathrm{cmf}} = \eta_0\ \rho(\mathbf{r})\ \phi(\nu_{\mathrm{cmf}} - \nu_0) \tag{6.1}$$

Here, $\delta P/\delta V$ is the radiative energy emitted per unit volume and time (in *all* directions), $\phi(\nu)$ is the normalised profile of the emitting line in the co-moving frame (with argument relative to the line's cmf mean frequency ν_0), and η_0 is a constant describing the total emission power per unit mass.

For $v \ll c$ one can calculate the power received by an observer from a volume element in the flow $\delta V = \delta A\ \delta s$ (where δA is perpendicular to the line-of-sight element δs):

$$\left.\frac{\delta P}{\delta\nu}\right|_{\mathbf{r}} = \eta_0\ \rho(\mathbf{r})\ \phi\!\left[\nu - \nu_0\left(1 + \frac{v_{||}(\mathbf{r})}{c}\right)\right]\ \delta A\ \delta s\ \frac{\delta\Omega}{4\pi} \tag{6.2}$$

(see Fig. 6.2 for an identification chart of the relevant quantities). $v_{||}$, the velocity along the line of sight, determines the Doppler shift of a photon, and $\frac{\delta\Omega}{4\pi}$ is the solid angle subtended by the observing instrument (seen from the point of emission).

Integrating over the volume (s being again the coordinate along the line of sight) yields for the observed flux F_ν:

$$F_\nu \;=\; \frac{\eta_0}{d^2}\int_{-r_{\max}}^{r_{\max}} \mathrm{d}s \int_{p^2_{\max}\pi} \mathrm{d}A\ \rho(\mathbf{r})\ \phi\!\left[\nu - \nu_0\left(1 + \frac{v_{||}(\mathbf{r})}{c}\right)\right]$$

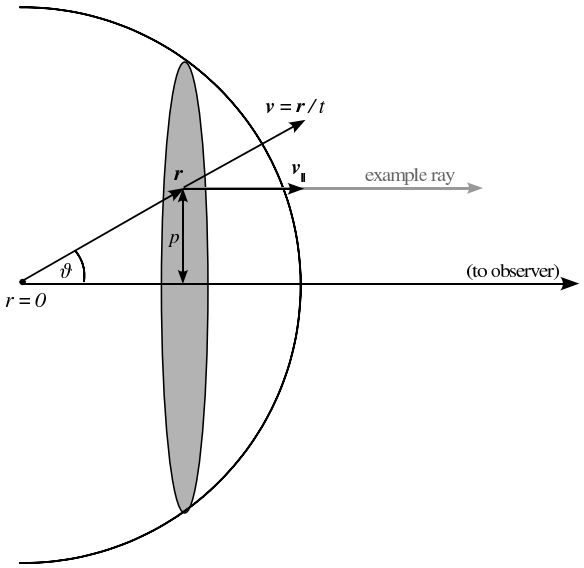

FIGURE 6.2— Identification chart for the quantities introduced for calculating an emission-line profile.

$$
\begin{aligned}
&= \frac{\eta_0}{d^2} \int_{-r_{\max}}^{r_{\max}} \mathrm{d}s \int_{p_{\max}^2 \pi} \mathrm{d}A \; \rho(\mathbf{r}) \, \phi\Big[\nu - \nu_0\Big(1 + \frac{s}{ct}\Big)\Big] \\
&= \frac{\eta_0}{d^2} \int_{\xi(r_{\max})}^{\xi(-r_{\max})} \mathrm{d}\xi \cdot \frac{ct}{\nu_0} \int_{p_{\max}^2(\xi)\pi} \mathrm{d}A \; \rho(\mathbf{r}) \, \phi(\xi) \qquad (6.3)
\end{aligned}
$$

where $\xi := \nu - \nu_0 \, (1 + \frac{s}{ct})$, $p_{\max} = \left(r_{\max}^2 - s^2\right)^{1/2}$ and d the distance to the observer. In the narrow-line limit [the Sobolev approximation is here equivalent to setting $\phi(\xi) = \delta(\xi)$], with a spherically symmetric density and $s_0 = \frac{\nu - \nu_0}{\nu_0} ct$ this becomes

$$F_\nu = \frac{\eta_0}{d^2} \frac{ct}{\nu_0} \int_0^{p_{\max}} \mathrm{d}p \; 2\pi p \; \rho\Big[p^2 + s_0(\xi)^2\Big] \qquad (6.4)$$

In spherically symmetric explosion models such as CO 110 (Nakamura et al., 2000) the radial density distribution $\rho(r)$ of the ejecta of stripped CC-SNe can be approximated well by a Gaussian:

$$\rho(r) = \rho_0 \left(\pi \, a^2 t^2\right)^{-3/2} e^{-\left(\frac{r}{at}\right)^2} \qquad (6.5)$$

Using Eq. 6.5 (with $a > 0$; $r_{\max} = +\infty$) as an analytical description of $\rho(r)$, and defining $\vartheta := \arccos(s_0/r)$, Eq. 6.4 can be written as

$$F_\nu = \frac{\eta_0}{d^2} \frac{ct}{\nu_0} \, \rho_0 \left(\pi \, a^2 t^2\right)^{-3/2} \int_0^{\infty} \mathrm{d}p \; 2\pi p \; e^{-\left(\frac{s_0}{at \cos\vartheta}\right)^2}$$

$$
\begin{aligned}
&= \frac{\eta_0}{d^2}\,\frac{ct}{\nu_0}\,\rho_0\left(\pi\,a^2t^2\right)^{-3/2}2\pi\int_0^{\pi/2}\mathrm{d}\vartheta\;\frac{s_0^2\,\sin\vartheta}{\cos^3\vartheta}\;e^{-\left(\frac{s_0}{at\cos\vartheta}\right)^2}\\
&= \frac{\eta_0}{d^2}\,\frac{ct}{\nu_0}\,\rho_0\left(\pi\,a^2t^2\right)^{-3/2}2\pi\,\frac{1}{2}(at)^2e^{-\left(\frac{s_0}{at}\right)^2}\\
&= \frac{\eta_0}{d^2}\,\rho_0\,\frac{\sqrt{\pi}c}{\nu_0\,a}\;e^{-\left(\frac{c}{a}\frac{\nu-\nu_0}{\nu_0}\right)^2} \qquad (6.6)
\end{aligned}
$$

This, in fact, is a Gaussian profile in frequency space for the emerging emission line. Hence, fitting the [O I] lines with Gaussians perfectly makes sense for spherically symmetric SNe.

Whenever deviations from spherical symmetry are observed, a more sophisticated density distribution would be required, and line profiles could only be computed numerically. The result would then also depend on the viewing angle. However, this approach is not practicable in the context of line-fitting, since without additional information on $\rho(r)$ the number of parameters would be infinite. Instead, we tried to reproduce more complex line profiles as a superposition of multiple (up to three) Gaussian components. This is methodologically straightforward, and provides at least some information on the distribution (through the position and strength of the various components) and radial extent (through the components' full width at half maximum) of oxygen in the SN ejecta.

6.3.2 [O I] λ6300 and [O I] λ6364

As mentioned in the previous section, an advantage of the oxygen feature is its isolated position, not blended with lines from other elements. However, the feature itself is a doublet of two oxygen lines, [O I] λ6300 and [O I] λ6364, both forbidden transitions which share the same upper level. Their lower levels are part of the not fully degenerate ground state of O I, and separated by 0.0196 eV.

The ratio of these two lines depends on the ambient O I density, and is hence not the same under all environmental conditions. This fact has been theoretically derived and observationally confirmed by Spyromilio & Pinto (1991) and Leibundgut et al. (1991), who studied the time-evolution of the [O I] line ratio in late spectra of SNe 1987A and 1986J, respectively. Following their deductions, the line optical depth in Sobolev approximation is given by

$$\tau_{lu} = \frac{\lambda^3 t\, g_u A_{ul} n_l}{8\pi g_l}\left(1 - \frac{g_l\, n_u}{g_u n_l}\right) \qquad (6.7)$$

where t is the time since explosion, g the degeneracy of the respective level (the subscripts u and l stand for *upper* and *lower*), A the transition strength and n the population of the respective level.

In general, local-thermodynamic-equilibrium (LTE) approximations cannot be applied to infer the level population in nebular SN ejecta. However, in the case of [O I] λ6364 / [O I] λ6300 the lower levels are part of the ground state, and hence much more strongly populated than the upper levels: $n_l \gg n_u$. Eq. 6.7 can therefore be simplified to

$$\tau_{lu} \approx \frac{\lambda^3 t\, g_u A_{ul} n_l}{8\pi g_l}. \tag{6.8}$$

The escape probability for a photon is given by

$$\beta_{lu} = \frac{1 - \exp(-\tau_{lu})}{\tau_{lu}}. \tag{6.9}$$

In the case of two competitive transitions (and assuming no interaction between the transitions, i.e. no re-absorption of emitted photons by the other transition, which is only partially true for the oxygen doublet), the product of transition strengths and escape probabilities defines the branching ratio:

$$\begin{aligned} \mathcal{R} &= \frac{A_{ul,6364}\ \beta_{lu,6364}}{A_{ul,6300}\ \beta_{lu,6300}} \\ &= \frac{g_{l,6364}\ n_{l,6300}\ \lambda^3_{6300}}{g_{l,6300}\ n_{l,6364}\ \lambda^3_{6364}} \cdot \frac{1 - \exp(-\tau_{lu,6364})}{1 - \exp(-\tau_{lu,6300})}. \end{aligned} \tag{6.10}$$

This can be regarded as a function of the ground-state number densities n_l and the time since explosion. To evaluate the behaviour of Eq. 6.10 in reasonable density and time regimes, first the numerical values of the other parameters have to be inserted.

The ground state of O I is formed by three levels with different angular-momentum quantum numbers J: the lowest level is $J = 2$, which is the lower level of the λ6300 line and fivefold degenerate ($g_{l,6300} = 5$; $m_J = -2 \ldots 2$). The next higher level, separated by 0.0196 eV, is the $J = 1$ level, lower level of the λ6364 line and threefold degenerate ($g_{l,6364} = 3$; $m_J = -1 \ldots 1$). Finally, the highest level belongs to the $J = 0$ state, and is not degenerate.

Since the ground state of O I can be treated in LTE owing to its small energetic separation, the population ratio of the $J = 2$ and $J = 1$ levels is given by

$$\frac{n_{l,6364}}{n_{l,6300}} = \frac{g_{l,6364}}{g_{l,6300}}\ \exp\left(-\frac{\Delta E}{kT}\right). \tag{6.11}$$

With $\Delta E = 0.0196\,\mathrm{eV}$ and $kT = 0.431\,\mathrm{eV}$ (for $T = 5000\,\mathrm{K}$) the exponential term is 0.9555 ($k = 8.6173 \times 10^{-5}\,\mathrm{eV\,K^{-1}}$), very close to 1 and rather

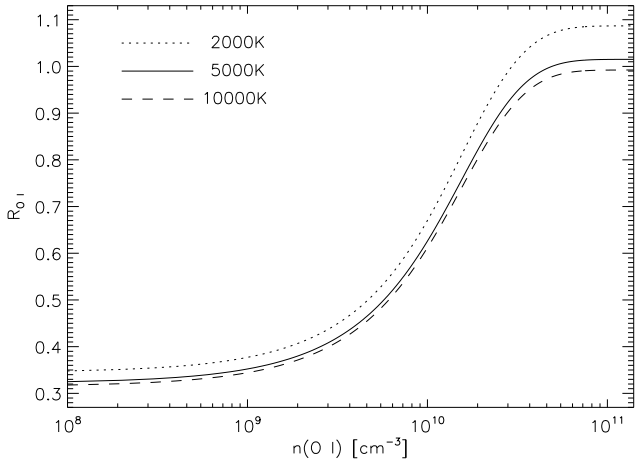

FIGURE 6.3— Oxygen line-strength ratio $\mathcal{R}_{[\mathrm{O\,I}]}$ calculated for a phase of 100 d after explosion, as a function of O I number density. Curves for 2000, 5000 and 10 000 K are plotted to illustrate the weak dependence on temperature.

insensitive to temperature changes. Hence, the ground state of O I consists of three levels with population ratio $\sim 5 : 3 : 1$ [i.e., $n_{l,6300} \approx 5/9\, n(\mathrm{O\,I})$ and $n_{l,6364} \approx 3/9\, n(\mathrm{O\,I})$]. Inserting this into Eq. 6.10, and employing transition strengths of $A_{ul,6300} = 5.65 \times 10^{-3}\,\mathrm{s}^{-1}$ and $A_{ul,6364} = 1.82 \times 10^{-3}\,\mathrm{s}^{-1}$, we end up with

$$\mathcal{R}_{[\mathrm{O\,I}]} = 0.97\ \exp\!\left(+\frac{\Delta E}{kT}\right) \cdot \frac{1 - \exp\left(-8.56 \cdot 10^{-13}\, n(\mathrm{O\,I})\,[\mathrm{cm}^{-3}]\ t\,[\mathrm{d}]\right)}{1 - \exp\left(-2.70 \cdot 10^{-12}\, n(\mathrm{O\,I})\,[\mathrm{cm}^{-3}]\ t\,[\mathrm{d}]\right)}. \tag{6.12}$$

At high densities [$n(\mathrm{O\,I}) \gg 10^{10}$ cm^{-3}], $\mathcal{R}_{[\mathrm{O\,I}]}$ is close to unity [precisely: $0.97 \exp(\Delta E/kT)$], while in the low-density limit [$n(\mathrm{O\,I}) \ll 10^{10}$ cm^{-3}] it is $\sim 1/3$ [precisely: $0.31 \exp(\Delta E/kT)$], with [O I] λ6300 being stronger. The transition between these asymptotic values happens (for times of 100 to 300 d after explosion) at O I number densities of the order of 10^9 to a few times 10^{10} cm^{-3} (Fig. 6.3). This transition was actually observed in SN 1987A, since this object, originating from the collapse of a compact blue supergiant and exhibiting low expansion velocities of the ejecta, had unusually high densities at the onset of the nebular phase. For SNe Ib/c such high densities are not expected, so that for our sample of SN spectra taken later than $\sim$100 d after explosion the low-density limit should always apply. This helps to reduce the number of parameters in our model, as it is sufficient to specify the amplitude,

central wavelength and *fwhm* of the λ6300 line, while the numbers for the λ6364 line are automatically determined requesting a fixed wavelength-offset of 63.5 Å, a line ratio of 3:1, and the same *fwhm* for both lines. From here on we refer to such a three-parameter set as one component in fitting the [O I] line profile; up to three such components were employed to obtain good fits.

6.3.3 The fitting procedure

The actual fitting was accomplished using the IRAF task NFIT1D, which is part of the STSDAS package. A user-defined fitting-function was introduced, which consisted of up to three components (each made of two Gaussian profiles at a fixed ratio to account for the two oxygen lines). The continuum level was determined on both sides of the [O I] feature and interpolated linearly. Thus, a single fit contained up to 11 parameters (three for each of the three line components plus zeropoint and slope of the continuum).

Obviously, optimisation in this multidimensional space is not trivial. Since the background parameters are determined from a different wavelength region than the actual line parameters, fitting the background can technically be decoupled from fitting the line, although of course the best-fit values are affected by the choice of the background. This can be a problem in relatively early spectra (up to ~ 150 d), where an underlying photospheric contribution can be discerned, and the background is more strongly inclined than later on. For the other up to nine parameters the main difficulty consisted in identifying the global minimum for a given number of components. As long as the fit was done with only one component (i.e. three parameters), the solution was unique and robustly found independent of the initial values to start with. However, adding a second or third component revealed a tendency of NFIT1D to get stuck in local minima. Furthermore, degeneracy turned out to be a problem. For some lines similarly good fits could be obtained by entirely different parameter configurations, which in turn entailed different interpretations concerning the ejecta geometry. To circumvent or at least milden this problem, a refined two-step fitting procedure was applied in these critical cases. In a first step a set of synthetic line profiles was computed on a grid, changing each parameter by fixed steps within reasonable limits. The resulting profiles were then compared to the observed ones, and the one which minimised χ^2 was identified. In a second step the so-derived values were used as initial guess for NFIT1D, ensuring that the fit converged to the global minimum.

For the one-component fits uncertainties in the position and *fwhm* were estimated in the following automated manner: for each observed spectrum a set of 50 spectra were generated, which slightly differed from the original within

the measured noise level. Starting from the best-fitting parameters determined as described before, line profiles were computed on a fine grid, varying the fit parameters in small steps. Subsequently, for each of the 50 artificial spectra the combination of parameters which minimised χ^2 of the fit was identified. The outcome of this exercise was a distribution of 50 estimates for both position and *fwhm*, whose standard deviation was adopted as error of the respective parameter. One should note that these errors only reflect the uncertainty in finding the best one-component fit parameters, but carry no information on the overall goodness of the fit (e.g., the best parameters for a single-component fit to a double-peaked line can be well determined although the true line profile is poorly reproduced).

The best-fitting values for single- and double-component fits for all spectra are reported in the Appendix (Section 6.9) in Table 6.5, the parameters of three-component fits to individual spectra are given in Table 6.6, and the best fits are compared with the observed line profiles in Fig. 6.4.

6.4 Blueshifted line centroids at early phases

Originally meant as a consistency check for the applied fitting procedure, we plotted the position of the λ6300-Gaussian in the one-component fits against the phase of the spectra (Fig. 6.5). The position should be a fair tracer of the actual line centroid, and in the absence of additional effects always be close to 6300 Å, with a certain scatter owing to the peculiarities of individual objects and uncertainties in their redshifts.

Instead, Fig. 6.5 tells us that there is a systematic trend of the [O I] feature being blueshifted in spectra taken earlier than $\sim$200 d after maximum light, and the earlier the phase the stronger the effect is. In the spectra taken around 100 d, the average blueshift amounts to $\sim$20 Å, corresponding to $\sim$1000 km s^{-1} in velocity space. In the following, possible interpretations of the observed effect are discussed, and their suitability to explain the observations is tested.

(i) *Ejecta geometry.* Line shifts such as that observed in [O I] could in principal arise from a very special ejecta geometry. Low-mode (especially $l = 1$) hydrodynamic instabilities (Scheck et al., 2004, 2006; Kifonidis et al., 2006) can generate strong anisotropies in the explosions, and one can think of situations where the net momentum carried by the oxygen-rich ejecta is compensated by an opposite motion of Fe-rich parts or by a recoil of the newly formed neutron star. However, while this may be suitable to explain the shift of a line, it can *not* explain the decrease thereof with time. Also, there is no reason why particular ejecta geometries should always result in a *blue*shift of the line centroid, since all spatial orientations should be equivalent.

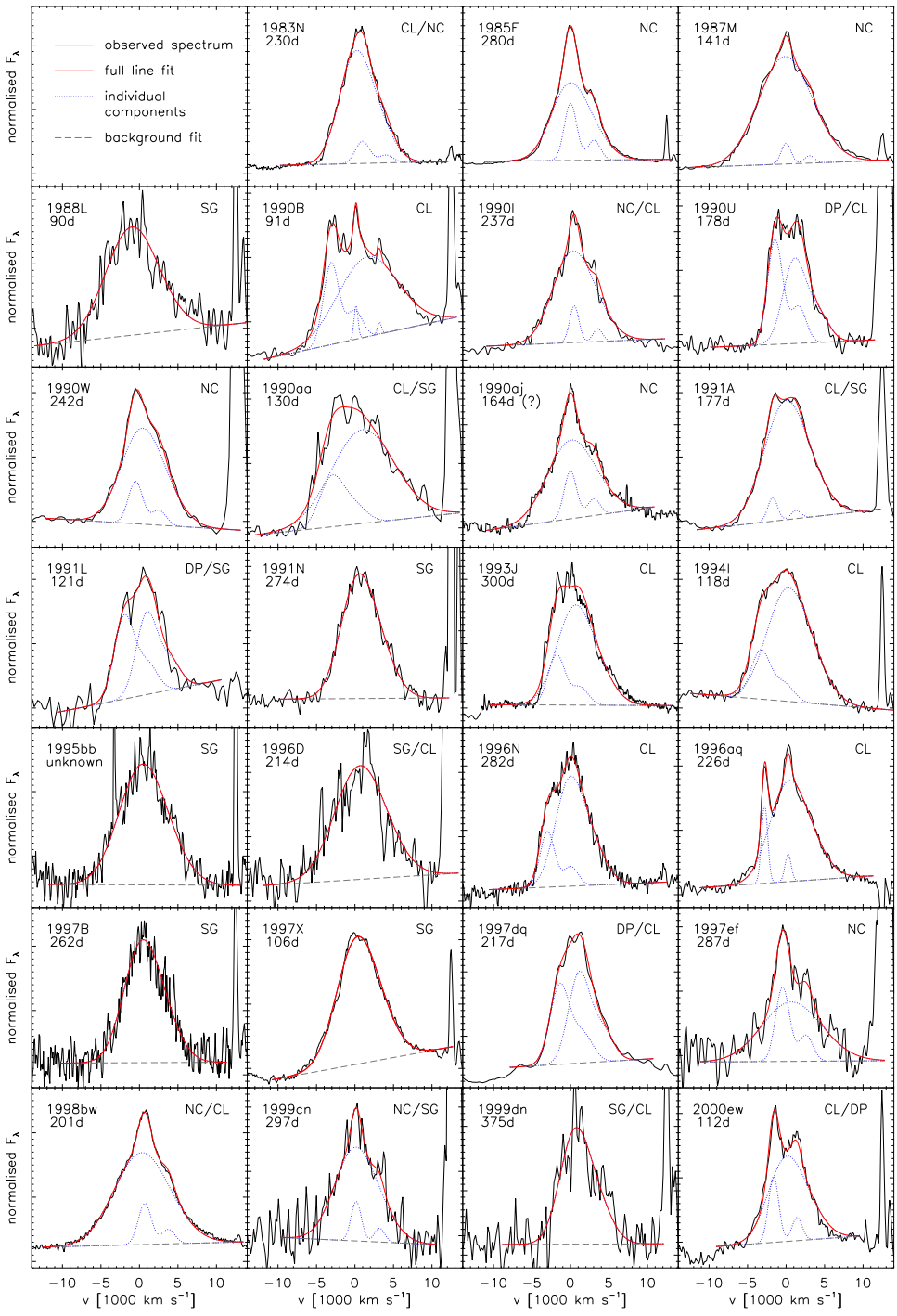
observed spectrum
full line fit
individual components
background fit
normalised F_λ
1983N 230d CL/NC
1985F 280d NC
1987M 141d NC
1988L 90d SG
1990B 91d CL
1990I 237d NC/CL
1990U 178d DP/CL
1990W 242d NC
1990aa 130d CL/SG
1990aj 164d (?) NC
1991A 177d CL/SG
1991L 121d DP/SG
1991N 274d SG
1993J 300d CL
1994I 118d CL
1995bb unknown SG
1996D 214d SG/CL
1996N 282d CL
1996aq 226d CL
1997B 262d SG
1997X 106d SG
1997dq 217d DP/CL
1997ef 287d NC
1998bw 201d NC/CL
1999cn 297d NC/SG
1999dn 375d SG/CL
2000ew 112d CL/DP
−10 −5 0 5 10
v [1000 km s^{-1}]

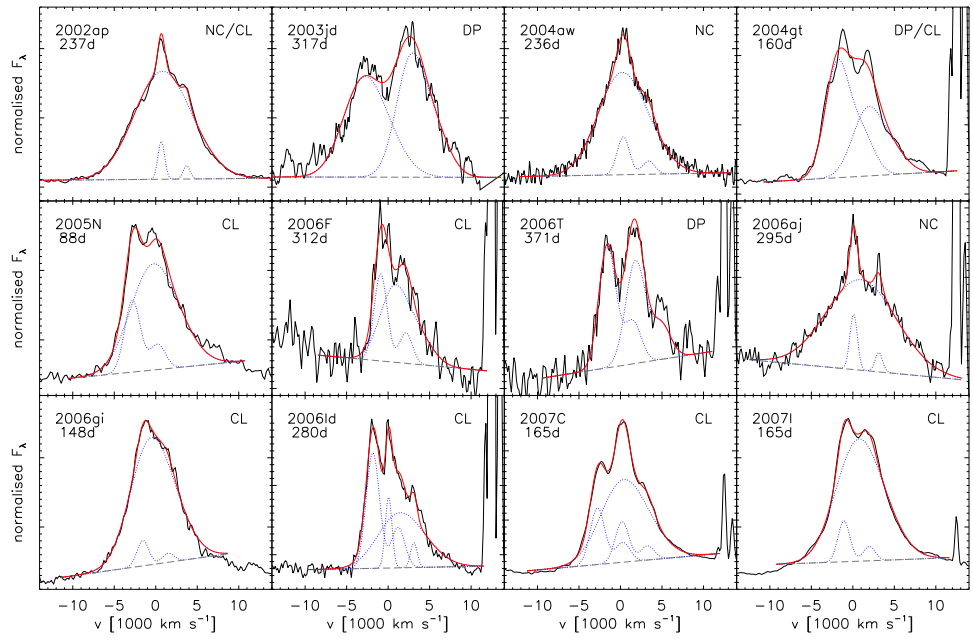

FIGURE 6.4— Observed spectra of our sample (solid black lines) with multi-Gaussian fits (Tables 6.5 and 6.6) overplotted (solid red lines). Individual components are overplotted as dotted blue lines, and the adopted linear background levels are indicated by dashed grey lines. Hα was subtracted from the spectrum of SN 1993J (cf. Table 6.5). The different line categories as defined in Section 6.5.1 are labelled as follows: SG for single Gaussian, NC for narrow core, DP for double peak, CL for clumps. Only one spectrum of each object is included in the figure.

(ii) *Dust formation.* As the SN ejecta expand and cool, at some point the temperature drops below the threshold where dust grains start to condense, so that dust (graphite or silicates) can form within the ejecta. Consequently, the light from the far side of the ejecta is partly absorbed, resulting in the suppression of the redshifted part of emission lines and in a net blueshift. Solid evidence of dust formation within the ejecta has been found in some Type II SNe, in particular SN 1987A, at very late phases (more than one year after explosion, cf. Danziger et al. 1989 and Lucy et al. 1989). In SNe Ib/c, on the contrary, this effect has never been unambiguously detected (see, e.g., Sollerman, Leibundgut & Spyromilio 1998 and Elmhamdi et al. 2004 for a discussion with respect to SNe 1996N and 1990I). Only in SN 1993J Matthews et al. (2002) detected an IR (L-band) excess from ~ 100 d after maximum onwards, which may indicate the formation of dust. However, from nebular emission-line profiles, Matheson

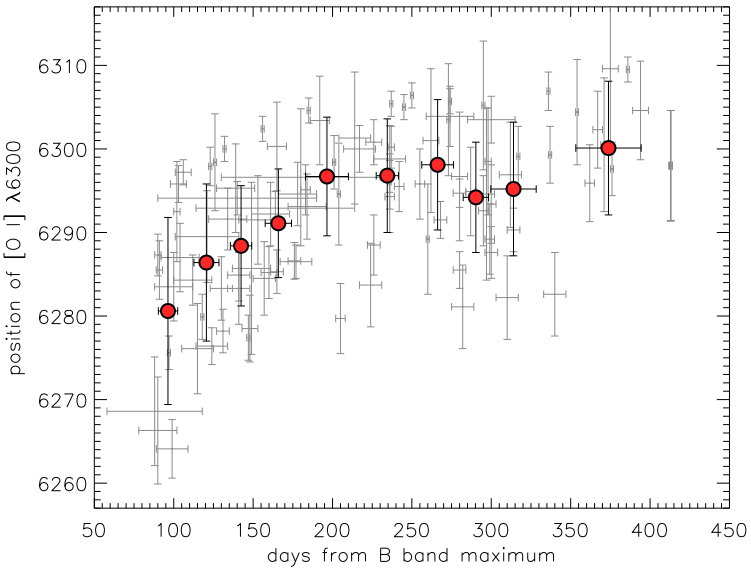

FIGURE 6.5— [O I] λ6300 line centroids (as inferred from the position of the λ6300 Gaussian in one-component fits), plotted vs. the phase of the spectra with respect to B-band maximum. The filled circles represent bins of 10 spectra. A systematic blueshift can be discerned at phases earlier than 200 d.

et al. (2000) found no evidence of dust-formation except for extremely late spectra ($\gtrsim$ 1000 d). The only exception seems to be the peculiar Type Ib SN 2006jc (Pastorello et al., 2007c; Foley et al., 2007; Pastorello et al., 2008), where dust formation is strong and starts at an unprecedentedly early phase of only 50 d after explosion (Smith, Foley & Filippenko, 2007), indicating exceptional physical conditions inside the ejecta. For the observed trend of blueshifted [O I] features in our sample of nebular SN Ib/c spectra, dust formation cannot be the right explanation. On the one hand the spectra studied here are too young ($\lesssim$ 400 d) to expect significant dust formation under normal conditions. On the other hand dust formation, if it played a role, should manifest in an *increasing* line blueshift with time, the exact opposite of what we observe.

(iii) *Contamination from other emission lines.* This is an issue which is difficult to verify, but equally hard to exclude. Contaminating lines blended into the blue wing of [O I] $\lambda\lambda$6300, 6364 could generate the observed blueshift. The contamination could arise from other forbidden nebular lines, but at earlier phases (when a strong blueshift is observed) also from residual emission of permitted photospheric lines. The biggest problem with this idea is the apparent lack of suitable candidates. Studying the blue shoulder visible in the [O I] line profile

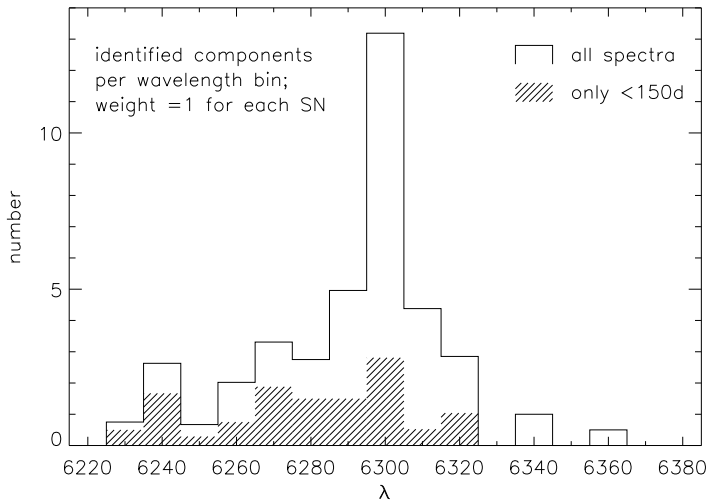

FIGURE 6.6— Histogram of components identified in the spectra with our Gaussian fitting procedure (wavelengths refer to [O I] λ6300; cf. Tables 6.5, 6.6 and Fig. 6.4). To give equal weight to all SNe, the numbers have been rescaled such that every SN yields a contribution equivalent to one component (hence the fractional numbers). The empty histogram refers to the full sample, the shaded region to a subsample of spectra taken earlier than 150 d after maximum.

of SN 1990I around +90 d, Elmhamdi et al. (2004) suggested a contribution of Fe II λ6239. However, this is not a particularly strong Fe line, and it is unclear why it should be so prominent while other, intrinsically stronger Fe lines are not. Looking at the fit components histogram in Fig. 6.6 one can find marginal evidence for a cluster of objects with fit components in the 6235–6245 Å bin. This could indicate the presence of another line at this wavelength. However, in Section 6.7 we demonstrate that in most of the objects that contribute to this cluster (SNe 1994I, 1996N and 1996aq) Mg I] λ4571 exhibits a line profile very similar to that of the [O I] λ6300 feature, suggesting a geometrical origin of the additional blue component rather than contamination from other lines. Also, concentrating on the subsample of spectra taken at < 150 d (shaded area in Fig. 6.6), it is evident that the bulk blueshift is not caused by an additional line at shorter wavelength, but by the rather flat distribution of components in the 6270–6300 Å range, and in particular the lack of a pronounced peak at 6300 Å. So, all in all we find no conclusive evidence for lines of other elements contributing to [O I] $\lambda\lambda$6300, 6364, but cannot finally exclude this option.

(iv) *Opaque inner ejecta.* The fact that the blueshift of [O I] at not too late phases is apparently not related to the presence of other lines, and the fact that

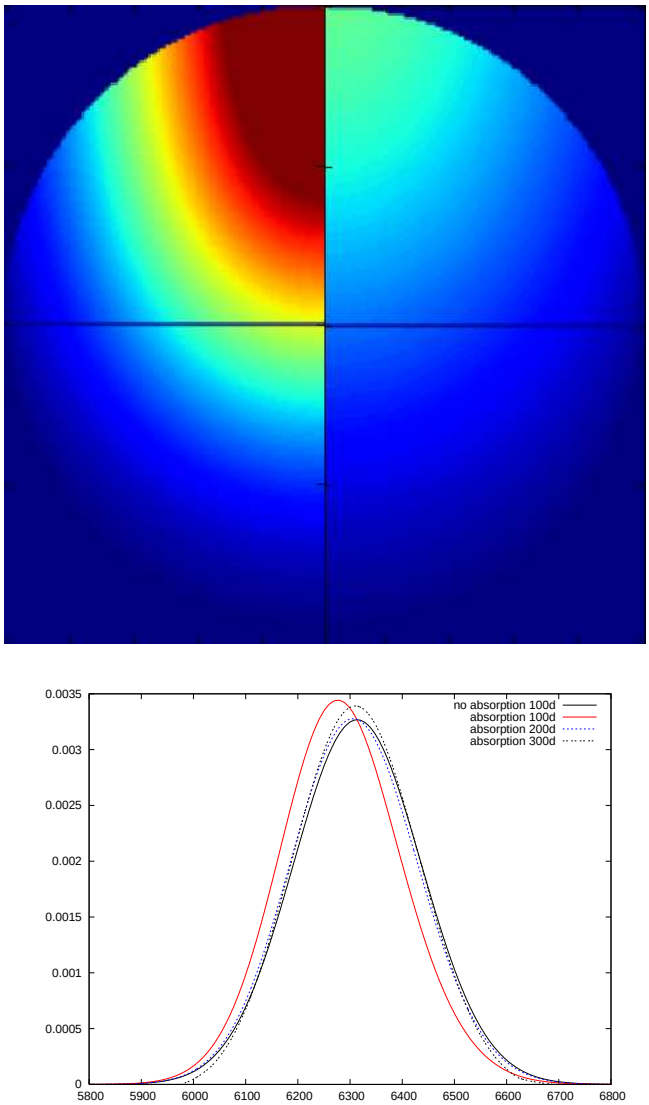

FIGURE 6.7— *Top panel:* Toy model of not completely optically thin ejecta, the absorption fraction being proportional to the column density between the observer and the emission site (the emission is assumed to be be proportional to the matter density). The flux from the rear side of the SN ejecta is partially absorbed before arriving at the observer, who is located at infinite distance to the bottom. The re-emission of absorbed photons is not considered. The left part of the figure shows the absorption fraction at a phase of 100 d, the right part at 200 d.
Bottom panel: Time-evolution of the [O I] $\lambda\lambda 6300, 6364$ line profiles in the above model, normalised to an integral flux of unity. For comparison, the unabsorbed profile is also shown in the figure.

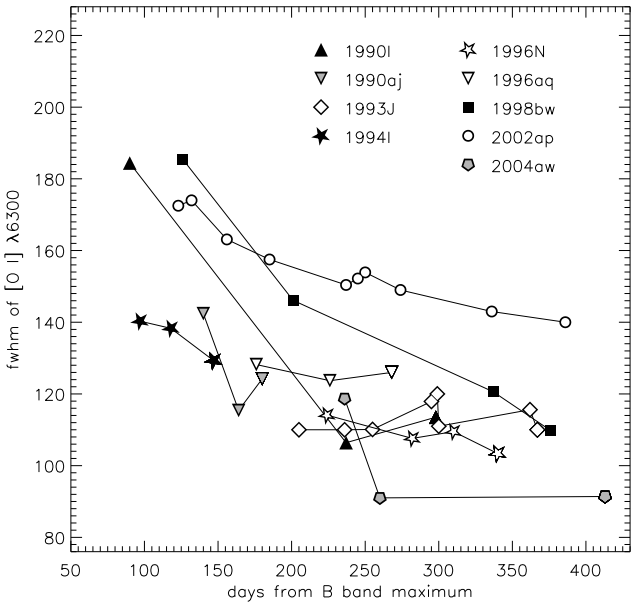

FIGURE 6.8— *fwhm* of the one-component Gaussian fit to the [O I] λ6300 line as a function of time. Only SNe with good temporal coverage are displayed.

in several of the affected spectra (e.g. SNe 1988L and 1991A) the blueshifted line has a nearly Gaussian profile, leaves us with residual opacity in the inner ejecta as the most likely explanation. This could be caused by densely packed weak Fe transitions, but also be pure electron-scattering opacity.[2] In any case the optically thick inner ejecta would prevent light from the rear side of the SN from penetrating, causing a flux deficit in the redshifted part of emission lines. To see the effect on the line profile, we created a simple toy model (see Fig. 6.7), in which photons are absorbed on their way to an observer with a probability proportional to the ambient matter density (grey opacity). The integral absorption fraction for photons from a certain point in the ejecta is hence proportional to the column density from the observer to this point. The re-emission of the absorbed photons is not considered. While the absolute effect on the line position depends on the assumed absorption cross-section, from construction it is clear that the column density scales with t^{-2}. Fig. 6.7 (lower panel) shows that even with settings that result in a 30 Å shift at 100 d, the

[2]The different mechanisms would leave a slightly different imprint on the resulting line profile, electron-scattering creating a characteristic faint but extended tail on the red side. However, the possible contamination from an underlying pseudo-continuum at the relevant phases prohibits a distinction of the two mechanisms on the basis of the observed profiles.

blueshift becomes almost negligible by 200 d, in good agreement with the observations. A problem arising from the idea of absorption or scattering within the ejecta is the prediction of increasing emission-line widths with time, when the suppression of the lines' red parts decreases. This is opposite to the trend observed in our sample (see Fig. 6.8). However, changes in the excitation conditions, in particular a decreasing γ-ray opacity and a transition to more local positron deposition as dominant excitation mechanism, may overcompensate other effects and ensure compatibility with the observations.

6.5 Statistical analysis, inferred ejecta geometries

Beyond achieving a better understanding of individual objects (which will be the subject of Section 6.6), the intention of the multi-Gaussian line fitting was to obtain an idea of the overall presence of particular ejecta geometries in the sample. Of course, without additional assumptions (such as spherical symmetry) it is not possible to restore the full 3D density distribution from its 1D projection given by the line profiles. While a forward calculation of emerging profiles for a given density distribution is staightforward, backward inference is often hindered by the degeneracy of different solutions.

A brief overview of some possible ejecta geometries ('genotypes', to use a nomenclature from genetics) and the corresponding observed line profiles ('phenotypes') is given in Table 6.3 and Fig. 6.9, illustrating the power, but also the limitations of backward inference. In fact, in numerous situations we cannot confidently say what the ejecta geometry should be, but in some of them we can at least say what it is definitely not.

6.5.1 Taxonomy

Based on the results of the multi-Gaussian fitting, we define four principal classes of line profiles. Note that this classification is neither natural nor unique. It is rather a choice based on the experiences during the actual fitting. Linking the different classes to actual matter-density distributions is not always straightforward.

(i) *Gaussian profiles*, well reproduced by one-component fits, with the residuals showing no evidence of a second component. These profiles probably come from almost spherically symmetric ejecta with a Gaussian-like density distribution (cf. Section 6.3.1), but could alternatively be generated by aspherical, jet-like explosions when viewed from intermediate angles (40–50°, depending on the degree of asphericity; Maeda et al. 2008).

(ii) *Narrow-core lines*, characterised by a component with small *fwhm* atop a broad base, fairly well centred at the rest wavelength (offset $\lesssim 15$ Å). This kind

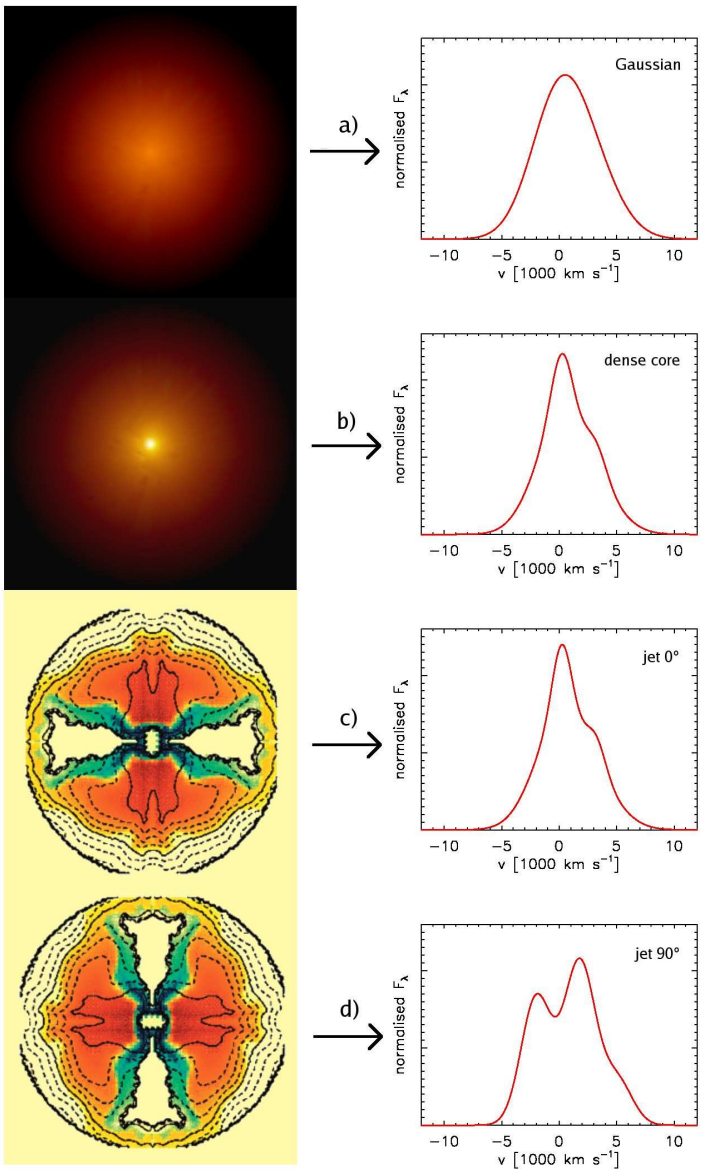

FIGURE 6.9— Correspondence between ejecta morphology (left) and the resulting [O I] $\lambda\lambda 6300, 6364$ profile (right) for selected cases. (a) shows spherically symmetric ejecta with a Gaussian density distribution, (b) a spherical profile with enhanced central density, while (c) and (d) represent a configuration as in the jet-model of Maeda et al. (2002) and Mazzali et al. (2005d), at viewing angles of 0° and 90° relative to the jet axis, respectively. The cases (b) and (c) yield similar [O I] profiles.

TABLE 6.3— Selected ejecta geometries and corresponding line profiles.

Oxygen density distribution ('genotype')	Line profile ('phenotype')	Global symmetry
radial Gaussian	Gaussian[a]	spherically symmetric
enhanced central density	narrow core on top	spherically symmetric
hard-edged homogeneous sphere	parabolic	spherically symmetric
spherical shell	flat-topped	spherically symmetric
torus viewed from top	narrow core	axisymmetric
torus viewed from the side	double peak, symmetric to λ_0	axisymmetric
torus viewed from intermediate angle	Gaussian-alike	axisymmetric
clumpy ejecta	fine-structured peak	asymmetric
unipolar jet, one-sided blob	extra-peaks / shoulders, shifted with respect to λ_0	asymmetric

[a] For the deduction see Section 6.3.1.

of appearance is quite frequent and can be explained either by axisymmetric explosions viewed from near the major axis, with the oxygen distributed in a torus or disk perpendicular to the line of sight (as inferred by Mazzali et al. 2001, Maeda et al. 2002 and Maeda et al. 2006 for SN 1998bw), or by spherically symmetric ejecta with a central density enhancement with respect to a Gaussian density distribution, i.e. a dense core in the ejecta. A clump of oxygen moving nearly perpendicular to the line of sight [cf. (iv)] could be another option.

(iii) *Double-peaked profiles* with two almost equally strong components, one blueshifted and the other redshifted by about the same amount, are most readily explained by a torus-shaped oxygen distribution viewed nearly sideways (from angles of $\sim$60–90°to the symmetry axis; Mazzali et al. 2005d and Maeda et al. 2008). In spherical symmetry, a thin oxygen shell may result in a flat-topped line, but no double peak can be realised. Hence, this type of line profile requires asphericity. The prototype of this class is SN 2003jd (Mazzali et al., 2005d; Valenti et al., 2007a).

(iv) *Multi-peaked or asymmetric profiles*, produced by additional components of arbitrary width and shift with respect to the main component. These profiles are either indicative of overall clumpy ejecta, a single massive (maybe Co-enhanced) blob, or a unipolar jet. They cannot be reproduced within spherical symmetry.

Dividing the SNe of our sample into these categories may in some cases be ambiguous. Care has to be taken not to confuse a blob, which together with the main peak may generate the appearance of a double-peaked feature, with

TABLE 6.4— SN taxonomy in terms of [O I] line profiles.

Category	Number[a]	Percentage
(i) Gaussian	7^{+4}_{-2}	18^{+10}_{-5}
(ii) Narrow core	11^{+1}_{-4}	28^{+3}_{-10}
(iii) Double peak	6^{+1}_{-4}	15^{+3}_{-10}
(iv) Asymmetric / clumps	15^{+8}_{-4}	39^{+21}_{-10}

[a] Cf. Fig. 6.4 for a linkage to the individual objects.

'true' double peaks arising from a toroidal oxygen distribution as defined in (iii). Furthermore, this pretty simple scheme is complicated by frequently observed global shifts of the [O I] feature with respect to its rest wavelength (see also Section 6.4). Relative offset between the main and the narrow components in narrow-core objects up to ~ 20 Å, i.e., 1000 km s^{-1}, are also encountered.

To facilitate the discussion, we define α_i as the flux of the i-th component of the fit normalised to the total flux of the oxygen feature. Fig. 6.10 shows an attempt to visualise the group-membership of a SN by plotting – for SNe of the classes (ii) to (iv) – the absolute wavelength offset between the two fit components versus $\alpha_{\rm minor}$, the normalised flux of the weaker component. In this diagram, narrow-core SNe of class (ii) populate a strip along the abcissa ($|\lambda_1 - \lambda_2| \lesssim 20$ Å), double peaks [class (iii)] an area of larger wavelength offset and $0.4 \lesssim \alpha_{\rm minor} \leq 0.5$, while SNe with asymmetric or clumpy profiles [class (iv)] are typically located in a region characterised by $\alpha_{\rm minor} \lesssim 0.3$ and $|\lambda_1 - \lambda_2| > 20$ Å. Note, however, that some objects lying in the narrow-core strip actually belong to class (iv) for their narrow component having too large an offset from the rest wavelength. In Table 6.4 the statistical summary of this analysis is presented.

6.5.2 Statistical evaluation

The number of SNe whose [O I] profiles are well fitted with single Gaussians is remarkably small (at most 11 out of 39 objects, or 28%). Also, the maximum number of potentially spherically symmetric objects (i.e., all SNe with Gaussian profiles or narrow cores, if the latter are interpreted as central density enhancement) is 23, or 59%. Considering that for some of these objects simply the S/N is too low to identify more than one component, that also jet-like explosions yield single-peaked symmetric profiles if viewed not too far from the jet axis, and that clumps moving roughly perpendicular to the line of sight can mimic narrow line cores, it is evident that 59% can only be a conservative upper limit,

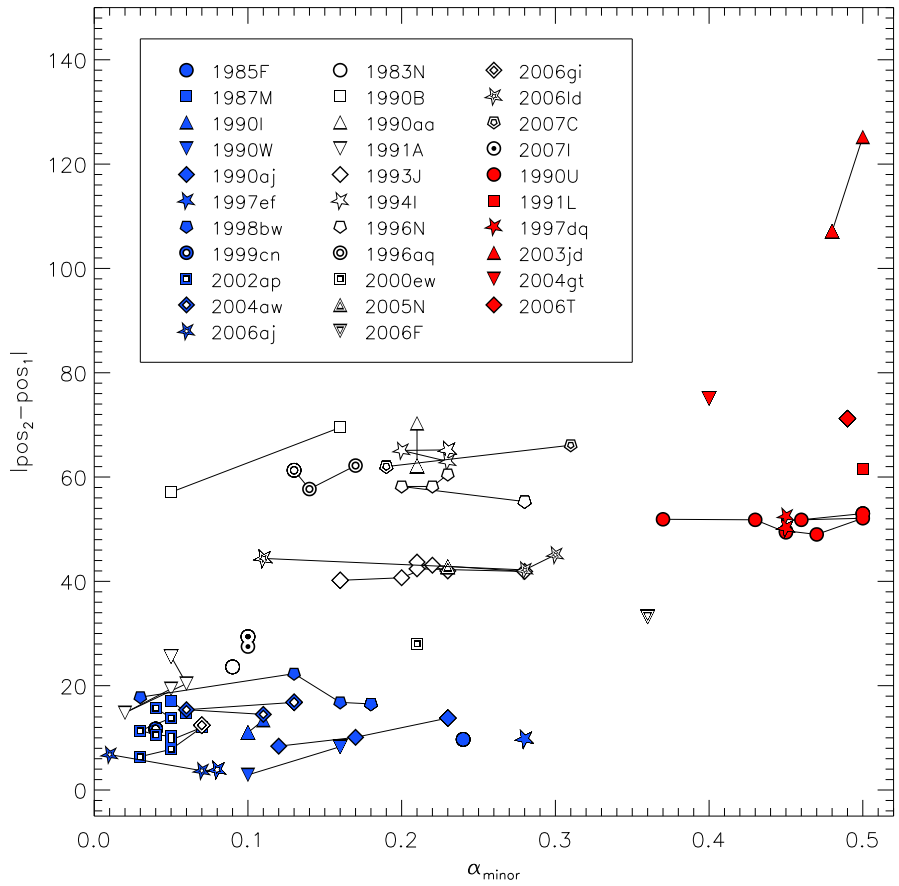

FIGURE 6.10— Absolute wavelength difference between two components found by multi-Gaussian fitting of [O I] λ6300, as a function of $\alpha_{\rm minor}$, the strength of the weaker component. Objects with single-Gaussian line profiles (cf. Fig. 6.4) have been omitted for clarity. Filled blue symbols stand for narrow-core SNe, filled red symbols for double peaks, and open symbols for SNe with asymmetric or clumpy ejecta. The different classes appear fairly well separated in this plot.

and that the actual number of spherically symmetric stripped-envelope CC-SNe is probably below 50%.

There are about 6 class (iii) objects with symmetric double peaks in the sample (i.e., 15%), but only for 2 of them (SNe 2003jd and 2006T) we consider this classification robust. This suggests a significantly lower percentage of double peaks than in the samples of Maeda et al. (2008) and Modjaz et al. (2008), where 5 out of 18 (28%) and 3 out of 10 (30%) SNe were double-peaked.

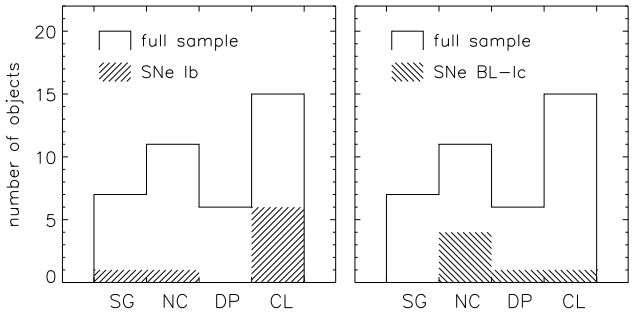

FIGURE 6.11— Allocation of the SNe in our sample to the line-profile classes defined in Section 6.5.1: SG stands for 'single Gaussian' [class (i)], NC for 'narrow core' [class (ii)], DP for 'double-peaked' [class (iii)] and CL for 'asymmetric / clumpy' [class (iv)] (cf. Table 6.4). SNe Ib and BL-Ic SNe are separately shown in the left and right panel, respectively.

However, it should be noted that some of these double-peak objects of Maeda et al. (2008) and Modjaz et al. (2008), such as SNe 2004ao, 2005aj and 2005bf, might not qualify for our class (iii) for their lack of symmetry about λ_0, and might rather end up in class (iv).

From the models of Maeda et al. (2006, 2008) it can be deduced that, almost independent of the degree of asphericity, for jet-explosions the ratio of narrow cores to double peaks should be $\sim 1:5$. This suggests about 1 narrow-core SN in our sample to be a jet-like event, while the majority of the narrow-core profiles should descend from a different configuration, maybe a dense core of the ejecta. In the sane sense, the low number of double peaks also limits the total number of jet-like explosions. For mildly aspherical models (BP2 of Maeda et al. 2006) 34% of all jet-like explosions should be seen as double peaks (Maeda et al., 2008), suggesting a total of ~ 18 jet-SNe in our sample (46%). For strongly aspherical models (BP8) 64% should appear double-peaked, yielding not more than ~ 9 jet-SNe (23%) for our sample.

Another honestly unexpected result is the way the traditional SN types (i.e., BL-Ic, Ic, Ib and IIb) are allocated to the different line-profile classes (Fig. 6.11). While SNe Ic, which form the majority of our sample (59%), are relatively homogeneously distributed, SNe Ib (21% of our sample) are strongly (to 75%) clustered in the multi-peaked / aspherical category. Although the total number of these objects is still too small for robust statements, we are tempted to attribute some significance to this finding. Similarly, broad-line SNe Ic ($\sim 15\%$ of our sample) exhibit a preference for nebular [O I] lines with narrow cores (67%). At first, this seems to support the jet model. However, as discussed above, if all broad-line SNe Ic of the narrow-core class were interpreted as jet-

events, a much larger number of double peaks should be observed. [3]

The *fwhm* of [O I] λ6300 (taken from the one-component fit), averaged over all epochs, increases from SNe Ib/IIb (109.3 ± 18.1 Å) over normal-energetic SNe Ic (124.9 ± 28.9 Å) to broad-line SNe Ic (154.2 ± 36.2 Å), reflecting the trend found in early-time spectra. However, also the variation of the *fwhm* increases in this direction, indicating particularly strong diversity in the ejecta geometry of BL-SNe Ic.

As a bottom line, strong deviations from spherical symmetry affect all types of stripped-envelope CC-SNe, and are not confined to particularly energetic or highly-stripped events. This is in perfect agreement with the results of Modjaz et al. (2008).

6.6 Discussion of individual objects

In the previous sections we have presented simple analytic fits to the [O I] $\lambda\lambda 6300, 6364$ features in 98 nebular spectra of 39 different stripped-envelope CC-SNe, and found a substantial amount of diversity in the line profiles, indicative of deviations from spherical symmetry in a majority of the objects. However, at a close look also remarkable patterns and similarities between different objects can be discerned within this zoo of line profiles. In the following the properties of individual SNe with either particularly-high-quality data or interesting line profiles are discussed in more detail.

6.6.1 SNe 1994I, 1996N and 1996aq: blueshifted blobs?

Studying the late-time (≥ 180 d) spectra of SN 1996N, Sollerman et al. (1998) noted an unusual blueshift of the [O I] $\lambda\lambda 6300, 6364$ feature. Indeed, fitting with one component we find a bulk blueshift of 18 Å, more than in any other SN of our sample at comparatively late epochs. The fit with one component is not fully satisfactory; to improve it, a second component has to be introduced. In the resulting setup the main component is nearly at rest, but the second component is strongly blueshifted by ~ 3000 km s^{-1} (cf. Fig. 6.4 and Table 6.5), and appears very prominent and broad (*fwhm* $= 2300$ km s^{-1}, $\alpha \sim 0.2$ to 0.3).

What has never been noticed so far is the similarity of the [O I] line profiles of SNe 1996N and 1994I (although the latter was only observed at earlier phases, not later than 150 d past maximum). In SN 1994I the oxygen feature is similarly blueshifted, and also here the shape of the line suggests the presence of a second

[3] Note that the BL-Ic SNe 1998bw and 2006aj, members of the narrow-core class, were discovered only after the detection of their associated GRBs, so that some bias may be introduced by them. Since we assert no claim to a strictly unbiased sample anyway, we included also these two objects in our analysis throughout this work.

component, resembling the configuration in SN 1996N. Finding such an unusual [O I] line profile in SN 1994I was unexpected, given that this is one of the most soundly studied SNe Ic to date and often utilised as prototype of the entire class. Even Modjaz et al. (2008) did not mention the blueshift and asymmetric profile in their recent work.

SN 1996aq, at a first glance, seems to feature a completely different, double-peaked [O I] line. However, the fitting suggests that the main difference is in the width of the blueshifted component, which is significantly narrower in SN 1996aq ($fwhm = 1000$ km s^{-1}), enabling a separation of the λ6300 and λ6364 lines and thus creating the impression of a double peak. The λ6364 line of the blueshifted narrow component is almost perfectly centred at 6300 Å, so that the main feature appears sharply peaked.

The most convincing explanation for the situation encountered in the three SNe is to assume that oxygen-rich blobs are moving towards the observer at high velocities. If such a blob is mostly made up of oxygen without enhanced Co abundance, it has to carry quite some mass to account for the observed emission. In fact, the mass fraction would be given by the fractional flux of the clump, $\alpha_{\rm cl}$. In SN 1996aq, $\alpha_{\rm cl}$ is about 0.15, in SNe 1994I and 1996N even 0.2–0.3. Moving at a velocity $\gtrsim 3000$ km s^{-1}, the blob would carry enormous momentum, which would have to be counter-balanced for the sake of momentum conservation. Since the remainder of the oxygen is perfectly centred at rest, the required compensation would have to be provided by Fe-rich material or the compact remnant of the core collapse. In fact, strong neutron star kicks have been observed (e.g. Cordes, Romani & Lundgren, 1993) and reproduced in simulations of anisotropic explosions with dominant dipole ($l = 1$) mode in the ejecta (Scheck et al., 2004, 2006). Nevertheless, the observed configuration in SNe 1994I and 1996N means an utmost challenge for this scenario, which could only be mitigated if the blob was enriched with ^{56}Co and therefore more strongly excited than the surrounding material, reducing the mass needed to explain the observed emission.

In our entire sample there is no single object with a similarly strong additional component redshifted. Since for a clump or a one-sided explosion there should be no preferential direction, this fact creates an uneasy feeling. However, the only alternative option one can think of, i.e., contamination from other lines, can be excluded for SNe 1994I and 1996N by comparison of the [O I] with the Mg I] λ4571 line (Section 6.7). In both objects the profiles of Mg I] and [O I] are nearly identical, excluding contamination effects, and leaving us with a rather exceptional ejecta geometry as the only viable explanation for the observed line profiles.

6.6.2 SNe 1990B, 1993J and 2006ld: clumpy ejecta

The presence of multiple clumps in the ejecta of SN 1993J was already noticed and extensively discussed by Spyromilio (1994) and Matheson et al. (2000), who identified at least 5 distinct very narrow components atop the broad [O I] $\lambda\lambda 6300, 6364$ feature in high-S/N good-resolution spectra. We made no attempt to reproduce these narrow components through Gaussian fitting, since the required large number of parameters would have made robust statements impossible. Instead we contented ourselves with fitting the overall peak profiles in the Hα-subtracted spectra (cf. Table 6.5), which already required two components to obtain a good match. Looking at the residuals of the fit, there is evidence of an additional emission line near 6410 Å, which was also noticed by Patat, Chugai & Mazzali (1995), who speculated on an identification with Fe II lines.

Evidence of clumpy ejecta can also be found in SNe 1990B, 2006ld and, possibly, 1990aa (see Fig. 6.4), but for the latter the S/N is rather low. In SN 1990B the number of clumps may be lower than in SN 1993J, but the line profile is highly complex, and even an attempt to reproduce it with 3 fit components was not fully satisfactory. Also in SN 2006ld at least 3 components were required to obtain an acceptable fit.

6.6.3 SNe 1998bw and 2002ap: narrow cores?

The nebular [O I] emission line of SN 1998bw has been subject to a number of studies (Mazzali et al., 2001; Maeda et al., 2002, 2006), in which the narrow line core was usually explained as emission from a disk- or torus-shaped oxygen distribution viewed nearly from top. Together with the nebular Fe lines being broader than [O I] $\lambda\lambda 6300, 6364$, this gave rise to the idea of a strongly aspherical, jet-like explosion, in perfect agreement with expectations for a GRB-related SN. The nebular spectra of SN 2002ap have not been studied in the same detail, but Foley et al. (2003) and Mazzali et al. (2007c) remarked the similarity of the SN 2002ap line profiles with those of SN 1998bw, and Mazzali et al. (2007c) suggested strong asphericity.

SNe 1998bw and 2002ap share an [O I] $\lambda\lambda 6300, 6364$ line with a narrow component on top of a much broader base, and in both SNe the narrow components are redshifted with respect to both the broad base and the rest wavelength λ_0 (Patat et al., 2001; Leonard et al., 2002; Foley et al., 2003). From the best-fit parameters reported in Table 6.5, mean redshifts of 12.3 ± 3.4 Å (586 ± 162 km s^{-1}) and 13.8 ± 1.3 Å (657 ± 62 km s^{-1}) with respect to λ_0 are inferred for SNe 1998bw and 2002ap, respectively (cf. Fig 6.12). Relative to the broad bases, mean offsets of 18.4 ± 2.7 Å (876 ± 129 km s^{-1}) and 10.5 ± 2.9 Å (500 ± 138

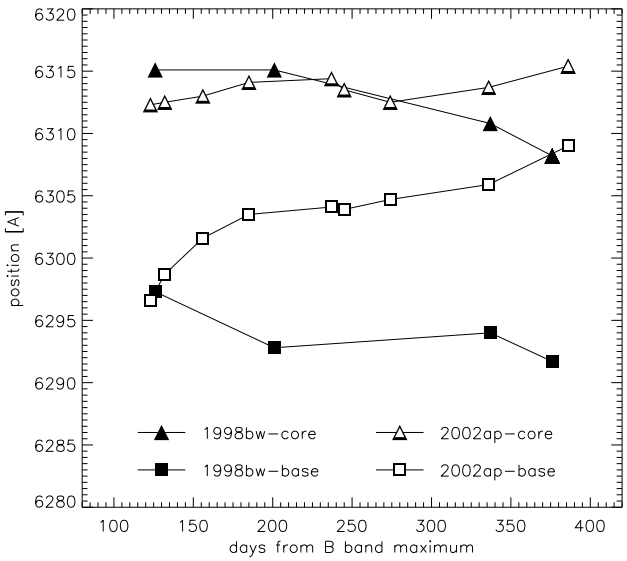

FIGURE 6.12— Position of the broad line bases and the narrow cores of the [O I] λ6300 feature in SNe 1998bw and 2002ap as a function of time (cf. Table 6.5).

$\mathrm{km\,s^{-1}}$) are observed.

Such large shifts challenge the jet-model favoured for SN 1998bw (and suggested as a possibility for SN 2002ap), since it predicts symmetric nebular lines centred at their rest wavelength. The same accounts for spherically symmetric models with enhanced central density. For this reason we conservatively labelled SNe 1998bw and 2002ap *uncertain* narrow cores in Fig. 6.4, considering the presence of a clump an alternative option. Other SNe of the narrow-core group exhibit similar line offsets, but mostly less pronounced than in SNe 1998bw and 2002ap.

6.6.4 SNe 2003jd and 2006T: classical double peaks

SN 2003jd was the first SN in which a broad double-peaked [O I] $\lambda\lambda 6300, 6364$ feature was reported and interpreted as the signature of a jet-like explosion viewed almost perpendicular to the jet axis (Mazzali et al., 2005d). Recently, further objects with similar characteristics have been identified. Based on a sample of 18 SNe, Maeda et al. (2008) estimated the fraction of objects with a double-peaked [O I] line to be as high as 28%.

Evaluating the line profiles by eye, the frequency of double peaks in our sample appears to be comparable or slightly lower, at most 11 out of 39 objects or 28.2%. However, the multi-Gaussian fitting reveals that several of these objects

do not fulfil the class (iii) double-peak criteria defined in Section 6.5, rendering explanations other than a toroidal or disk-like geometry more favourable. SN 2006aj, for instance, merely exhibits a narrow component atop a broad peak with a *fwhm* sufficiently small for the λ6300- and λ6364-lines to be resolved. The blueshifted narrow peak of SN 1996aq is better explained assuming a blob at high velocity (Section 6.6.1). In SN 1990B the broad and highly structured peak is indicative of overall clumpy ejecta (Section 6.6.2), and for SNe 2000ew and 2004gt the situation is unclear and pretty complicated. These objects are therefore discussed in Section 6.6.5. The only robust cases of double peaks likely originating from a jet-like geometry are SNe 2003jd and 2006T. In SNe 1990U, 1991L and 1997dq, though nicely fitted with a double-peak configuration, the separation of the two fit components is not nearly as wide as for instance in SN 2003jd, and the line profiles could also be explained in a different way (e.g. by emission from a shell).

For its high ejecta velocities and its double-peaked [O I] profile, SN 2003jd has been proposed to be associated with a GRB viewed strongly off-axis (Mazzali et al., 2005d). In such a case, the γ- and X-ray emission of the GRB would not be seen because of the strong collimation of the jet and the relativistic forward-beaming of the radiation caused by the high Lorentz factors of the jet material. However, at radio wavelengths the beaming is much weaker, so that radio emission should be observable at late phases. SN 2003jd was not detected at radio wavelengths (Soderberg et al., 2006), making an association with a GRB unlikely. SN 2006T was classified as Type IIb (Blondin et al., 2006), meaning that at least a part of the H and the entire He envelope are left. The relativistic jet of a GRB would have to penetrate these layers, and – according to simulations – would probably die before reaching the surface.[4] Hence, SN 2006T may not be a good candidate GRB-SN either, supporting the view of Modjaz et al. (2008) that strong asphericity is ubiquitous in core-collapse SNe, and not necessarily a sign of a particularly energetic explosion.

6.6.5 SNe 2000ew and 2004gt: jet-events or 'fake' double peaks?

At a first glance, SNe 2000ew and 2004gt exhibit double-peaked [O I] profiles, and – like for SNe 2003jd and 2006T – one might be tempted to assume that they originate from jet-like explosions viewed from near the equatorial plane (cf. Section 6.6.4). However, in the case of SNe 2000ew and 2004gt the conclusion is not all that clear. First of all, the two peaks are closer to each other, separated by not more than 60 to 80 Å. Then, their intensity ratio appears inverted with

[4] It has been speculated that also some Type IIn SNe might be related to GRBs (Germany et al., 2000; Turatto et al., 2000). However, to date no firm association could be established.

respect to those of the objects in Section 6.6.4, the blue peak being stronger than the red one.

Attempting to reproduce these observed line profiles with a two-component fit in a classical double-peak configuration (i.e., two components of similar *fwhm* and intensity, one blue- and one redshifted), always the red peak will come out stronger, since, for the given separation of the peaks, the λ6364-line of the blue component adds to the λ6300-line of the red one. Avoiding this problem requires to reduce significantly the strength of the redshifted component, which in turn makes the interpretation of toroidal oxygen distribution less straightforward. Only if the density was high enough for the emission from the rear side of the ejecta to be damped significantly (cf. Section 6.4), could SNe 2000ew and 2004gt be explained by a jet-configuration. Since the spectra of SNe 2000ew and 2004gt are both relatively young (≤ 160 d), at least compared to those of SNe 2003jd and 2006T (cf. Table 6.1), and since in both of them a fairly strong net blueshift of the [O I] feature of about 15 Å is observed, this may be a valid option.

Despite the similarity of the [O I] line profiles of SNe 2000ew and 2004gt, the lowest-χ^2 two-component fits invoke different principal configurations (cf. Fig. 6.4). While for SN 2004gt indeed a setup with one blue- and one redshifted component of similar width (but with the intensity of the redshifted one being reduced) provides the best fit, the line profile of SN 2000ew can be better reproduced by a broad component almost at rest, and a narrow one (*fwhm* = 1600 km s^{-1}) blueshifted by ~ 34 Å on top (with $\alpha \sim 0.2$). With this ambiguous result, SNe 2000ew and 2004gt also demonstrate the limitations of the multi-Gaussian fitting method to enable a reliable analysis.

6.6.6 SNe 1991N and 1997X: spherical explosions?

Eventually, some of the [O I] lines in Fig. 6.4 seem to be well reproduced by one-component fits, as expected for spherically symmetric explosions with a density profile not too different from CO 110. This includes SNe 1988L, 1991N, 1995bb, 1996D, 1997B, 1997X and 1999dn, corresponding to $\sim 18\%$ of all objects. Note that even though this is remarkably low a number, it may still be an overestimate, since many of the spectra in this group suffer from poor S/N, and higher-quality data might reveal a more complex structure, requiring additional fit components to be properly reproduced.

Furthermore, as shown by Maeda et al. (2006, 2008), also aspherical, axi-symmetric explosions may produce line-profiles almost indistinguishable from spherical ones when viewed from intermediate angles of 40–50°(i.e., neither close to the polar axis nor to the equatorial plane). This effect may further

reduce the number of spherically symmetric objects in our sample, as some of the SNe mentioned above could be of this type. In fact, from the Maeda models one would expect their number to be similar that of double-peaked SNe [class (iii)], i.e. 2–7 in our sample. SN 1997X, for which Wang et al. (2001) – based on exceptionally strong continuum polarisation of the order of 4% – suggested highly aspherical ejecta, may be such a case. Hence, from our set of spectra, even the most extreme assumption that none of the objects under investigation is spherically symmetric cannot be excluded.

6.7 The profile of Mg I] λ4571

From hydrodynamic explosion models for SN 1998bw, Maeda et al. (2006) inferred that Mg and O should have a similar spatial distribution within the SN ejecta, even in strongly aspherical explosions. This distribution can deviate significantly from those of heavier elements such as Fe or Ca, as demonstrated by Mazzali et al. (2005d) comparing the widths and profiles of Fe and O emission lines in nebular spectra of SNe 1998bw and 2003jd. The similar distribution of Mg and O should manifest in the profiles of isolated Mg and O emission lines being similar. To verify this, we had a look at the profile of the semi-forbidden Mg I] λ4571 line in all spectra with sufficient S/N in the respective wavelength range.

What complicates a direct comparison of the Mg I] and [O I] lines is the fact that the [O I] feature is not a single line, but a superposition of [O I] λ6300 and [O I] λ6364. However, as described in Section 6.3.2, in nebular SN Ib/c spectra the conditions are always such that the λ6300 and the λ6364 line should have a ratio of 3 : 1. Making use of this information, we first isolated the Mg I] λ4571 feature, subtracting a linearly fitted background that accounts for any kind of pseudo-continuum. Then we rescaled the Mg I] line to 1/3 of its initial intensity, shifted it by 46 Å (which is the equivalent of the 64 Å offset of the two [O I] lines for the rest wavelength of 4571 Å) and added it to the original profile. The so-derived modified Mg I] profile could then be compared with the observed [O I] feature.

For most spectra of our sample, even those with rather complex ejecta geometry, we find an impressive similarity of the Mg I] and [O I] line profiles within the noise level and the uncertainty in subtracting the continuous background (see Fig. 6.13). This indicates that the spatial distribution of Mg and O in the ejecta is indeed mostly similar. However, in some spectra differences are evident. This can be seen in Fig. 6.14, where examples with a poor overlap of the [O I] and modified Mg I] features are shown. Most of these spectra are not very late, typically < 200 d, which leaves room for different speculations.

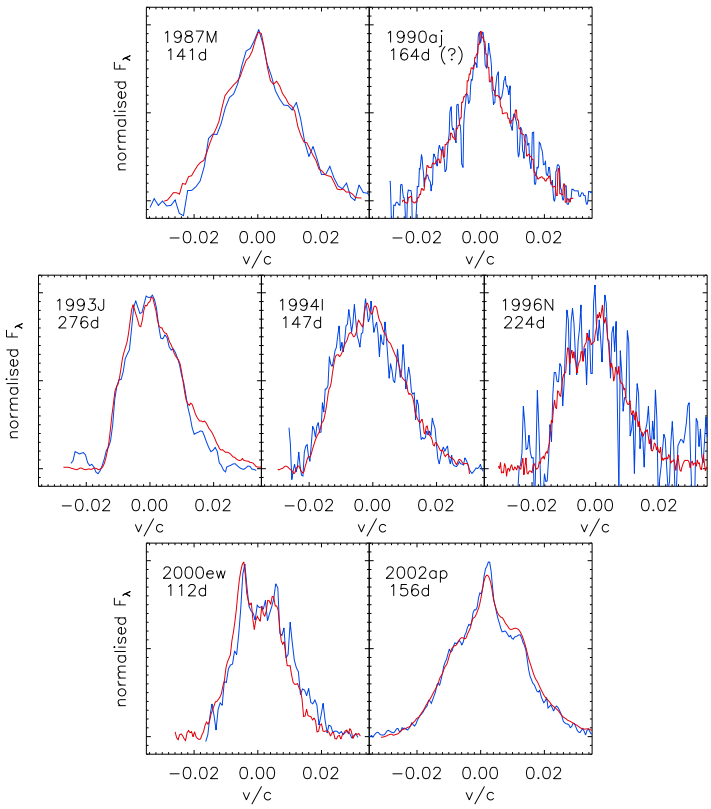

FIGURE 6.13— Comparison of Mg I] λ4571 and [O I] $\lambda\lambda$6300, 6364 line profiles (with a second component added to Mg I] artificially to account for the doublet nature of [O I], see discussion). A subsample of objects with a good overlap is shown. The modified Mg is plotted in blue, O in red. For SN 1998bw cf. Fig. 6.15.

(i) The O- and Mg-rich parts of the ejecta may indeed have different geometry owing to the chemical stratification of the progenitor star and the hydrodynamic details of the explosion. In this scenario, however, the differences in the line profiles should remain constant during the entire nebular phase. In our sample we have only one object, SN 1998bw, where this can be studied over a sufficiently long period, and the results do not support this scenario. While initially (at 126 and 201 d after maximum) the supposed Mg I] line is much broader than the [O I] feature and lacks the narrow core, by 376 d the profiles have turned indistinguishable (see Fig. 6.15).

(ii) Alternatively, the Mg I] or [O I] features may be contaminated by emission lines of other elements. For the [O I] feature a possible contamination on the blue side has already been discussed in Section 6.6.1, and indeed several of

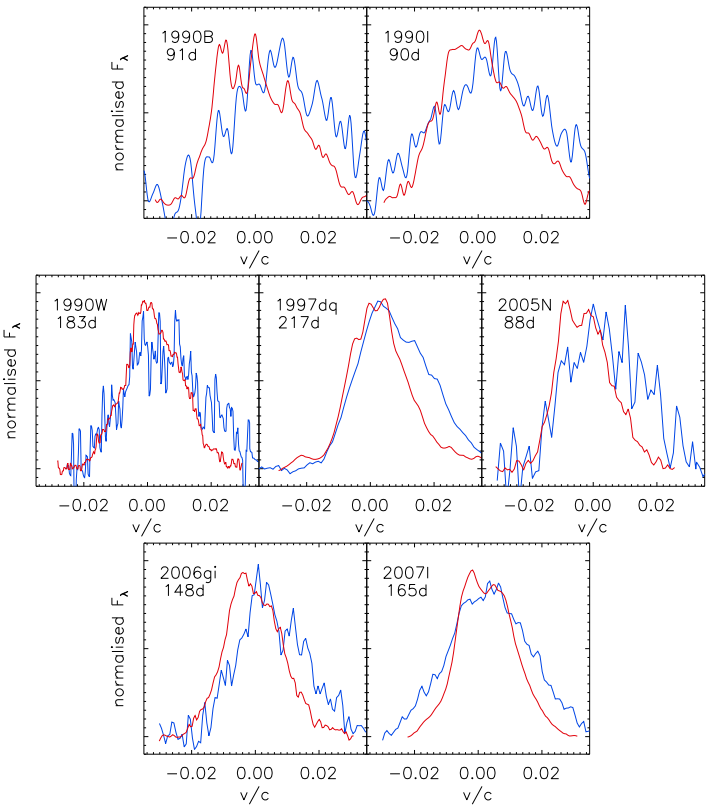

FIGURE 6.14— The same as Fig. 6.13, but showing spectra with evident differences in the [O I] $\lambda\lambda 6300, 6364$ and the modified Mg I] $\lambda 4571$ profiles.

the spectra affected by a mismatch of the Mg I] and [O I] profiles show evidence of an additional blueshifted contribution to [O I]. However, the fact that in most of these spectra the Mg I] line is broader than the [O I] line (cf. Fig. 6.14) suggests that a contamination should rather be searched for in the former.

(iii) The Mg I] $\lambda 4571$ line emerges out of the re-emission of the trough formed by Fe II and Mg II lines in photospheric spectra, and the transition is gradual. Hence, it is well possible that the emission peak tentatively identified as Mg I] is mostly photospheric re-emission in some of the earlier spectra. This would naturally explain the observed evolution in SN 1998bw and especially the mismatch at early phases (Fig. 6.15), since Fe features are particularly strong in this object (e.g. Mazzali et al., 2005d). SN 2002ap, on the other hand, is the SN with the strongest Mg I] $\lambda 4571$ line ever observed, and it is not unexpected that here Mg I] dominates over photospheric residuals already much earlier (Fig. 6.15).

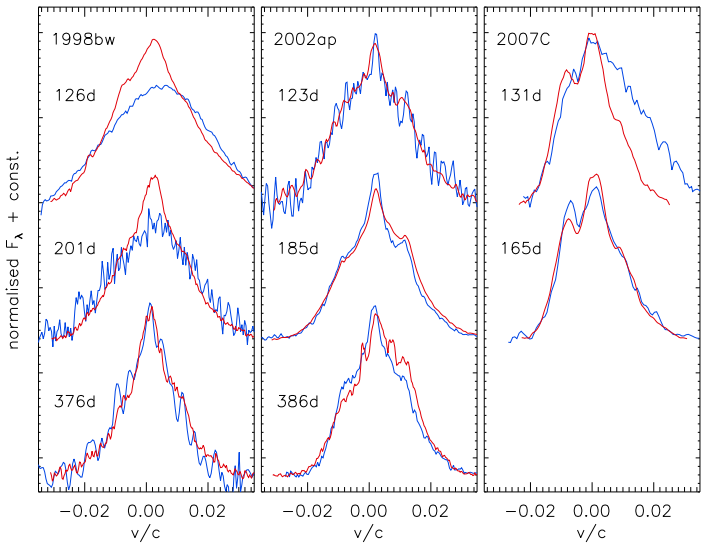

FIGURE 6.15— Evolution of the [O I] $\lambda\lambda$6300, 6364 and the modified Mg I] λ4571 line profiles of SNe 1998bw, 2002ap and 2007C with phase. While in SN 2002ap the profiles are always similar, significant differences are apparent in the earlier spectra of SNe 1998bw and 2007C.

6.8 Conclusions

We have conducted a study on the profiles of nebular emission lines in stripped-envelope CC-SNe, with the aim to constrain the ejecta morphology, and in particular the degree of asphericity of the explosions. The study was based on 98 nebular spectra of 39 different SNe, some of which were not published before, while others were taken from the literature. The size of the sample makes it statistically relevant.

We have concentrated on the profile of [O I] $\lambda\lambda$6300, 6364, since this is usually the strongest feature in nebular SN Ib/c spectra, and not severely contaminated by other lines. In the low-density limit (which is adequate for the ambient conditions in the nebular ejecta of SNe Ib/c), the line-strength ratio within the oxygen doublet can be fixed to be 3:1, making this doublet an equally good tracer of geometric effects as a single line.

Assuming a spherical matter-density distribution described by a Gaussian profile in radius (which is a good approximation for fairly massive CO cores), and an emissivity proportional to the ambient matter density, we have demonstrated that the resulting line profiles are also Gaussians. We therefore performed a multi-parameter Gauss-fitting of the [O I] $\lambda\lambda$6300, 6364 feature in all spectra, with the position, *fwhm* and intensity of the λ6300 Gaussian being free

parameters (the λ6364 line was automatically added with fixed offset and intensity ratio). While being aware that for non-spherical explosions, or emission regions whose density profiles deviate strongly from a Gaussian, this approach loses its immediate physical justification, it still proved to be extremely useful for the identification of emission components, their widths and Doppler shifts. In particular, compared to proper spectral modelling this method has the advantage of being fast, capable of reproducing also complex profiles, and independent of a reliable flux calibration of the spectra.

Despite the large variety in line profiles encountered, a rough separation of the SNe into four morphologically different groups on the basis of the best-fit parameters is proposed: SNe with simple Gaussian line profiles ($\sim$18% of all objects belong to this group), those whose lines show narrow cores atop broad bases ($\sim$28%), symmetric double peaks ($\sim$15%) and objects with evidence for clumps or overall asymmetric line profiles ($\sim$39%). Note that this classification refers to the structure inferred from the fitting procedure, since this is believed to be more significant for the true ejecta geometry than a pure visual inspection of the line. The connection between the two is not always intuitive. Double peaks as inferred from the fit can appear single-peaked if the separation of the two components is small. On the other hand, apparent double peaks may require the presence of a clump to be explained using the fit. Our numbers suggest that at most 59% (but probably significantly less) of all SNe Ib/c may be spherically symmetric. Furthermore, the fraction of double peaks is too small for a jet to be at work in a majority of the objects. In fact, from the number of double-peaked profiles, one can estimate that only in a small fraction of all narrow-core SNe the line profile should be generated by a jet-like ejecta morphology. Instead, a central density enhancement appears a likely solution for most members of the narrow-core class.

In spectra taken earlier than $\sim$200 d after maximum light, a systematic blueshift of the [O I] $\lambda\lambda$6300, 6364 line centroids can be discerned, getting more pronounced with decreasing phase. Geometrical effects and dust formation within the ejecta can be excluded as origin of the blueshift. Contamination from other elements may play a role in some, but definitely not all SNe. Hence, residual opacity in the inner ejecta remains the most likely explanation for the observed shift, as photons emitted on the rear side of the SN are scattered or absorbed on their way through the ejecta, giving rise to a flux deficit in the redshifted part of spectral emission lines.

In all spectra with sufficient S/N in the blue part, a comparison of the [O I] $\lambda\lambda$6300, 6364 profile with that of Mg I] λ4571 (modified to account for the doublet nature of the oxygen feature) was performed. A surprisingly good agreement of the profiles was found for most SNe regardless of their morpho-

logical class. This indicates that the line profiles are indeed determined by the ejecta geometry (since exactly the same contamination pattern in both features is highly unlikely), and that Mg and O are similarly distributed within the SN ejecta. Exceptions with a poor match of the Mg and O line profiles are mainly found in relatively early spectra, and we propose a blending of the emerging nebular Mg I] emission with residual photospheric Fe II lines as most likely reason for the differences.

6.9 Appendix: fit parameters

In the following tables the parameters of the best fits to the [O I] features of our sample spectra are reported. All numbers refer to the λ6300 line, since the λ6364 line is automatically added by the fitting algorithm at 1/3 of the stength. One- and two-component fits have been obtained for all SNe of the sample. They are listed in Table 6.5, along with the errors for the one-component fit parameters, estimated as described in Section 6.3.3. Three-component fits have only been performed for SNe 1990B, 2006ld and 2007C, whose line profiles are highly complex and not satisfactorily reproduced with fewer components. Their parameters are reported in Table 6.6.

TABLE 6.5— Parameters of the best one-component (cols. 4–6) and two-component (cols. 7–13) fits of [O I] λ6300.

SN (1)	Date (2)	Sample region (3)	λ (4)	*fwhm* (5)	χ^2 (6)	λ_1 (7)	$fwhm_1$ (8)	α_1 (9)	λ_2 (10)	$fwhm_2$ (11)	α_2 (12)	χ^2 (13)
1983N	1983/03/01	6195.9–6455.8	6300.8 ± 2.7	97.1 ± 1.5	16.02	6297.3	100.6	0.91	6320.9	46.0	0.09	8.72
1985F	1985/03/19	6165.0–6477.0	6294.7 ± 1.7	87.1 ± 3.0	650.75	6290.7	112.0	0.76	6300.4	40.4	0.24	40.62
1987M	1988/02/09	6125.9–6530.6	6284.9 ± 3.1	151.8 ± 3.0	17.36	6283.3	158.8	0.95	6300.4	31.6	0.05	8.58
	1988/02/25	6114.3–6495.3	6284.5 ± 4.4	141.0 ± 9.0	2.88	6282.8	149.4	0.94	6297.6	37.6	0.06	2.23
1988L	1988/07/17	6114.2–6491.7	6266.3 ± 6.4	157.7 ± 13.0	2.40	-	-	-	-	-	-	-
	1988/09/15	6147.8–6467.0	6285.7 ± 10.3	147.1 ± 30.0	1.11	-	-	-	-	-	-	-
1990B	1990/04/18	6132.1–6499.7	6285.5 ± 3.5	183.2 ± 3.0	40.87	6305.1	185.8	0.84	6235.6	36.6	0.16	9.42
	1990/04/30	6192.4–6499.6	6292.5 ± 6.0	194.5 ± 12.0	2.53	6299.4	198.7	0.95	6242.3	16.7	0.05	1.74
1990I	1990/07/26	6114.5–6563.7	6287.3 ± 2.5	184.4 ± 3.0	17.18	6309.4	192.1	0.76	6250.8	86.3	0.24	5.92
	1990/12/21	6171.2–6458.0	6300.2 ± 2.5	106.4 ± 2.0	21.00	6297.1	119.0	0.89	6310.5	30.0	0.11	9.54
	1991/02/20	6178.6–6466.8	6298.5 ± 6.4	113.5 ± 15.0	1.29	6296.1	125.4	0.90	6307.1	24.9	0.10	1.08
1990U	1990/10/20	6189.8–6443.9	6283.5 ± 4.1	91.3 ± 6.0	2.06	6267.3	63.7	0.63	6319.2	73.1	0.37	1.19
	1990/10/24	6197.7–6435.5	6287.0 ± 4.1	88.2 ± 3.6	14.07	6268.0	54.1	0.57	6319.8	65.8	0.43	4.91
	1990/11/23	6186.7–6436.1	6291.6 ± 3.7	92.1 ± 2.0	6.85	6272.4	53.4	0.55	6321.8	67.4	0.45	1.64
	1990/11/28	6203.2–6457.3	6295.3 ± 5.3	89.7 ± 9.0	1.69	6270.0	47.9	0.45	6319.7	69.1	0.55	0.63
	1990/12/12	6195.7–6451.1	6291.5 ± 5.3	96.4 ± 6.0	2.39	6268.6	54.3	0.47	6317.6	77.5	0.53	1.48
	1990/12/20	6215.4–6448.5	6292.2 ± 3.8	92.8 ± 2.0	7.69	6269.0	48.8	0.50	6321.1	66.4	0.50	1.96
	1991/01/06	6193.9–6443.0	6294.6 ± 3.8	93.3 ± 5.0	8.69	6270.5	48.9	0.46	6322.3	71.6	0.54	2.33
	1991/01/12	6198.4–6465.8	6293.1 ± 3.9	93.9 ± 4.0	22.36	6270.3	52.4	0.50	6323.3	73.9	0.50	6.91
1990W	1991/02/21	6168.0–6449.5	6295.1 ± 3.0	106.9 ± 3.0	3.63	6295.6	120.2	0.90	6292.7	40.6	0.10	1.81
	1991/04/21	6144.0–6496.8	6295.5 ± 3.0	107.9 ± 1.0	4.72	6298.0	125.1	0.84	6289.7	46.5	0.16	1.37
1990aa	1991/01/12	6128.2–6516.7	6283.3 ± 3.8	184.4 ± 8.8	15.46	6306.8	191.0	0.79	6236.5	77.5	0.21	9.55
	1991/01/23	6128.5–6504.9	6283.3 ± 4.3	165.8 ± 13.0	2.38	6300.5	164.7	0.79	6238.4	96.2	0.21	2.17
1990aj	1991/01/29	6150.1–6498.6	6294.1 ± 2.0	142.4 ± 3.0	5.64	6292.2	162.7	0.88	6300.6	46.2	0.12	2.77
	1991/02/22	6170.4–6450.2	6292.9 ± 2.0	115.4 ± 5.0	8.02	6289.7	141.1	0.83	6299.8	40.6	0.17	2.30
	1991/03/10	6149.3–6492.6	6296.6 ± 8.2	124.2 ± 19.0	1.63	6290.8	158.6	0.77	6304.6	44.3	0.23	1.15
1991A	1991/03/22	6134.9–6467.6	6264.1 ± 3.5	112.5 ± 5.5	2.46	6266.0	116.2	0.95	6246.6	34.5	0.05	1.65
	1991/04/07	6137.7–6469.1	6276.1 ± 5.4	124.4 ± 11.0	1.39	6276.8	127.7	0.98	6262.0	18.9	0.02	1.25
	1991/04/16	6135.6–6480.0	6276.4 ± 2.2	120.8 ± 3.0	4.30	6278.5	125.3	0.94	6258.1	39.8	0.06	2.78
	1991/06/08	6137.1–6508.2	6286.5 ± 2.0	126.1 ± 3.0	8.10	6289.1	130.4	0.95	6263.5	31.7	0.05	2.75
1991L	1991/06/08	6156.3–6444.7	6289.5 ± 5.5	105.2 ± 6.5	3.30	6258.9	65.5	0.50	6320.4	67.6	0.50	2.29
1991N	1991/12/14	6191.9–6457.6	6303.9 ± 3.6	106.1 ± 8.0	2.69	6303.7	106.1	0.77	6304.3	105.9	0.23	2.82
	1992/01/09	6191.0–6472.7	6303.5 ± 2.8	104.0 ± 5.0	2.29	6304.5	123.9	0.68	6302.8	74.9	0.32	2.16

TABLE 6.5— *continued.* Parameters of the best one-component (cols. 4–6) and two-component (cols. 8–13) fits of [O I] λ6300.

SN (1)	Date (2)	Sample region (3)	λ (4)	*fwhm* (5)	χ^2 (6)	λ_1 (7)	$fwhm_1$ (8)	α_1 (9)	λ_2 (10)	$fwhm_2$ (11)	α_2 (12)	χ^2 (13)
1993J[a]	1993/10/19	6172.2–6512.2	6279.7 ± 4.2	110.0 ± 2.0	22.92	6307.1	115.7	0.55	6257.6	73.4	0.45	12.04
	1993/11/19	6192.2–6512.2	6294.3 ± 4.3	110.0 ± 2.0	37.38	6307.3	114.4	0.77	6265.3	54.2	0.23	15.12
	1993/12/08	6195.7–6512.2	6295.8 ± 4.2	110.1 ± 2.0	52.47	6308.4	109.2	0.79	6264.7	54.4	0.21	24.11
	1994/01/17	6176.4–6512.0	6292.6 ± 4.2	117.9 ± 2.0	41.67	6304.2	110.1	0.79	6261.8	54.2	0.21	20.84
	1994/01/21	6188.6–6513.1	6289.2 ± 4.2	120.0 ± 1.5	38.95	6303.8	114.7	0.72	6261.9	63.4	0.28	16.38
	1994/01/22	6178.6–6514.3	6293.4 ± 4.7	111.0 ± 4.0	31.71	6305.2	110.0	0.78	6262.1	54.3	0.22	14.87
	1994/03/25	6183.9–6514.1	6295.9 ± 4.6	115.6 ± 4.0	5.40	6306.4	108.9	0.80	6265.7	57.1	0.20	3.10
	1994/03/30	6191.3–6518.9	6302.3 ± 4.6	110.0 ± 6.0	7.12	6309.7	104.0	0.84	6269.5	50.5	0.16	4.52
1994I	1994/07/14	6130.9–6497.4	6275.6 ± 2.0	140.3 ± 2.0	15.65	6294.6	129.2	0.77	6231.6	62.4	0.23	2.65
	1994/08/04	6140.0–6493.2	6279.9 ± 2.7	138.3 ± 2.0	4.22	6296.3	127.5	0.80	6231.2	62.0	0.20	0.88
	1994/09/02	6160.3–6469.5	6277.4 ± 2.7	129.3 ± 4.0	4.67	6294.9	111.3	0.77	6229.7	60.0	0.23	1.35
1995bb	1995/12/17	6157.7–6470.4	6296.6 ± 6.9	145.0 ± 12.0	1.56	6292.3	152.3	0.93	6321.8	45.6	0.07	1.45
1996D	1996/09/10	6150.8–6483.0	6301.3 ± 7.9	152.2 ± 15.0	1.50	6288.6	158.0	0.87	6337.4	39.6	0.13	1.15
1996N	1996/10/19	6164.7–6471.2	6283.7 ± 5.0	114.1 ± 5.0	8.02	6299.5	94.4	0.77	6239.0	46.1	0.23	3.32
	1996/12/16	6177.7–6465.1	6281.1 ± 5.0	107.6 ± 5.0	3.85	6295.6	89.6	0.78	6237.4	47.0	0.22	1.73
	1997/01/13	6174.5–6458.2	6282.2 ± 5.0	109.5 ± 5.0	2.60	6294.9	94.9	0.80	6236.7	51.2	0.20	1.96
	1997/02/12	6173.0–6453.2	6282.6 ± 5.0	103.4 ± 5.0	2.47	6300.4	81.8	0.72	6245.1	45.8	0.28	0.96
1996aq	1997/02/11	6140.1–6494.1	6286.6 ± 2.2	128.2 ± 2.0	512.64	6300.7	112.5	0.83	6238.5	25.4	0.17	53.47
	1997/04/02	6165.2–6468.4	6288.5 ± 3.6	123.7 ± 6.0	25.24	6299.5	112.2	0.86	6241.8	19.9	0.14	2.28
	1997/05/14	6143.0–6508.3	6291.5 ± 2.2	126.0 ± 1.0	90.49	6302.1	114.2	0.87	6240.8	19.6	0.13	6.65
1997B	1997/09/23	6186.0–6438.9	6301.0 ± 8.6	110.7 ± 10.0	0.94	6295.5	93.6	0.63	6317.7	143.0	0.37	0.95
	1997/10/11	6206.4–6432.3	6296.7 ± 7.7	96.2 ± 15.0	0.84	6280.6	83.1	0.56	6318.8	86.0	0.44	0.88
	1998/02/02	6201.3–6481.6	6304.6 ± 5.9	97.3 ± 15.0	1.25	6286.3	71.1	0.37	6318.4	95.2	0.63	1.21
1997X	1997/05/10	6156.4–6495.1	6295.8 ± 2.2	106.3 ± 4.0	3.65	6298.4	146.5	0.53	6294.7	77.0	0.47	2.53
	1997/05/13	6143.4–6517.7	6297.2 ± 1.5	122.6 ± 3.0	4.93	6295.3	145.3	0.76	6300.2	72.2	0.24	2.79
1997dq	1998/05/30	6205.0–6446.5	6300.0 ± 2.8	97.8 ± 1.0	42.93	6323.7	68.7	0.55	6271.2	63.6	0.45	25.40
	1998/06/18	6202.2–6439.8	6298.8 ± 4.0	98.6 ± 7.0	1.63	6320.5	71.5	0.55	6270.2	72.7	0.45	1.37
1997ef	1998/09/21	6166.1–6470.1	6294.9 ± 5.3	120.2 ± 15.0	2.14	6300.6	179.2	0.72	6290.8	44.8	0.28	1.04
1998bw	1998/09/12	6090.0–6549.7	6298.4 ± 5.8	185.5 ± 6.0	17.83	6297.3	191.2	0.97	6315.1	31.6	0.03	13.01
	1998/11/26	6135.6–6504.6	6298.4 ± 3.2	146.1 ± 4.0	21.61	6292.8	166.1	0.87	6315.1	42.6	0.13	2.69
	1999/04/12	6134.6–6500.3	6299.3 ± 3.4	120.6 ± 5.0	12.58	6294.0	142.8	0.84	6310.8	39.1	0.16	1.34
	1999/05/21	6162.3–6460.7	6297.6 ± 3.2	109.8 ± 3.0	13.45	6291.7	132.7	0.82	6308.2	39.0	0.18	2.19
1999cn	2000/08/04	6198.2–6421.9	6294.6 ± 10.3	108.4 ± 20.0	0.93	6292.0	123.0	0.96	6303.7	32.9	0.04	0.73
1999dn	2000/09/01	6214.1–6455.2	6309.6 ± 10.2	94.3 ± 20.0	2.25	6304.1	112.9	0.81	6322.9	33.8	0.19	2.07

TABLE 6.5— *continued.* Parameters of the best one-component (cols. 4–6) and two-component (cols. 7–13) fits of [O I] λ6300.

SN	Date	Sample region	λ	*fwhm*	χ^2	λ_1	$fwhm_1$	α_1	λ_2	$fwhm_2$	α_2	χ^2
(1)	(2)	(3)	(4)	(5)	(6)	(7)	(8)	(9)	(10)	(11)	(12)	(13)
2000ew	2001/03/17	6189.4–6420.2	6284.3 ± 3.0	99.3 ± 5.0	2.54	6294.3	109.6	0.79	6266.3	33.0	0.21	1.26
2002ap	2002/08/06	6082.7–6529.4	6297.9 ± 2.3	172.5 ± 5.0	2.47	6296.6	179.2	0.96	6312.3	21.9	0.04	1.52
	2002/06/17	6064.6–6516.5	6300.0 ± 1.5	174.0 ± 3.0	10.64	6298.7	181.5	0.95	6312.5	22.5	0.05	2.70
	2002/07/11	6084.1–6514.9	6302.4 ± 1.5	163.1 ± 1.0	27.22	6301.6	164.6	0.97	6313.0	20.0	0.03	8.82
	2002/08/09	6103.9–6503.4	6304.6 ± 1.5	157.5 ± 1.0	21.94	6303.5	165.7	0.96	6314.1	21.6	0.04	3.60
	2002/10/01	6094.6–6513.3	6305.4 ± 1.5	150.4 ± 2.0	19.99	6304.1	157.9	0.95	6314.4	20.2	0.05	4.32
	2002/10/09	6104.7–6511.7	6305.0 ± 1.5	152.2 ± 4.0	7.16	6303.9	160.6	0.95	6313.5	20.3	0.05	2.62
	2002/10/14	6104.0–6511.2	6306.4 ± 1.5	153.9 ± 3.0	9.15	6304.2	166.4	0.93	6316.2	31.0	0.07	3.98
	2002/11/06	6149.5–6500.5	6305.7 ± 1.5	149.0 ± 1.0	97.58	6304.7	157.8	0.95	6312.5	22.2	0.05	24.14
	2003/01/07	6137.7–6519.0	6306.9 ± 2.3	143.0 ± 2.0	37.95	6305.9	150.8	0.95	6313.7	21.7	0.05	14.14
	2003/02/27	6145.0–6490.0	6309.5 ± 1.5	140.0 ± 2.0	38.23	6309.0	140.8	0.97	6315.4	17.1	0.03	20.43
2003jd	2004/09/11	6087.3–6505.8	6299.1 ± 3.6	219.6 ± 8.0	5.52	6232.0	116.7	0.50	6357.2	87.0	0.50	2.40
	2004/10/18	6150.7–6488.2	6304.4 ± 6.3	187.5 ± 15.0	3.27	6251.4	87.0	0.52	6358.5	67.8	0.48	1.91
2004aw	2004/11/14	6124.1–6498.6	6296.1 ± 3.3	118.7 ± 7.0	2.25	6293.1	133.0	0.89	6307.6	37.0	0.11	1.14
	2004/12/08	6191.6–6430.1	6289.2 ± 6.6	91.0 ± 14.0	0.85	6287.5	94.7	0.94	6302.9	34.8	0.06	0.75
	2005/05/11	6199.0–6442.0	6298.0 ± 6.6	91.4 ± 16.0	0.63	6294.0	101.8	0.87	6310.8	32.7	0.13	0.41
2004gt	2005/05/24	6174.8–6485.3	6285.2 ± 3.1	125.1 ± 3.0	61.98	6260.7	72.5	0.60	6335.8	87.1	0.40	30.39
2005N	2005/01/21	6160.0–6476.3	6268.6 ± 6.5	117.3 ± 7.5	14.33	6284.0	126.3	0.77	6241.2	46.8	0.23	5.06
2006F	2006/11/16	6223.0–6450.9	6296.9 ± 6.3	75.8 ± 20.0	2.60	6314.6	84.7	0.64	6281.4	38.9	0.36	1.32
2006T	2007/02/18	6203.0–6452.4	6300.5 ± 8.0	123.6 ± 16.0	3.72	6266.8	50.7	0.51	6338.0	57.9	0.49	1.14
2006aj	2006/09/19	6101.0–6498.7	6294.6 ± 6.1	188.5 ± 9.0	1.75	6295.0	192.2	0.99	6301.8	18.1	0.01	1.56
	2006/11/27	6096.0–6515.7	6303.5 ± 6.7	203.4 ± 11.0	2.50	6304.5	222.4	0.93	6300.8	35.3	0.07	1.47
	2006/12/19	6119.2–6507.0	6305.2 ± 7.7	177.1 ± 12.0	2.49	6306.2	197.4	0.92	6302.3	22.4	0.08	1.02
2006gi	2007/02/10	6138.3–6433.0	6278.5 ± 4.0	107.0 ± 2.0	10.86	6280.1	114.5	0.93	6267.7	35.2	0.07	4.97
2006ld	2007/07/17	6176.4–6492.5	6285.5 ± 2.2	97.2 ± 5.5	17.39	6304.8	104.0	0.70	6259.7	43.9	0.30	9.95
	2007/08/06	6173.5–6491.2	6287.6 ± 3.1	102.1 ± 9.0	10.58	6305.7	115.1	0.72	6263.5	43.8	0.28	5.62
	2007/08/20	6175.5–6482.4	6290.3 ± 2.6	92.7 ± 7.0	14.42	6296.3	87.3	0.89	6251.9	33.9	0.11	13.50
2007C	2007/05/17	6131.0–6501.4	6278.2 ± 3.6	122.5 ± 2.0	82.47	6301.1	92.3	0.69	6235.0	52.4	0.31	36.80
	2007/06/20	6134.0–6502.5	6285.3 ± 2.6	121.5 ± 1.5	144.11	6299.6	103.2	0.81	6237.6	41.6	0.19	49.59
2007I	2007/06/18	6157.1–6494.7	6300.3 ± 5.3	118.8 ± 1.0	140.38	6305.3	126.1	0.90	6277.8	35.8	0.10	17.07
	2007/07/15	6159.2–6504.8	6303.4 ± 5.3	111.9 ± 1.5	207.65	6308.2	116.3	0.90	6278.8	33.7	0.10	26.84

[a] The fitting was performed in Hα-subtracted spectra. For this purpose, a smoothed symmetric Hα profile was subtracted, constructed by reflecting the red wing around the rest wavelength (see also Patat et al. 1995).

TABLE 6.6— Parameters of the best three-component fits of the [O I] λ6300 line for selected spectra with complex line profiles.

SN	Date	Sample region	λ_1	$fwhm_1$	α_1	λ_2	$fwhm_2$	α_2	α_3	$fwhm_3$	α_3	χ^2
(1)	(2)	(3)	(4)	(5)	(6)	(7)	(8)	(9)	(10)	(11)	(12)	(13)
1990B	1990/04/18	6132.1–6499.7	6319.9	180.7	0.71	6235.5	50.0	0.26	6303.1	13.0	0.03	5.73
2006ld	2007/07/17	6176.4–6492.5	6320.8	121.4	0.48	6261.6	40.1	0.40	6301.6	20.0	0.12	2.80
	2007/08/06	6173.5–6491.2	6320.4	136.6	0.53	6264.2	39.4	0.36	6302.1	21.1	0.11	2.24
	2007/08/20	6175.5–6482.4	6322.3	117.5	0.47	6264.4	46.5	0.37	6303.2	19.9	0.16	4.94
2007C	2007/05/17	6131.0–6501.4	6299.0	127.1	0.56	6239.5	54.2	0.29	6301.1	43.1	0.15	7.29
	2007/06/20	6134.0–6502.5	6297.7	125.6	0.68	6242.0	43.5	0.19	6304.4	41.4	0.13	8.70

7

Summary and outlook

In the various parts of this thesis I have tried to demonstrate that important insight on the nature of supernovae can be gained by means of observations, careful data analysis, the comparison of larger samples of objects and elementary modelling.

In Chapter 4 carbon lines were identified in early-phase spectra of the underluminous Type Ia SN 2005bl. This constitutes the first carbon detection ever in an object of this class. Computing synthetic spectra, the presence of a large amount of unburned material was established even beyond the clear carbon signature, suggesting that at pre-maximum epochs the ejecta above the photosphere are entirely dominated by oxygen. This finding is in contradiction to what had been suggested in previous studies (Mazzali et al., 2007c), and is an indication of a low burning efficiency in objects of this class.

We also learned that by restricting the models to a $M_{\rm Ch}$-progenitor and a standard W7 ejecta density structure of the ejecta, we failed to reproduce some important aspects of the observations. Matching the observed line strengths was not an issue as long as there was enough freedom to adjust the ejecta composition. However, matching the positions and widths of all features simultaneously was not possible. Introducing composition stratification within the ejecta may mitigate this problem, but additional ongoing tests, which are not reported here, indicate that this alone cannot remove all discrepancies. Instead, we believe that underluminous SNe Ia have a density profile different from ordinary SNe Ia, with a steeper gradient and less mass at high velocity. It may well be that better fits can be obtained if also the $M_{\rm Ch}$-constraint is dropped.

Besides the mismatch of line positions in synthetic spectra, also the re-

markably low, significantly sub-solar Fe content of SN 2005bl, again inferred from spectral modelling, points at properties of the progenitors of underluminous SNe Ia which may be fundamentally different form those of other SNe Ia. Unless gravitational settling of heavier elements in the progenitors works very efficiently, concentrating Fe at the centre of the WDs and thus hiding it from visibility at early phases, the progenitors must have had low metallicities. In early-type, presumably metal-rich host galaxies this requires them to be very old, implying long delay times for underluminous SNe Ia.

More sophisticated spectral modelling, including abundance stratification and variations in the density structure, will allow us to address some of the issues mentioned above in greater detail. Merging the spectral data bases of SN 2005bl and SN 1991bg could help in that respect, as these two objects are very similar, but have different and complementary temporal coverage. The combined set would extend from a week before maximum light to the nebular phase, providing information on the ejecta composition in various layers. Nevertheless, what the progenitors and explosion mechanism of 91bg-like SNe Ia really are will remain a puzzle until full, self-consistent simulations become available which include the progenitor evolution, the explosion hydrodynamics and radiative transfer (all in 3D), and which compare well with the observations. For the moment, however, detailed observations and improved modelling of the data are maybe the most promising way to further constrain the nature of these objects.

Further diversity among SNe Ia, this time on the opposite side of the luminosity range, has just recently been introduced by the discovery of several overluminous (by a factor ~ 2) objects (Branch, 2006; Howell et al., 2006; Hicken et al., 2007). To explain the light curves and spectra of these events within spherical symmetry, a ^{56}Ni mass exceeding 1 $M_\odot$ and a total ejecta mass in excess of 1.4 $M_\odot$ are required, suggesting the explosion of a super-$M_{\rm Ch}$ WD which had been stabilised by strong differential rotation (Howell et al., 2006; Branch, 2006), or a merger of two WDs (Hicken et al., 2007), in sum again exceeding $M_{\rm Ch}$. Only by invoking strong deviations from spherical symmetry, with the ignition being far off-centre and the Ni distribution very one-sided, could these objects possibly be produced by $M_{\rm Ch}$-WDs (Hillebrandt et al., 2007; Sim et al., 2007).

Another interesting class are 2002cx-like SNe Ia (Li et al., 2003; Branch et al., 2004; Jha et al., 2006b; Phillips et al., 2006; Stanishev et al., 2007a; Sahu et al., 2007), few in number and highly peculiar, but remarkably homogeneous within their class. Their early-time spectra indicate high temperatures like in the high-luminosity SN Ia 1991T (Filippenko et al., 1992b; Phillips et al., 1992), but they are underluminous and exhibit low ejecta velocities. Even one year after the explosion their ejecta have not become transparent, their spectra

being dominated by *very* narrow ($fwhm \sim 600$ km s^{-1}) P-Cygni lines of Fe II.

Pinning down the nature of all these peculiar SNe Ia is a challenging task, since their intrinsic rareness prevents large samples and good statistics. For the same reason, they are often thought to have only minor implications for cosmology and the chemical enrichment of the universe. However, this may be short-sighted. First, if SNe Ia showed significant evolution with redshift, the relative frequency of what we refer to as 'peculiar objects' nowadays might have been different in the past. And second, once we have understood what makes some SNe Ia so outstanding, we will also have gained a better understanding of the comparatively small differences among the otherwise remarkably homogeneous 'normal' SNe Ia, and may be able to evaluate more accurately where the limits of their standardisability are. In that sense, studying peculiar SNe Ia may even be more valuable for cosmological purposes than large campaigns focused on normal objects only.

In Chapter 5 of this thesis, the data of the stripped-envelope CC-SN 2004aw are presented. The lack of clear evidence of He I lines in both optical and near-IR spectra justify a classification as SN Ic, and indicate that SN 2004aw originated indeed from the collapse of a bare C/O core, with the entire He envelope lost prior to explosion.

Contrary to the majority of SNe Ia which probably have a fixed ejecta mass ($M_{\rm Ch}$, since there is no compact remnant), CC-SNe come from a variety of massive ($M_{\rm ZAMS} \geq 8\ M_{\odot}$) stars. Depending on the initial mass of the progenitor, the mass loss during its lifetime and the remnant formed by the core collapse (a neutron star or black hole), CC-SNe can have completely different ejecta masses and explosion energies, resulting in a significant spectrophotometric diversity. From the light-curve shape and measured ejecta velocities, and using Arnett's (1982) relation, an ejecta mass of 3.5–8 $M_{\odot}$ and an explosion energy of $3.5–9 \times 10^{51}$erg was estimated for SN 2004aw, placing it about half way between ordinary, low-energy SNe Ic and very powerful (GRB-related) hypernovae. With this particular location in parameter space, SN 2004aw may eventually help to shed light on details of the SN-GRB connection, although for the moment it only seems to add complexity. As of this writing, possible combinations not only include normal-energetic SNe Ic unrelated to a GRB and very energetic, broad-lined hypernovae associated with a GRB (e.g. Galama et al., 1998), but also less energetic BL-SNe Ic with (Pian et al., 2006; Mazzali et al., 2006; Ferrero et al., 2006; Mazzali et al., 2007a) and without (Foley et al., 2003; Yoshii et al., 2003; Tomita et al., 2006; Mazzali et al., 2007b) a GRB or XRF connection, and even one recent XRF which is related to an apparently normal SN Ib (Xu et al. 2008; Mazzali et al. in prep.). With SN 2004aw the option

of a fairly energetic, yet not broad-lined SN Ic without an associated GRB has been added. Moreover, a number of long-duration bursts without detectable SN signature have been found in recent years. It is clear that only a significant extension of the data base of stripped-envelope CC-SNe can improve our understanding of the exact nature of the SN-GRB connection.

One possible way to address this relationship is by studying the ejecta geometry. GRB-SNe are supposed to be strongly aspherical, jet-like explosions (Maeda et al., 2002) with a characteristic spatial distribution of oxygen on the one hand, and Fe-group elements on the other hand. Once the SN ejecta have become transparent at late phases, the innermost regions closest to the site of core collapse are probed, and the observed emission-line profiles can be linked to the spatial distribution of the emitting material (Matheson et al., 2000; Maeda et al., 2002; Mazzali et al., 2005b; Maeda et al., 2006). This is exactly what we have tried in Chapter 6, concentrating on [O I] $\lambda\lambda 6300, 6364$ and Mg I] $\lambda 4571$, both prominent and fairly isolated features in nebular spectra of stripped-envelope CC-SNe. The diversity found in the line profiles is remarkable, with a majority of all SNe Ib/c showing signs of global asphericity or clumpiness. This reveals that asphericity is by no means limited to GRB-SNe, but ubiquitous among *all* stripped-envelope CC-SNe, thus diminishing the hope that a GRB-connection can be robustly recognised in nebular spectra.

It would be a rewarding future project to investigate the links between the nebular line profiles of stripped-envelope CC-SNe and their explosion energetics, ejecta mass and photospheric properties (such as $v_{\rm ph}$ or the peak luminosity) in greater detail. While this has already been accomplished for individual SNe with particularly good photometric and spectroscopic coverage, only the extension to a statistically relevant sample can provide the overview necessary to find possible correlations. Ideally, but feasible only for the most nearby objects, this should be complemented by early-time spectropolarimetry to infer also the degree of asphericity in the outer layers of the ejecta and compare it with that deduced from nebular spectra for the central regions. Such a programme would eventually provide a more coherent picture of how asymmetry influences the outcome of SN explosions. Our present knowledge suggests that it may indeed be another key parameter to explain the diversity encountered in CC-SNe.

SNe also play a key role in the chemical evolution of galaxies, as they return to the interstellar medium (ISM) the heavy elements synthesised during the lifetime of the star (hydrostatic burning) and the explosion (explosive nucleosynthesis). Their amount and composition depends on the structure of the star and the explosion physics. Because of the degeneracy of the precursor, burning in SNe Ia proceeds mostly to NSE and produces large amounts of Fe-group

elements ($0.6 M_{\odot}$ on average). The progenitors of CC-SNe also synthesise large amounts of Fe, but most of it remains locked in the compact central remnant and is not made available for further generations of stars. Their contribution to the chemical enrichment of the ISM is, therefore, mostly in intermediate-mass elements.

Lifetimes of CC-progenitors are short (< 100 Myr), so that on cosmic timescales their contribution to the chemical enrichment of the ISM is almost immediate. This distinguishes them from SNe Ia, whose delay times are significantly longer and not well constrained. Hence, while the major uncertainty in the contribution of SNe Ia is the lack of reliable delay-time estimates, the dominant uncertainty in CC-SNe arises from the ejecta composition. Therefore, studying in detail the ejecta of CC-SNe is of utmost importance not only for SN research, but also other fields of astrophysics.

In an ongoing project dedicated to this aspect, we collect extended data sets of nearby stripped-envelope CC-SNe. The data will be analysed using methods similar to those successfully applied to SNe Ia in the past, e.g., spectral modelling with abundance stratification. Studying the composition of the ejecta of these SNe, their kinematics and possible CSM-interaction, one can also reconstruct the progenitor's late evolution, its mass loss history, and hence the amount of unburned, primordial material released to the ISM.

All these various aspects show that supernova research is not an isolated field, but closely related to stellar evolution, the chemical enrichment of the universe, and cosmology. The relationship is symbiotic, in a sense that these related fields have a vital interest in a better understanding of SNe, but also SN research profits from advances there. The physical conditions encountered in SNe are hardly matched anywhere else in the universe, and 'lightyears away' (in a very true sense) from what can be studied in controlled laboratory experiments. As in most areas of astronomical research, remote diagnostics are required. While this surely means a complication of our work, it also makes up a large part of its fascination. In any case, supernovae as tremendous cosmic explosions will remain an interesting playground for physicists and astronomers for several more decades.

Bibliography

Abbott D. C., Lucy L. B., 1985, ApJ, 288, 679

Alard C., 2000, A&AS, 144, 363

Altavilla G., et al., 2007, A&A, 475, 585

Arbour R., Papenkova M., Li W. D., Filippenko A. V., Armstrong M., 1999, IAUC 7156, 1

Arnett W. D., 1969, Ap&SS, 5, 180

Arnett W. D., 1982, ApJ, 253, 785

Asplund M., Grevesse N., Sauval A. J., 2005, in Barnes T. G., III, Bash F. N., eds, ASP Conference Series, Vol. 336. San Francisco, p. 25

Barbon R., Benetti S., Cappellaro E., Patat F., Turatto M., 1993, MmSAI, 64, 1083

Barbon R., Benetti S., Cappellaro E., Patat F., Turatto M., Iijima T., 1995, A&AS, 110, 513

Baron E., Branch D., Hauschildt P. H., Filippenko A. V., Kirshner R. P., 1999, ApJ, 527, 739

Benetti S., Elias-Rosa N., Blanc G., Navasardyan H., Turatto M., Zampieri L., Cappellaro E., Pedani M., 2004a, IAUC 8312

Benetti S. et al., 2004b, MNRAS, 348, 261

Benetti S., et al., 2005, ApJ, 623, 1011

Bessell M. S., 1990, PASP, 102, 1181

Bessell M. S., Brett J. M., 1988, PASP, 100, 1134

Blondin J. M., Mezzacappa A., DeMarino C., 2003, ApJ, 584, 971

Blondin S., Modjaz M., Kirshner R., Challis P., Matheson T., 2006, CBET 386

Boles T., Itagaki K., 2004, IAUC 8310

Branch D., 2006, Nature, 443, 283

Branch D., et al., 2002, ApJ, 566, 1005

Branch D., Baron E., Thomas R. C., Kasen D., Li W., Filippenko A. V., 2004, PASP, 116, 903

Branch D., et al., 2006a, PASP, 118, 560

Branch D., Jeffery D. J., Young T. R., Baron E., 2006b, PASP, 118, 791

Branch D., et al., 2007a, PASP, 119, 709

Branch D., et al., 2007b, PASP accepted (arXiv:0712.2436)

Bravo E., García-Senz D., 1999, MNRAS, 307, 984

Brown G. E., Lee C.-H., Wijers R. A. M. J., Lee H. K., Israelian G., Bethe H. A., 2000, NewA, 5, 191

Buras R., Rampp M., Janka H. Th., Kifonidis K., 2006, A&A, 447, 1049

Burrows A., 2005, in Turatto M., Benetti S., Zampieri L., Shea W., eds., Supernovae as Cosmological Lighthouses. ASP, San Francisco, p. 184

Burrows A., Livne E., Dessart L., Ott C. D., Murphy J., 2006, ApJ, 640, 878

Burrows A., Livne E., Dessart L., Ott C. D., Murphy J., 2007, ApJ, 655, 416

Candia P., et al., 2003, PASP, 115, 277

Cardelli J. A., Clayton G. C., Mathis J. S., 1989, ApJ, 345, 245

Clocchiatti A., 1995, PhD thesis, University of Texas at Austin

Clocchiatti A., Wheeler J. C., Brotherton M. S., Cochran A. L., Wills D., Barker E. S., Turatto M., 1996, ApJ, 462, 462

Clocchiatti A., et al., 1997, ApJ, 483, 675

Clocchiatti A., et al., 2000, ApJ, 529, 661

Clocchiatti A., et al., 2001, ApJ, 553, 886

Colgate S. A., 1968, Canadian J. Phys., 46, 476

Conley A., et al., 2006, AJ, 132, 1707

Contardo G., Leibundgut B., Vacca W. D., 2000, A&A, 359, 876

Cordes J. M., Romani R. W., Lundgren S. C., 1993, Nature, 362, 133

Danziger I. J., Gouiffes C., Bouchet P., Lucy L. B., 1989, IAUC 4796, 1

de Vaucouleurs G., Corwin H. G. Jr., 1985, ApJ, 295, 287

Della Valle M., et al., 2006, Nature, 444, 1050

Drenkhahn G., Spruit H. C., 2002, A&A, 391, 1141

Elias J. H., Matthews K., Neugebauer G., Persson S. E., 1985, ApJ, 296, 379

Elias-Rosa N., 2007, PhD thesis, Universidad de La Laguna

Elias-Rosa N. et al., 2006, MNRAS, 369, 1880

Elias-Rosa N., et al., 2008, MNRAS, tmp, 18E (arXiv:0710.4503)

Elmhamdi A., Danziger I. J., Cappellaro E., Della Valle M., Gouiffes C., Phillips M. M., Turatto M., 2004, A&A, 426, 963

Elmhamdi A., Danziger I. J., Branch D., Leibundgut B., Baron E., Kirshner R. P., 2006, A&A, 450, 305

Ferrarese L., et al., 2000, ApJ, 529, 745

Ferrero P., et al., 2006, A&A, 457, 857

Fesen R. A., 2005, in Turatto M., Benetti S., Zampieri L., Shea W., eds., Supernovae as Cosmological Lighthouses. ASP, San Francisco, p. 409

Fesen R. A., Gerardy C. L., McLin K. M., Hamilton A. J. S., 1999, ApJ, 514, 195

Fesen R. A., Höflich P. A., Hamilton A. J. S., Hammell M. C., Gerardy C. L., Khokhlov A. M., Wheeler J. C., 2007, ApJ, 658, 396

Filippenko A. V., 1982, PASP, 94, 715

Filippenko A. V., 1988, AJ, 96, 1941

Filippenko A. V., 1992, ApJ, 384, L37

Filippenko A. V., 1997, ARA&A, 35, 309

Filippenko A. V., Sargent W. L. W., 1986, AJ, 91, 691

Filippenko A. V., Porter A. C., Sargent W. L. W,, Schneider D. P., 1986, AJ, 92, 1341

Filippenko A. V., Porter A. C., Sargent W. L. W., 1990, AJ, 100, 1575

Filippenko A. V., et al., 1992a, ApJ, 384, L15

Filippenko A. V., et al., 1992b, AJ, 104, 1543

Filippenko A. V., et al., 1995a, ApJ, 450, L11

Filippenko A. V., Barth A. J., Bower G. C., Ho L. C., Stringfellow G. S., Goodrich R. W., Porter A. C., 1995b, AJ, 110, 2261

Filippenko A. V., Li W. D., Treffers R. R., Modjaz, M. 2001, in Chen W. P., Lemme, C., Paczyński B., eds., 'Small Telescope Astronomy on Global Scales'. Astron. Soc. of the Pacific, San Francisco, p. 121

Filippenko A. V., Desroches L., Ganeshalingam M., Chornock R., Serduke F. J. D., 2004, IAUC 8331

Fink M., Hillebrandt W., Röpke F. K., 2007, A&A, 476, 1133

Fisher A. K., 2000, PhD thesis, The University of Oklahoma

Foley R. J., et al., 2003, PASP, 115, 1220

Foley R. J., Smith N., Ganeshalingam M., Li W., Chornock R., Filippenko A. V., 2007, ApJ, 657, L105

Fransson C., Chevalier R. A., 1987, ApJ, 322, L15

Fransson C., Chevalier R. A., 1989, ApJ, 343, 323

Freedman W. L., et al., 2001, ApJ, 553, 47

Fukugita M., Ichikawa T., Gunn J. E., Doi M., Shimasaku K., Schneider D. P., 1996, AJ, 111, 1748

Fynbo J. P. U., et al., 2006, Nature, 444, 1047

Galama T. J., et al., 1998, Nature, 395, 670

Gallagher J., Garnavich P. M., Modjaz M., Kirshner R. P., Challis P., 2005a, IAUC 8514, 3

Gallagher J. S., Garnavich P. M., Berlind P., Challis P., Jha S., Kirshner R. P., 2005b, ApJ, 634, 210

Gal-Yam A., et al., 2006, Nature, 444, 1053

Garnavich P., Jha S., Kirshner R., Challis P., 1997a, IAUC 6778

Garnavich P., Jha S., Kirshner R., Challis P., Balam D., Brown W., Briceno C., 1997b, IAUC 6786

Garnavich P., Jha S., Kirshner R., Challis P., Balam D., Berlind P., Thorstensen J., Macri L., 1997c, IAUC 6798

Garavini G., et al., 2005, AJ, 130, 2278

Garavini G., et al., 2007, A&A, 471, 527

Garnavich P. M., et al., 2004, ApJ, 613, 1120

Gaskell C. M., Cappellaro E., Dinerstein H. L., Garnett D. R., Harkness R. P., Wheeler J. C., 1986, ApJ, 306, L77

Gehrels N., et al., 2006, Nature, 444, 1044

Gerardy C. L., et al., 2004a, ApJ, 607, 391

Gerardy C. L., Fesen R. A., Marion G. H., Höflich P., Wheeler J. C., Nomoto K., Motohara K., 2004b, in Höflich P., Kumer P., Wheeler J. C., eds., 'Cosmic Explosions in Three Dimensions'. Cambridge University Press, p. 57

Germany L. M., Reiss D. J., Sadler E. M., Schmidt B. P., Strubbs C. W., 2000, ApJ, 533, 320

Gingerich O., 2005, in Turatto M., Benetti S., Zampieri L., Shea W., eds., Supernovae as Cosmological Lighthouses. ASP, San Francisco, p. 3

Gómez G., López R., 1994, AJ, 108, 195

Gómez G., López R., 2002, AJ, 123, 328

Goodrich R. W., Stringfellow G. S., Penrod G. D., Filippenko A. V., 1989, ApJ, 342, 908

Greggio L., 2005, A&A, 441, 1055

Hachinger S., 2007, Diploma thesis, Technische Universität München

Hachinger S., Mazzali P. A., Benetti S., 2006, MNRAS, 370, 299

Hamuy M., 2003, ApJ, 582, 905

Hamuy M. et al., 1992, PASP, 104, 533

Hamuy M. et al., 1994, PASP, 106, 566

Hamuy M., Phillips M. M., Schommer R. A., Suntzeff N. B., Maza J., Avilés R., 1996a, AJ, 112, 2391

Hamuy M., et al., 1996b, AJ, 112, 2408

Hamuy M., Phillips M. M., Suntzeff N. B., Schommer R. A., Maza J., Smith R. C., Lira P., Avilés R., 1996c, AJ, 112, 2438

Hamuy M., Trager S. C., Pinto P. A., Phillips M. M., Schommer R. A., Ivanov V., Suntzeff N. B., 2000, AJ, 120, 1479

Hamuy M., et al., 2002, AJ, 124, 417

Hamuy M., et al., 2003, Nature, 424, 651

Harkness R. P., et al., 1987, ApJ, 317, 355

Harutyunyan A., et al., 2008, A&A submitted

Hatano K., Branch D., Fisher A., Baron E., Filippenko A. V., 1999, ApJ, 525, 881

Hicken M., Garnavich P. M., Prieto J. L., Blondin S., DePoy D. L., Kirshner R. P., Parrent J., 2007, ApJ, 669, L17

Hillebrandt W., Niemeyer J. C., 2000, ARA&A, 38, 191

Hillebrandt W., Sim S. A., Röpke F. K., 2007, A&A, 465, L17

Höflich P., Khokhlov A., 1996, ApJ, 457, 500

Höflich P., Gerardy C. L., Fesen R. A., Sakai S., 2002, ApJ, 568, 791

Horne K., 1986, PASP, 98, 609

Hough J. H., Bailey J. A., Rouse M. F., Whittet D. C. B., 1987, MNRAS, 227, 1

Howell D. A., 2001, ApJ, 554, L193

Howell D. A., Höflich P., Wang L., Wheeler J. C., 2001, ApJ, 556, 302

Howell D. A., et al., 2006, Nature, 443, 308

Hoyle F. & Fowler W. A., 1960, ApJ, 132, 565

Hunt I. K., Mannucci F., Testi F., Migliorini S., Stanga R. M., Baffa C., Lisi F., Vanzi L., 1998, AJ, 115, 2594

Hurley K., Briggs M. S., Kippen R. M., Kouveliotou C., Meegan C., Fishman G., Cline T., Boer M., 1999, ApJS, 120, 399

Iben I. Jr., Tutukov A. V., 1984, ApJS, 54, 335

Iwamoto K., et al., 2000, ApJ, 534, 660

Janka H.-T., Scheck L., Kifonidis K., Müller E., Plewa T., 2005, in Humphreys R., Stanek K., eds, ASP Conference Series, Vol. 332. San Francisco: Astron. Society of the Pacific, p. 372

Janka H.-T., Langanke K., Marek A., Martínez-Pinedo G., Müller B., 2007, PhR, 442, 38

Jeffery D. J., Branch D., Filippenko A. V., & Nomoto K., 1991, ApJ, 377, L89

Jha S., et al., 2006a, AJ, 131, 527

Jha S., Branch D., Chornock R., Foley R. J., Li W., Swift B. J., Casebeer D., Filippenko A. V., 2006b, AJ, 132, 189

Jordi K., Grebel E. K., Ammon K., 2006, A&A, 460, 339

Kasen D., 2006, ApJ, 649, 939

Kasen D., Plewa T., 2005, ApJ, 622, L41

Kasen D., Plewa T., 2007, ApJ, 662, 459

Kasen D., Woosley S. E., 2007, ApJ, 656, 661

Kawabata K. S., et al., 2002, ApJ, 580, L39

Khokhlov A. M., 1991, A&A, 245, 114

Kifonidis K., Plewa T., Scheck L., Janka H.-T., Müller E., 2006, A&A, 453, 661

Kippenhahn R., Weigert A., 1967, ZA, 65, 251

Kirshner R. P., Oke J. B., 1975, ApJ, 200, 574

Kobayashi C., Tsujimoto T., Nomoto K., Hachisu I., Kato M., 1998, ApJ, 503, L155

Kotak R., et al., 2005, A&A, 436, 1021

Krisciunas K., et al., 2001, AJ, 122, 1616

Krisciunas K. et al., 2003, AJ, 125, 166

Krisciunas K., et al., 2004, AJ, 128, 3034

Krisciunas K., Prieto J. L., Garnavich P. M., Riley J.-L. G., Rest A., Stubbs C., McMillan R., 2006, AJ, 131, 1639

Landolt A. U., 1992, AJ, 104, 340

Leibundgut B., 2000, A&ARv, 10, 179

Leibundgut B., 2001, ARA&A, 39, 67

Leibundgut B., Suntzeff N. B., in "Supernovae and Gamma-Ray Bursters", Weiler K. W., ed, series: Lecture Notes in Physics, vol. 598, Springer, Berlin, p. 77

Leibundgut B., Kirshner R. P., Pinto P. A., Rupen M. P., Smith R. C., Gunn J. E., Schneider D. P., 1991, ApJ, 372, 531

Leibundgut B., et al., 1993, AJ, 105, 301

Leonard D. C., Filippenko A. V., Chornock R., Foley R. J., 2002, PASP, 114, 1333

Leonard D. C., Li W., Filippenko A. V., Foley R. J., Chornock R., 2005, ApJ, 632, 450

Li W., Filippenko A. V., Treffers R. R., Riess A. G., Hu J., Qiu Y., 2001a, ApJ, 546, 734

Li W., et al., 2001b, PASP, 113, 1178

Li W., et al., 2003, PASP, 115, 453

Lira P., 1995, Master thesis, Univ. Chile

Livio M., 2000, in Niemeyer J. C., Truran J. W., eds., Type Ia Supernovae, Theory and Cosmology. Cambridge University Press, p. 33

Lombardi A., 2005, in Turatto M., Benetti S., Zampieri L., Shea W., eds., Supernovae as Cosmological Lighthouses. ASP, San Francisco, p. 21

Lucy L. B., 1991, ApJ, 383, 308

Lucy L. B., 1999, A&A, 345, 211

Lucy L. B., Danziger I. J., Gouiffes G., Bouchet P., 1989, in Tenorio-Tagle G., Moles M., Melnick J., eds, Proceedings of IAU Colloquium 120 "Structure and Dynamics of the Interstellar Medium". Springer, Berlin, p. 164

Lundmark K., 1920, Sven. Vet. Handlingar, 60, 8

Lyutikov M., Blackman E. G., 2001, MNRAS, 321, 177

MacFadyen A. I., Woosley, S. E., 1999, ApJ, 524, 262

McKenzie E. H., Schaefer B. E., 1999, PASP, 111, 964

McNaught R. H., 1991, IAUC 5179, 3

Maeda K., Nakamura T., Nomoto K., Mazzali P. A., Patat F., Hachisu I., 2002, ApJ, 565, 405

Maeda K., Nomoto K., Mazzali P. A., Deng J., 2006, ApJ, 640, 854

Maeda K., et al., 2007, ApJ, 658, L5

Maeda K., et al., 2008, Science submitted (arXiv:0801.1100)

Mannucci F., Della Valle M., Panagia N., 2006, 370, 773

Massey P., 1997, A User's Guide to CCD Reductions with IRAF, http://iraf.noao.edu/docs/recommend.html

Massey P., Valdes F., Barnes J., 1992, A User's Guide to Reducing Slit Spectra with IRAF, http://iraf.noao.edu/docs/recommend.html

Matheson T., Filippenko A. V., Ho L. C., Barth A. J., Leonard D. C., 2000, AJ, 120, 1499

Matheson T., Filippenko A. V., Li W. D., Leonard D. C., Shields J. C., 2001, AJ, 121, 1648

Matheson T., Challis P., Kirshner R., 2004, IAUC 8311

Matheson T., et al., 2008, AJ accepted

Matthews K., Neugebauer G., Armus L., Soifer B. T., 2002, AJ, 123, 753

Mazzali P. A., 2000, A&A, 363, 705

Mazzali P. A., Lucy L. B., 1993, A&A, 279, 447

Mazzali P. A., Lucy L. B., 1998, MNRAS, 295, 428

Mazzali P. A., Podsiadlowski P., 2006, MNRAS, 369, L19

Mazzali P. A., Danziger I. J., Turatto M., 1995, A&A, 297, 509

Mazzali P. A., Chugai N., Turatto M., Lucy L. B., Danziger I. J., Cappellaro E., Della Valle M., Benetti S., 1997, MNRAS, 284, 151

Mazzali P. A., Iwamoto K., Nomoto K., 2000, ApJ, 545, 407

Mazzali P. A., Nomoto K., Patat F., Maeda K., 2001, ApJ, 559, 1047

Mazzali P. A., et al., 2002, ApJ, 572, L61

Mazzali P. A., Deng J., Maeda K., Nomoto K., Filippenko A. V., Matheson T., 2004, ApJ, 614, 858

Mazzali P. A., Nomoto K., Deng J., Maeda K., Tominaga N., 2005a, ASPC, 342, 366

Mazzali P. A., et al., 2005b, Sci, 308, 1284

Mazzali P. A., Benetti S., Stehle M., Branch D., Deng J., Maeda K., Nomoto K., Hamuy M., 2005c, MNRAS, 357, 200

Mazzali P. A., et al., 2005d, ApJ, 623, L37

Mazzali P. A. et al., 2006, Nature, 442, 1018

Mazzali P. A., et al., 2007a, ApJ, 661, 892

Mazzali P. A., et al., 2007b, ApJ, 670, 592

Mazzali P. A., Röpke F. K., Benetti S., Hillebrandt W., 2007c, Sci, 315, 825

Mezzacappa A., 2005, Ann. Rev. Nucl. Part. Sci., 55, 467

Millard J., et al., 1999, ApJ, 527, 746

Minkowski R., 1941, PASP, 53, 224

Modjaz M., Halderson E., Shefler T., King J. Y., Li W. D., Treffers R. R., Filippenko A. V., 1998, IAUC 6977, 1

Modjaz M., Li W., Filippenko A. V., King J. Y., Leonard D. C., Matheson T., Treffers R. R., Riess A. G., 2001, PASP, 113, 308

Modjaz M., Kirshner R. P., Challis P., 2008, ApJL submitted (arXiv:0801.0221)

Morrell N., Folatelli G., Phillips M., Contreras C., Hamuy M., 2005, IAUC 8514, 2

Nakamura T., Nomoto K., Iwamoto K., Umeda H., Mazzali P. A., Danziger I. J., 2000, MmSAI, 71, 345

Niemeyer J. C., 1999, ApJ, 523, L57

Nishihara E., Kinugasa K., Hashimoto O., Okuda H., Yamaoka H., 2002, in Ikeuchi J., Hearnshaw J., Hanawa T., eds., Proc. of the IAU 8th Asian-Pacific Regional Meeting, Vol. II. The Astronomical Society of Japan, p. 347

Nomoto K., 1980, Space Sci. Rev., 27, 563

Nomoto K., Thielemann F.-K., Yokoi K., 1984, ApJ, 286, 644

Nomoto K., Filippenko A. V., Shigeyama T., 1990, A&A, 240, L1

Nomoto K., Yamaoka H., Pols O. R., van den Heuvel E. P. J., Iwamoto K., Kumagai S., Shigeyama T., 1994, Nature, 371, 227

Nomoto K., Maeda K., Umeda H., Ohkubo T., Deng J., Mazzali P. A., 2003, in van der Hucht K. A., Herrero A., Esteban C., eds., Proc. of IAU Symposium No. 212. Astron. Soc. of the Pacific, San Francisco, p. 395

Nomoto K., Maeda K., Tominaga N., Ohkubo T., Deng J., Mazzali P. A., 2005, Ap&SS, 298, 81

Nomoto K., Saio H., Kato M., Hachisu I., 2007, ApJ, 663, 1269

Nugent P., Phillips M., Baron E., Branch D., Hauschildt P., 1995, ApJ, 455, L147

O'Donnell J. E., 1994, ApJ, 422, 158

Oke J. B., 1990, AJ, 99, 1621

Oliva E., 1987, ApJ, 321, L45

Paczyński B., 1985, in Lamb D. Q., Patterson J., eds., Cataclysmic variables and low-mass X-ray binaries. Astrophysics and Space Science Lib. 113, p. 1

Paczyński B., 1998a, American Institute of Physics Conference Series, 428, 783

Paczyński B., 1998b, ApJ, 494, L45

Pandey S. B., Anupama G. C., Sagar R., Bhattacharya D., Sahu D. K., Pandey J. C., 2003b, MNRAS, 340, 375

Pandey S. B., Sahu D. K., Anupama G. C., Bhattacharya D., Sagar R., 2003a, BASI, 31, 351

Pastorello A., 2003, PhD thesis, Osservatorio Astronomico di Padova

Pastorello A., et al., 2007a, MNRAS, 376, 1301

Pastorello A., et al., 2007b, MNRAS, 377, 1531

Pastorello A., et al., 2007c, Nature, 447, 829

Pastorello A., et al., 2008, MNRAS submitted (arXiv:0801.2277)

Patat F., Chugai N., Mazzali P. A., 1995, A&A, 299, 715

Patat F., et al., 2001, ApJ, 555, 900

Patat F. et al., 2007, Science, 317, 924

Patil M. K., PandeyS. K., Sahu D. K., Kembhavi A., 2007, A&A, 461, 103

Perlmutter S. et al., 1997, ApJ, 483, 565

Perlmutter S. et al., 1998, Nature, 392, 311

Perlmutter S. and the Supernova Cosmology Project, 1999, ApJ, 517, 565

Pfannes J. M. M., 2006, PhD thesis, Bayerische Julius-Maximilians-Univ., Würzburg, http://www.astro.uni-wuerzburg.de/∼pfannes/

Phillips M M., 1993, ApJ, 413, 105

Phillips M. M., Phillips A. C., Heathcote S. R., Blanco V. M., Geisler D., Hamilton D., Suntzeff N. B., 1987, PASP, 99, 592

Phillips M. M., Wells L. A., Suntzeff N. B., Hamuy M., Leibundgut B., Kirshner R. P., Foltz C. B., 1992, AJ, 103, 1632

Phillips M. M., Lira P., Suntzeff N. B., Schommer R. A., Hamuy M., Maza J., 1999, AJ, 118, 1766

Phillips M. M., et al., 2006, AJ, 131, 2615

Pian E. et al., 2006, Nature, 442, 1011

Pignata G., 2004, PhD thesis, Univ. Padova (Italy)

Pignata G., et al., 2004, MNRAS, 355, 178

Pignata G., et al., 2008, in prep.

Plewa T., Calder A. C., Lamb D. Q., 2004, ApJ, 612, L37

Plewa T., 2007, ApJ, 657, 942

Porter A. C., Dickinson M., Stanford S. A., Lada E. A., Fuller G. A., Myers P. C., 1992, AAS, 181, 7607

Pozzo M. et al., 2006, MNRAS, 368, 1169

Pskovskii Y. P., 1984, SvA, 28, 658

Puckett T., Langoussis A., 2005, IAUC 8515, 3

Richardson D., Branch D., Baron E., 2006, AJ, 131, 2233

Richmond M. W., et al., 1996, AJ, 111, 327

Riess A. G., Press W. H., Kirshner R. P., 1996, ApJ, 473, 88

Riess A. G. et al., 1998, AJ, 116, 1009

Riess A. G., et al., 1999, AJ, 118, 2675

Riess A. G. et al., 2004, ApJ, 607, 665

Riess A. G., et al., 2007, ApJ, 659, 98

Röpke F. K., 2005, A&A, 432, 969

Röpke F. K., 2007, ApJ, 668, 1103

Röpke F. K., Niemeyer J. C., 2007, A&A, 464, 683

Röpke F. K., Woosley S. E., Hillebrandt W., 2007, ApJ, 660, 1344

Röpke F. K., Hillebrandt W., Schmidt W., Niemeyer J., Blinnikov S. I., Mazzali P. A., 2007, ApJ, 668, 1132

Ruiz-Lapuente P., Cappellaro E., Turatto M., Gouiffes C., Danziger I. J., Della Valle M., Lucy L. B., 1992, ApJ, 387, L33

Ruiz-Lapuente P., et al., 1993, Nature, 365, 728

Saffer R. A., Livio M., Yungelson L. R., 1998, ApJ, 502, 394

Sahu D. K., Tanaka M., Anupama G. C., Kawabata K. S., Maeda K., Tominaga N., Nomoto K., Mazzali P. A., 2007, arXiv e-print (arXiv:0710.3636)

Salvo M. E., 2006, PhD thesis, The Australian National University

Salvo M. E., et al., 2008, in prep.

Sauer D., Mazzali P. A., Deng J., Valenti S., Nomoto K., Filippenko A. V., 2006, submitted to MNRAS

Savage B. D. & Mathis J. S., 1979, Ann. Rev. Astr. Ap., 17, 73

Scheck L., Plewa T., Janka H.-T., Kifonidis K., Müller E., 2004, PhRvL, 92, 963

Scheck L., Kifonidis K., Janka H.-T., Müller E., 2006, A&A, 457, 1103

Schlegel D. J., Finkbeiner D. P., Davis M., 1998, ApJ, 500, 525

Seaton M. J., 1979, MNRAS, 187, 73

Sharina M. E., Karachentsev I. D., Tikhonov N. A., 1996, A&AS, 119, 499

Shea W., 2005, in Turatto M., Benetti S., Zampieri L., Shea W., eds., Supernovae as Cosmological Lighthouses. ASP, San Francisco, p. 13

Shimasaki K., Li W., 2005, IAUC 8512, 2

Sim S. A., Sauer D. N., Röpke F. K., Hillebrandt W., 2007, MNRAS, 378, 2

Smith J. A., at al., 2002, AJ, 123, 2121

Smith N., Foley R. J., Filippenko A. V., 2007, arXiv e-print (arXiv:0704.2249v1)

Soderberg A. M., Nakar E., Berger E., Kulkarni S. R., 2006, ApJ, 638, 930

Sollerman J., Leibundgut B., Spyromilio J., 1998, A&A, 337, 207

Sollerman J., et al., 2002, A&AS, 386, 944

Spergel D. N., et al., 2003, ApJS, 148,175

Spyromilio J., 1994, MNRAS, 266, L61

Spyromilio J., Pinto P. A., 1991, in Danziger I. J., Kjär K., eds, Proceedings to the ESO/EIPC Workshop "Supernova 1987A and other supernovae". ESO, Garching, p. 423

Stanishev V., 2007, AN, 328, 948

Stanishev V., et al., 2007a, American Institute of Physics Conference Series, 924, 336

Stanishev V., et al., 2007b, A&A, 469, 645

Stehle M., 2004, PhD thesis, Technische Universität München

Stehle M., Mazzali P. A., Benetti S., Hillebrandt W., 2005, MNRAS, 360, 1231

Stephenson F. R., Green D. A., 2005, in Turatto M., Benetti S., Zampieri L., Shea W., eds., Supernovae as Cosmological Lighthouses. ASP, San Francisco, p. 63

Stritzinger M., et al., 2002, AJ, 124, 2100

Stritzinger M., Mazzali P. A., Sollermann J., Benetti S., 2006, A&A, 460, 793

Strovink M., 2007, ApJ, 671, 1084

Suntzeff N. B., 1996, in McCray R., Wang Z., eds, AU Colloquium 145 'Supernovae and Supernova Remnants'. Cambridge: University Press, p. 200

Suntzeff N. B., 2000, American Institute of Physics Conference Series, 522, 65

Swartz D. A., Filippenko A. V., Nomoto K., Wheeler J. C., 1993, ApJ, 411, 313

Tanaka M., et al., 2007, ApJ accepted (arXiv:0712.2823)

Taubenberger S. et al., 2006, MNRAS, 371, 1459

Taubenberger S., et al., 2007, MNRAS accepted (arXiv:0711.4548)

Thomas R. C., et al., 2007, ApJ, 654, L53

Tominaga N., Deng J., Mazzali P. A., Maeda K., Nomoto K., Pian E., Hjorth J., Fynbo J. P. U., 2004, ApJ, 612, L105

Tomita H., et al., 2006, ApJ, 644, 400

Tonry J. L., Dressler A., Blakeslee J. P., Ajhar E. A., Fletcher A. B., Luppino G. A., Metzger M. R., Moore C. B., 2001, ApJ, 546, 681

Tornambé A., Piersanti L., 2005, in Turatto M., Benetti S., Zampieri L., Shea W., eds., Supernovae as Cosmological Lighthouses. ASP, San Franc., p. 169

Toth I., Szabo R., 2000, A&A, 361, 63

Tsvetkov D. Y., 1986, SvAL, 12, 328

Tsvetkov D. Y., Pavlyuk N. N., 1995, AstL, 21, 606

Turatto M., 2000, MmSAI, 71, 573

Turatto M., 2003, in "Supernovae and Gamma-Ray Bursters", Weiler K. W., ed, series: Lecture Notes in Physics, vol. 598, Springer, Berlin, p. 21

Turatto M., Benetti S., Cappellaro E., Danziger I. J., Della Valle M., Gouiffes C., Mazzali P. A., Patat F., 1996, MNRAS, 283, 1

Turatto M., Piemonte A., Benetti S., Cappellaro E., Mazzali P. A., Danziger I. J., Patat F., 1998, AJ, 116, 2431

Turatto M., et al., 2000, ApJ, 534, L57

Turatto M., Benetti S., Cappellaro E., 2003, in Hillebrandt W., Leibundgut B., eds., Proceedings to the ESO/MPA/MPE Workshop 'From Twilight to Highlight: The Physics of Supernovae'. Springer, Berlin, p. 200

Turatto M., Benetti S., Pastorello A., 2007, American Institute of Physics Conference Series, 924, 187

Uomoto A., Kirshner R. P., 1985, A&A, 149, L7

Valenti S., et al., 2007a, MNRAS, 383, 1485

Valenti S., et al., 2007b, ApJ, ApJ, 673, L155

van den Bergh, S., 1994, ApJ, 424, 345

van den Bergh S., Li W., Filippenko A. V., 2005, PASP, 117, 773

Vietri M., Stella L., 1998, ApJ, 507, L45

Vinkó J., Kiss L. L., Csák B., Fűrész G., Szabó R., Thomson J. R., Mochnacki S. W., 2001, AJ, 121, 3127

Wainscoat R. J., Cowie L. L., 1992, AJ, 103, 332

Wang L., Howell D. A., Höflich P., Wheeler J. C., 2001, ApJ, 550, 1030

Wang L., et al., 2003, ApJ, 591, 1110

Wang L., Baade D., Höflich P., Wheeler J. C., Kawabata K., Khokhlov A., Nomoto K., Patat F., 2006, ApJ, 653, 490

Wang X., et al., 2007, ApJ accepted (arXiv:0708.0140)

Wang Z., 2005, in Turatto M., Benetti S., Zampieri L., Shea W., eds., Supernovae as Cosmological Lighthouses. ASP, San Francisco, p. 48

Weaver T. A., Woosley S. E., 1980, American Institute of Physics Conference Series, 63, 15

Webbink R. F., 1984, ApJ, 277, 355

Wheeler J. C., Harkness R. P., 1990, RPPh, 53, 1467

Wheeler J. C., Levreault R., 1985, ApJ, 294, L17

Wheeler J. C., Harkness R. P., Barker E. S., Cochran A. L., Wills D., 1987, ApJ, 313, L69

Wheeler J. C., Yi I., Höflich P., Wang L., 2000, ApJ, 537, 810

Woosley S. E., 1980, in Wheeler J. C., ed., Texas Workshop on Type I Supernovae. Univ. Texas, Austin, p. 96

Woosley S. E., 1993, ApJ, 405, 273

Woosley S. E., Bloom J. S., 2006, ARA&A, 44, 507

Woosley S. E., Heger A., 2006, ApJ, 637, 914

Woosley S. E., Janka H. Th., 2005, Nat. Phys., 3, 147

Woosley S. E., Weaver T. A., 1986, ARA&A, 24, 205

Woosley S. E., Weaver T. A., 1994, in Bludman S. A., Mochkovitch R., Zinn-Justin J., eds., NATO ASI Series C, Supernovae. Elsevier Science, Amsterdam / New York, p. 63

Xu D., Zou Y.-C., Fan Y.-Z., 2008, arXiv e-print (arXiv:0801.4325)

Yokoo T., Arimoto J., Matsumoto K., Takahashi A., Sadakane K., 1994, PASJ, 46L, 191

Yoshii Y., et al., 2003, ApJ, 592, 467

Zhao C., Newberg H. J., 2006, arXiv e-print (astro-ph/0612034)

Zwicky F., 1964, Annales d'Astrophysique, 27, 300

Acknowledgments

I am indebted to my supervisor, Prof. Wolfgang Hillebrandt, for his guidance, encouragement and patience during the last three years. While always keeping an eye on the progress of my work, he granted me a high degree of scientific freedom, enabling me to pursue my own research interests.

I am also grateful to my numerous collaborators at MPA and many other places around the world, for providing their advice and technical expertise. Special thanks goes to the visiting observers and the staff teams at the various telescopes who collected the data presented and analysed in this thesis. Without their dedication, research of this kind would not be possible.

The last couple of years at MPA have been enriched by the friendship with many great colleagues. Thank you everyone, and in particular thank you, Nancy and Stephan, for your mental and practical support during the writing-up of this thesis.

Last but not least, I am extremely grateful to my parents and my grandmother. Without your support, your encouragement and your open ears for my concerns, I may not have travelled this path.